FIELD EMISSION SENSING

FOR NON-CONTACT PROBE RECORDING

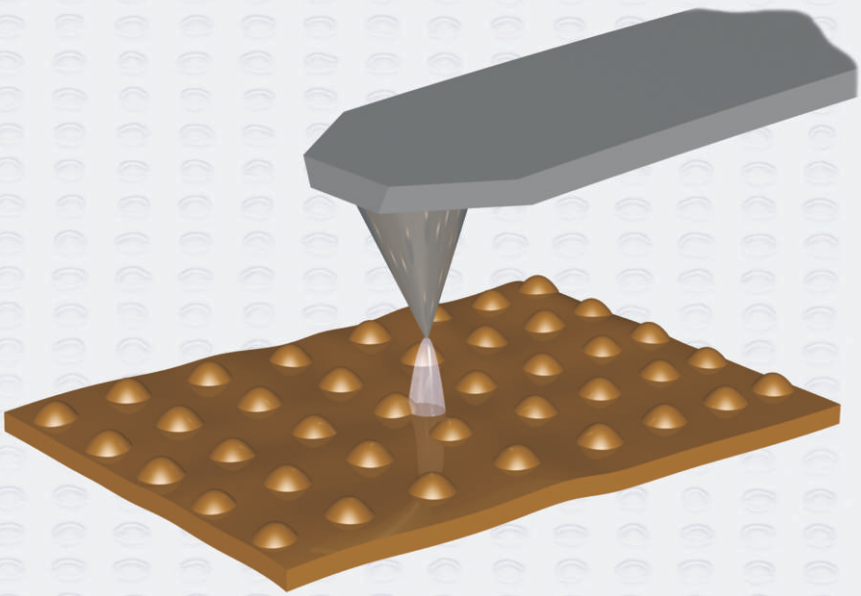

Alexander le Fèbre

Cover:

In the micro scanning probe array memory (μSPAM) concept, magnetic probes are used to write and read on a patterned recording medium. A single probe consists of a sharp tip on a flexible cantilever, that is used to detect the small magnetic forces from its bending. By maintaining a constant current of electrons, field emitted from the probe tip to the conducting medium, the distance between the tip apex and the patterned sample can be controlled, also when scanning over the medium surface. For experimental demonstration of this method, we used a scanning probe microscope mounted inside an ultra-high vacuum system, which is depicted on the back cover.

FIELD EMISSION SENSING FOR NON-CONTACT PROBE RECORDING

Promotiecommissie:

Voorzitter, secretaris	Prof. dr. A.J. Mouthaan	Universiteit Twente
Promotor	Prof. dr. J.C. Lodder	Universiteit Twente
Assistent promotor	Dr. ir. L. Abelmann	Universiteit Twente
Leden	Prof. dr. ir. G.J.M. Krijnen	Universiteit Twente
	Prof. dr. ir. H.J.W. Zandvliet	Universiteit Twente
	Prof. dr. T. Thomson	University of Manchester, UK
	Dr. ir. T.H. Oosterkamp	Universiteit Leiden
	Prof. dr. P.J. French	Technische Universiteit Delft

The research described in this thesis was carried out in the Systems and Materials for Information storage group (SMI) and the Transducer Science and Technology group (TST) at the MESA$^+$ Institute for Nanotechnology of the University of Twente. It was funded by the Dutch Technology Foundation (STW) within the framework of the project 'A high capacity, low volume Scanning Probe Array Memory for application in embedded systems (TES 5178)'.

Published by the Transducer Science and Technology group, University of Twente
P.O. Box 217, 7500 AE, Enschede, The Netherlands.

Printed by Koninklijke Wöhrmann, Zutphen, The Netherlands.

Field emission sensing for non-contact probe recording
ISBN 978-90-8570-300-6

FIELD EMISSION SENSING FOR NON-CONTACT PROBE RECORDING

PROEFSCHRIFT

ter verkrijging van
de graad van doctor aan de Universiteit Twente,
op gezag van de rector magnificus,
prof. dr. W.H.M. Zijm,
volgens besluit van het College voor Promoties
in het openbaar te verdedigen
op vrijdag 28 maart 2008 om 15.00 uur

door

Alexander Jonathan le Fèbre
geboren op 6 oktober 1977
te Apeldoorn

Dit proefschrift is goedgekeurd door

de promotor:	Prof. dr. J.C. Lodder
en de assistent promotor:	Dr. ir. L. Abelmann

Abstract

In probe recording an array of thousands of nanometer-sharp probes is used to write and read on a storage medium. By using micro-electromechanical system technology (MEMS) for fabrication, small form factor memories with high data density and low power consumption can be obtained. Such a system is expected to offer a promising route towards extremely high-density recording, with bits of several nanometer or even atomic size. To reach these densities, individual control over the position of the probes is essential, to be able to operate the probes in non-contact as is for instance done in scanning tunneling microscopy (STM).

At the MESA$^+$ Institute for Nanotechnology at the University of Twente, we currently investigate the possibilities of probe recording using a magnetic medium. In the micro scanning probe array memory (μSPAM) concept, an array of magnetic probes is used to write and read on a patterned recording medium. In such a probe storage system, there is also a need to position individual probes at several nanometers above the recording medium, to be able to detect the small magnetic forces. For this non-contact operation, individual z-feedback should be achieved by integration of an actuator, proximity sensor and feedback loop for each probe of the probe array. As reported in literature, the fabrication of probe arrays and integration of actuators and logic circuitry have already been proven to be attainable, however current research still lacks a proximity sensor with sufficient lateral resolution that can be integrated in each probe.

The objective of this thesis is to investigate whether field-emission can be used as an integrated method to control probe-medium distance for non-contact probe recording. Field emission can be used as a proximity sensing method, since the emission current varies exponentially with the electric field, which in turn is proportional to the electrode gap. The lateral resolution is determined by the probe tip radius, on the same order as the targeted bit size of about 10 nm. The signal to noise ratio is not affected by the small sensing area, which is an important advantage over other sensing methods. Moreover it provides an elegant solution for the problem of sensor integration in each probe of the array, since only one wire per probe is needed to connect to the field emitting tip.

In this thesis, a theoretical model was developed to determine the dependence of

the field emission current on the distance between the field emitter tip and a counter-electrode. The field emission current for a constant electric field is calculated using the model introduced by Fowler and Nordheim, treating the effect as quantum-mechanical tunneling of the electrons through the surface potential barrier. We identified that the distance dependence of this current is mainly associated with the variation in the shape of the electric field when the tip is approached to or retracted from the sample, which can be described by the field enhancement factor. To find an expression for this factor as function of distance, we used finite element calculations. The results were approximated by an analytical relation that can be used to predict the sensitivity for probe-medium distance control.

For experimental demonstration of the method of field emission sensing, an ultra-high vacuum (UHV) scanning probe microscope was assembled, improved and tested. The system is operated in vacuum conditions to prevent instabilities in the field emission current, which occur due to ion bombardment of the tip and surface migration of adsorbed molecules. Vibration isolation is applied to avoid mechanical coupling from the environment. The field emission characteristics were measured for two types of probes: one custom made with a fixed tip on a substrate base and the other a commercially available atomic force microscopy (AFM) probe with the tip on a cantilever. By measuring current-voltage characteristics for nanometer distances, the dependence of the field emission effect on distance could be investigated. From the measurement results for both probe types the variation in field enhancement was deduced, by fitting the measurements to Fowler-Nordheim theory. An iterative fitting procedure was developed to calculate the right error correction factors in the Fowler-Nordheim relation and determine the emission area and the field enhancement factor. It was found that the general dependence of the field emission effect on distance is correctly described by our model and is a function of the exact emitter geometry and the tip radius.

Cantilever probes are used in the concept of magnetic probe recording, to be able to sense the small magnetic forces by shifts in the resonance frequency. The bending behaviour of the cantilever was calculated using a model for the electrostatic interaction between the probe and the samples, showing that a probe with a high spring constant will only deflect a few nanometers before the current set-point is reached, whereas a probe with a low spring constant snaps to the surface before the tip starts emitting. This behaviour was confirmed by measurements in a modified fiber interferometer atomic force microscope: a high spring constant of the cantilever is sufficient to limit the cantilever deflection and prevent pull-in.

By operating the probes in constant current mode and varying the applied voltage, it is possible to control the tip-sample distance. The sensitivity of this positioning method depends strongly on the variation in field enhancement and therefore on the specific emitter geometry. At low voltage, the probe is close to the sample and the field enhancement factor is ~ 1. By increasing the voltage the probe is retracted and the field enhancement increases, resulting in a higher sensitivity. Although the positioning accuracy and repeatability was found to be rather limited by instabilities in the current, the main outcome of these measurements is that the field emission current signal can

indeed be used for position control.

In order to test the method of using field emission currents for high-resolution lateral positioning, special patterned samples with well-defined topography were made. Laser interference lithography in combination with reactive ion etching was used to create patterns of dots with small periodicities of 160 - 280 nm and thin-film metal coatings were applied to improve the conductivity. Bias-dependent imaging was used to scan on these conducting patterned samples for increasing probe-sample distance. As a result of the tip-sample separation becoming larger, the lateral resolution reduces, but at 50 V the resolution is still sufficient to detect features of ~ 20 nm on the sample. Scanning at higher voltage allows higher scan rates compared to scanning in the tunneling regime, by increasing the average tip-sample distance beyond the height of the dots on the sample. Two damaging effects have to be prevented when using field emission currents during scanning: ablation of the tip and sample surfaces due to large current peaks and electron-beam induced deposition of contaminants. These effects can be prevented by using a large resistor in the current path to limit the capacitive discharge currents and by annealing the probe and sample under UHV conditions before use.

As a general conclusion of this work, the measurements confirm that field emission can be applied to control the spacing between probe and medium, with sufficient resolution needed for probe storage applications. The applicability of field emission currents in a practical probe recording device is however seriously limited due to the stringent requirements of UHV conditions and ultra-clean surfaces and the short emitter lifetime. Since the sensitivity depends on the material work function, tip radius and emitter geometry, very uniform emitters are required to prevent the need for individual calibration when using an array of probes. For practical applications, the current stability and emitter lifetime should be further improved in order to increase the accuracy and reproducibility of positioning also in poor vacuum conditions.

Samenvatting

In een op probes gebaseerd geheugen wordt een rooster van duizenden nanometer-scherpe naaldjes (probes) gebruikt om te schrijven en te lezen in een opslagmedium. Door gebruik te maken van micro elektromechanische systeemtechnologie (MEMS) voor de fabricage kunnen klein formaat geheugens met een hoge informatiedichtheid en een laag energieverbruik worden verkregen. Van zo'n systeem wordt verwacht dat het een veelbelovende weg is naar opslag met extreem hoge dichtheid, met bits van een paar nanometer of zelfs atomaire grootte. Om deze dichtheden te bereiken is het essentieel om controle te hebben over de positie van elke afzonderlijke probe, om de probes te kunnen gebruiken zonder dat zij contact maken met het medium, zoals bijvoorbeeld wordt gedaan in raster tunnel microscopie (STM).

In het MESA$^+$ Instituut voor Nanotechnologie op de Universiteit Twente onderzoeken we de mogelijkheden voor probe recording met gebruikmaking van een magnetisch medium. In het model van de micro Scanning Probe Array Memory (μSPAM) wordt een rooster van magnetische probes gebruikt om in een gepatroneerd opslagmedium te schrijven. In zo'n op probes gebaseerd geheugen-systeem is het eveneens noodzakelijk om individuele probes te kunnen positioneren op enkele nanometers afstand boven het opslagmedium, om zo de kleine magnetische krachten te kunnen detecteren. Voor deze contactloze methode moet individuele z-regeling worden verkregen door het integreren van een actuator, een afstandssensor en een regellus voor elke probe in het probe rooster. Zoals in de literatuur is beschreven, is al aangetoond dat het maken van parallelle probes en het integreren van actuatoren en elektronica realiseerbaar is, maar in de huidige stand van onderzoek ontbreekt nog een afstandssensor met voldoende laterale resolutie die in elke probe zou kunnen worden geïntegreerd.

Het doel van dit proefschrift is te onderzoeken of veldemissie kan worden gebruikt als een geïntegreerde methode om de afstand tussen probe en medium constant te houden voor probe-gebaseerde opslag en te voorkomen dat de probe in contact komt met het opslagmedium. Veldemissie kan worden gebruikt voor afstandsdetectie, omdat de emissie-stroom exponentieel varieert met het elektrische veld, dat weer een functie is van de afstand tussen de elektrodes. De laterale resolutie wordt bepaald door de straal van het probe-uiteinde en is in dezelfde orde van grootte als bits van ongeveer 10 nanometer.

De signaal/ruis-verhouding wordt niet beïnvloed door het kleine waarnemingsoppervlak, wat een belangrijk voordeel is boven andere meetmethodes. Bovendien biedt het een elegante oplossing voor het probleem van het integreren van een sensor in elke afzonderlijke probe van het rooster, aangezien er slechts een draad per probe nodig is om elektrisch contact te maken met de veldemissie tip.

In dit proefschrift is een theoretisch model ontwikkeld om te bepalen in hoeverre de veldemissie-stroom afhangt van de afstand tussen de veldemissie tip en een tegen-elektrode. De veldemissie-stroom voor een constant elektrisch veld wordt berekend met gebruikmaking van het theoretische Fowler-Nordheim model, dat het effect behandelt als het kwantummechanisch tunnelen van elektronen door de potentiaal-barrière van het oppervlak. We hebben ontdekt dat de afstandsafhankelijkheid van deze stroom vooral bepaald wordt door de variatie in de vorm van het elektrische veld die optreedt als de tip het sample nadert, of juist teruggetrokken wordt van het sample, wat kan worden beschreven door de veldversterkingsfactor. Om te bepalen hoe deze factor als functie van afstand varieert, hebben we gebruik gemaakt van eindige-elementen berekeningen. De resultaten zijn benaderd door een analytische relatie die kan worden gebruikt om de gevoeligheid voor het beheersen van de afstand tussen probe en medium te voorspellen.

Om te kunnen meten aan deze methode van veldemissie-detectie, werd een ultra hoog vacuüm (UHV) scanning probe microscoop geïnstalleerd, verbeterd en getest. Het systeem wordt gebruikt in vacuümcondities om te voorkomen dat de veldemmissie-stroom instabiel wordt, hetgeen optreedt als gevolg van beschadigingen van de tip door versnelde ionen en oppervlaktemigratie van geadsorbeerde moleculen. Trillingsisolatie wordt toegepast om mechanische koppeling van invloeden uit de omgeving te voorkomen. De kenmerken van veldemissie zijn gemeten aan twee soorten probes: de één een speciaal gemaakte probe met een tip vast op de substraatondergrond en de ander een commercieel beschikbare atomaire kracht microscoop (AFM) probe, met de tip op een kleine bladveer (cantilever). Door het meten van stroom - spanning karakteristieken voor afstanden op nanometer schaal, kon de afstandsafhankelijkheid van het veldemissie-effect worden onderzocht. Uit de meetresultaten van de beide soorten probes werd de veldversterking afgeleid, door de metingen aan de Fowler-Nordheim theorie te toetsen. Er is een iteratieve fitting procedure ontwikkeld om de juiste correctiefactoren in de Fowler-Nordheim relatie te berekenen en het emissiegebied en de veldversterkingsfactor te bepalen. Gebleken is dat de algemene afhankelijkheid van het veldemissie-effect van de afstand correct wordt beschreven door ons model en een functie is van de precieze geometrie van de emitter en de straal van de tip.

Cantilever probes worden in het concept van de magnetische probe opslag gebruikt om het detecteren van de kleine magnetische krachten door verschuivingen in de resonantiefrequentie mogelijk te maken. Het doorbuiggedrag van de cantilever werd berekend met gebruikmaking van een model voor de elektrostatische interactie tussen de probe en het oppervlak, dat aantoont dat een probe met een hoge veerconstante slechts een paar nanometers buigt voor de gewenste stroom is bereikt, terwijl een probe met een lage veerconstante inklapt voordat de tip een emissie-stroom levert. Dit gedrag werd bevestigd door metingen in een aangepaste glasvezel interferometer atomaire kracht

microscoop: een hoge veerconstante van de cantilever is voldoende om de doorbuiging van de cantilever te beperken en inklappen te voorkomen.

Door de stroom van de probes constant te houden en de aangebrachte spanning te variëren is het mogelijk de afstand tussen tip en sample te regelen. De gevoeligheid van deze positioneringsmethode is sterk afhankelijk van de variatie in de veldversterking en daardoor van de specifieke emitter-geometrie. Bij een lage spanning is de probe dichtbij het sample en is de veldversterkingsfactor ongeveer 1. Met het verhogen van de spanning wordt de probe teruggetrokken en stijgt de veldversterkingsfactor, hetgeen resulteert in een hogere gevoeligheid. Ondanks dat de nauwkeurigheid van het positioneren en de herhaalbaarheid vrij beperkt is gebleken door instabiliteit van de stroom, is de belangrijkste uitkomst van deze metingen dat het veldemissie-stroomsignaal inderdaad kan worden gebruikt voor het regelen van de positie van de probe.

Om de methode van het gebruik van veldemissiestroom voor positioneren met hoge laterale resolutie te testen, werden speciale gepatroneerde samples met een goed gedefinieerde topografie gemaakt. Laser Interferentie Lithografie in combinatie met een etsmethode door middel van reactieve ionen werd gebruikt om patronen van dots te creëren met kleine intervallen van 160 tot 280 nanometer en metalen dunne-film lagen werden toegepast om het geleidingsvermogen te verbeteren. Spanningsafhankelijke rasterafbeeldingen werden gebruikt om deze geleidende gepatroneerde samples af te tasten (scannen) bij toenemende afstand tussen probe en sample. Het gevolg van het vergroten van die afstand is dat de laterale resolutie kleiner wordt, maar bij 50 V is de resolutie nog voldoende om kenmerken van ongeveer 20 nanometer op het sample te kunnen detecteren. Scannen bij een hogere spanning maakt hogere rastersnelheden mogelijk ten opzichte van scannen in het tunnel-regime, door de gemiddelde afstand tussen tip en sample te vergroten boven de hoogte van de dots op de samples. Twee beschadigende effecten moeten worden voorkomen als veldemissie-stroom wordt gebruikt tijdens het scannen: erosie van de tip en het oppervlak van het sample door pieken in de stroom en depositie met verontreinigingen veroorzaakt door de elektronenbundel. Deze effecten kunnen worden voorkomen door het gebruik van een grote weerstand in het stroompad om de capacitieve ontladingsstromen te beperken en door probe en sample voor gebruik uit te stoken onder UHV condities.

De algemene conclusie van dit werk is dat de metingen bevestigen dat veldemissie toegepast kan worden om de afstand tussen probe en medium te regelen, met voldoende resolutie nodig voor toepassing in op probes gebaseerde opslag. De praktische toepasbaarheid van veldemissie-stroom in een probe-gebaseerd opslagsysteem wordt echter in behoorlijke mate beperkt door de strikte vereisten als UHV condities en ultra-schone oppervlakken en door de korte levensduur van de emitter. Omdat de gevoeligheid afhangt van het materiaal, de straal van de tip en de geometrie van de emitter, zijn zeer uniforme emitters noodzakelijk om te voorkomen dat deze individueel moeten worden gekalibreerd bij het gebruik in een rooster. Voor praktische toepassing zouden de stabiliteit van de stroom en de levensduur van de emitter daarom verder moeten worden verbeterd, zodat de nauwkeurigheid en de reproduceerbaarheid van het positioneren kan worden vergroot, ook in minder goede vacuümcondities.

Contents

Chapter 1

The path to non-contact probe recording

In this chapter an introduction is given to the field of probe recording and a motivation for using field emission to achieve non-contact probe recording. First, the current status of high-density recording and the research on probe recording is shortly described, after which the choice for a non-contact method is motivated. Next, the sensing principles that can be used to operate a recording probe in non-contact will be compared and the choice for field emission clarified. Finally, the objectives and outline are given for the work presented in this thesis.

1.1 High-density data storage based on probe recording

Storage of information has been a fundamental basis for our cultural evolution, since it was required to pass on experiences, knowledge and ideas. With the advent of digital data storage, the amount of information that needs to be stored has increased tremendously [1]. A current trend is the storage of information in high-performance portable products, such as in mobile phones, digital cameras and handheld computers. Therefore high-capacity non-volatile memories are needed with a small form-factor and low power consumption. The present-day storage devices used for this are commonly grouped in random access memories, such as FlashRAM, and mechanically addressed storage devices, such as magnetic and optical recording systems [2].

In random access memories each bit is addressed by a matrix of fixed electrode lines. This architecture facilitates short access times, independent of the location of the data, and a low power consumption. However, the maximum bit density is limited by the minimum lithographic resolution that can be obtained in semiconductor technology. The key challenges in FlashRAM memory devices are the non-scalability of the tunnel dielectric material, writing speed and rewritability [3].

On the contrary, mechanically addressed storage devices are composed of only one read/write head that is positioned with respect to the recording medium, enabling extremely high bit densities at a relatively low price. In portable products, miniaturised hard-disks can be used when a high capacity is required. In hard-disks however, there is also a limit in the maximum storage density that can be achieved. When the energy stored in a magnetic bit becomes comparable to the ambient thermal energy, the *super-paramagnetic limit* is reached [4, 5]. Currently, two approaches are followed to overcome this: heat-assisted magnetic recording (HAMR) [6] and recording on patterned magnetic media [7]. Patterned media allow to record data in a uniform array of magnetic dots, storing one bit per dot, whereas in conventional recording each bit is stored in a few hundred magnetic grains. The highest achievable bit density lies around 7 Tbit/in^2, restricted by the saturation magnetization of the dot material [8].

An important limitation in mechanically addressed systems such as the hard-disk is its architecture: a spinning disk with only one head per diskside. Whereas over time the areal bit density has increased by eight orders of magnitude, there has been little improvement in the access time, which is now the limiting factor in the hard-disk performance [9]. The access time can only be lowered by increasing the rotational speed of the disk, however, the maximum rotational speed is restricted by the maximum writing speed of the head. This coupling leads to a bad scaling of the hard-disk architecture with an ever increasing gap between capacity and performance in access-time and data-rate.

A solution to these problems may be provided by using a completely different architecture. A probe recording system is such an architecture, that can be used to pass the limits in bit density, access time and data rate. The probe recording architecture offers specifications in between the two technologies of random access memories and conventional mechanically addressed storage devices: it provides a small, low-cost but high capacity storage system and allows to make a trade-off between data-rate, access time and power consumption. Moreover it is the sole conceivable route towards single molecular or atomic storage.

1.1.1 Probe recording systems

The probe recording architecture is derived from Scanning Probe Microscopy (SPM). The development of scanning probe microscopes started with the invention of the Scanning Tunneling Microscope (STM) in 1981 [10] and was followed by the Atomic Force Microscope (AFM) in 1986 [11]. SPMs are used for studying surface properties of materials at the nanometer or even atomic level, by scanning a probe with a sharp tip over a surface. The sharpness of such a tip is several nanometer and gives its most important functionality: the local confinement of interaction with the surface. Since these inventions, exploiting the sharp probe tip for writing and reading has always been mentioned as a promising route towards extremely high-density recording [12]. In 1992, Mamin and Rugar at the IBM Almaden Research Center first exploited the possibilities of using an AFM probe for the purpose of data storage [13]. They demonstrated thermomechanical writing and reading using a single AFM probe in contact with a

rotating polymer surface. Data was written through heating of the probe tip using laser pulses and read back by scanning the surface using normal AFM. Densities up to 30 Gb/inch^2 were achieved, which was a significant increase compared to the densities in recording applications at that time. The maximum data rate that can be achieved in this configuration is limited to 10 megabits per second [14], due to the mechanical resonance frequency of the single probe. This is a low rate compared to the data rates of more than 1 Gb/s achieved in hard-disk recording nowadays [15] and too low for normal recording applications.

A substantial increase in the data rate of probe-based storage devices is achieved by using an array of probes operating in parallel [16]. The general concept of such a probe recording system is given in figure 1.1.

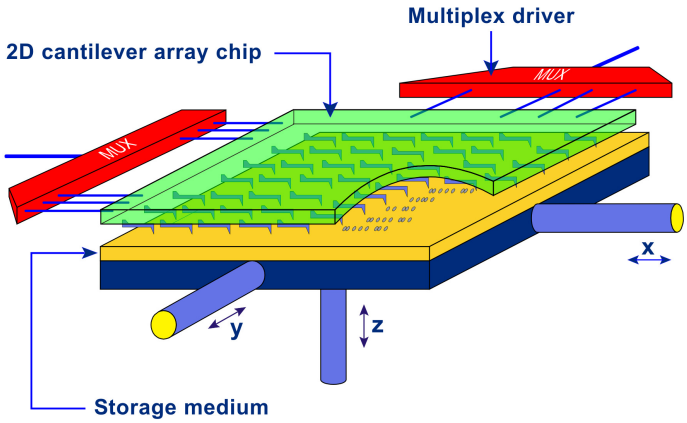

Figure 1.1: *General concept of a probe recording system. The probe array (2D cantilever array chip), the (polymer) storage medium, the displacement actuator and the electronics are shown. Image taken from [17].*

Four main components can be identified: the 2D array of probes, the medium, the positioning actuator for scanning in x and y directions and the electronics needed for control, multiplexing and data channel. By parallel operation of thousands of probes simultaneously, high data rates can be reached while the data rate per probe is still relatively low. Each individual probe is used for writing, reading and erasing data in only a small area of the medium. Positioning of the probe array with respect to the medium is needed to address the individual bits in such areas. The use of a probe recording system increases the storage capacity and data rate and can have a better rewritability compared to FlashRAM. It also decouples the access time from the data rate. Now it is possible to seek the data very fast and read at lower speeds, which means an important improvement compared to the architecture of the hard-disk system.

The Millipede concept

The pioneer in this field, IBM, has developed the most advanced probe recording system to date in the so-called Millipede project [18]. This system uses the thermomechanical

writing scheme to create indentations in a thin polymer film as the storage medium. The indentations represent stored data bits and can be read back and erased by using the same tips. The current Millipede design exploits a large 2D array of 4096 (64×64) cantilevers with integrated tips, sensors and actuators, see figure 1.2.

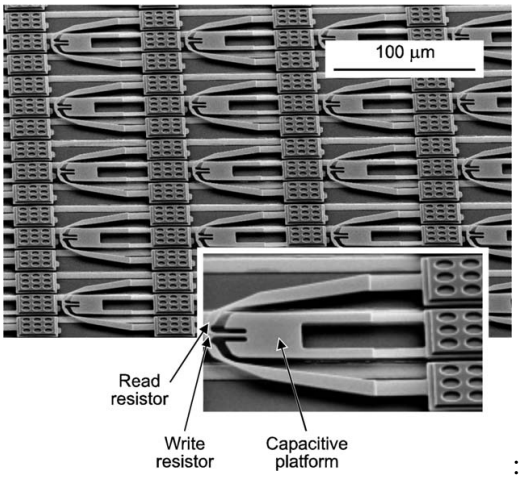

Figure 1.2: *SEM image of the cantilever array used in the Millipede project. Image taken from [19].*

A silicon-based scanner with a micromachined voice-coil actuator is used for the *xy*-displacement of the medium [20]. Each cantilever has three terminals to connect to two resistive heaters and a capacitive platform to apply an electrostatic force. Writing with these probes is achieved by applying a local force with the tip on the polymer film and simultaneously softening the polymer layer by local heating. The tip is heated to about 400°C by applying a current through the write resistor. During reading, a second resistor is operated at a temperature in the range of 200-250 °C. When the tip moves into a bit indentation, the thermal conductance between this heater and the storage medium increases. This results in a lower temperature of the heater, which can be detected by measuring its resistance and used as a read signal. To overwrite data thermo-mechanical effects are used. They cause the stressed polymer material closely around a newly created bit to relax. This enables overwriting of bits by creating very close new ones

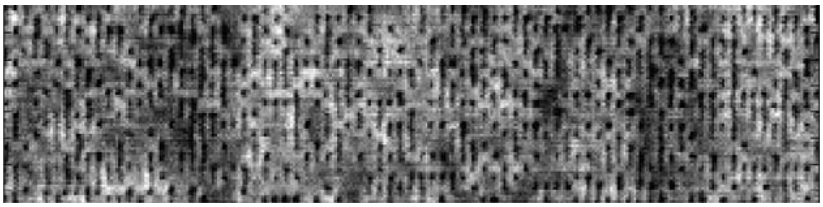

Figure 1.3: *AFM image of data stored by means of indentations at a pitch of 18 nm, leading to a storage density of* ~ 2 *Tb/in*^{2}*. Taken from [19].*

and makes the medium rewritable [19]. The typical heating rates on the order of 10 µs result in a relatively low data rate per probe, which is scaled by parallel operation of the probes.

In the Millipede concept, indentations at a pitch of 18 nm have been achieved, shown in figure 1.3, corresponding to a storage density 2 Tb/in^2. To validate the system as a real candidate for storage, a recording demonstration was given, resulting in an areal bit density of 641 Gb/in^2 and a bit error rate better than 10^{-4} [21]. The expectations are that this storage technique is capable of achieving data densities exceeding 10 Tb/in^2, well beyond expected limits of magnetic recording.

The μSPAM concept

A probe recording system using a *magnetic* medium is currently in development at the MESA$^+$ institute for nanotechnology at the University of Twente [22, 23]. The micro Scanning Probe Array Memory (μSPAM) concept is schematically illustrated in figure 1.4.

An array of magnetic probes is used to write bits in a magnetic recording medium. Each individual probe is positioned in an area of 100 μm $\times$ 100 μm, using silicon electrostatic microactuators [24, 25]. The use of many of these integrated positioning systems enables parallel operation of multiple medium tiles, to reduce power consumption for low read/write loads and increase redundancy [26, 27]. Writing is achieved by bringing a magnetic tip close to or in contact with the magnetic medium [8]. Due to the field from the tip, in combination with an external magnetic background field, the magnetic orientation of the dot below the tip will switch up or down. This magnetic orientation represents the stored data bit. Read-out can be achieved by measuring the magnetic forces as in Magnetic Force Microscopy (MFM). Since switching times in magnetic media are typically below 1 ns, the data rate per probe is in principle only limited by the resonance frequency of the probes. By parallel operation of multiple probes, this rate can be scaled and in principle high data rates of several Gbit/s can be obtained.

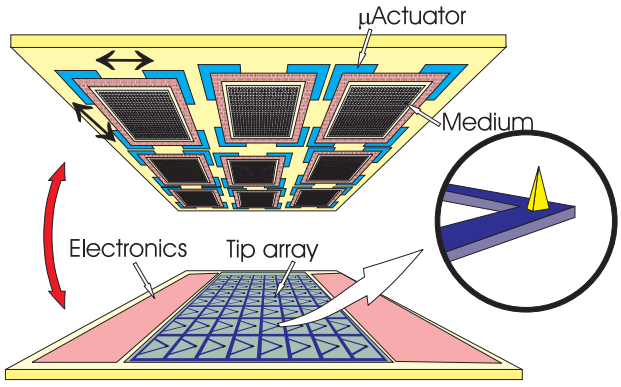

Figure 1.4: *Schematic representation of the μSPAM concept.*

Property	Target
Dimensions [mm×mm×mm]	$15 \times 15 \times 2$
Total capacity [Gbyte]	20
Density [Tbit/in^2]	1
Tip array size	128×128
Max. data rate [Gbit/s]	1
Data rate per tip [kbit/s]	10
Scan height [nm]	10
Scan resolution [nm]	10
Scan speed [mm/s]	>1
Seek velocity [mm/s]	>40
Access time [ms]	<2.5
Power consumption read/write [W]	<1
Power consumption standby [W]	10^{-6}

Table 1.1: *General design specifications for µSPAM.*

The targeted specifications for the µSPAM concept are given in Table 1.1. Of course this set of specifications is only a guideline and to achieve them, a number of difficult issues should be solved. In particular positioning each probe above the track would be a major achievement. Assuming a data rate of 10 kbit/s per probe and 25 nm pitched magnetic bits, a positioning speed higher than 1 mm/s is required during reading and writing of data. This scan-speed should be realised with a lateral resolution better than 25 nm to be able to follow the densely packed magnetic bits. Moreover, each probe should be kept constantly at a distance of about 10 nm from the medium, with an accuracy of several nanometers!

Other concepts

Inspired by the promising prospects of probe recording, many researchers have proposed techniques for probe recording, based on topographic transformation [13], conductance modification [28], ferroelectric polarization [29], charge storage [30], changes of phase [31] and near-field optical recording [32]. Several companies and universities have presented more extensive plans for probe recording systems. Carnegie Mellon University has elaborated on the Ultra-High-Density Data Cache, utilizing an array of CMOS micromachined tip actuators, a single MEMS-based media actuator and magnetic recording technology [33, 34]. Hewlett Packard worked on the Atomic Resolution Storage project, using a microfabricated array of electron-beam sources to read and write bits on a phase-change medium [35, 36, 37]. LG Electronics proposed the Nano Data Storage System, using arrays of probes with integrated heaters and piezoelectric sensors for thermomechanical data storage in a polymer medium [38, 39]. Samsung, supported by several Korean universities, is developing the Resistive Probe Storage system, by applying transistor technology on the probes and ferroelectric media [40, 41].

To conclude, Nanochip, a start-up funded by Intel Capital and JK&B Capital, recently announced commercialization of a storage chip using arrays of atomic force probe tips to write, read, and record data bits in a phase-change medium [42]. Although this list is far from complete and some projects were stopped, it clearly shows that there is a global interest in probe recording applications.

1.1.2 Why non-contact?

The use of scanning probe techniques for recording opens up a path which ultimately might lead to molecular or even atomic storage. If we would extend the current hard-disk storage roadmap into the future, as is shown in figure 1.5, we can foresee that it is not long before the individual bits indeed need to be of molecular or even atomic size.

The limit in the bit areal density for AFM-like storage, such as in the Millipede concept, is seen as the mechanical switching of individual polymer molecules [19]. However, a critical issue in the current Millipede design is the endurance of the surface of the polymer and the tip. Although the medium can be reused thousands of times, the repeated scanning does result in wear of the polymer and tip. The wear rate is sensitive to variations in the force between tip and medium [43]. By stringent control of the tip height and the bending of the probe cantilevers, these variations can be controlled, but to minimize or prevent wear at all, individual z-feedback for each probe is needed. This individual z-feedback can be achieved by integrating an actuator and a proximity sensor in each probe to feed a control loop and keep the distance between probe and medium constant.

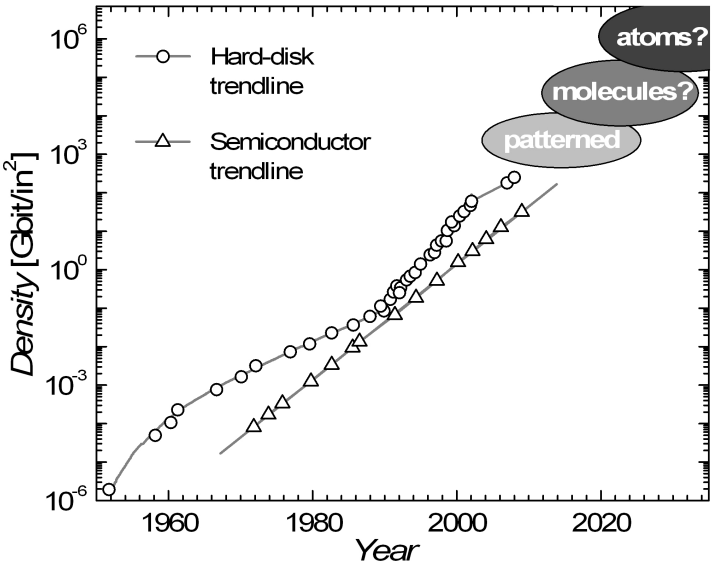

Figure 1.5: *Trends in areal storage density for hard-disk drives compared to the trendline for semiconductors. Data from [15].*

The developments in probe recording may ultimately lead to storage at the atomic level. That this is not science fiction is demonstrated beautifully by the work of Bennewitz *et al* [44], as shown in figure 1.6. Here silicon atoms are positioned on gold monolayer tracks on a silicon surface by means of STM, leading to a 'bit' spacing of 1.7 nm. As an illustration, this bit size is compared to storage on a CD-ROM, leading to a density increase of 10^6 times. Next to moving atoms, one could modify their charge state [45, 46, 47]. As in these approaches the surface modification rate is exceedingly slow, a parallel probe array has to be used. Operation of the probes in a non-contact mode, as in STM, is essential to ultimately reach these atomic storage densities.

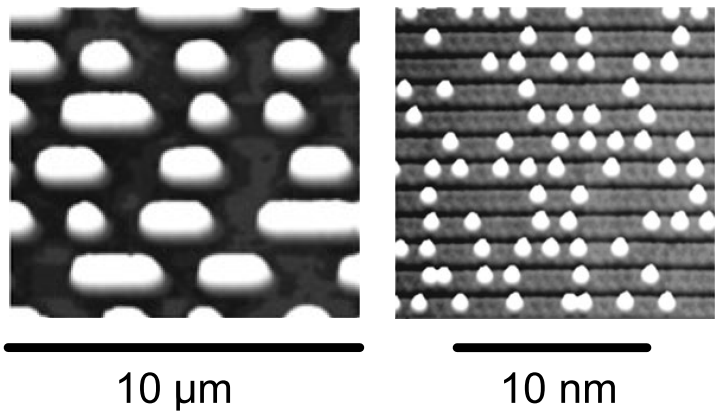

Figure 1.6: *Comparison of the atomic memory on silicon with a CD-ROM. Extra silicon atoms occupy lattice sites on top of tracks that are five atom rows wide (1.7 nm). The scale is reduced from µm to nm, which leads to a 10^6 times higher density. Taken from [44].*

On the road towards the goal of atomic resolution probe storage, we will at least see the transition from continuous media towards patterned media. The first occurrence of patterned media will be in magnetic recording, but soon after that, single molecular storage will become an option [48, 49]. Much could be learnt about storage in molecular and atomic patterned media by studying magnetic patterned media, as proposed in the μSPAM concept. On these magnetic media, a distance on the order of 10 nm has to be maintained between the probe and the medium in order to minimize Van der Waals forces and still be able to sense the small magnetic stray fields [50]. The requirement for individual z-feedback for each probe in the μSPAM concept is therefore a good motivation for a fundamental study on non-contact methods that can be used in probe recording, as presented in this thesis.

To achieve individual control over the probe position, a z-positioning actuator, a proximity sensor and a feedback loop should be integrated in each probe of the probe array. Since each probe in the probe array needs to have its own electronics, it is crucial that these are incorporated in the MEMS structure with as minimum wiring as possible. Individual actuation of probes in arrays and integration of logic circuitry has already been demonstrated by various authors. Piezo-electric materials can be deposited on the

probe cantilever to be able to induce a deflection [51, 52]. Another method is to use cantilevers with parallel plate electrodes to provide an electrostatic force for actuation, as is done in the Millipede concept [21, 53]. Integrated deflection sensing has also been demonstrated, using e.g. piezoresistive probes [52, 54]. However, if we focus on non-contact probe recording, something more is needed: a proximity sensor with sufficient lateral resolution that can be integrated in each probe. In the next section, an overview will be given on the different types of proximity sensing that can be used to individually control the probe-medium distance in a future non-contact probe recording system.

1.2 Proximity sensing principles

Proximity sensing is considered to be any sensing method that provides a measurable signal when it is brought into close proximity of a surface. Often probes are used as means of communicating a translation from a relatively small area on a surface, such as in a coordinate measuring machine (CMM), stylus profilometer or scanning probe microscope. In these systems an actuator is used to move the probe and record subsequent displacements to map the topography of the object under test. The crucial elements for the lateral resolution of this local probing method are the size of the probe, the distance between probe and object and the distance dependence and lateral variation of the interaction with the object.

Many transducer principles can be employed for proximity sensing in local probe methods, based on interactions between probe and object, including optical near fields, capacitance, thermal conductance, force, tunneling and field emission. Most of these methods do not have the intrinsic capability for absolute distance metrology because of their non-linear nature and therefore only provide proximity information. By controlling the probes to maintain a set signal level they can still be used for sensing displacements with high accuracy. Not all methods are equally suitable for integration in a probe recording system. To understand the distance dependence of the various interactions acting at the nanoscale, first the origins are shortly discussed. Then in section 1.3 the relative merits and limitations of these interactions and the trade-off leading to the choice for field emission as a proximity sensing method are given.

1.2.1 Near-field optical sensing

Laser interferometry is well-known for combining high accuracy with long range since it is an incremental sensing method due to the periodic nature of the interfering light. The detection limit is estimated to be as low as $10^{-15}\, m/\sqrt{Hz}$ [55]. Diffraction effects place a limit on the lateral resolution of the technique of about $\lambda/2$. Near-field optical techniques can be used to obtain resolutions beyond this diffraction limit [56], by using an optical probe with a sub-wavelength sized aperture to illuminate the sample. When the probe is brought very close to the sample surface, the sample interacts with the near field of the optical probe, changing the optical signal. The intensity strongly depends

on the distance between the tip of the optical probe and the sample surface, since the evanescent waves are damped out with a fourth power when increasing the distance from the interface [57].

In scanning near-field optical microscopy (SNOM) the near-field optical interaction is used to study samples with an optical resolution below 30 nm [58]. Since only a slight change of the distance is enough to considerably change the measured optical signal, it is important to keep the optical probe at a constant distance of about 6 - 10 nm from the sample. This distance control is normally achieved by non-optical means, such as tunneling [59] or by using a piezoelectric tuning fork force sensor for shear force detection [60]. In a near-field optical recording system developed at Royal Philips Electronics, stable distance control has been shown for a constant air gap of 25 nm between the optical lens and a spinning disc [61].

For optical sensing three components are needed: a light source, photodetector and guidance to transport or focus the light, such as lenses, optical fibers and mirrors. For application of near-field optical sensing in MEMS, integrated waveguides can be used to transmit the light. The possibility of such integration of optical sensors has been demonstrated before, using interferometry for displacement sensing [62].

1.2.2 Capacitive sensing

Capacitive sensing can be used for proximity sensing by measuring displacements in the gap between two plates from changes in the capacitance. When assuming a parallel plate configuration, the capacitance is inversely related to the spacing. There is a variety of techniques to measure capacitance changes, including charge amplifiers, charge balance techniques, AC bridge impedance measurements and various oscillator configurations [63].

In Scanning Capacitance Microscopy (SCM) a conductive tip is used to detect the charge distribution in a sample. To avoid large, low-frequency drifts in the signal output caused by stray capacitance, high-frequency electronic circuitry is needed. Capacitance changes can be detected with a sensitivity on the order of $10^{-22} F/\sqrt{Hz}$ and lateral resolutions of 5 nm have been shown [64]. SCM has also been used for data storage, by charge injection and detection in Si_3N_4 films, resulting in bit sizes of 75 nm [30].

In MEMS capacitive sensing is often used because of the ease of integration in the fabrication process and its high accuracy. When used for position feedback sub-nanometer accuracies and ranges up to hundreds of micrometers can be obtained [65, 66]. An important limitation is that electrostatic forces and parasitic capacitances limit the sensitivity and resolution that can be obtained [63].

1.2.3 Thermal sensing

Thermal sensing can be implemented by using a heat flow between sensor and surface. This heat flow is proportional to the surface area and inversely proportional to the gap distance. A resistor can be used as a heater to operate the sensor at elevated temperatures.

When the gap increases, the thermal conductance between this heater and the storage medium decreases. This results in a lower temperature of the heater, which can be detected by measuring its resistance and used as a read signal. The exact distance dependence of this effect depends on many factors, such as the heater configuration, thermal conductance (air, humidity) and the presence of heat sinks.

It is this sensing principle that is employed in the Millipede concept during reading. By optimizing the thermal probe, a sensitivity of $\Delta R/R = 10^{-4}$ was shown at a power consumption of 0.5 mW. An impressive lateral resolution of ~ 2 Å was obtained [67], although this resolution originates from the sharp tip that is scanned in contact with the sample rather than being the true thermal resolution in non-contact. IBM has shown another impressive result in employing thermal sensing by showing a lateral position sensor for a MEMS based actuator with a resolution of 2.1 nm on a total range of $>100\,\mu$m, at a bandwidth of 10 kHz and a power consumption of 10 mW [68].

1.2.4 Force sensing

When a tip is brought into close proximity with a point on a sample, the atoms start to interact. The potential energy of this interaction causes a force $F_{ts} = -\frac{\partial U}{\partial z}$. Atomic force microscopy probes are normally used to measure contact forces. Contact AFM is used to map the topography of the sample with a resolution on the order of the tip radius. Non-contact forces can also be detected by keeping the probe at a distance of several ångström above the surface. Since these forces are attractive, a sudden jump to contact has to be prevented. Stable operation is achieved by dynamic AFM, where the cantilever is oscillated at or close to its resonance frequency. Variations of the frequency shift as a function of the tip-surface distance can be used to determine the force between the probe and the sample [69]. In the non-contact mode the cantilever is used in a closed feedback loop and the frequency of the loop is adjusted to have attractive tip-surface interaction. This method has been used to obtain true atomic resolution in non-contact AFM [70]. Besides the frequency shift there is another signal available, the damping signal, which is the error signal of the gain control used to keep the amplitude of the oscillation constant. The damping signal gives information about dissipative forces and can be used to keep a constant tip-sample distance and achieve atomic resolution [71]. Although several theories have been developed, the physical meaning of the large dissipations that are measured is not yet completely understood [72].

In practice, given sufficient sensitivity, it is possible to monitor both contact (hard core repulsion, capillary) and non-contact (chemical bonds, Van der Waals, magnetic and electrostatic) forces. With increasing distance these forces have different decay rates, as is illustrated in figure 1.7. They will be treated here in more detail since they are important to understand tip-sample interactions in general.

- **Hard core repulsion and Van der Waals forces** The fundamental origin of these forces is the quantum-mechanical zero point energy in interacting atoms. The most common representation for this interaction between two atoms as function

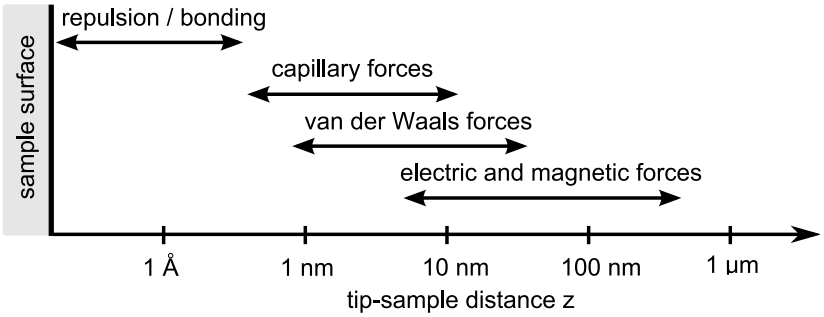

Figure 1.7: *Different forces acting between tip and sample. Illustration from [73].*

of distance z is given by the Lennard-Jones potential [74]:

$$U_{LJ}(r) = 4u_0 \left[\left(\frac{\sigma}{z} \right)^{12} - \left(\frac{\sigma}{z} \right)^{6} \right] \tag{1.1}$$

where u_0 is the depth of the potential well and σ the equilibrium distance. The 'power 12' term represents the hard core repulsion and the 'power 6' term is the Van der Waals attraction between two atoms. The energy obtains its minimum value of u_0 at a distance $z = 1.12\sigma$, so the hard core repulsion regime starts when the separation distance decreases below several ångström. The Van der Waals attraction is caused by the intermolecular pair interaction. Below 10 nm tip-sample distance the influence of these Van der Waals forces increases. For two macroscopic bodies the interaction energy decays much slower than it does for two molecules and can be calculated by integration over the volume. The force strongly depends on the shape of the tip and for a spherical tip with radius r near a surface this yields [75]:

$$F_{VdW}(z) = \frac{A_H\, r}{6z^2} \tag{1.2}$$

The Hamaker constant A_H depends on the type of material of the tip and sample and is found to lie in the range $(0.4 - 4) \cdot 10^{-19}$ J [75]. The Van der Waals interaction can be quite large: with a typical radius of an AFM tip of 10 nm and $z = 1$ nm, the Van der Waals force is ~ 2.5 nN.

- **Chemical bonding** For a distance between two atoms on the order of several ångström, chemical bonding can occur. In the simplest view of a so-called covalent bond, one or more electrons are shared between the participating nuclei, holding the repelling nuclei of the two atoms in a relatively fixed configuration of equilibrium. Covalent forces operate only over very short distances on the order of 0.1 - 2 nm and are expected to dominate all other processes [75].

- **Electrostatic forces** When the tip and sample are both conductive and have an electric potential difference, electrostatic forces are important. The electrostatic force under constant tip-sample potential V_{ts} is given by:

$$F_{el} = \frac{1}{2}\frac{\partial C}{\partial z}V_{ts}^2 \tag{1.3}$$

This force is proportional to the square of the potential difference between the two surfaces and therefore always attractive. It scales with the distance by the derivative of the capacitance C. For a spherical tip with radius r and $z > r$, this capacitance derivative changes according to a parallel plate approximation, yielding for an area of overlap $2\pi r^2$ [74]:

$$\frac{\partial C_{ts}}{\partial z} = -2\pi\varepsilon_0\varepsilon_r\frac{r^2}{z} \tag{1.4}$$

with ε_0 the dielectric constant for vacuum and ε_r the relative dielectric constant. The electrostatic interaction can cause large forces: for a tip radius $r = 10\,\text{nm}$, $V_{ts} = 5\,\text{V}$ and $z = 1\,\text{nm}$, the electrostatic force is $\sim 7\,\text{nN}$.

- **Magnetic forces** When using a magnetic tip and a magnetic sample, as is done in Magnetic Force Microscopy to probe micromagnetic structures, the magnetic stray field emanating from the surface of the sample generates force on the magnetic tip. This force can be approximated by considering the tip to be a point magnetic dipole. When the dipole moment is purely directed in z direction, this gives for a tip with magnetic moment m_z and a medium with stray field H_z [76]:

$$F_{mag} = \mu_0 m_z\frac{\partial H_z}{\partial z} \tag{1.5}$$

with μ_0 the permeability of vacuum. The magnetic forces typically measured in MFM applications are small, in the order of 30 pN, with typical cantilever deflections in the order of nanometers [77]. Therefore to be able to detect magnetic stray fields all other forces should be minimized, by keeping the tip at a distance of several nanometers from the sample.

- **Capillary forces** In ambient conditions meniscus forces can occur by interaction between adsorbed thin films on tip and sample. These surface surfactant films are present on most surfaces in air and contain mostly water and hydrocarbons. When approaching a tip to a sample the film is attracted due to Van der Waals forces and migrates under the tip, reducing the effective tip to sample separation. At small distance a meniscus will be formed, strongly pulling the tip towards the sample surface. The capillary force between a flat surface and a sphere of radius r is given by [75]:

$$F_{cap} = 4\pi r\gamma_L cos(\theta) \tag{1.6}$$

where γ_L is the surface energy and θ is the contact angle. This effect can cause large forces and a strong reduction in sensitivity when scanning over the surface. Only by using the tip and sample in vacuum or special (dry air) conditions this can be prevented.

By detecting one or more of the forces listed above, as done in many scanning force microscopy techniques, the force signal can be used to detect displacements. This method can be used for applications other than microscopy and has been applied e.g. in MEMS devices. For example, long range electrostatic forces are used for non-contact operation of an accelerometer, where the proof mass incorporates a tip that can be moved towards an opposing surface. The displacement sensitivity of this device using feedback to control the tip-surface separation is approximately 1 nm [78].

Normally the interaction force is transformed into a deflection of a cantilever and it is this deflection that is then measured to determine proximity. Sarid [74] gives an overview of various cantilever deflection sensing methods, including optical beam deflection, interferometry, capacitive, piezo-electric, piezo-resistive and tunneling current sensing. Optical techniques and piezo-resistive deflection sensing are the most commonly applied techniques. MEMS techniques have been used for fabrication of high-density arrays of AFM probes. Minne *et al* produced arrays of AFM probes with integrated piezo-electric actuators and piezo-resistive sensors that could be used for high-speed parallel atomic force microscopy [79].

Operating the AFM probe in non-contact is not trivial. Since the tip-sample force has long- and short-range components, it is not monotonic. Van der Waals forces are always attractive and, if chemical bonding between tip and sample can occur, chemical forces also. Because the tip is mounted on a cantilever, approaching the sample therefore can cause pull-in when the stiffness of the cantilever is too small, making the force become repulsive. This greatly complicates the design for a feedback loop based on force sensing: stable feedback is only possible on a monotonic branch of the force curve.

1.2.5 Tunneling sensing

When the separation between an electrically conductive tip and a conductive sample is a few atomic diameters, transport of electrons occurs by tunneling. When a voltage is applied that is small compared to the work function, the tunneling barrier is roughly rectangular with a width s and a height given by the work function. According to elementary quantum mechanics, the tunneling current depends exponentially on the separation between probe and sample, given by [57]:

$$I(z) = I_0 \, exp(-2\kappa s)$$

The decay length $1/\kappa$ is related to the tunnel barrier height and I_0 is proportional to the local density of states involved in the tunneling process, which are selected by the voltage applied between probe tip and sample. With $s \approx 6\,\text{Å}$, $V \approx 1\,\text{V}$ and $\phi \approx 5\,\text{eV}$

for metallic samples, $I \approx 1\,\text{nA}$ and $\kappa \approx 1\,\text{Å}^{-1}$. Thus an increase of s of 1 Å typically decreases I by an order of magnitude.

Due to the strong distance dependence, the tunneling current flows from the outermost asperity of the tip and is therefore extremely localized. This is the key reason for atomic resolutions that can be obtained with STM. Binnig and Rohrer were the first able to reduce the mechanical noise so that atomic scale images on silicon could be achieved, for a brief review see [80].

Some examples of tunneling applied for proximity sensing in MEMS applications are high-sensitivity micromachined tunneling accelerometers with μg resolution [81], gyroscopes [82] and a magnetic field sensor [83]. Due to the limited range, the tunneling probes are often combined with an actuator to form a feedback control loop keeping the tip-sample distance constant at about 1 nm.

1.2.6 Field emission sensing

Field emission is the emission of electrons from a surface through the potential barrier into vacuum due to the presence of high electric fields. This process is described by Fowler-Nordheim theory and will be discussed in more detail in chapter 2. Although based on the same tunneling effect described for tunneling sensing, field emission occurs at larger tip-sample distances, provided that the electric field is high enough to cause field emission to take place. The exponential relation between field emission current and electric field can be used for proximity sensing, since this electric field depends on the electrode spacing between the field emitter tip and counter-electrode.

This sensing method was applied in the first successful scanning probe microscope, developed by Young, Ward and Scire between 1966 and 1972 [85, 86]. A schematic representation of this instrument can be found on the left of figure 1.8. The topografiner was mounted inside a vacuum chamber operated at a pressure of $5 \cdot 10^{10}\,\text{mbar}$. A tungsten emitter tip was spot-welded to a molybdenum bridge in order to clean the tip by heating. The emitter-sample distance was controlled by a feedback controller that adjusted the voltage on the vertical piezo to maintain a constant field emission current. No computerized data acquisition systems were available at that time, so to form the images, the voltage applied to this piezo was recorded with an x-y recorder and a storage oscilloscope during scanning. An example of such an image can be found on the right of figure 1.8. Using this very early scanning probe microscope, an accuracy in tip-sample distance better than 3 nm and lateral resolution of 400 nm was obtained, with ranges up to 100 nm. The ultimate perpendicular accuracy that would be achievable was estimated to be 0.3 nm with a lateral resolution on the order of twice the tip radius. The same instrument was used with the feedback loop inactive to measure the first current-voltage (I-V) curves in the MVM tunneling regime [87]. Unlike later STMs, the Topografiner was rigidly attached to the vacuum chamber and vibration isolation was all external. Due to problems with relative vibrations between probe tip and surface, the expected resolution was never obtained until a decade later STM was invented.

In MEMS, various types of sensors based on field emission have been developed,

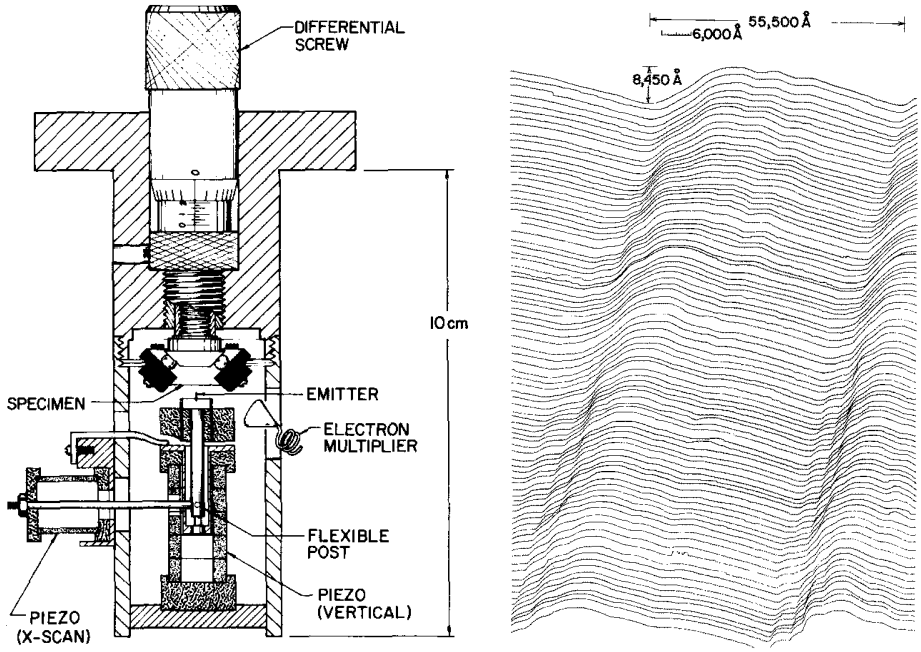

Figure 1.8: *Left: schematic drawing of the Topografiner. Right: topographic image of a diffraction grating obtained with the Topografiner. Taken from [84].*

e.g. for pressure [88], acceleration [89] or RF [90] applications. The main advantage of using field emission for sensing applications is that the critical sensing area can be scaled down to the nanometer range, without sacrificing sensitivity or signal-to-noise ratio. Furthermore, the measured current signal is largely temperature independent, which is an advantage over other sensing methods that suffer from drift, especially when scaling down dimensions. The field emission effect can be used to detect displacements up to hundreds of nanometers with nanometer resolution. Therefore field emission is expected to be suitable for sensing especially in very small-scale systems (NEMS), where there is a need for transducers that can be realized at the nanoscale [91].

An important drawback of using field emission for sensing applications is that instabilities in the field emission current are difficult to prevent and strongly reduce the applicability of this method in practical devices. This unstable behaviour is inherent to the field emission process and the causes for this will be discussed in chapter 2. To improve the stability of the field emission current, emitters and counter-electrode are generally operated in vacuum.

1.3 Trade-off

From the survey and examples on transducer principles described in the previous section, a comparison has been made between the sensing methods that can be used for proximity

Criteria	Optical	Capacitive	Thermal	Force	Tunneling	Field emission
Integration	- -	+ +	+/-	+/-	+ +	+ +
Cross-talk	+ +	- -	?	+	+	+
Sensitivity	+	+	+	+/-	+ +	+
Resolution	+/-	-	- -	+	+ +	+
Range	+	+ +	?	+	- -	+ +
Bandwidth	+ +	+ +	-	+	+	+
Power	- -	+	- -	+	+	+
Noise	+	-	+/-	+	-	-
Stability	+	+	?	-	+	- -
Control loop	+ +	+	+ +	- -	-	-
Vacuum	+ +	+/-	+	-	-	-

Table 1.2: *Benefits and drawbacks of transducer principles applicable for proximity sensing for non-contact probe recording.*

sensing in non-contact probe recording. The comparison is given in Table 1.2. The used criteria are deduced from the design specifications given in Table 1.1 and are listed in order of importance: ease of integration within MEMS, signal cross-talk, sensitivity (perpendicular to sample surface), lateral resolution, total range, bandwidth, power consumption, noise level, signal stability, control loop (stable feedback) and the vacuum conditions needed.

The selection procedure that will be described below is of course arbitrary and depends on many presumptions. In a similar discussion about sensing methods for probe recording by Pohl in 1995 [92], similar criteria were stated but the outcome was more or less in favour of optical sensing. Still a trade-off has to be made in order to be able to choose a proximity sensing method to be used in probe recording.

The integration criterion is put at the first place and has the highest weight. This involves the ease of fabrication of the sensors in a MEMS process, the amount of wires needed per probe and interfacing of the output signals with electronics. Since in the probe array thousands of probes will be used in parallel, a simple detection scheme is essential with as minimum wires per probe as possible. The electrical methods (capacitive, tunneling, field emission) therefore have a clear advantage, since in principle they only need one wire per probe and one wire to the sample to make the electrical connections needed. The thermal and force sensing methods would need at least two wires per probe to read-out the probe resistance, as an indirect measure of cantilever deflection or probe temperature.

The optical sensing method is not very suitable for integration. Although integration of multiple sensors is possible using optical waveguides, fabrication becomes quite complex. For read-out of parallel signals, a CCD or array of photodetectors would be required to convert the signals to the electrical domain. Another important drawback of this sensing method is the optical loss that occurs due to the low efficiency of coupling

out the light through the aperture. Normally in SNOM this intensity loss is overcome by coupling in additional light into the fiber to compensate, but at the cost of an increase in power consumption as well as increased heating.

The thermal sensing method suffers from high power consumption. Although in the Millipede concept the thermal sensing method is used with extraordinary results and relatively good power figures, it will be difficult to employ this method for non-contact probe recording, since the lateral resolution in non-contact is severely limited due to lack of control over the heat flow.

The capacitive sensing principle is advantageous in terms of obtainable accuracy, bandwidth, displacement range and ease of fabrication. However, since the capacitance scales with area of overlap, the lateral resolution in capacitive sensing directly competes with the capacitive signal that is obtained. Since parasitic capacitances are present in every system, and often many orders of magnitude larger, the electronic detection of these small signals will be very difficult, especially for a system operating thousands of capacitance probes in parallel.

This leaves us with the methods of detecting force, tunneling or field emission for proximity sensing in non-contact probe recording. The tunneling and field emission current are strictly monotonic increasing functions of distance, i.e. the magnitude of the current increases continuously as the tip-sample distance decreases. This property allows a simple implementation of the feedback loop: the tunneling current is fed into a fast amplifier to produce an error signal that is proportional with the tip-sample distance. As discussed before, the tip-sample force is not monotonic. Although it is possible to establish a z-distance feedback loop for non-contact AFM, this is more complicated than for tunneling and difficult to integrate for a parallel probe array. To detect the interacting force, it is necessary to measure the deflection of the cantilevers of the probes, by means of optical sensors, piezo-resistive strain gauges or capacitive or tunneling sensors. This increases the footprint of such a proximity sensor and requires a more complicated sensing scheme. Additionally, in the μSPAM concept, magnetic forces have to be distinguished from the other forces acting. As described, these magnetic forces are very small and will be difficult to separate from the forces used for sensing. Therefore it does not seem wise to use force sensing as a feedback for non-contact operation of the probes.

The tunneling sensing method would clearly excel in terms of resolution. Since STM has proven to allow atomic surface modification, it might be used in a probe recording system aiming for atomic resolution as envisaged in the data storage roadmap. However, the tunneling sensing method requires extreme control over the tip-sample distance, since the range is limited to $\sim 1\,\mathrm{nm}$. This places strong requirements on the speed of the electronics which will be difficult to integrate with current MEMS technology. Since at this moment the expected bit densities in parallel probe recording systems are in the nanometer range rather than of atomic size, field emission seems to be favourable over the tunneling sensing principle.

Therefore, as outcome of this survey on transducer principles, it is concluded to further investigate the field emission sensing principle for proximity sensing. The

combination of good lateral resolution, range, accuracy, small sensing area, low power consumption and possibilities for integration and parallel operation in an array of probes appears to be favourable over the other methods. The early work by Young *et al* on the first successful scanning probe microscope, has already shown that field emission can indeed be applied for z-positioning. Parallel operation of field emission probes requires individual current-control and individual actuation of each individual probe, which is not trivial but feasible as was shown by Wilder [93] and Minne *et al* [52]. Next to proximity sensing, integration of field emitters on probes may open possibilities for heat-assisted writing in magnetic [94] or phase-change media [95], using the field emission currents to locally heat the medium.

1.4 Objective and outline of this thesis

Probe recording employing field emission for proximity sensing might bridge the gap between current *contact* probe recording, proven to be attainable in the Millipede project, and future *non-contact* probe recording techniques that can be used to achieve even higher bit densities. Although there are no fundamental objections, many obstacles are seen on this path to non-contact probe recording using field emission, among which are the stability of field emission current, the integration of thousands of field emission probes for parallel operation and the expected cross-talk affecting the highly sensitive current amplifiers.

The aim of this thesis is to investigate the applicability of field emission for probe-medium distance control in a probe recording system. We focus on the concept of field emission for proximity sensing in general, to provide more insight in field emitter materials, system conditions and electronics needed for stable operation of field emission. Finally we will apply this method to scan in non-contact on patterned samples using the same type of probes as intended for the recording applications.

The outline of this thesis is as follows: in the next chapter 2 the field emission sensing method will be further examined. The mechanisms responsible for field emission will be discussed and the causes for the instabilities in the field emission current are given. A theoretical model is developed to describe the dependence of the field emission current on tip-sample distance. Next the electrostatic interaction between the field emission probe and the medium due to the applied voltages is evaluated. Chapter 3 is used to describe the measurement setup and the methods that were used to characterize the probes used as field emitters. In chapter 4 the preparation methods are discussed that have been developed to fabricate the used probes and patterned samples. In chapter 5 the results are given of the characterization measurements on the probes that have been tested in field emission measurements to investigate the dependence of the field emission effect on distance. Chapter 6 then presents the results that have been obtained by scanning probes in the field emission regime over the patterned samples. Finally, chapter 7 ends this thesis with a summary and conclusions of the main results obtained in this work.

Chapter 2

Field emission sensing

In this chapter a theoretical framework is given for the concept of using field emission from a probe at small distances. Since we are interested in the application of field emission as a proximity sensing method, we limit ourselves to a qualitative description of the physical processes in field emission and focus on the calculations that we can use to choose our parameters. First a description will be given of the definitions used for electron emission in general. Secondly a model is discussed that will be used to fit our experimental data, in order to be able to extract typical field emission parameters for a given emitter. Then a so-called field enhancement model is developed to determine the electric field at the apex of an emitter tip as function of the tip-sample distance, emitter geometry and applied voltage. These models are used to predict the characteristics of the field emission sensing method for varying tip-sample spacings. Third an elaboration will follow on the causes for instabilities in the field emission current in order to deduce the parameters for the materials and vacuum conditions to be used for field emission sensing. Finally a model for the electrostatic interaction between a field emitter tip mounted on a cantilever and a sample is given and used to predict the mechanical stability of such a probe during operation in constant current feedback control.

2.1 Electron emission

The phenomenon of the emission of electrons under high electric fields was first observed by Wood in 1897 [97]. A theoretical description used to describe this process was first provided by Schottky in 1923, who assumed that the electrons are emitted *over* a potential barrier at the surface, lowered by the applied electric field. In 1928, Fowler and Nordheim introduced the concept of quantum-mechanical tunneling of electrons *through* the surface potential barrier, to explain the high field emission currents at low temperatures [98]. A combination of both concepts teaches that the emission of electrons is a function of three physical parameters: the emitter temperature, the electric field strength and the work function of the materials used. Since the dependence of

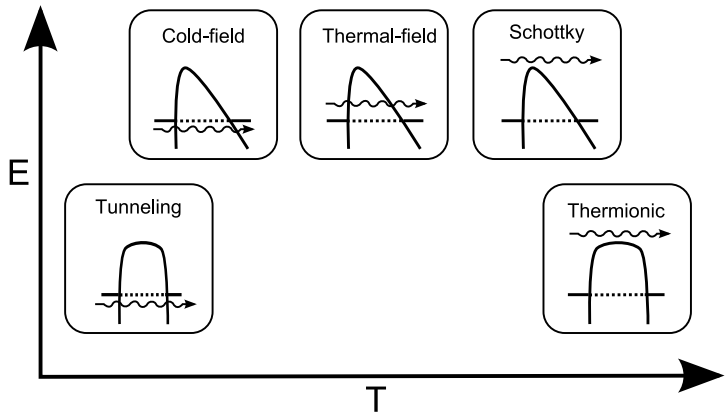

Figure 2.1: *Comparison of electron emission mechanisms and their dependence on temperature T and electric field E. Image from [96].*

the emission current on these parameters is quite complex, different parameter ranges are used, each describing the main mechanisms responsible for the electron emission. Five main mechanisms are depicted in figure 2.1: metal-vacuum-metal tunneling, normal (cold) field emission, thermal field emission, Schottky emission and thermionic emission. They are distinguished according to the way potential energy is supplied, i.e. by temperature or electric field, and each will be discussed shortly in the next sections.

2.1.1 Tunneling

In metal-vacuum-metal tunneling, two metal surfaces are brought close together, separated by a vacuum which acts as a barrier. The energy levels that the electrons occupy in the metals are distributed according to Fermi-Dirac statistics. For the low temperature limit, these energy levels are filled up to the Fermi level E_F and empty above. Classically, the vacuum barrier is inaccessible for electrons because of the potential step between the metal Fermi level and the vacuum barrier height. The height of this step, known as the work function ϕ, is for most high-melting metals around 4.5 eV [99]. Quantum-mechanically, electrons are described by wave-functions, which extend in the barrier with an exponentially decaying tail. When the tails of the wave-functions from both metals overlap, electrons do cross the barrier by tunneling. The resulting tunneling current is determined by the probability that the electrons tunnel through the barrier. In the limit of low voltage and low temperature, Simmons [100] found the following expression for the current density J of a planar tunnel junction using a rectangular barrier shape:

$$J = \frac{3}{4\pi}\frac{e^2}{h}V\frac{\kappa}{s}exp(-2\kappa s) \tag{2.1}$$

where e is the electron charge, h Planck's constant, V is the applied voltage, s is the barrier width and κ is the decay constant of the wave-function in the barrier, determined by $\kappa = 2\pi\sqrt{2m\phi}/h$ with m_e the free electron mass and ϕ the work function.

2.1.2 Thermionic emission

For non-zero temperatures the filling of the electron energy levels is distributed around E_F. The distribution of electrons with energy E and temperature T is then given by the well-known Fermi-Dirac function. At sufficiently high temperatures, normally higher than 1500 K, electron states above the work function are filled, and emission of electrons from the metal into vacuum becomes possible. This process is known as thermionic emission and is treated in more detail in [101].

2.1.3 Schottky emission

In the tunneling equation 2.1 presented above, the barrier shape is assumed to be simply rectangular, however, there are several effects that affect the barrier shape. From classical electrostatics it is known that an electron situated at a finite distance from the surface of a perfect conductor is attracted by the well-known image force, giving the electron a potential energy of $-e^2/16\pi\varepsilon_0 z$, with ε_0 the electric constant. Adding this to the barrier potential results in rounding of the barrier edges and a slightly reduced average barrier height and width, increasing the overall tunneling probability. By applying an electric field the effective work function can be further lowered, enhancing the emission *over* the barrier. This lowering of the barrier height was first described by Schottky [102] and is therefore known as the *Schottky effect*. The enhanced emission is called *Schottky emission*.

2.1.4 Field emission

The emission current can be greatly increased by applying an external electric field between the emitting metal surface and the metal anode surface. The potential for an electron due to a uniform external field E shows a linear decrease with increasing distance z from the interface ($-eEz$).

In figure 2.2, the influence of the electric field on the potential barrier at the emitter side is illustrated. Here the metal Fermi level is taken as a reference level and the total potential barrier can be represented by three components; the work function ϕ, the effect of the electric field E and the image charge potential:

$$V(z) = \phi - eEz - e^2/16\pi\varepsilon_0 z \tag{2.2}$$

It can be seen that for an increasing electric field the barrier becomes triangular. Adding the image potential leads to rounding of barrier edges. The first effect of the increasing electric field is a lowering of the potential barrier, thus the effective work function, with an amount $\Delta\phi$ (Schottky effect):

$$\Delta\phi = \sqrt{e^3E/4\pi\varepsilon_0} \tag{2.3}$$

As a second effect, with increasing fields the effective barrier width is reduced, by an amount Δs. If the reduced distance s is on the order of 10 Å or less, electrons in the

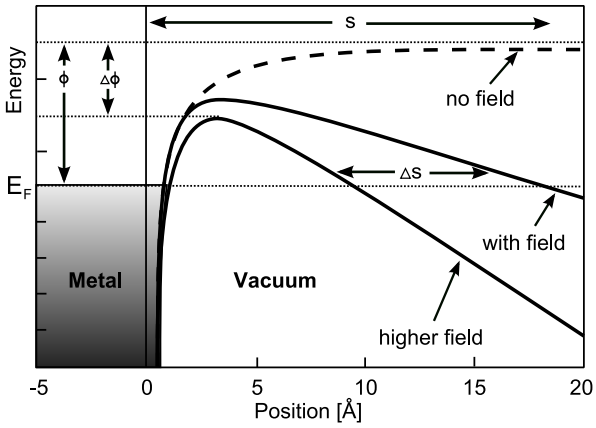

Figure 2.2: *Potential barrier diagram for the metal-vacuum interface with and without applied field. An increase of the electric field leads to a lowering of the work function with $\Delta\phi$ and a reduction of the barrier width with Δs, enabling electrons to be emitted into vacuum. Image taken from [103].*

vicinity of the Fermi level will be able to tunnel through the barrier. This process is known as *field emission*. For most metals, this requires a field on the order of $10^9 - 10^{10}$ V/m. As the field strength becomes larger, more and more electrons below the Fermi level begin to contribute to the emission current. For high temperatures and high applied electric fields, more electrons will tunnel from the energy levels at the top of the barrier, referred to as *thermal field emission*. The transition from the cold field emission regime to this thermal field emission regime can be defined as the value for which more than 10% of the total emission current is due to emission above the Fermi level. From [104] the transition temperature is determined to be according to the simplified relation:

$$T_{FE,thermal} = 3.23 \cdot 10^{-7} \phi^{-\frac{1}{2}} E \tag{2.4}$$

with de work function ϕ in eV, temperature T in Kelvin and the electric field E in V/m. For the emission fields normally used, temperatures well beyond room temperature are needed for the transition from cold to thermal field emission.

For our application we expect to be in the regime of cold field emission, since we are not heating our emitter tips and use relatively low current values. By using a field emitter tip, the electric field will not be constant within the barrier, but will increase close to the sharp apex. In principle the barrier is therefore not triangular, however we will assume that close to the tip, the field can still be approximated by a constant value. Rather than taking this field as the potential divided by electrode distance, we need to include the effect of field enhancement at the tip apex. In the next section therefore a model description of this process and its use for proximity sensing will be given.

2.2 Distance dependence of the field emission effect

To derive the characteristics of cold field emission for proximity sensing, here a model is described that is used to determine the dependence of the field emission current on the distance between a field emitter tip and a counter-electrode. We have adapted the standard Fowler-Nordheim model to incorporate the distance effects and use the resulting model to fit our experimental data. This enables us to extract typical field emission parameters from measurements on a given emitter.

2.2.1 Fowler-Nordheim theory for planar field emitters

The model description of the process of cold field emission of electrons from metal into vacuum is often called Fowler-Nordheim theory, after the first authors correctly describing this effect using quantum-mechanics [98]. In order to calculate the field emission current density as function of the electric field, the Fowler-Nordheim theory uses the following assumptions:

1. The metal obeys the free electron band model.
2. The electrons are distributed according to the Fermi-Dirac statistics.
3. The calculations are performed for the zero-temperature limit.
4. The work function is uniform across the emitting surface.
5. The problem is considered to be a one-dimensional, so the electrode configuration is taken to be planar.
6. The potential barrier shape is calculated using the classical image force whereas the potential inside the metal is considered to be constant.
7. The barrier transmission coefficient may be evaluated using the Jeffreys-Wentzel-Kramers-Brillouin (JWKB) approximation [105].

In the original Fowler-Nordheim analysis an exact solution of the Schrödinger equation was carried out to determine the tunneling probability using the assumptions given above. Since then, many analytical treatments have been developed to refine the theory and to compensate for one or more of these assumptions. Excellent reviews on the developments in Fowler-Nordheim theory and a discussion of the extensions can be found in [101, 105, 106]. In 1956, Murphy and Good set up a general expression for the emitted current as function of field, temperature and work function, to be able to describe the process of both field emission and thermionic emission and the transition region [107]. Recently, this general approach was updated and refined by Jensen [108]. Many authors have shown that the assumption for planar electrodes can give inaccurate results when using emitters with small radii and extensions have been developed to

account for more realistic curved field emitter shapes [109, 110]. Deviations from Fowler-Nordheim behaviour at very high current densities were first detected by Barbour *et al* in the 1950s and are explained as caused by lowering of the electric field due to space charges from the emitted electrons [111]. Field emission from semiconductors is a much more complicated process compared to emission from metals, due to the lower carrier concentration in the emitter bulk, which influences the characteristics of the field emission process [112].

Since we are mainly interested in the results of fitting our experimental data, here we follow the formulation and parameter conventions as given in a recent treatment especially developed for this purpose by Forbes [113, 114], who uses the same assumptions as stated above. In this approach, the generalised Fowler-Nordheim equation describing the emission current I is given by [113]:

$$I = t_N^{-2} \frac{aA}{\phi} E^2 \exp\left\{ v_N \frac{-b\phi^{3/2}}{E} \right\} \tag{2.5}$$

where E is the local electric field and ϕ is the work function. A is the area of emission which is here assumed to be constant, and a and b are universal constants given by:

$$a = \frac{e^3}{8\pi h_p} = 1.54 \cdot 10^{-6} \quad [AeVV^{-2}]$$
$$b = \frac{\frac{3}{2}\sqrt{2m_e}}{e\hbar_p} = 6.83 \cdot 10^9 \quad [eV^{-3/2}Vm^{-1}]$$

with e the elementary positive charge, m_e the electron mass, h as Planck's constant and $\hbar = h/2\pi$.

The values for v_N and t_N result from the mathematical functions $t(y)$ and $v(y)$, which were introduced by Murphy and Good to include the classical image-potential contribution to the potential barrier. The values have been tabulated by various authors [113, 115]. In many works, simplified functions can be found to approximate the values in a certain range for y [116, 117, 118]. In our calculations we use the original functions for $t(y)$ and $v(y)$, which are given in figure 2.3: $t(y)$ in the in the pre-exponential factor in equation 2.5 is close to unity and varies weakly with the argument, $v(y)$ in the exponent varies significantly with y and has therefore a strong effect on the field emission current.

Both are functions of the Nordheim parameter y_N, defined by the electric field and work function:

$$y_N = c\sqrt{E}\phi^{-1} \tag{2.6}$$
$$c = \sqrt{e^3/4\pi\varepsilon_0} = 3.794687 \cdot 10^{-5} \quad [eVV^{1/2}m^{1/2}] \tag{2.7}$$

The original function for v_N is a complex function which is real for $y_N < 1$ [107]:

$$v_N = \sqrt{1+y_N} E_{ell}\left[\frac{\sqrt{1-y_N}}{\sqrt{1+y_N}}\right] - y_N K_{ell}\left[\frac{\sqrt{1-y_N}}{\sqrt{1+y_N}}\right] \tag{2.8}$$

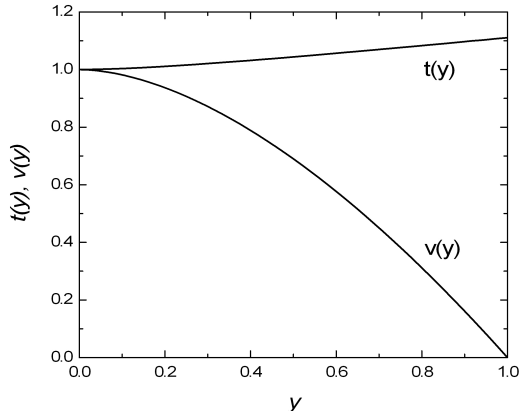

Figure 2.3: *The behaviour of the error correction factors t and v as a function of y.*

with $K_{ell}(k)$ and $E_{ell}(k)$ being elliptic integrals:

$$K_{ell}(k) = \int_0^{\pi/2} \frac{1}{\sqrt{1-k^2\sin^2\theta}} d\theta$$
$$E_{ell}(k) = \int_0^{\pi/2} \sqrt{1-k^2\sin^2\theta}\, d\theta$$

Since for the electric fields we apply, the values for y_N will always be smaller then 1, this equation for v_N will be used in our model. The function t_N can then be described as function of v_N and y_N:

$$t_N = v_N - \frac{2}{3} y_N \frac{dv_N}{dy_N} \tag{2.9}$$

The formulation as given above gives an excellent description of the experimentally observed exponential dependence of the emission current on the field strength E and work function ϕ. In testing the above equations using experimental data, generally a so-called *Fowler-Nordheim plot* is used, by plotting the data as $\log_{10}(I/E^2)$ *versus* $(1/E)$. For metals this results in an almost straight line over a wide range of emission current values. This straight line of data points can be fitted by using the linearised form of the Fowler-Nordheim relation:

$$\begin{aligned} \ln\left\{\frac{I}{E^2}\right\} &= \ln\left\{p\frac{aA}{\phi}\right\} + s\frac{-b\phi^{3/2}}{E} \\ &= \ln(P) + \frac{S}{E}, \end{aligned} \tag{2.10}$$

where $\ln(P)$ and S are the intercept and the slope of the fitted line, respectively. The factors p[1] and s are correction factors to the intercept and slope values that originate

[1] Please note that where Forbes uses r to indicate the correction factor to the intercept, here we use p to discriminate it from the parameter r that we use in this thesis for the tip radius.

from the mathematical functions v_N and t_N and the Nordheim parameter y_N:

$$p = t_N^{-2} \exp\left\{ -\frac{1}{2} bc^2 \phi^{-1/2} \frac{1}{y_N} \frac{dv_N}{dy_N} \right\} \tag{2.11}$$

$$s = v_N - \frac{1}{2} y_N \frac{dv_N}{dy_N} \tag{2.12}$$

When using these relations to fit real measurement data to extract parameter values, the correction factors can make a difference by two orders of magnitude [114], and therefore should be used. The correction factors introduce an additional dependence of the current on the electric field E, however this effect is relatively small and generally it is assumed that the linear relation of the Fowler-Nordheim plot is not significantly affected and thus still linear regression can be used for fitting. A weakness of the formulation described above, is that it neglects a possible dependence of the work function and the emission area on the applied electric field [119]. Here we assume that they are small compared to the variability of the experiments and the measurement errors and therefore may be neglected.

2.2.2 Distance dependence of field enhancement for non-planar field emitters

Since the electric field is proportional to the applied voltage and the emitter-sample distance, the field emission current signal can be used for displacement sensing. In geometrical configurations resembling a parallel-plate capacitor, the electric field E_{planar} is defined by:

$$E_{planar} = V/d \tag{2.13}$$

When using field emitter tips, the field emission current is determined by the local electrical field E_{local} close to the apex of the emitting tip which is often significantly higher than E_{planar}. The ratio of these fields is given by the *field enhancement factor* γ [120]:

$$\gamma = E_{local}/E_{planar} \tag{2.14}$$

In the geometrical configuration of a tip and flat electrode, the maximum electric field E_{local} at the tip end is then defined by:

$$E_{local} = \gamma V/d \tag{2.15}$$

Commonly in literature the field-enhancement factor is denoted by the symbol β. However, this symbol β is also used for the conversion of the voltage to the local field as introduced by Dyke *et al* [121]:

$$\beta = E_{local}/V \tag{2.16}$$

Therefore here we follow the convention as introduced by Forbes [120] and use the symbol γ as a definition for the field enhancement factor, which is related to β by $\gamma = \beta d$.

The enhancement factor γ at the apex of the tip is of particular interest if we want to determine the dependence of the field emission current on the distance between the tip and sample. This field enhancement is determined by the shape of the emitter-sample geometry and depends non-linearly on the separation distance. Precise knowledge of this distance dependence is therefore required to be able to determine its influence on the field emission current.

Different approaches for the derivation of this field enhancement factor can be found in literature. Normally it is assumed that the emitter and sample surfaces are at fixed potentials which reduces the problem to solving Laplace's equation for a given applied voltage between the tip and sample. Because of the specific shapes of practical field emitters, the solution of this problem can still be difficult, and several simplified models of the tip shapes have been introduced [120, 122, 123, 124, 125]. As a first approximation, the emitter-sample geometry can be modelled as a floating sphere in between a parallel plate configuration. See figure 2.4 for an illustration and definition of the parameters used. Here the emitter tip end is represented by a sphere at uniform potential, connected to the top electrode while the bottom electrode is at ground potential. Since the potential of the floating sphere and the emitter plane are equal, the potential between these two on average is zero, which explains that this representation provides a correct approximation of the field emitter geometry.

In the treatments given in literature, it is normally assumed that the distance between the field emitter tip apex and the counter-electrode is much larger than the tip radius and the length of the field emitter. For this case the floating-sphere model can be solved analytically by calculating the field contributions of a charged sphere and its image charges. In reference [120] a summary can be found of the various results that were obtained by various authors. For such geometries, the mathematical expressions found

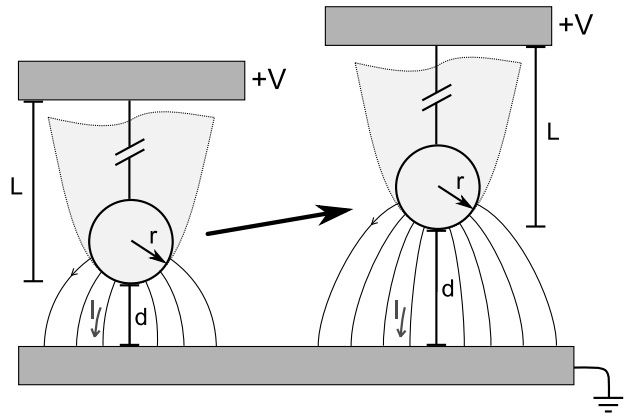

Figure 2.4: *Geometric model and symbol definitions used for calculating the field enhancement factor for an emitter tip of length L with radius r, at distance d from the counter-electrode.*

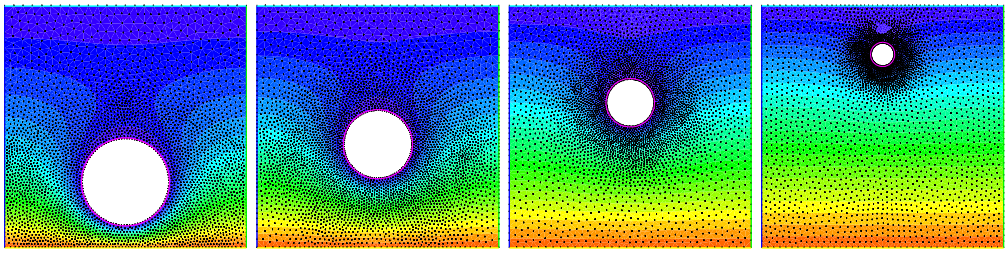

Figure 2.5: *FEM calculations of the electrostatic potential fields for the biased emitter sphere at $L = 10r$ from the top electrode, for increasing distance $d = 0.5r$, $2r$, $5r$ and $15r$ from the grounded bottom electrode. The boundaries of the calculation domain scale with the distance d: for $L = 10r$ and $d = 15r$ calculated domain has a width of $25r$.*

for the field enhancement factor at large distance γ_∞, typically have the form

$$\gamma_\infty = L/r + m \tag{2.17}$$

where L is the height of the sphere above the emitter-plane, r is the sphere radius and m is a constant variously determined to be between 0 and 3.

Since most field enhancement studies are performed at large distances ($d \gg r$), a model to estimate the field enhancement valid at small distance needs further study. An often mentioned model was presented by Miller [122] that used the same geometric definitions as described above. Miller gives the distance dependence by the formula $\gamma(d) = \gamma_\infty d/(d+L)$. This equation suggests that γ decreases with the separation distance d and approaches zero as d becomes very small. However, we know that γ should approach unity when the separation distance is much smaller than the tip radius, since then the geometry approaches that of a parallel plate and effectively there is no field enhancement. Hence we would expect a field enhancement factor that is unity for very small separation distance and saturates to the value of γ_∞ for large separation.

To find the precise expression describing the distance dependence of the field enhancement factor, we calculated γ for the floating sphere configuration by finite element method with FREEFEM++ software [126]. Although this geometry approximation is probably not valid for the complicated emitter shape that we will utilize in our experiments, this simple model is used to study the effect of tip radius and tip-electrode distance on the field enhancement. Since our geometry is cylindrical symmetric about the z axis, the electric field is calculated using the Laplace equation in cylindrical coordinates, omitting the dependence on θ:

$$\frac{\partial^2\phi}{\partial r^2} + \frac{1}{r}\frac{\partial\phi}{\partial r} + \frac{\partial^2\phi}{\partial z^2} = 0 \tag{2.18}$$

The input for FREEFEM++ requires this Laplace equation to be written in the weak form, which is given by [127]:

$$\int_\Omega \nabla\phi \cdot \nabla\eta \; d\Omega = \int_\Omega \left(\frac{\partial\phi}{\partial r}\frac{\partial\eta}{\partial r} + \frac{\partial\phi}{\partial z}\frac{\partial\eta}{\partial z} \right) r \; d\Omega \tag{2.19}$$

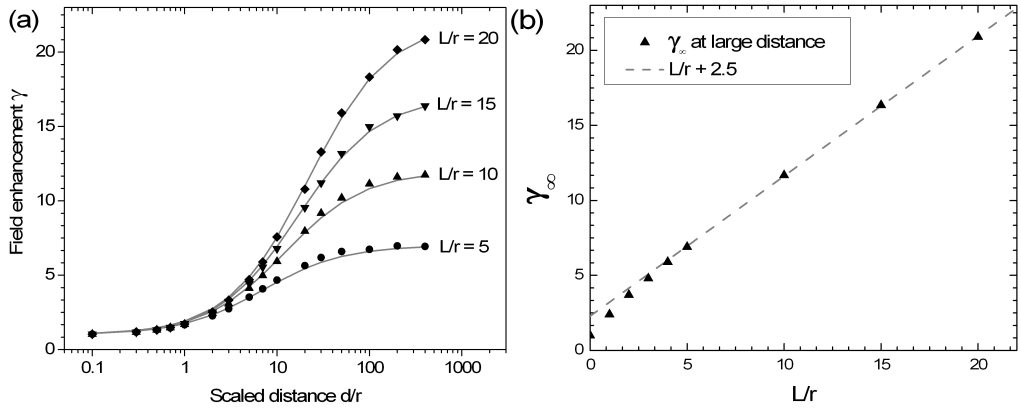

Figure 2.6: *Field enhancement factors determined by FEM calculations (a) as function of scaled distance L/r for increasing tip lengths $L = 5r$, $L = 10r$, $L = 15r$ and $L = 20r$. (b) Maximum field enhancement factors γ_∞ determined for large distance for increasing tip lengths $L/r = 0, 1, 2, 3, 4, 5, 10, 15$ and 20.*

where η represents the help function needed in the weak form representation. The above equation is used to compute the electrostatic potential fields as a function of the distance between the floating sphere and the counter-electrode. The resulting equipotential line plots can be found in figure 2.5. Since the electric potential changes rapidly at the apex of the sphere, a very high density of finite element nodes is needed at this point to obtain an accurate solution. The repeated use of the `adaptmesh` function was used to generate a mesh with high density in this region. The size of the calculated geometry and the number of mesh refining iterations was increased until the relative error between two subsequent calculations was less then 10^{-3}. With increasing distance d the size of the geometry under calculation increases, which requires even more nodes to be calculated, up to 10^6.

From the FEM calculations, the value of the electric field was determined at the apex of the sphere, closest to the counter-electrode. As expected here the electric field is highest. By dividing this value by the planar electric field V/d the field enhancement factor is obtained. In figure 2.6a the FEM results for this field enhancement factor are plotted as function of the scaled distance d/r. It was found that the outcomes of the finite-element analysis of this geometrical model can be approximated by using the following relation:

$$\gamma = \frac{\gamma_\infty (r+d)}{\gamma_\infty r + d} \tag{2.20}$$

which describes the field enhancement at the apex of a sphere with radius r at a distance d from a flat counter-electrode, with γ_∞ the field enhancement at large distance. Although this relation does not perfectly fit the FEM results, it is in good agreement with our expectations for the distance dependence of the field enhancement factor: for small distance, the electrode configuration approaches a parallel plate configuration

($\gamma \approx \gamma_\infty r/\gamma_\infty r = 1$); for large distance, the field enhancement factor saturates to a maximum value ($\gamma = \gamma_\infty$).

The influence of the emitter tip length L was determined by repeating the FEM calculations for $L/r = 0, 1, 2, 3, 4, 5, 10, 15$ and 20. The results are shown in figure 2.6b. For $L/r = 0$ the configuration is that of a parallel plate and the maximum field enhancement is unity, as expected. For $L \gg r$ the value for the maximum field enhancement is found to saturate to:

$$\gamma_\infty = L/r + 2.5 \tag{2.21}$$

which is in agreement with formula 2.17 and analytical results obtained by others [120].

Using the model for γ together with the Fowler-Nordheim equation results in a complete description of the dependence of the field emission current on distance and applied voltage. The value for the area of emission A and the radius of the emitter r are coupled; if the area of emission is considered to be a half sphere this relation can be simply described by $A = 2\pi r^2$. Then the Fowler-Nordheim equations becomes:

$$I(d) = t_N^{-2} \frac{a\, 2\pi r^2}{\phi} \left(\gamma(d)\frac{V}{d}\right)^2 \exp\left\{ v_N \frac{-b\phi^{3/2}}{\gamma(d)\frac{V}{d}} \right\} \tag{2.22}$$

By means of this formula we are able to predict the exponential dependence of the field emission current on the applied voltage *as function of distance*. As an example, figure 2.7a shows a plot of the emission current, calculated using equation 2.22 as function of voltage V. The parameters used to obtain the curves are $\phi = 4.5$ eV, which is a typical work function for metals and $r = 10$ nm, which is a typical tip radius for an uncoated AFM probe. The distances are $d = 10, 20, 30, 40$ and 50 nm. The plot shows that for increasing distances, a higher voltage is required to extract a certain field emission current. The increase in required voltage is not linearly dependent on distance, due to the effect of the changing field enhancement.

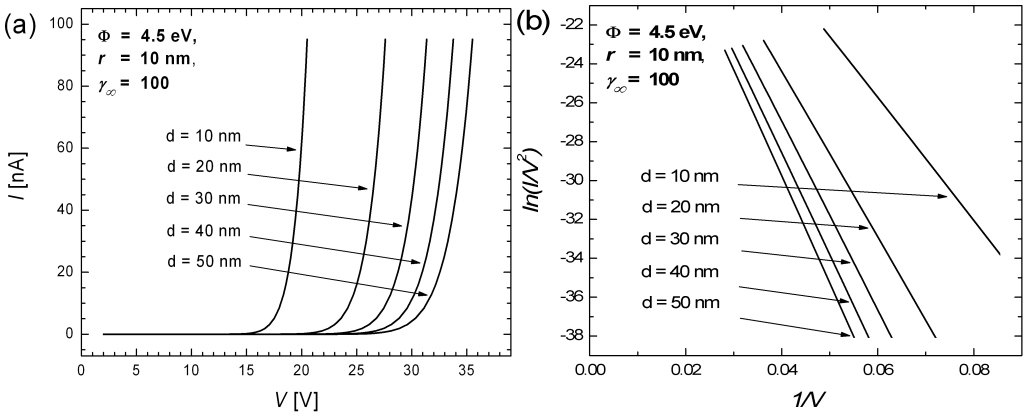

Figure 2.7: *Theoretical emission current as function of the applied voltage for varying values of the emitter-sample distance $d = 10, 20, 30, 40$ and 50 nm (a) in I-V representation and (b) represented as a Fowler-Nordheim plot.*

In figure 2.7b the same curves are plotted in Fowler-Nordheim coordinates. This figure illustrates the linearization of the *I-V* curves when plotting the *I-V* data on a semi-logarithmic scale according to $f(1/V) = \ln(I/V^2)$. To find the field enhancement factor $\gamma(d)$ and area of emission A for a real emitter, the Fowler-Nordheim relation should be fitted to the experimental data. For this a Fowler-Nordheim plot and the linearised form of the Fowler-Nordheim relation can be used:

$$\begin{aligned} \ln\left\{\frac{I(d)}{V^2}\right\} &= \ln\left\{p\,\frac{a\,2\pi r^2}{\phi}\left(\frac{\gamma(d)}{d}\right)^2\right\} + s\left\{\frac{-b\phi^{3/2}}{\gamma(d)\frac{V}{d}}\right\} \\ &= \ln(P_V) + \frac{S_V}{V} \end{aligned} \tag{2.23}$$

where $\ln(P_V)$ and S_V are the intercept and slope of this voltage-based Fowler-Nordheim plot.

The values for P_V and S_V can be derived from the value of the fitted line at $f(0)$ and the fitted line slope. The values found for P_V and S_V can then be used to determine the parameters γ and r. This is not a trivial procedure since p and s and thus P_V and S_V are depending on the electric field. Therefore an iterative procedure for fitting data has to be used, which will be further discussed in chapter 5.

The model presented above can be used to predict the ideal sensing characteristics for a given emitter. In practical field emitters, the current however suffers from several types of instabilities. In the next section the causes for these instabilities will be discussed in order to be able to find the materials and vacuum conditions that can be used to apply the field emission probes for proximity sensing.

2.3 Field emission current stability

A well-known challenge for application of cold field emission in practical devices is the inherent instability of field emission, which causes large current fluctuations. This instability induces large noise in the current signal as well as problems in maintaining stable device characteristics and a limitation in the usable life-time. The instabilities in the field emission current arise from atomic changes of the field emitter and sample surfaces and can be categorized in three major causes [128]:

1. Electron- and ion-bombardment of the field emitter and sample surfaces.
2. Surface diffusion of adsorbed atoms (contamination)
3. Thermal instability of the field emitter and sample surfaces.

In the following sections these causes will be further discussed in order to draw conclusions at the end of this chapter for the materials and operating conditions that should be used to relieve the stability problems for application of field emission for proximity sensing.

2.3.1 Surface changes by electron- and ion-bombardment

A severe limitation to the stable operation of normal field emitter devices is the ion-bombardment of the tip surface. Residual gasses can be ionized by the field emitted electrons, and the ions then are accelerated towards the emitter where they may degrade the tip apex at impact [129]. This ion bombardment causes sputtering of the field emitter surface and changes the surface roughness or creates sharp nanoprotrusions. Since the electrons are expected to be emitted from the sharpest points, where the local field is largest, the surface changes can cause shifts in the location of the emission sites and consequently large variations in the emitter current.

The total number of ions that is formed per second is given by [130]:

$$\frac{dn_{ions}}{dt} = \frac{I_e}{e} S\, n\, \sigma\, \Delta z \tag{2.24}$$

where I_e is the electron current, e the electronic charge, S the electron beam spot size which we assume constant over the distance, n the number density of gas molecules ($= p/kT$ molecules/cm^3), σ the ionization rate and Δz the distance between tip and sample. Assuming an electron current of 100 nA, approximately 10^{12} electrons are emitted per second. At 10^{-9} mbar, n is about $2.5 \cdot 10^7$ cm^{-3}. When assuming an ionization rate of one ion per 10^5 electrons [130], approximately 10^7 ions can be formed every second per cm^3. The ions that are formed will be mostly hydrogen, oxygen and nitrogen. The sputtering yield of these ions depends on their mass and kinetic energy. For hydrogen, this yield is about two orders of magnitude lower so its contribution can be neglected whereas for oxygen and nitrogen the yield can be assumed to be equal. Smith showed that for ions created in the inter-electrode gap, the average energy of those striking the emitting portion of the surface is $\sim$ V/10, with V the voltage applied between the emitter tip and counter-electrode [130]. For an applied voltage of 100 V the ions thus have a relatively low average energy ($\sim$ 10 eV) but this is already near the threshold energy for sputtering of e.g. molybdenum [131].

Using equation 2.24 we find that the problem of surface changes by ion bombardment can be alleviated by operating the device in a better vacuum, by lowering the applied voltage but also by reducing the distance between the electrodes. At the very short emitter-sample distances that are intended to be used in this work, it would be expected that the number of created ions *decreases* rapidly since there are simply less gas molecules that can be ionized in the electrode gap. However, ions can also be created from adsorbed molecules at the sample surface that desorb due to electron stimulation [132]. The number of desorbed molecules is determined by a balance between the adsorption rate of incoming gas molecules and the desorption rate caused by the incoming electrons. The probability of such desorbed ions hitting the emitter tip can be calculated and in turn *increases* steeply with the decreasing tip-sample distance [133]. For bad vacuum conditions the rate of desorption is determined by the electron density and can be very high. For vacuum conditions better than 10^{-6} mbar and at small distance, electron stimulated desorption occurs as soon as a gas molecule is adsorbed on the

surface and the number of desorbing molecules is effectively determined by the coming rate of the gas molecules [134].

Therefore in our work the pressure is the most important parameter in preventing ion bombardment of the field emitter tip and should be at least better than 10^{-6} mbar to prevent build-up of adsorbates. Since there is also transport of adsorbates over the sample surface, like field-enhanced surface diffusion that will be discussed in section 2.3.3, the ion creation rate will be larger than calculated above. Therefore surface diffusion should be reduced, e.g. by cooling the sample surface and by preventing (water) contamination films that can reduce the surface binding energy.

2.3.2 Surface changes due to contamination

Another well-known phenomenon leading to instabilities is the changing of the emitter due to physical adsorption and chemisorption of gas molecules on the surface. Once contaminants are attached to the emitter, electron-excited chemistry is possible that can lead to tip corrosion and reactions between the adsorbates [131]. The chemical reactions lead to deposition effects at the tip surface. Moreover the high electric field at the tip region cause electrostatic forces on adsorbates towards the tip, which can lead to a spike of material growing at the end of the emitter [135]. The adsorption and diffusion phenomena have been studied extensively in the past using field emission and field ion microscopy on mono-layers and even single atoms of adsorbates on clean and mostly mono-crystalline field emitter tips [101, 129]. The effect of such adsorbed contamination layers affect the field emission process since they change the electron tunneling probability through modification of the local work function. Changes in the effective work function thus are reflected in the (local) field emission current and in its stability in time.

For practical applications, the emitter surface is therefore one that is chemically inert. Also a low work function is desired, since this would enable lower voltages needed for a certain field emission current. This can be achieved by overcoating the field emitter tips with other materials. Unfortunately, for materials with a lower work function, such as Cs [136], the chemical reactivity of the surface increases which causes rapid degradation. To achieve more chemically inert emitter-tip materials, studies have therefore been conducted for the emission properties of metal carbides, such as metal nitrides [103], carbides like ZrC and HfC [137], or conductive oxides [138]. Other classes of materials that have received much attention for their good and potentially chemically inert field emission properties are overcoatings of conductive diamond [139, 140] and carbon nanotubes [141, 142].

Even when using chemically inert materials and initially clean emitter surfaces, any residual pressure will gradually contaminate the emitter and counter-electrode surface. The contamination rate can be calculated from the number of molecules incoming per second [129]:

$$\frac{dn_{gas}}{dt} = \frac{P}{\sqrt{2\pi m k T}} \tag{2.25}$$

with P the (partial) pressure [Pa] and m the molecule mass [kg]. In reality, the gas supply to the tip is greatly enhanced. Due to the presence of the strong electric field near the tip surface, gas molecules are polarized and attracted to the tip surface [143]. Equation 2.25 is therefore only used as an approximation for the monolayer formation time. At $P = 10^{-6}$ mbar and $T = 300$ K, approximately 10^{18} molecules impinge per cm^2 per second. If we assume that there are 10^{15} adsorption sites per cm^2 and every molecule sticks to the surface, the time for one atomic layer of gas to adsorb is approximately 1 s. If we want to prevent rapid contamination of the emitter and counter-electrode surface we therefore need pressures lower than 10^{-9} mbar. Moreover if clean surfaces are needed, the emitter and counter-electrode should be heated in the vacuum to the point where the contaminants decompose or evaporate.

2.3.3 Surface changes due to thermal effects

Instabilities in the field emission current can also arise from disturbances in the thermal equilibrium of the field emitter surface itself. Of course at room temperature, the field emitter surface is by no means static. From the earlier work on field ion microscopy it was well-known that kinetic processes at the surface had a significant influence on the stability and resolution and therefore the emitter tips had to be cooled down to reduce the hopping motion of surface atoms [143]. For field emission applications, surface migration is already substantial at room temperature. Moreover the emitter tip is heated as a result of two processes: Joule heating and heating due to the Nottingham effect. In the following these two processes will be shortly described, after which we will discuss two kinetic processes that can take place at elevated temperatures: field-enhanced surface diffusion and field evaporation.

Joule heating

The high current densities that flow through the small emitter tip can give rise to significant Joule heating. The amount of heat produced by current flowing at a density J [A/m^2] through a material of resistivity ρ [Ωcm], is given by $\Delta H = \rho J^2$ [W/m^2]. The resulting effect on the emitter temperature has been estimated analytically by neglecting radiation cooling and assuming that only the emitter dissipates power. For a simple cylindrical tip geometry, this temperature increases with increasing distance from the substrate heat sink until the highest temperature is reached at the emitting end [144]:

$$\Delta T_{max} = \frac{\rho L^2 J^2}{2k} \tag{2.26}$$

with $\Delta T_{max} = T - T_0$, T_0 the substrate temperature, L the emitter height, ρ the electrical resistance and k the thermal conductance of the emitter to the substrate. The main problem in estimating ΔT_{max} is that the ρ and k values are dependent on this temperature. Karain *et al* therefore used averaged values to calculate the Joule heat given to a silicon tip with 10 nm radius and a height of 10 μm. An emitted current density of 10^{10} A/m^2

would be needed to reach high enough temperatures (>1690 K) to melt the tip, which for the given tip radius would require a very high total current of 3 μA through a single tip [145].

Since the material resistivity increases with temperature, resistive heating alone creates a very unstable situation at high current densities, eventually leading to a voltage breakdown in the form of a field emission initiated vacuum arc. This failure mechanism proposed by Dyke *et al* is thought to occur at high current densities. The tip temperature then rises very rapidly to the temperature where the tip surface layer evaporates. Due to the high electric fields, arcing initiates and destroys the emitter.

Despite this effect, very high field emission current densities have been achieved experimentally, close to the theoretical limit of 10^{15} A/m [105]. A strong and stabilizing influence on the emitter temperature preventing early breakdown at these high-density emission currents is addressed to the Nottingham effect.

Nottingham effect

An important contribution to the thermal balance during field emission is given by the Nottingham effect. Due to this quantum-mechanical energy exchange process, the emitter tip temperature is balanced by electrons tunneling from above and below the Fermi level. At low temperatures most of the electrons tunnel from energy levels below the Fermi level and since their energy is lower than that of the conduction band electrons that replace them, the emitter tip is heated. As the temperature increases, the Nottingham effect begin to cool the emitter, since most of the electrons are emitted from energy levels above the Fermi energy and thus extract energy from the field emitter tip [105]. The balance temperature is related to the electric field needed for field emission E [V/m] and the work function of the material ϕ [eV] [146]:

$$T_c = 5.32 \cdot 10^{-7} E / \sqrt{\phi} \tag{2.27}$$

Hence the Nottingham effect tends to stabilize the tip temperature at a value near this inversion temperature. For a typical field emission field of $8 \cdot 10^9$ V/m and a work function of 4.5 eV this occurs at a temperature of ~ 2040 K. For materials having melting points below this inversion temperature, this will result in emitter destruction.

Field-enhanced surface diffusion

As a result of the emitter heating and the applied electric field, atomic transport can take place, not only of adsorbed contaminants, but also of lattice atoms. The surface shape of the emitter under an applied field is therefore not stable, but a dynamic equilibrium between the surface tension on the emitter and the electric field that is applied to the emitter. On the one hand, the emitter-tip surface energy causes blunting of the tip. On the other hand, the electric field energy causes surface migration of emitter material towards the emitter apex. At high temperatures and when the electric field is low, the emitter tends to re-shape towards a larger radius of curvature. If the electric field is high

enough so that electrostatic forces dominate over surface tension forces, atoms move from the emitter sides to the tip apex by the directional surface diffusion and form a sharper tip. From a model developed by Barbour *et al* it was shown that this sharpening is only to occur when the electric field E obeys [147]:

$$E > 2.24 \cdot 10^5 \sqrt{\frac{\sigma}{r}} \tag{2.28}$$

in which σ is the surface tension and r the emitter radius. If we take $\sigma = 0.72\,\mathrm{N/m}$ for silicon [148] and $r = 30\,\mathrm{nm}$, E should be about $10^9\,\mathrm{V/m}$ to have sharpening of the emitter tip. Materials with a lower surface tension, such as contaminants, will migrate to the tip apex before that value is reached.

The field-enhanced surface diffusion thus can be used to sharpen the tip, but for small tip-sample spacings the atoms on the sample surface directly under the probing tip will also be attracted. Due to the high field gradient, adatoms at the sample surface will be polarized and perform a directional walk towards the emitter tip [149]. The drift velocity of an adatom is related to its surface-induced dipole moment μ and to its effective polarizability α through [150]:

$$\frac{dx}{dt} = 2\nu_0 l\, exp\left(-\frac{E_d}{kT}\right) sinh\left[\frac{\beta l(\mu + \alpha E_c)}{2kT}\right] \tag{2.29}$$

Here ν_0 is the hopping frequency, typically taken as $10^{13}\,s^{-1}$, l the hopping distance, E_d the activation energy of surface diffusion, E_c the electric field under the emitter tip and β the lateral gradient of the field. The activation energy that is needed for surface diffusion is thus lowered by the polarization energy. Since the polarization energy is higher near the tip because of the higher field, the net migration of adatoms will be towards the centre under the emitter tip. The electric field gradient on the sample surface thus will increase the transport of adatoms. Moreover, contamination of the sample surface may lead to a lowering of the activation energy needed for diffusion, further increasing the diffusion on the sample surface [151].

Field evaporation

When the electric field reaches a few volts per ångström, atoms start to emit out of the surface due to the high electric field strength, a process known as *field evaporation*. This effect is used in field ion microscopy to produce greatly magnified and atomically resolved images of the emitter surface by radial projection of the field evaporated and ionized atoms. The capability of field evaporating the surface atoms layer-by-layer is used in the atom-probe to determine the chemical composition of the emitting sample [143]. Since the local electric fields are largest above protrusions of the emitter surface, atoms at these protrusions will start to evaporate before atoms at more smooth parts of the surface. Field evaporation is thus a self-regulating process that enables preparation of the emitter tip in order to remove surface contamination and protrusions.

A model to describe the basic mechanism for field evaporation is given by the image-hump model [152]. This model describes the process as the thermal activation of a metal ion of charge n over a potential barrier. The evaporation field E as calculated by this model is given by:

$$E_{evap} \simeq (\Lambda + \sum_i I_i - n\phi)^2 / n^3 e^3 \tag{2.30}$$

Here Λ is the atom binding energy, $\sum_i I_i$ the energy needed to ionize the atom into an n-fold charged ion and $n\phi$ the electron energy that is returned to the emitter. Since the evaporation rate, when increasing the field beyond this value, is a thermally activated process, it is given by the following Arrhenius equation:

$$\chi = \nu_0 \, e^{-Q_n(E)/kT} \tag{2.31}$$

where $Q_n(E)$ represents the activation energy that is needed to form the ion in an applied field E:

$$Q_n(E) = \Lambda + \sum_i I_i - n\phi - (ne)^{3/2} E^{1/2} \tag{2.32}$$

The theoretical evaporation fields that can be calculated using this simple model are found to fit well with experimental data and are given for various materials in [143, 152].

Whereas in field ion microscopy these evaporation fields are typically higher than $3 \cdot 10^{10}$ V/m, at small distances in the configuration of an STM, threshold evaporation fields are reported to be smaller, from $0.4 \cdot 10^{10}$ V/m for Au atoms [153] to $1.0 \cdot 10^{10}$ V/m for Si atoms [154]. Another major difference in the results obtained with STM, compared to FIM studies, is the field evaporation of *negative* ions. In FIM only field evaporation of *positive* ions could be shown by applying a high positive bias voltage to the emitter tip, since for a negative voltage the simultaneous field electron emission current would melt the tip at the fields needed for negative ion evaporation. In STM however the close proximity of the emitter and sample surface causes overlap of the atomic potentials, which can lower the activation energy needed for field evaporation [155]. This property has been utilized as a tool for controlled modification of the sample surface by material transfer between the tip and sample. Mamin *et al* used 600 ns voltage pulses between 3.5 and 4 V to create ordered arrays of gold mounds on a gold surface, 10-20 nm wide and 2-3 nm high. These mounds were attributed to a field evaporation process of both positive and negative gold ions, depending on the sign of the applied voltage pulse. When using a tungsten tip however only pits could be created in the gold sample, which was attributed to the field evaporation from the gold surface towards the tip [153].

Field evaporation thus has been used to explain the effect of material transfer in STM and since in our application field emitters will be operated at similar field strengths, this effect could very well lead to instabilities. However for interpretation of the same results also other mechanisms have been proposed. Pascual *et al* deny the atom mounds formation in STM to be a field evaporation process but assumes the formation

to be due to a direct mechanical contact [156]. This mechanical contact could have been established by field-enhanced surface diffusion or by large electrostatic forces causing mechanical deformation. Also tip melting followed by a tip-sample contact and subsequent break junction has been proposed as an explanation for the mounds formation [155, 157].

Apart from the instabilities inherent to the field emission process that have been discussed above, in our specific application mechanical instabilities can occur due to the electrostatic interactions between the medium and cantilever probe that we intend to use. These interactions and the effect on the mechanical stability of the probe-medium system will be separately discussed in the next section.

2.4 Electrostatic interaction of the probe-medium system

An important complication of the intention in our work to use magnetic media to store data is that a cantilever probe has to be used. The bending action of the cantilever is required to be able to sense magnetic information from shifts in the resonance frequency. The incorporation of a cantilever however introduces a highly unstable component in the mechanical loop of our system. Due to electrostatic interaction between the cantilever probe and the sample, the cantilever deflects when applying a bias voltage. When the tip is in close proximity, the forces between tip and sample can result in pull-in, thus bringing both in physical contact. This effect is well-known from electrostatic actuators, where the pull-in is an important problem and limits the maximum travel range to one-third of the original gap [158].

In order to avoid this problem in our measurements, we used an analytical model to predict the bending behaviour of our cantilever for increasing bias voltage. Various of such models have been developed in literature to calculate the deflection as function of voltage, used to understand the results obtained in electrostatic force miscroscopy (EFM) [74, 159, 160]. Other models have been developed to calculate the theoretical distance and voltage at which a cantilever collapses irreversibly onto the substrate [161, 162].

Here we use a model that was developed by Toset *et al* [163]. The advantage of using this model over others is that it describes the bending of an AFM probe due to electrostatic force and includes the effect of electrostatic pull-in. Moreover, in their work the theoretical model has been validated experimentally using probes similar to those used in our experiments, which increases its reliability.

In this model, a tip on a flexible cantilever in front of a counter-electrode sample is considered. The AFM probe-sample system and the forces acting on the tip and cantilever are shown schematically in figure 2.8. The involved forces are the cantilever elastic force F_K, the electrostatic force F_C and the Van der Waals short range interaction force F_{vdW} (see section 1.2.4). In order to determine the tip-sample distance for a given applied bias voltage, we calculate the minimum energy of this system. The total energy

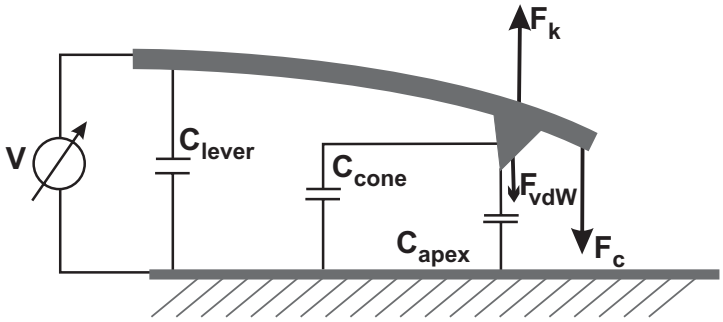

Figure 2.8: *Schematic representation of the forces acting in the probe-medium system and the capacitances that are used to calculate the electrostatic force interaction.*

consists of the following contributions:

$$|E_{total}| = |E_K| + |E_C| + |E_{vdW}| \tag{2.33}$$

The elastic energy stored in the cantilever is given by its mechanical properties [161]:

$$E_K = \frac{1}{2}\frac{Y t^3 w}{2l^3}(z_0 - z)^2 \tag{2.34}$$

where Y is the Young's modulus for silicon, t the thickness and w the width of the cantilever and z_0 and z are the initial (zero applied bias) and actual tip-sample distance, respectively. By using the spring constant K of the cantilever, the elastic energy can be replaced by:

$$E_K = \frac{1}{2}K(z_0 - z)^2 \tag{2.35}$$

The electrostatic energy E_C is modelled as the energy of the total capacitance C_T formed between the probe and the sample for an applied voltage V:

$$E_C := \frac{1}{2}C_T(z)V^2 \tag{2.36}$$

The capacitance C_T is a non-linear function of the tip-sample spacing z and is used to describe the dependence of the electrostatic force on distance. To find this dependence it is usually assumed that the probe-sample capacitance C_T can be modelled by the individual contributions of the cantilever and tip elements. The total capacitance is therefore split in three parallel capacitances representing the capacitance between the sample and the cantilever, tip cone and tip apex:

$$C_T(z) = C_{lever}(z) + C_{cone}(z) + C_{apex}(z) \tag{2.37}$$

Explicit expressions for the capacitances in terms of the geometric properties of metallic probes are found in literature [159, 160, 164]. The capacitance associated with the

cantilever C_{lever} is characterized by its length l, its width w, the distance between sample and cantilever $z+L$ and a tilt angle θ_{lever} with respect to the sample surface and can be approximated for small tilting angles by [160]:

$$C_{lever} = \varepsilon_0 w \frac{\tan^2(\theta_{lever})}{\theta_{lever}^2 \tan(\frac{1}{2}\theta_{lever})} \ln\left(1 + \frac{2l\tan(\frac{1}{2}\theta_{lever})}{z+L}\right) \tag{2.38}$$

where ε_0 is the electric constant.

The probe tip consists of a truncated cone of height L and an opening angle θ_{cone} which ends smoothly in a tip apex with radius r. For tip-sample distances smaller than the cone height L the capacitance for the probe cone can be approximated by [159][2]:

$$C_{cone} = \frac{-8\pi\varepsilon_0}{(\pi-\theta_{cone})^2}\left[f_1\ln((f_1)-1) - f_2(\ln(f_2)-1) - \sin(2\theta_{cone})(L\ln(2f_1) - \delta\ln(2f_2))\right] \tag{2.39}$$

The factors f_1 and f_2 are defined as $f_1 = z+H-\delta/2$, $f_2 = z+\delta/2$ where δ is the height of the truncated part of the cone, given by $\delta = r/\tan^2(2\theta_{cone})$.

Finally, the probe apex is assumed to be a parabolic cap which is connected to the truncated cone. The spherical apex is characterized by the radius of curvature r and the angular aperture of the cone θ_{cone}. The contribution to the capacitance by this apex as function of distance can be given by [164]:

$$C_{apex} = 2\pi\varepsilon_0 r \ln\left[\frac{z+r(1-\sin(\theta_{cone})}{z}\right] \tag{2.40}$$

For the Van der Waals energy E_{vdW} we use a slightly different version of equation 1.2 used in chapter 1 to describe the Van der Waals force. There it was assumed that the distance z is small compared to the tip radius r, however this assumption is generally not valid at the length scales involved in AFM, where the tip radius can be ~ 5 nm and the distance is on the same order of magnitude. Without this assumption, the Van der Waals interaction energy between the apex sphere of radius r and the substrate sample becomes [165]:

$$E_{vdW} = \frac{A_H r}{6 r_0^2}\left[\frac{1}{28}\left(\frac{r_0^8}{z^7}\right) - \left(\frac{r_0^2}{z}\right)\right] \tag{2.41}$$

where A_H is the Hamaker constant and r_0 is the interatomic spacing (~ 0.4 nm). More advanced models for the Van der Waals interaction can be developed to include the effect of the tip cone [165, 166], but for simplicity we assume that this influence can be neglected.

[2] Note that in reference [160] and [163] the first appearance of θ_{cone} in this equation has been erroneously replaced by θ_{lever}

The equations given above can be used to determine the bending behaviour of the cantilever. For a given DC bias voltage, the equilibrium tip-sample distance is found by calculating the minimum of the system energy, which corresponds to the situation where the net force is zero. For zero applied voltage, this minimum is determined by the elastic energy and the tip-sample distance is at the initial tip-sample distance z_0. For increasing bias voltage, the energy minimum moves to a smaller distance due to the effect of the electrostatic interaction. The location of this electrostatic minimum is essentially determined by the elastic and electrostatic forces, as long as the probe tip is far enough from the sample surface and Van der Waals forces can be neglected. For voltage control, the location of this minimum can be calculated from the derivative to z of the Legendre transformed energy function [167]:

$$\frac{\partial E'_T}{\partial z} \approx K(z_0 - z) - \frac{1}{2}\frac{\partial C_T}{\partial z}V^2 = 0 \tag{2.42}$$

When the voltage is further increased, the electrostatic minimum disappears and the tip moves quickly to the Van der Waals minimum, corresponding to the pull-in of the cantilever. The system becomes unstable when also the second derivative of E'_T equals zero, given by

$$\frac{\partial^2 E'_T}{\partial^2 z} \approx K - \frac{1}{2}\frac{\partial^2 C_T}{\partial^2 z}V^2 = 0 \tag{2.43}$$

This relation describes the 'effective spring constant' of the system. When the factor $\frac{1}{2}\frac{\partial^2 C_T}{\partial^2 z}V^2$ completely negates the mechanical spring constant, the system becomes unstable and the cantilever snaps in.

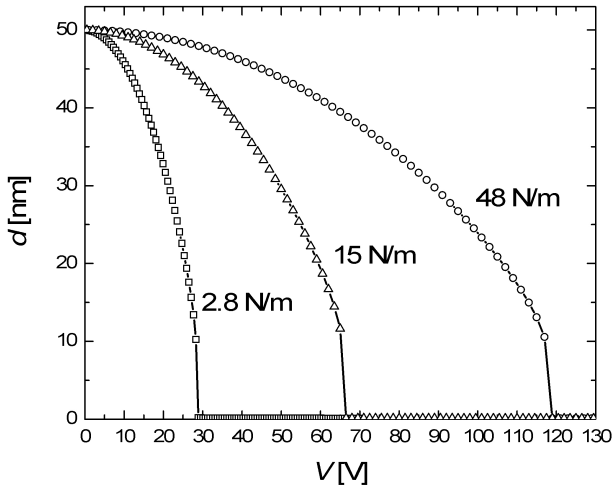

Figure 2.9: *Calculation of theoretical cantilever deflection as function of applied voltage for an initial distance of 50 nm, for three values of the cantilever spring constant $K = 2.8$ N/m, $K = 15$ N/m and $K = 48$ N/m.*

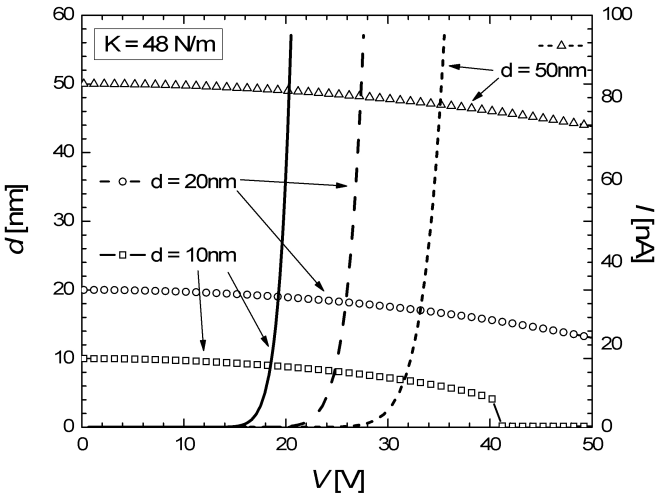

Figure 2.10: *Theoretical cantilever deflection compared to the field emission current as function of applied voltage, for varying initial distances $d = 10$ nm, $d = 20$ nm and $d = 50$ nm.*

The analytical model was used to determine the voltage dependence of the cantilever bending. By iteratively calculating the minimum of the system energy, including the Van der Waals effect, the deflection-voltage curve can be obtained. For the calculations we took the parameters for the typical AFM probe (see chapter 4) that is used in our experiments: $l = 225 \cdot 10^{-6}$ m, $w = 38 \cdot 10^{-6}$ m, $L = 17 \cdot 10^{-6}$ m, $\theta_{cone} = 10°$, $\beta_{lever} = 20°$, $r = 10 \cdot 10^{-9}$ m, and for the other parameters we use $A_H = 4 \cdot 10^{-19}$ J and $\varepsilon_0 = 8.854 \cdot 10^{-12}$.

In figure 2.9 the characteristic results for the cantilever bending as a function of applied voltage for an initial distance of 50 nm have been plotted. At this distance the resulting capacitances have the following values: $C_{lever} = 3.60 \cdot 10^{-15}$ F, $C_{cone} = 3.62 \cdot 10^{-15}$ F, $C_{apex} = 1.24 \cdot 10^{-18}$ F and thus $C_{total} = 7.22 \cdot 10^{-15}$ F. From this result we see that using these parameters and a relatively large distance of 50 nm, the interaction between the probe and the sample will be dominated by the cantilever and tip cone, and not by the tip apex, which is in agreement with claims by Gil *et al* [160].

Whether pull-in occurs depends strongly on the spring constant for this type of AFM probe and several values can be chosen from the supplier: $K = 2.8$ N/m, $K = 15$ N/m and $K = 48$ N/m. By comparing the deflection curves for these three values, the effect of the spring constant on the bending behaviour can be observed. From the graph it can be determined that for an initial distance of 50 nm the probe with a spring constant of 2.8 N/m will pull-in at ~ 30 V, whereas for 10 N/m and 48 N/m this is ~ 65 V and ~ 120 V, respectively. When we compare this result to the theoretical field emission curves for $d = 50$ nm in figure 2.7 we can conclude that the probe with a spring constant of 2.8 N/m is too soft and snaps to the sample surface before the field emission current grows to measurable values. According to the calculations, the probes with a spring constant of 15 N/m and 48 N/m deflect only several nanometers before the field emission

current can reach its setpoint value.

For decreasing tip-sample distance, the electrostatic forces on the probe tip will increase and a larger spring constant will be required to prevent collapse of the probe. In figure 2.10, the cantilever deflection for the probe with $K = 48$ N/m as function of voltage has been plotted for varying initial distance $d = 10$ nm, $d = 20$ nm and $d = 50$ nm. By adding the theoretical *I-V* curves as calculated in figure 2.7 we can compare the cantilever bending to the expected field emission as a function of bias voltage. From the intersection of the deflection curves with the field emission *I-V* curve we can determine the cantilever deflection for a given field emission current. The calculations show that by choosing a high enough spring constant for the probe's cantilever, sufficient field emission current can be achieved before pull-in of the cantilever occurs. For distances < 5 nm the electrostatic forces on the tip apex quickly increase and together with Van der Waals forces cause instability in the cantilever probe position.

2.5 Conclusions

This chapter started with a short overview of the different electron emission phenomena. There are five main regimes for the emission of electrons, depending on the emitter temperature and the applied electric field: metal-vacuum-metal tunneling, cold field emission, thermal field emission, Schottky emission and thermionic emission.

In our application, we intend to use field emitters in the cold field emission regime, where the emission process can be described by Fowler-Nordheim theory. The Fowler-Nordheim model was discussed that is used to calculate the field emission current as function of the applied voltage. This model is the basis for the procedure that is developed to fit our measurement data and will be discussed in chapter 5. To include the effect of the tip-sample distance on the field emission current, the model needed an extension. The distance dependence is associated with the variations in the local electric field at the tip and can be described by the field enhancement factor γ. Finite-element calculations were used to determine an expression for this factor as function of tip-sample distance. This new model in combination with the Fowler-Nordheim equation was used to calculate example *I-V* curves to illustrate the distance dependence of the field emission current.

Various factors that influence the field emission current stability have been discussed. Instabilities in the emission current are a well-known problem in field emission applications and arise from atomic changes at the field emitter surface. The causes for this behaviour were divided among three main categories: surface changes by electron- and ion-bombardment, changes due to contamination and changes due to thermal effects. It is expected that many of the various effects that have been discussed are acting on the emitter stability simultaneously and therefore the solutions can be in contradiction with each other. For better stability, it is important to use vacuum conditions, in order to prevent ion-bombardment and contamination of the surfaces. The operating pressure should be at least better than 10^{-6} mbar to prevent build-up of adsorbates and if possible

better than 10^{-9} mbar to prevent rapid contamination of a clean emitter and sample surface. Heating of the emitter and sample in vacuum should be used to reduce the contamination and should be repeated periodically to maintain these conditions. In a practical probe recording system, continuous heating of the tips as done in *thermal* and *thermionic* field emission will not be a viable option because of the issue of power consumption. On the contrary, unintended heating of the tips should be avoided to prevent melting of the tip end. Therefore materials with a low resistivity should be used and the emission current should be kept well below $1\,\mu$A, in order to prevent excessive Joule heating. They should be chemically inert to have a good resistance against corrosion. A low material work function is desirable to reduce the voltage required for field emission and reduce sputtering effects. Lower voltages can also be achieved by using sharper tips, since this results in a higher field enhancement. Finally, the emitter material should have a high melting point and a high tensile strength, to reduce the surface diffusion of lattice atoms and prevent the effect of field evaporation.

To determine the influence of the electrostatic interaction between the cantilever probe and the medium, a theoretical model was developed. With this model we are able to calculate the theoretical cantilever deflection as function of applied voltage. According to the calculations, a spring constant of 48 N/m is sufficiently high to prevent pull-in of the biased probe when it is used at distances larger than 5 nm. The cantilever deflection calculations were compared to the theoretical field emission curves and showed that with decreasing tip-sample distance, the voltage required to extract a field emission current is decreased. Therefore indeed a probe with a high enough spring constant can be used for field emission without the problem of cantilever pull-in. It should be noted however that the lowering of the *effective spring constant* by the electrostatic forces might have a negative influence on the mechanical stability of the system.

Chapter 3

Measurement setups and characterization methods

This chapter describes the measurement setups that have been used for the work presented in this thesis. The first instrument is a scanning tunneling microscope (STM) that has the possibility to mount atomic force microscopy (AFM) probes. With this setup we are able to measure with high accuracy field emission currents as function of tip-sample distance and to scan in field emission mode over a sample. The field emission current stability is very susceptible to adsorption and desorption of residual gas atoms on the emitter surface, therefore the measurements are performed in ultra-high vacuum (UHV). Since a UHV STM was not available at the start of the work, a commercially available STM was acquired and assembled to a custom built vacuum system. The setup was modified to be able to connect a high voltage source needed for field emission currents. A second existing high-vacuum fiber interferometer AFM setup was modified to be able to use it for field emission measurements as well. This chapter will describe the main components of both experimental setups, as well as the measurement procedures that are used to characterize the field emitter probes and the method of tip-sample distance control.

3.1 Measurement setups

The majority of the measurements that are presented in this thesis has been done using a commercially available STM from RHK Technology. A second fiber interferometer AFM setup was used for additional measurements that require detection of the cantilever deflection and exact measurements of the sample topography. Below a more detailed description of these systems will be given in order to explain the measurements that have been carried out by applying them.

3.1.1 RHK scanning tunneling microscope

In the scope of this thesis, a new STM was obtained from RHK Technology [168]. This STM was selected after a comparison of the properties of several systems that are available on the market. An important advantage of this instrument is the possibility to exchange tips and samples without breaking the vacuum and causing long delays. Since we intend to characterize different tips and samples, this option will save a considerable amount of time. Moreover, the scan head design allows coarse positioning over the entire area of the sample, which is a benefit if we want to change locations when the sample has been locally damaged or modified by our experiments. The total UHV STM system as depicted in figure 3.1 consists of several items that will be shortly described. The description will be given in the following order:

- Scan head and sample holder
- Sample and tip exchange
- Control electronics and software
- Vacuum system and vibration isolation
- System modifications for field emission experiments

Scan head and sample holder

The scan head designed by RHK is a so-called Beetle type, where the scanner is standing on top of the sample holder. Using three piezo legs the entire scan head can 'walk' on top of the sample holder by means of a stick-slip motion. The STM tip or AFM probe is mounted to a central piezo that adjusts the tip height. During image acquisition scan voltages are applied to the three piezo legs for xy scanning motion with maximum $5 \times 5\,\mu$m range and to the center piezo for z-positioning of the probe with 200 nm range [169]. Calibration of the scanner piezos was done by means of a highly oriented pyrolytic graphite (HOPG) sample and a conducting patterned sample with a known grid. In figure 3.2 a picture of the scan head is given showing the three piezo legs and the central piezo with an STM tip mounted.

The sample holder has three molybdenum helical ramps that surround the sample mounted in the center. By using the three piezo legs to walk in clock- or anti-clockwise motion on these ramps, the tip can be coarsely approached to or retracted from the sample. By walking in xy-direction the tip can be coarse-positioned to a certain location. Figure 3.3 shows the scan head standing on top of the sample holder inside the UHV chamber.

Due to its compact geometry, the mechanical loop of the scanner has a high resonance frequency of 2.1 kHz and together with the symmetric design also provides good thermal stability. The entire scan head can be lifted by picking it up with a manipulator tube that can be lowered or raised through a linear motion vacuum feedthrough from the scan head manipulator flange. This enables replacement of the sample holder or exchange of the tip.

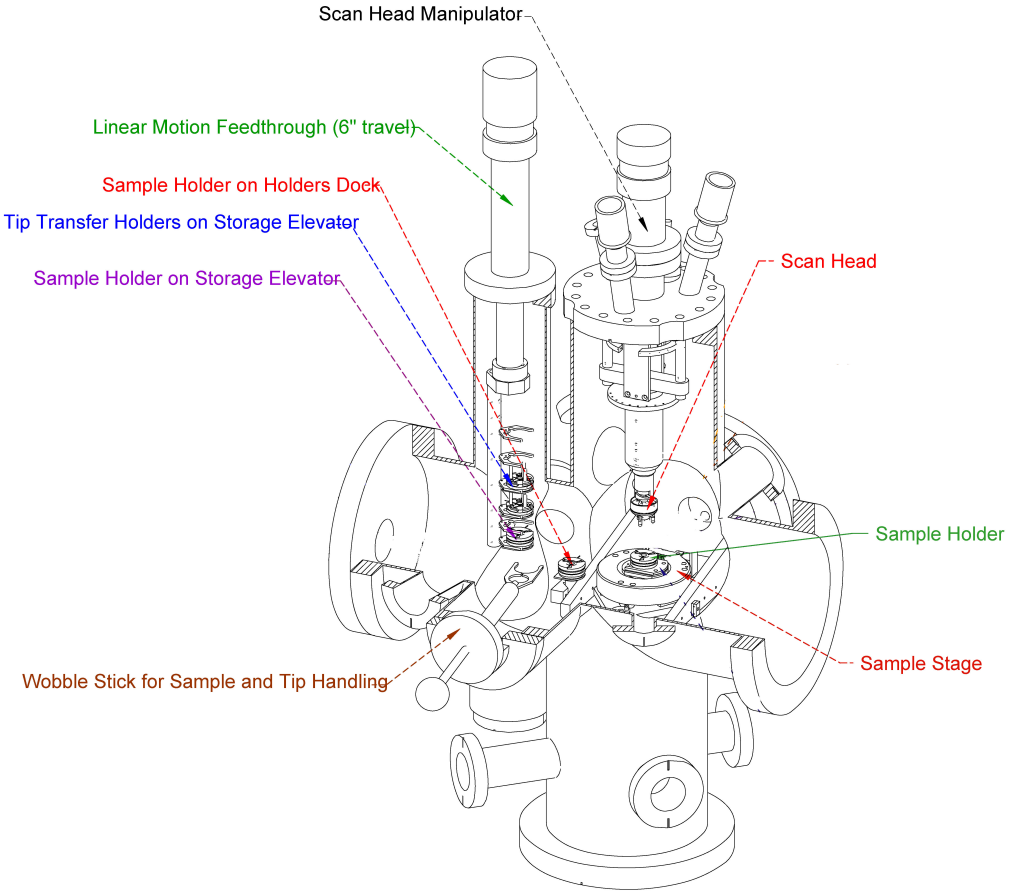

Figure 3.1: *Cross-section of the RHK UHV 300 system showing the main components of the STM instrument used. From [168].*

Sample and tip exchange

So-called tip exchange holders are used to carry small aluminium tip holders and facilitate *in-situ* tip exchange. STM wire tips can be put inside the small tip holders that fit on the scan piezo of the scan head. AFM probes can be fixed to similar tip holders by using Electrolube silver conductive paint [170]. In order to outgas the solvent and binder in the silver paint, tips and holders are heated to 120 °C for 2 hours before loading them in the vacuum system. Three tip exchange holders and three sample holders can be stored in the storage elevator inside the vacuum chamber. For *in-situ* exchange, a wobble stick is used to transfer the sample holder or tip exchange holder from the storage elevator to underneath the scan head and vice-versa.

A tip is loaded by lowering the scan head on top of the tip exchange holder, using the wobble stick to unlock the tip and raising the scan head again. The loading procedure of the tip holder is illustrated by the photographs in figure 3.4. In these images also small

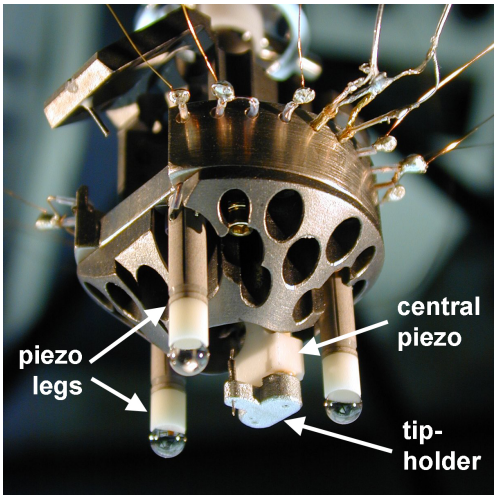

Figure 3.2: *Photograph of the RHK scan head showing the three piezo legs used for sample positioning and the center piezo to control the tip-sample distance.*

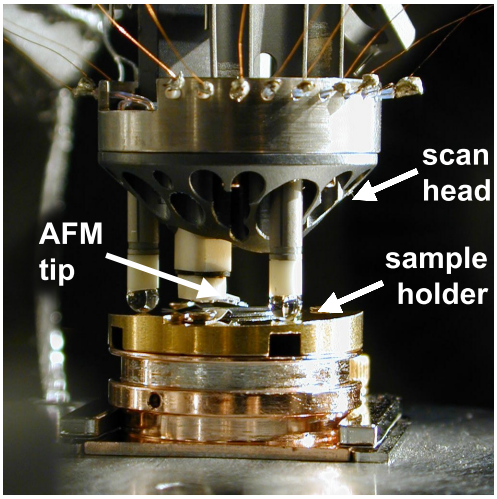

Figure 3.3: *Photograph of the scanner with an AFM probe mounted, standing on the sample holder inside the vacuum chamber.*

viton rings can be noticed that are fitted around the metal sockets in the ceramic piece. During initial measurements, it was found that tunneling currents were very unstable due to a resonance of the tip holder in the sockets. The viton washers are needed to damp mechanical resonances and solve this instability problem. The thickness of the washers is a delicate balance between making sufficient contact between the tip holder and the ceramic piece to damp oscillations and preventing substantial drift in the z-direction by expansion of the viton.

A tungsten filament heater is located on the side of the sample stage. The sample and tip exchange holders can be positioned on top of this heater. A two conductor power feedthrough is used to connect to the filament with a DC power supply. A thermocouple

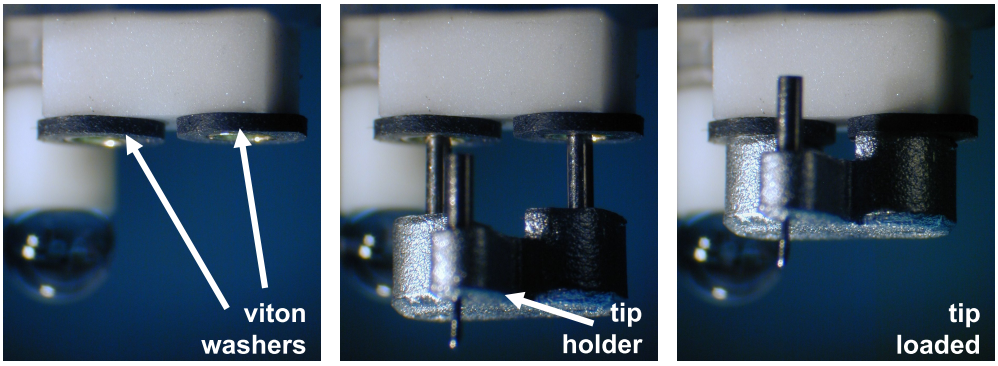

Figure 3.4: *Photograph sequence illustrating the loading procedure of the tip holder. The viton washers in between the tip holder and sockets are to prevent mechanical resonance of the tip holder leading to instabilities in the tunneling current.*

connected to the side of the heater can be used to monitor the temperature of the sample holder. The heater is used to radiatively heat the samples for 1 hour at 300 °C after they have been introduced in the vacuum system, in order to reduce contamination, as discussed in chapter 2.

Control electronics and software

As control electronics an SPM1000 Control System from RHK Technology is used. The SPM1000 has 10 high-voltage (± 130 V) outputs that supply the scanning and control voltages to the piezos. A switch box (RHK PPC100) is employed to switch the piezo voltages between a rotational movement needed for coarse z-positioning and a lateral movement needed for coarse xy positioning and scanning. In STM mode the tunneling current preamplifier that is used in conjunction with the SPM1000 is an RHK IVP-200 with a gain of 10^8 V/A and a maximum measurable current of 100 nA. The output is connected through a second-stage amplifier with unity gain and 150 kHz bandwidth to the feedback input of the SPM1000. The preamplifier connects the tip to signal ground while the bias voltage is supplied to the sample with ± 10 V range. Proper grounding of the UHV chamber is a delicate matter, since the voltages that are supplied to the ion pump and pressure gauges have high-frequency components that are picked up by the high transimpedance amplifier. The best results are obtained by making a solid connection from the ground connector on the rear of the SPM1000 to the ion pump *and* to the ground of the isolated BNC feedthrough connector on the scan head manipulator flange where the preamplifier is connected.

Data acquisition occurs through a 16-bit data acquisition card (Data Translation DT3016) in the computer and XPMPRO software [171]. The software takes care of the automated tip-sample approach and is used to record scanning images and spectroscopy measurements. By programming the input and output voltages of the SPM1000, custom experiments can be defined. Four D/A outputs are available for this and have been used to control the external inputs 'Inertial input' (for coarse approach), 'Bias modulation', 'Z modulation' and 'Z position offset'. These functions and more details on the custom measurements used in this work are described in section 3.2.

Vacuum system and vibration isolation

The UHV chamber used is part of the UHV 300 subsystem from RHK Technology. The chamber is designed with multiple ports targeted at the tip/sample interface. This provides optical access to the sample to control the exact position of the tip with the help of a telescope. The top 6" flange port is for the scan head manipulator and the electrical feedthroughs. Electrical connections to the scan head are made by extra thin (0.075 mm) Kapton-insulated copper wires and fine coaxial cables, to reduce the transfer of vibrations from the chamber to the scan head. The sample stage is mounted on a 8" flange port on the back of the chamber. Vibration isolation is incorporated in the sample stage by means of viton rope to separate the stage from the flange port. The

UHV chamber is mounted on a custom made steel frame that is filled with sand to add weight and lower the resonance frequency of the frame. The frame rests on the external air leg vibration isolation system consisting of 4 Newport I–2000 Pneumatic Isolator Lablegs [172].

The vacuum system that is used to evacuate the vacuum chamber was assembled in-house. In figure 3.5 a schematic of the pumps and electronics that are used is given. The vacuum system consists of:

- Varian SH100 Dry Scroll Pump
- Varian Turbo V301 Navigator System
- Varian 6" Valve, Swing Gate, Air Operated
- Varian Vacion Plus 300 Starcell Combi Pump with Midivac Controller (one pump negative)
- Titanium Sublimation Pump with TSP Controller
- Varian Multigauge Controller with Varian UHV Gauge and Baratron Capacitance Manometer

The pumps, valves and pressure meters can all be electronically read and controlled by custom made software. This has been chosen instead of using a load-lock to transfer samples and tips to and from the vacuum chamber under UHV conditions. Since it is expected that a practical probe recording device can be operated at only a moderate vacuum level, it is our intention to create in our system a controlled environment that is preferably not UHV. Therefore a variable leak valve has been chosen as an extra option that can be mounted to investigate if inert gasses can be used to achieve field emission currents with sufficient stability. Because of the lack of a load-lock, the system has to be vented and evacuated every time we want to load or unload a batch of tips and/or samples. To enable relatively fast execution of this procedure, the whole cycle has been automated by using the electronic control and software program. The most important benefit of this software control is that it is possible to pump-down or vent the system by one press on the button. A robust decision scheme is implemented that decides which pump to start or stop or valve to open or close. Meanwhile the system pressure is recorded and used in the decision scheme for the next step in the pump-down or vent sequence, or to safely close down the system in case of an emergency (e.g. sudden increase in pressure). For safety, also interlocks are implemented that close valves and turn off pumps in case of a power failure.

The software is written in LabView [173] and is built modular, so that it can be easily adjusted to any vacuum system. All instruments are connected by the RS-232 communication protocol using an 8-port RS-232 serial interface (Quatech ESU-100) [174]. The scroll pump and UHV valve do not have a RS-232 connection but are controlled by a RS-232 Relay I/O interface (Ontrak ADR2205) [175]. For each instrument a separate control block was written that is used in the main program. It is thus possible to change the different building blocks when a different pump or pressure gauge is introduced. The program starts with the main window, where the pressure plot, pumping down, venting or a manual control mode can be chosen. The core of the

software program is a circular data buffer that logs the pressure from the Multigauge and the state of the system as a function of time. The data from the logger can be plotted using the button 'Plot pressure' in the main window. If 'Pump down' or 'Vent' is selected, the software performs a full pump down or a full vent action, sequentially starting or stopping each pump, valve or measurement gauge. A decision scheme is implemented to decide on the next step. If finished a pop-up informs the user. It is also possible to control the individual instrumentation by entering the manual mode, for example for testing purposes. A screenshot of the graphical interface that is shown to the user in this manual mode is shown in figure 3.6.

The pumpdown time after loading fresh tips or samples from atmospheric pressure to $5 \cdot 10^{-9}$ mbar is typically several hours, which practically means that pumping can be done overnight and the system is ready for measurements the next morning. For UHV conditions however, a bake-out of the system at 120 °C is needed which typically takes 48-72 hours. The base pressure of the system that is obtained after bake-out is $5 \cdot 10^{-10}$ mbar. When tips or samples are unloaded the system is vented by letting in nitrogen gas. To prevent vibrations and electric noise being coupled into the system, during measurements all connections to the pumps and pressure gauges are decoupled and only the ion pump is connected to its high voltage source.

System modifications for field emission experiments

The SPM1000 in combination with the IVP200 current amplifier can supply bias voltages from – 10 to +10 V with a maximum detectable current of 100 nA. In the field emission experiments, higher bias voltages are needed to extract field emission currents at increased tip-sample distance. We therefore use a Keithley 6487 Picoammeter that can measure currents from 20 fA up to 20 mA [176]. The instrument includes a ± 500 V

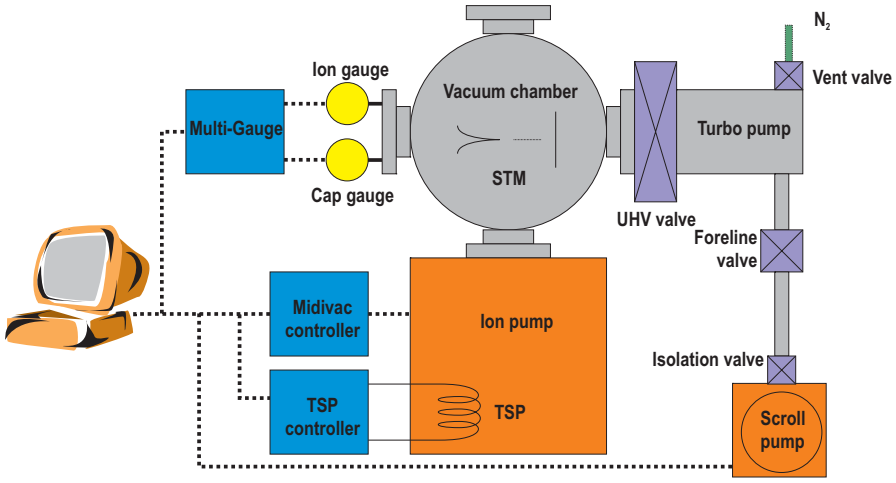

Figure 3.5: *Schematic drawing of the vacuum system used to evacuate the RHK UHV 300 setup.*

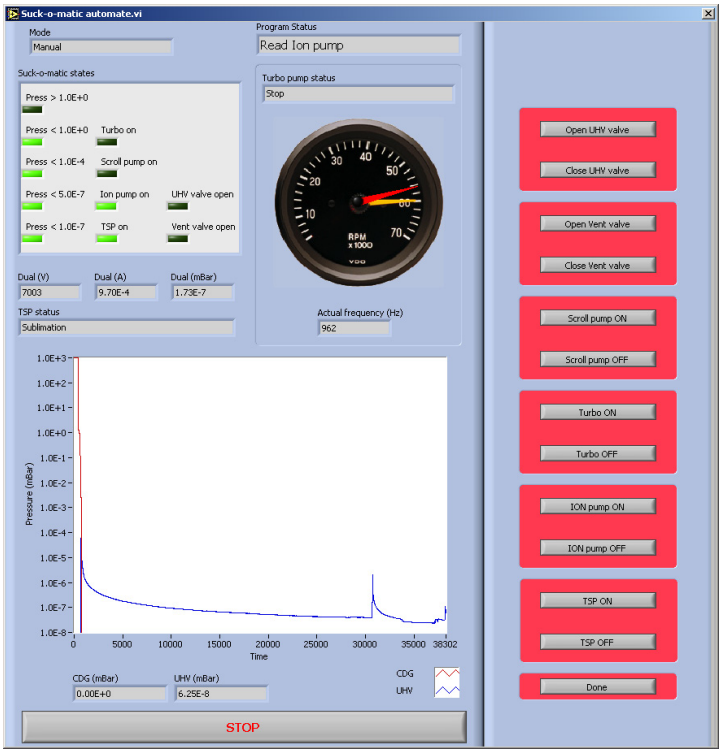

Figure 3.6: *Graphical user interface screenshot of the software used for automatic pump-down and venting of the vacuum chamber. The revolution counter gives an instant overview of the rotational speed of the turbomolecular pump.*

voltage source with a high overload protection that tolerates overflows when the source is accidentally shorted directly into the meter. The source can also be turned off when the measured current exceeds a selectable current limit, which is important to protect our STM from too high currents. Triax cable is used to carry the tunneling current signal from the scan head manipulator flange to the rear panel triax input of the 6487, in order to keep the electrical pickup noise level as low as possible. The meter has a fast analog output, that allows to transmit the measured current value to the BNC feedback input of the SPM1000. The bandwidth of the analog output depends on the range setting: at 200 nA range setting (resolution 1 pA) the bandwidth is 3.3 kHz, sufficient for scanning at high peed during imaging. The GPIB (IEEE-488) remote interface connection makes it possible to program the 6487 to define custom measurements. Voltage sweeps can be recorded with a reading rate of 1000 readings/second, which enables fast recording of *I-V* characteristics. The custom written code used to characterize field emission properties with the Keithley 6487 will be treated in section 3.2.

Since the Picoammeter cannot be controlled by the SPM1000 control system, an additional high-voltage source is used for the characterization measurements that require feedback to the tip position. For these measurements a PI-P863 piezo-controller with 10× amplification is placed between the bias output of the SPM1000 and the sample

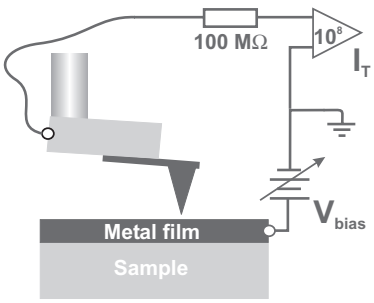

Figure 3.7: *Electronic diagram of the system set up for field emission experiments. Electrons are field emitted from the tip towards the sample. The 100 MΩ resistor limits the current to prevent tip and sample damage.*

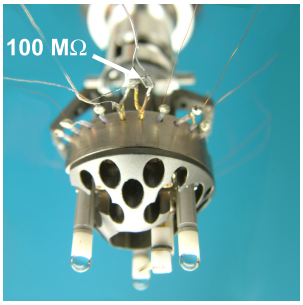

Figure 3.8: *The RHK scan head showing the position of the 100 MΩ SMD resistor placed in between the scan head and the current lead to prevent high current peaks.*

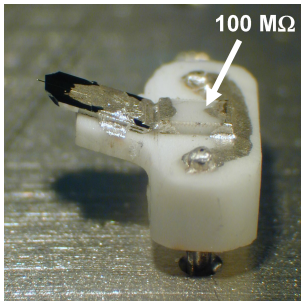

Figure 3.9: *Photograph of a customized isolating tip holder with an AFM probe connected through a 100 MΩ SMD resistor to the holder pins.*

connector. This high-voltage source is only used in combination with a high value resistor in the current path to the emitter tip, to suppress possible high current peaks that can damage the current amplifier in case the tip accidentally hits the sample surface.

As will be discussed in chapter 6, a high value resistor is also needed when the emitter probe is operated at moderately high bias voltages. It is found that mechanical or field emission instabilities can cause large peaks in the emission current, leading to damage to the tip and sample. To prevent this, the resistor is added in the current lead to the emitter tip, as is shown schematically in the electronic diagram of figure 3.7. The resistor acts as a suppressor for high field emission currents: if the emission current becomes too large, the voltage drop over the resistor increases and leads to a decrease of the effective applied tip-sample voltage, and therefore to a lowering of the field emission current. In field emitter applications such as field emission displays, often the addition of a high value series resistor is used because of this damping effect in order to obtain a more stable current. Also issues like burn-in and turn-on failure can be prevented with a high value series resistance [139, 103]. In our case we need the applied bias to be constant to be able to control the tip-sample distance for a certain field emission current setting. Since we intend to use currents of several nano-amperes, we have selected a 100 MΩ resistor with 5% tolerance precision for the series resistance. With this value and a field emission current of 3 nA the voltage drop will only be 0.3 V, which can be considered negligible for most measurements. However, when higher field emission currents are used, the resulting data has to be corrected for the voltage drop over the series resistor.

The integration of the series resistance has an influence on the performance of the system in terms of signal bandwidth. This has been tested by placing the resistor at various positions in the measurement setup. First the resistor was placed simply in a shielded housing in between the preamplifier and the BNC connector to the tip at the scan head manipulator flange, outside the vacuum system. In this configuration the DC

current is restricted as intended, however the measurable bandwidth of the current signal is also severely degraded. Since the high value resistor is combined with the capacitance of the wiring to the emitter tip, an electrical low-pass filter is formed, thereby limiting the bandwidth and the minimum response time of the feedback loop. The wiring to the tip consists of two short coaxial wires in the scan head that are connected to the two metal sockets in which the small metal tip holder is loaded. A long and very thin coaxial cable connects one of these wires with the electrical feedthrough connector on the scan head manipulator flange. We have measured a capacitance of 15 pF for this connection, which is mostly due to the thin coaxial cable. Together with the 100 MΩ resistance this results in a significant limitation of the bandwidth.

Secondly the resistor was placed inside the vacuum chamber in between the scan head connection and the thin coaxial wire, as is shown in figure 3.8. This greatly reduces the capacitive load to the tip and increases the detectable bandwidth. An SMD type resistor (124.4 MΩ) is used so that a minimum of unbalanced weight is added to the scan head. It is desirable that one can also measure without this resistor added in the current path, e.g. for measurements in STM mode. Therefore on the scan head manipulator flange we have made two connections to the tip: one through the 100 MΩ resistor and one directly to the tip, by adding a second thin coaxial cable connecting to the second tip-wire in the scan head. This enables measurements with and without resistor in the current path while avoiding the need to open the vacuum system to place or remove the resistor.

As a third possibility, we developed an isolating tip holder custom made from Macor [177], to be able to place the resistor closer to the tip. The result is shown in figure 3.9. Here the AFM probe is mounted on the protruding part of the insulating ceramic. The 100 MΩ SMD resistor is glued to the ceramic and electrically connected by thin traces of silver conductive paint to the AFM probe at one end and at the other end to the metal pins that are used to load the holder and connect to the tip wire. By placing

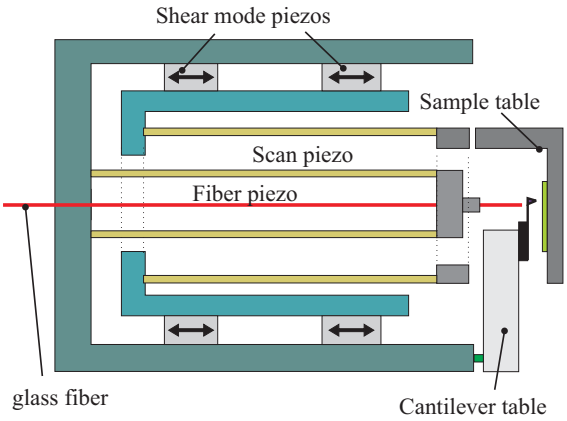

Figure 3.10: *Schematic drawing of the fiber interferometer AFM.*

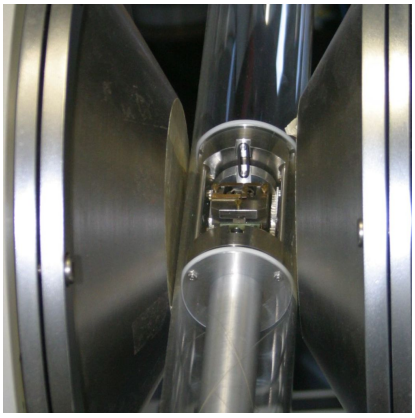

Figure 3.11: *Fiber AFM in between the poles of a magnet and inside the vacuum tube.*

the resistor close to the probe on an insulating holder, the capacitance of the tip is only determined by the dimensions of the AFM probe. We estimate the total capacitance to be less than 1 pF, by using the equations from section 5.2.1 that model the contribution from the tip, the cone and the cantilever. The major contribution to the tip-sample capacitance comes not from the cantilever or tip but from the handling chip on which the cantilever is fabricated. The silicon chip is 3.4×1.6 mm and its contribution to the capacitance is estimated to be 120 fF. The capacitance of the probe can thus be further lowered by reducing the size of this handling chip, or by integrating the resistance in the AFM probe itself. Since such probes are not commercially available, the lowest capacitance we could obtain was by using this ceramic tip holder with integrated resistor. Measurement results obtained by using this holder will be presented in chapter 6.

3.1.2 Fiber interferometer atomic force microscope

The second system, used for quantitative analysis of the cantilever deflection and sample topography, is a fiber interferometer force microscope. This system is normally used for magnetic force microscopy and operated inside a high magnetic field (1.8 T) at arbitrary angles and in vacuum [73]. In the schematic in figure 3.10 an overview is given of the scan head design: a tube scanner to laterally move the sample, a piezo shuffle motor using shear modes piezos for coarse approach and a fiber interferometer to detect the cantilever deflection. The microscope is mounted inside a vacuum tube with an outer diameter of only 60 mm, so that it can be positioned in between the poles of the magnet, as can be seen in the photograph depicted in figure 3.11. The vacuum system consists of an oil diffusion pump connected to a rotary backing pump and can achieve a base pressure of $1 \cdot 10^{-6}$ mbar in a pump-down time of 30 minutes.

The fiber optic detection system consists of a highly sensitive fiber interferometer and a high quality trans-impedance amplifier [178, 179]. For maximum performance of the interferometer the cantilever has to be aligned exactly parallel to the clieved end of the fiber. As a laser a pigtailed solid state laser diode with a Faraday insulator and wavelength of 780 nm is used. For maximum stability the laser is kept at a constant temperature with a peltier cooler. The laser interference is the result of one beam reflecting on the glass air transition at the clieved end of the fiber and a second beam that passes through the interface, reflects off the cantilever and couples back into the fiber. The interference of the two beams is constructive or destructive depending on the path length difference with a maximum modulation of 4%. The detector signal is therefore periodic as function of the fiber-cantilever distance, with a periodicity of half the laser wavelength. The fiber is mounted on a piezo-tube which allows to adjust the fiber-cantilever distance or keep it constant by using feedback.

For the field emission experiments, the system was modified in order to be able to apply a voltage bias and measure the small currents. The cantilever holder and sample table were electrically isolated by using sapphire elements. Ultra-thin coax cable (0.5 mm) is used to connect the tip and sample table to the electrical vacuum feed-throughs at the end of the vacuum tube. To restrict the maximum field emission currents,

again a 100 MΩ resistor is placed in between the coax cable and the tip connection on the scan head. The Keithley 6487 Picoammeter is used to apply the bias between the tip and sample and measure the resulting field emission currents.

Imaging of the sample surface using this modified setup can now be done in AFM as well as STM mode. The scan voltages are generated by using a V-Scan 100 DSP control module from RHK Technologies and amplified through a three-channel high-voltage amplifier with a range of 400 V. In AFM the topography of the sample surface can be measured by detecting the cantilever deflection using the signal from the interferometer output or by recording the feedback signal to the z-piezo while keeping the cantilever deflection constant. For magnetic measurements (MFM), the cantilever is excited by means of a small piezo and phase shifts in the cantilever resonance are measured by using a lock-in amplifier. During this work also a non-contact AFM method was implemented, to be able to scan the sample without touching the surface and so prevent tip and sample damage. By connecting the output from the lock-in amplifier to the V-Scan DSP module, it is possible to control the z-piezo such that a constant phase shift is maintained. This constant phase shift can be chosen so that there is a constant attractive force between the probe tip and sample, corresponding to the non-contact regime on the force-distance curve [180]. Drawback of this method is that the phase shift signal can change sign when there is a large topography change which cannot be compensated by the feedback loop. This greatly limits the maximum scan rate and can result in a severe tip-crash. A simple but elegant solution to this problem was found by preventing the output from the lock-in amplifier to change sign by using a custom electronic circuit. For STM, the analog output of the Keithley Picoammeter is used as the input signal for the feedback loop. The interferometer output is not used anymore for feedback but to measure the cantilever deflection instead. Further details on the measurement procedure used with this instrument will be given in section 3.2.

3.2 Characterization of field emitter properties

In this section we focus on the various modes of operation and the information that can be obtained using the instruments described above. Our intention is to characterize the dependence of the field emission current on tip-sample separation and the influence of the used probes and materials on stability and sensitivity. To achieve this we will use various tips and especially prepared samples, that will be described in chapter 4. The tips and samples differ from those that are normally used in STM and the bias voltages that are used for field emission are higher. As we are interested in the sensing characteristics rather than characterization of the samples, the usage of the instruments is fairly non-typical. To avoid confusion, in the sections below a short description will be given of the measurement procedures that have been used to obtain the results presented in chapters 5 and 6. The definitions of the modes of operation and of the used probes given here will be used throughout the rest of the thesis.

3.2.1 Operating modes

To image our samples we use the *constant current* method to scan the tip over the sample surface. The bias voltage is fixed and the feedback loop adjusts the height of the tip during scanning so that the current flowing between tip and sample is kept constant. The height is determined by the voltage that is applied to the z-piezo and the lateral tip position is determined by the voltages applied to the scan piezos. Therefore the recorded z-signal as function of the x- and y-position can be translated into a map of the 'topography' of the scanned surface. In contrast another method that can be used is the *constant height* method, where the information on the sample surface structure is obtained by recording the (large) variations in the current signal as function of lateral position. Although the image that is obtained using the constant current method is often, also in this thesis, interpreted as a *topographic image* of the sample surface, care should be taken in the exact interpretation of the results. The plot only reflects the position that is needed to keep the current constant and not only depends on the topography of the sample, but also on the local conductivity or density of states of the sample surface.

Typically in STM the bias voltage applied between tip and sample ranges from 1 mV up to 4 V [57]. The voltage is kept below the work function so that the local barrier height can be considered constant and the current is solely due to the tunneling effect. This mode of operation using low bias voltages will in this thesis be referred to as the *STM mode* and the imaging method *STM imaging*. If the voltage applied is higher than the work function, the system is operated in the field emission regime. The current that flows at these voltages is in accordance with the Fowler-Nordheim expression (equation 2.5) and is characteristically different from the bias dependence in the low-bias tunneling regime. To distinct this from the STM mode, it will be called the *field emission mode* and the generally used term for scanning at these increased bias voltages is *scanning field emission microscopy (SFEM) imaging*. Please note that the acronym STM is also used for the instrument itself. So we can use the STM system in both the STM mode and the field emission mode to obtain STM or SFEM images, depending on the bias voltage applied.

When higher voltages are used, the area of the tip that contributes to the tunnel current increases. At low voltages, tunneling only occurs from the outermost atom, which allows the high resolution that is normally obtained in STM. To get atomic resolution STM images on relatively flat sample surfaces, the macroscopic shape of the tip is therefore of little importance, as long as the tip terminates in a single atom. Generally for STM measurements, an *STM tip* is used, made from metal wire such as PtIr or W by cutting or (electrochemical) etching. When the voltage is increased, parts of the tip that are at larger distance from the sample also start to contribute significantly to the current [181]. For scanning in the field emission mode, the macroscopic shape of the tip therefore becomes important. Especially when rough (patterned) samples are used, the tip should have a small cone angle in order to be able to distinct the topographic features on the sample surface.

In our measurements we use conducting *AFM probes* and custom micromachined

fixed-tip probes instead of STM tips. Details on the fabrication and preparation of these probes will be presented in chapter 4. The reason for using AFM probes is that they are in closest resemblance to the individual cantilever probes that will be used in a probe array for (magnetic) probe recording. Moreover, the shape of the tip at the end of the cantilever of the AFM probe is well-defined and allows measurements obtained for various probes to be compared as the tip shape among the probes can be assumed equal. In the fiber interferometer AFM setup, we have the capability to detect the deflection of the cantilever by using the fiber optic detection system. Since the deflection of the cantilever is a measure for the force between the tip and sample, *AFM imaging* is used to obtain a true topographic image of the sample, by recording the cantilever deflection as function of lateral position. After adaptation of the fiber interferometer AFM system we have the possibility to measure the tunneling or field emission current from the AFM probe. Therefore in this system we are able to record images both in AFM mode and in STM or SFEM mode. In the RHK STM system however we do not have the capability to measure the cantilever deflection as is normally done in AFM. In this setup the AFM probes are not used to detect the cantilever deflection, but to image the sample surface in STM mode and to characterize the field emission properties of the probes by increasing the bias voltage.

3.2.2 Single position characterization measurements

The RHK STM is not only used as a tool for topographic imaging but also to perform quantitative measurements to determine the typical characteristics of the field emission process. Any measurement that is performed in the setup is characterized by five variables: x, y, z, I and V. In constant current imaging, the variables I and V are kept constant and the variables x, y, and z are recorded to build the topographic image. By varying other parameters it is possible to obtain other information on the tip or sample properties. Generally in STM, *tunneling spectroscopy* is used to yield information on the sample's electronic structure, by varying V and measure the dependence of the tunneling current on the applied bias. When the spectroscopy measurements are performed as function of lateral position, the spatial distribution of the spectroscopic information can be determined. In our measurements the main interest is not in the local variation of the electronic properties of the sample surface, but in the field emission properties of the used probes. Therefore the measurement curves are taken only at single positions on the sample surface, so by keeping x and y constant, and increasing the bias voltage. We assume that the properties of the sample are constant over the sample surface, which is confirmed by testing at different positions. The following measurements are used to investigate the properties of the field emitters and the distance dependence of the field emission current:

- I-V at constant z
- I-z at constant V
- z-V at constant I

Below the procedures for these single point characterization measurements will be treated in more detail.

Current-voltage (constant spacing)

The common method to obtain more information on the emission properties of a field emitter is by measuring the emission current as a function of the extraction voltage. When using metals for the field emitter and sample, these *I-V* curves should show the Fowler-Nordheim behaviour as discussed in chapter 2. This is different from the ohmic behaviour between metal electrodes in the low-bias regime, where the tunnel current is linearly proportional to the applied bias voltage (equation 2.1) [57].

For generating the voltage sweep and measuring the resulting current, we use the Keithley 6487 Picoammeter that is programmed through the IEEE-488 bus using LABVIEW software. The measurement procedure and data collection are automated to ensure that sequential measurements are carried out consistently, with sufficient data points and equal time per measurement. The software was custom developed and optimized for a fast measuring rate of 50 ms per reading. This enables recording of a complete *I-V* curve within several seconds and limits the effect of possible instabilities in the field emission current. For each measurement, the bias voltage is ramped up and down, resulting in two *I-V* curves that are stored individually. During the up-ramp, the measured current is monitored and when the current setpoint is reached, the voltage is ramped down. When a current peak is detected that is larger than a maximum value setting, the voltage is immediately returned to the starting value and the measurement is ended, to prevent tip damage. After recording of the *I-V* curves, they are plotted within the user interface window. The same data is also plotted in the Fowler-Nordheim representation. See figure 3.12 for a screenshot of the user interface with example measurements.

If the *I-V* relationship is due to the field emission effect, the Fowler-Nordheim plot shows a linear behaviour and can be used for fitting. The current is a function of the field enhancement factor γ, emitter radius ρ and the work function ϕ (equation 2.23). If one of these three parameters is known, the other two can be determined from the linear fit. As in most field emitter characteristics reported in literature [103], we assume the work function to be the value of a clean emitter tip. For fitting of the Fowler-Nordheim plots we use a separate fitting program that has been developed in MAPLE software, using an iterative routine to find the right correction factors v_N and t_N (equations 2.8 and 2.9). This routine is given in appendix A and will be discussed in more detail in chapter 5. Due to its complexity, the MAPLE program is only used after a sequence of measurements has finished and all necessary data has been recorded. However, already during the measurements we would like to have a first estimate of the fitting parameters to check if they are in the correct range. Therefore a greatly simplified fitting procedure is programmed in LABVIEW, using approximations for the correction factors. For the emission current values used in our measurements, we can apply the same approximations as used in [117]. The factor v_N is expected to vary between 0.6

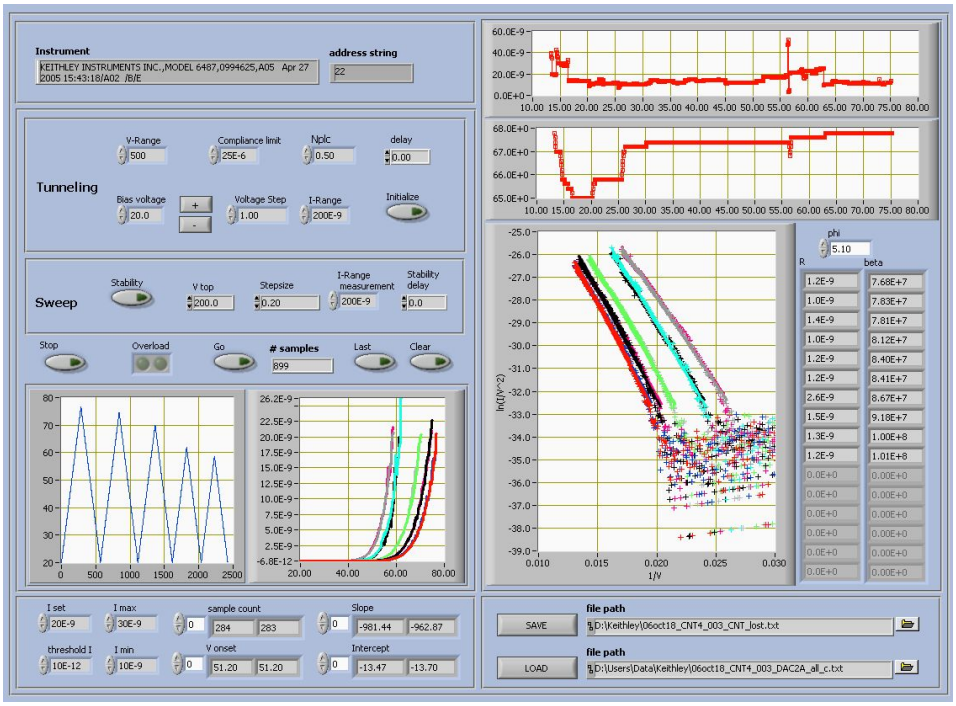

Figure 3.12: *Screenshot of the program used for fast recording and fitting of the Fowler-Nordheim curves.*

and 0.71 and will be approximated by the function $v_N = 0.958 - 1.05\ {y_N}^2$, where y_N is given by equation 2.6. The factor t_N varies between 1.041 and 1.054 and will be approximated by $t_N = 1.05$. The resulting simplified fitting routine gives approximations of the parameters γ and r with a 10% error.

The series resistor that has been added in the current path to the tip leads to a voltage drop over the resistor. This voltage drop increases with increasing current values and affects the linearity of the Fowler-Nordheim plot. For high field emission currents, the voltage drop becomes a large part of the total applied bias and leads to a saturation of the Fowler-Nordheim curve. Including the effect of a series resistance in the Fowler-Nordheim equation is not trivial. Instead, the *I-V* curves are corrected for this influence, by calculating the voltage drop over the series resistor and subtracting this from the voltage supplied by the power supply. Note that the addition of the series resistance does not change the extracted values of γ and A [182].

As the field enhancement factor γ is a function of the tip-sample distance d, the tip height at which the *I-V* curve is recorded is important. To investigate the influence of d on the Fowler-Nordheim behaviour, a sequence of *I-V* curves is measured for a set of tip-sample distances. First the tip is brought in the tunneling regime by a standard approach of the sample at low bias voltage (3 V). After the feedback signal has stabilized, the tip position is registered and used as starting position for the subsequent measurements. The control loop is then stopped by means of a sample-and-hold command and the tip is

immediately retracted and kept at a fixed distance, where the *I-V* measurement is started. The displacement range of the centre *z*-piezo is 200 nm and during the measurements it was found that a larger range would be desirable. Therefore we used the three piezo legs of the scan head to set the tip-sample distance, by applying an offset voltage to the inner electrodes of all piezo legs at the same time. The resulting motion in *z*-direction is calibrated at 3.1 nm/V. One of the D/A outputs (-10 V to +10 V) is connected to external control 'Z-Offset' input (gain 13.0) on the SPM1000, so that the tip-sample distance can be controlled within 800 nm. When combined with the centre *z*-piezo, a total range for the tip-sample distance of 1 μm can be used. The linearity over the whole range is within several nm, but a hysteresis of $\pm$ 10 nm is observed when large variations are made. Therefore each sequence of *I-V* curves is recorded twice, from small to large tip-sample distance and vice versa, to check the consistency of the measured data. To compensate for the influence of local sample properties, each *I-V* curve is taken at a different position on the sample surface.

Current-spacing (constant voltage)

According to the models for the Fowler-Nordheim and the field enhancement behaviour, the field emission current is exponentially dependent on the tip-sample distance. In our measurement setup, we have the possibility to measure this behaviour with high resolution, by recording the emission current while retracting probe from the sample surface with sub-nanometer precision. In STM such measurements are typically used to provide information about the local tunneling barrier height variation on the sample surface. By measuring the slope of the *I-z* characteristics under low applied bias voltage, in principle the material work function can be deduced [57]. However, the experimental values that are found are generally not equal to the tabulated work function due to contamination on the tip and sample surfaces [10]. For surfaces that are not atomically flat, the shape of the tip has an influence on the obtained values. Measuring the true work function is therefore not a trivial procedure and requires clean surfaces, preferably obtained by *in-situ* preparation methods, in UHV and low-temperature conditions. Since we do not intend to use such conditions in a practical probe recording application, this measurement is not used to determine the true work function values. On the contrary, the current-spacing measurements are used to determine whether the vacuum level and used materials are sufficient to be able to distinct the Fowler-Nordheim behaviour in the field emission current decay.

The *I-z* measurements are performed by using the spectroscopy option in the XPM-PRO control software. First the tip is approached to the sample and kept at a fixed bias voltage and current setpoint until the field emission current and feedback signal are sufficiently stabilized. After a finite time interval the actual tip position is stored and the feedback loop interrupted. Then the tip is retracted several nanometers by ramping the *z*-piezo voltage. Meanwhile the exponential change in the field emission current signal is recorded by using the RHK or Keithley current amplifier which is connected to the analog input of the SPM1000 electronics. The voltage ramp is supplied by one

of the D/A outputs and connected to the external control 'Z modulation' input. The calibration factor used for the z-motion is 0.75 nm/V. After the curve has been recorded, the feedback loop is enabled again and the tip ramped back to its initial position. Each curve is measured ten times to check the repeatability and enable averaging.

The measurement procedure is repeated for different bias voltages, each of which corresponds to another initial tip-sample distance. This distance is recorded just before the ramp is started and allows us to determine the absolute distance offsets between the different bias voltages. Each measurement is obtained at a different lateral position on the sample surface in order to avoid effects from changes of the local sample properties due to the high voltages. The prevention of these effects is confirmed by recording curves from low to high bias voltage and back to check if the position offsets in both sequences are equal.

Spacing-voltage (constant current)

The most straightforward method to determine the sensitivity of using field emission current for tip-sample distance control is by measuring the spacing as function of sample bias in constant current mode. The feedback loop will automatically adjust the tip-sample spacing and prevent the field emission current to move out of the measurable range when instabilities occur. Since only small changes in the electric field are needed to compensate for large variations in current, instabilities are expected to appear as small variations in the measured curves. Only few results are reported in literature on this type of measurement. The results obtained using the Topografiner setup are difficult to compare since the feedback was implemented to keep a constant voltage instead of a constant current [86]. In the field of STM-based nanolithography a tip is operated at increased tip-sample spacing using field emission as well, in order to produce a low energy electron beam. The main focus there is on the influence of the tip-sample distance on the beam diameter which can be calculated [183, 184]. Several authors give experimental results that show the increase in tip height as function of sample bias, but do not give a theoretical interpretation of these results [185, 186]. Adams *et al* have measured a z-V curve for a tip with $\sim 1\,\mu$m radius and compared this with simulations. They conclude that the tip radius is important for the measured tip-sample separation: sharper tips require a larger tip-sample distance to achieve the same field emission current [187]. This conclusion is in agreement with our model of field enhancement, which account the effect of tip radius. Besides topographic imaging or nanolithography, some special spectroscopic measurements can be performed in the field emission regime. By using high-frequency bias-modulation as function of DC bias voltage, the electron transmission probability can be measured and can reveal the existence of field emission resonances due to electron standing waves, as predicted by Gundlach [188]. In these measurements, next to the resonances, the gap distance is also recorded for increasing bias voltage. Measurement results such as reported in [189, 190] show that the measured oscillations do not have a significant effect on the measured z-V curves.

In the z-V measurements, we monitor the tip-sample distance during a voltage

ramp at constant current by measuring the feedback signal applied to the z-piezo. The measurement is started at a low bias voltage of 3 V with a constant tunneling current of 3 nA. The spectroscopic function in XPMPRO is used to start a ramp on the D/A output that is connected to the 'Bias Modulation' control input. The bias voltage output from the SPM1000 is first amplified $10\times$ by the PI-P863 high-voltage supply before it is connected to the sample, to be able to ramp up to a voltage of 100 V. While the bias voltage is ramped, the feedback loop is kept enabled, so that the tip-sample separation is adjusted in order to maintain a constant emission current. The feedback signal to the z-piezo is recorded as function of bias voltage ramp in order to obtain the required z-V curve. The z-piezo motion is indirectly calibrated at 0.75 nm/V by means of a conducting patterned sample, with a height variation known from measurements by a calibrated AFM. For each measurement, the bias voltage is ramped from low to high voltage and back again, so that the tip can return to its original position. Since the feedback loop is active during the complete measurement, field emission current instabilities are compensated by a change in the tip position and large current peaks that can damage tip or sample are expected to be prevented.

The measured curves do not provide an absolute measurement of the tip-sample distance. Since the absolute tip-sample separation at low bias voltage from which the ramp is started is unknown, the curves are measured relative to this starting position. For the low bias regime in general the tip-sample separation is estimated to be ~ 1 nm, therefore we take this value to define the starting position for plotting the z-V curves. The total increase in tip-sample distance is expected to depend on the specific field enhancement of the used probe and therefore the sensitivity will vary from probe to probe. Sharper tips produce a higher field for a given bias, which will result in a larger tip-sample spacing to keep a constant emission current. By comparing the shapes of the experimental and calculated z-V curves it will be possible to determine the specific field enhancement characteristics as function of distance for the measured probe.

3.2.3 Emission current stability

Next to the characterization measurements that are described above and used to determine the emitter sensitivity for distance variation, measurement of the stability of the field emission current is important to determine the applicability of a field emission probe. We use two methods to determine the effects of field emission instabilities, first by measuring the field emission current with the feedback loop disabled (open-loop) and second by measuring the variations in the tip position with the feedback loop enabled (closed-loop).

To measure the open-loop stability, we use the Keithley 6487 Picoammeter and LABVIEW control software to record the field emission current as function of time. First the tip is approached to the sample at 3 V and stabilized to achieve a stable tunneling current. Then the feedback is interrupted and the tip is displaced relative to the tunneling distance by applying an offset voltage to the 'Z-Offset' control input. The subsequent measurements are performed at a fixed distance of 200 nm to prevent electrical contact

between tip and sample, that might occur due to drift or by material deposition on the sample surface during the relatively long measurement time. Before starting a stability measurement, recording of a sequence of *I*-*V* curves is used to improve the emitting properties. By ramping up the bias voltage, the field emission current is increased to 800 nA, which can lead to desorption of surface contaminants and reshaping of the tip due to heating and field-enhanced surface diffusion. When the *I*-*V* curves for ramping up and down give reproducible results, the initialization sequence is considered to be complete.

By selecting the option for measuring stability in the LABVIEW software, this measurement is executed in between the up- and down-ramp of an *I*-*V* curve. The bias is ramped up until a user-defined current setpoint is reached. The emission current is than recorded during a custom time interval with a maximum acquisition rate of one data point per 50 ms. In our measurements the current is typically recorded for an interval of 5 minutes with maximum resolution. After the stability measurement is ended, the bias is ramped down while recording the corresponding *I*-*V* curve. By comparing both *I*-*V* curves before and after the stability measurement, it is possible to check whether the measurement has affected the field emission properties. In the software it is possible to set a minimum and maximum value for the field emission current to prevent loss of the current signal and damage by Joule heating of the tip or the sample. When during the measurement the field emission current decreases below the minimum value, the bias voltage is increased in small steps to make the current rise. When the field emission current exceeds the maximum current setting, the bias voltage is decreased in order to reduce the current. Of course when the field emission current is stable enough, variation of the bias voltage is not required since the current will only slightly vary within the minimum and maximum limits.

The effect of the emission current stability on the feedback signal to the tip position is measured in closed-loop using the XPMPRO software. This measurement is done at a closer distance to the sample surface compared to the open-loop measurements, at the intended voltages for non-contact operation of the probes during scanning. Only moderate voltages up to 20 V are used, to prevent that tip and sample are damaged due to capacitive discharges when unwanted tip-sample contacts occur. The feedback loop is enabled at a constant current setpoint of 3 nA, the same as used for scanning. After adjusting the bias voltage to the desired value, we wait until drift effects are minimized and the current and feedback signal are constant. Then the z-motion is recorded for a fixed time interval, in our experiments for a period of 60 s. Together with the z-motion, also the field emission current is measured, to see if the control loop is able to keep the current constant.

3.2.4 Cantilever deflection

The fiber interferometer AFM setup is used to determine the cantilever deflection as function of applied bias voltage. Using the theoretical model given in chapter 2, we have predicted a series of voltage-deflection curves, for different spring constants and

different initial distances. However, during the field emission experiments, the tip-sample distance is not constant but increases with increasing voltage. Therefore in our experiments, the main interest is in the amount of cantilever deflection when field emission current is used to keep a constant tip-sample distance.

The presence of the interferometer detection system in the used setup enables a sensitive and absolute measurement of the cantilever deflection during constant current feedback. Since for large displacements the interferometer output gives a sine wave signal, first the fiber piezo is adjusted to change the distance between the fiber and the cantilever and select a zero crossing in the signal. At this optimal working point the interferometer output signal varies linearly with the cantilever deflection and the sensitivity is maximum. The calibration of the z-piezo motion is obtained by bringing the cantilever probe in contact with the sample and using the interferometer output signal to determine the absolute displacement.

A major complication during the cantilever deflection measurements is the occurence of electron-beam induced deposition as will be shown in chapter 6. During this work it was found that material is deposited on the sample surface when the tip is operated in the field emission regime. Since the fiber AFM setup is pumped through a oil-diffusion pump and therefore does not provide UHV conditions, this deposition effect was found to be relatively large. To be able to measure the cantilever deflection without this disturbing effect, the measurements are therefore performed while *scanning* the probe over the sample. By moving the lateral position while increasing the bias voltage, the build-up of large amounts of material under the probe tip is prevented.

The cantilever deflection is measured by applying the same procedure as used for the z-V measurement, which has been described above. Both the z-piezo feedback signal as the cantilever deflection signal are monitored while the bias voltage is ramped. The Keithley 6487 Picoammeter is used again in this setup to provide the bias voltage to the sample and measure the field emission current from the tip. The analog output of the current amplifier is connected to the V-Scan 100 DSP control module that is used to provide the feedback signal to the z-piezo. The measurement is started at a low bias voltage of 5 V with a constant tunneling current of 3 nA. For each measurement, the bias voltage is ramped up and then back to the initial voltage again. A storage oscilloscope is used to record the bias voltage, z-piezo voltage and interferometer output signal simultaneously. The logged data is used together with the calibration values to plot the z-position and cantilever deflection of the probe as function of bias voltage.

Chapter 4

Preparation of probes and samples

Several different probes and samples have been used in our experiments to test the applicability of field emission sensing for tip-sample distance control. Here the preparation methods will be given that have been used to produce these. First the two different probe types will be discussed that were needed to separate the effects of field emission and cantilever deflection in the characterization measurements. Then the requirements and the fabrication results of the patterned samples will be described.

4.1 Probe preparation

For application as an electron beam source or in an emitter array, field emitters are generally fabricated on top of a fixed base platform or inside a cavity surrounded by a gate electrode. In our intended application of probe recording however, the emitting tips are used at the end of a cantilever. An important complication when using such probes for field emission is the effect of cantilever deflection due to the electrostatic interaction with the medium. Therefore, in a collaboration with the Electronic Instrumentation Labs at the University of Delft, a fabrication process was developed to produce a fixed-tip that resembles the emitter intended for magnetic probe recording, but is fixed to the substrate so that there is no bending cantilever. Measurements performed on this tip can then be compared to results on commercially available AFM probes that do have a cantilever. In the following sections the preparation of these two types of probes will be discussed.

4.1.1 Fabrication of fixed-tip probes

By fabricating tips protruding from a 'fixed' substrate without a cantilever, we will be able to very accurately control the distance between the emitter tip and sample without the electrostatic bending that is expected for cantilever probes. We have chosen not to use STM tips, made of a fine metal wire, since we do not have sufficient control over the

fabrication process for such tips. Tips not properly prepared might have several mini-tips, of which the closest to the surface gives the image. However, with the increased bias voltages and the rough (patterned) samples that we use for the field emission experiments, the emitting current may come from more than one tip, resulting in multiple imaging of features on the sample. Although there are advanced STM tip preparation methods available, instead tips made by silicon micromachining are used as these are in closest resemblance of the tips present on cantilever probes that will be used for later experiments.

Since tips on a fixed base are not commercially available, they were custom made at the Electronic Instrumentation Labs at the University of Delft [191]. The fabrication process requires several steps that are depicted in figure 4.1.

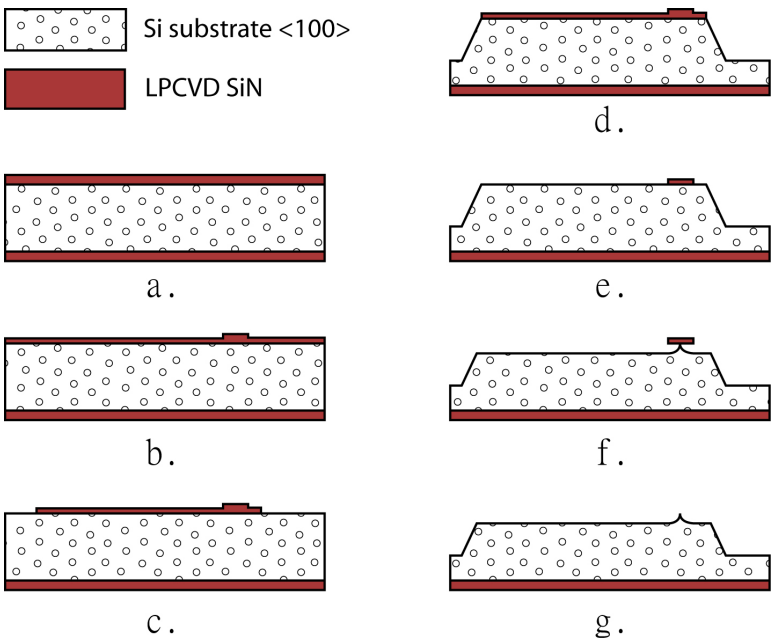

Figure 4.1: *Cross sections of the fabrication process of a silicon tip on a fixed base: a). Deposition of 300 nm silicon nitride by LPCVD. b). Patterning of tip mask by etching 150 nm deep. c). Patterning of base mask by etching remaining thickness of silicon-nitride. d). Silicon etch by KOH. e). Silicon nitride etch (maskless) onto silicon. f). Isotropic silicon etch by SF_6 plasma. g). Silicon nitride pad removed in phosphoric acid. Figure courtesy of C.K. Yang [191].*

First a low-stress LPCVD silicon nitride layer is deposited on the silicon substrate that is used as an etching mask for both the tip and the base (a). The tip mask is patterned by plasma etching half of the nitride layer (b) and a second lithographic step is used to etch so much of the nitride that only the base and tip mask remain (c). The sample is then put in KOH solution to etch into the silicon and form the base platform for the tip (d). Subsequently the nitride is etched so that only the tip mask remains (e). Finally the

silicon sample was isotropically etched to form the tip (f) and dipped in phosphoric acid to remove the fallen tip mask (g).

The technique of using only one layer of silicon-nitride for etching both the base platform and the tip enabled the possibility to fabricate the tip very close to the platform base edges, which is otherwise challenging due to large step heights that prevent resist spinning. Having tips close to the platform edge allows us to approach the tips without the platform sides touching the sample when using the tips in the measurement setup. This greatly relaxes the tilting requirements for mounting the tips. The tips fabricated by this process are typically $2-3\,\mu$m high and have a tip radius of $10-25$ nm, which is close to the tip radii of the AFM probes that will be used in further experiments. Figure 4.2 shows the typical result after fabrication. Since the probes are fabricated from standard p-type <100> silicon wafers with a specific resistance of 5 - 10 Ω·cm, they require a metal coating before use as a field emitter.

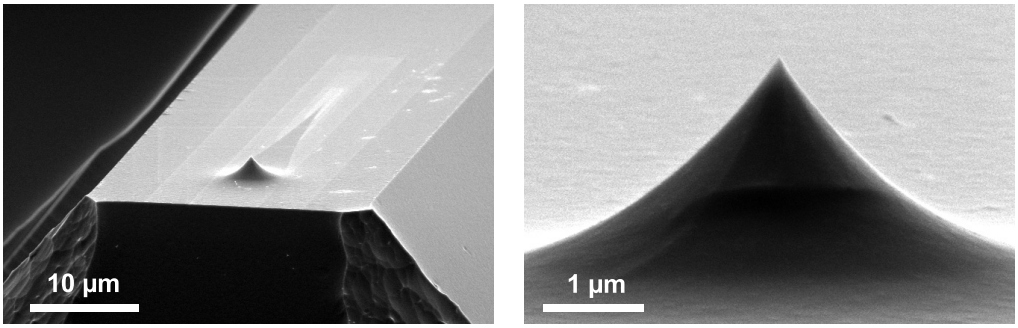

Figure 4.2: *SEM image of the silicon tip on a fixed base platform made by micromachining. The left image shows an overview of the tip situated at the end of the substrate base platform. The right image gives a closer look at the tip shape, showing a tip height of $2-3\,\mu$m and a typical tip radius of 10-25 nm. Figures courtesy of C.K. Yang [191].*

4.1.2 Preparation of AFM probes

To investigate if cantilever probes can be used for field emission and determine the effect of cantilever bending, we decided to use commercially available AFM probes. Although this type of probe is not designed to be used for field emission experiments, the properties of the probe tip make it actually rather suitable as a field emitter. Since the tips have a very small tip radius and high aspect ratio, the extraction voltages that are required for field emission can be relatively low due to a high field enhancement. Generally the probes are micromachined from monocrystalline and highly n-type doped silicon which also is also used in field emitter arrays as a very suitable field emitter material [139]. Only the native oxide that will be present on the silicon surface may be a limiting factor in obtaining good field emission properties. Moreover, since the probes are made with high reproducibility, the variation in field emission properties among different probes may be low and allow a comparison of the measurement results. When the measurements

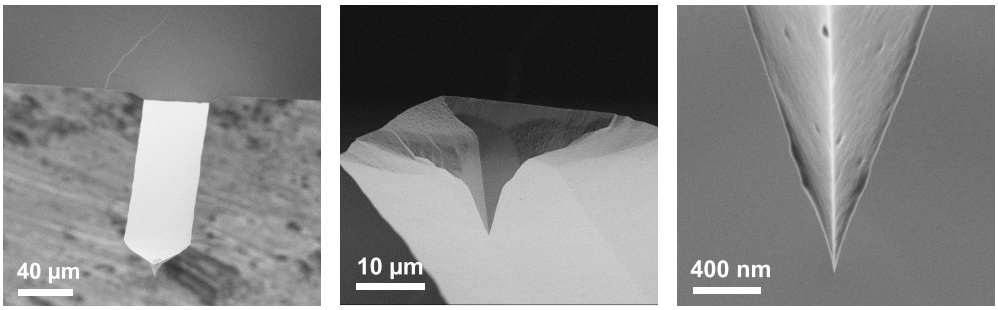

Figure 4.3: *SEM images of a typical AFM probe that was used for the field emission sensing experiments. The images show an uncoated single crystal silicon probe with a tip radius of* < 10 *nm.*

using AFM probes demonstrate that field emission from such a probe can indeed be used to control the tip-sample distance, the next step would be to use arrays of probes with similar properties.

The AFM probes that we used are Nanosensors Pointprobe Plus probes [192]. The same type of probe is used in our lab for MFM after applying a magnetic coating to the tip. The probes are single crystal and etched from highly *n*-type doped silicon, with a doping level of $5{\cdot}10^{18}$ atoms/cm^3. This doping level results in a specific resistance of $< 0.01\,\Omega{\cdot}$cm. They are available with various spring constants of which we chose the highest value (48 N/m) to prevent pull-in of the cantilever. The cantilever is specified to be 225 μm long and 38 μm wide with a resonance frequency of 190 kHz. The tip height is 10 - 15 μm with a tip radius of typically < 7 nm. This tip radius is smaller than what is achieved for the fixed-tip probe, but will increase by the metal thin-film coatings that we apply. In figure 4.3 some example SEM images of this probe are given.

Next to the standard AFM probes, in the experiments we also used special probes coated with a conductive diamond layer, so-called conductive diamond tip (CDT) probes. The hardness of the diamond material provides a good wear resistance and since they are doped, the probes are generally used for applications that require a wear resistant and electrically conductive tip. Diamond is a material with unique properties such as a low electron affinity and high thermal conductivity. Electron emission from diamond has been experimentally observed to yield a high emission current at relatively low applied electric field compared to emission from metal and silicon [140, 139]. Moreover, one of the remarkable properties of diamond is the high thermal conductivity. Therefore the CDT probes are a promising candidate to be used in our field emission experiments. The probes that we used are obtained from Nanosensors [192]. The general tip features are equal to the Pointprobe Plus tip. The diamond coating is ~ 100 nm thick and because of this thickness, the tip radius of curvature is also around 100 nm. Due to sharp edges of single diamond crystals at the end of the tip, for small features the 'microscopic' tip radius can be smaller, on the order of ~ 10 nm. The coating is highly doped to a specific resistance of $\sim$3 - 5 m$\Omega{\cdot}$cm, to lower the electrical resistance of the probe. Typical SEM images for such a CDT probe are depicted in figure 4.4.

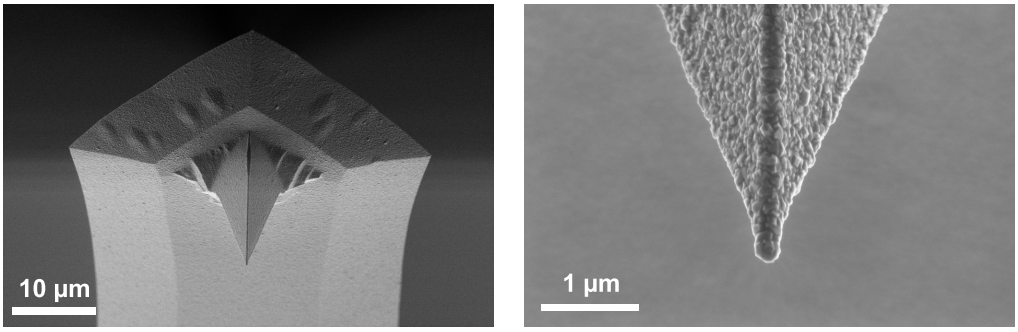

Figure 4.4: *SEM images of a typical conductive diamond (CDT) tip probe, showing the surface roughness resulting from the diamond crystals in the* $\sim$ *100 nm coating layer. Due to the thick coating, the radius of the tip is increased to* $\sim$ *100 nm.*

4.1.3 Probe coatings

Both the fixed-tip and the AFM probes have been coated with various materials to be able to measure the effects of the emitter material on the stability and on the field emission properties. The deposition technique that we used for coating our probes is sputtering. Most studies reported in literature involve coating of the field emitter (arrays) by evaporation, since this technique can be used to obtain cone formation due to line-of-sight effects. It has been demonstrated that sputtering can be used in place of evaporation and has the advantage that a larger variety of materials can be used [103]. More important for our application is that it gives an excellent step coverage, so that deposition also takes place on the sidewalls of the emitter tip and on the probe cantilever and holder piece, so that we can make a good electrical connection to the emitter tip end. Coatings of molybdenum, tungsten, platinum and chromium have been used, for which the characterization results will be presented in chapter 5.

4.2 Samples patterned by laser interference lithography

In order to test the method of using field emission currents for high-resolution lateral positioning, a special patterned sample with a well-defined topography is needed. Below the requirements are discussed for such a sample and the fabrication process is given that has been applied to obtain the patterned samples used for the scanning experiments presented in chapter 6.

4.2.1 Sample requirements

In the magnetic probe recording application that is pursued in this work, the patterned medium will ultimately have small magnetic dots with a size on the order of 10 - 25 nm. This sets the requirement for the lateral positioning accuracy and thus a test sample should preferably have features with this same density. A relaxation for the test sample is that it does not need to have magnetic materials, it should only be sufficiently conductive

to enable the field emission currents to flow. The dots should have such a height, that they can be distinguished in the positioning feedback signal from the variations due to the field emission instabilities. From the experiments that will be presented in chapter 5 it was found that the accuracy to which a probe can be positioned at a certain distance from a single location on the sample surface is limited to $< 20\,\text{nm}$, due to noise and instabilities in the field emission current. Therefore we should use dots with a height larger than $\sim 20\,\text{nm}$. However, they should not be too high, since the maximum scan speed in scanning probe techniques is greatly reduced when rough samples are used, due to limitations in the feedback loop.

Several techniques can be used to prepare the patterned surfaces that we need. The most straight-forward method is done by using conventional photolithography to define an etch or lift-off mask. However, the critical dimensions that can be obtained in our cleanroom facilities are limited to $1\text{-}2\,\mu\text{m}$. Techniques like focused ion beam etching or electron beam lithography can define much smaller structures but are less suitable since they are limited to small areas. Patterns created using these techniques would be difficult to trace, since the scanner of the RHK STM that we use has a scan range of $5 \times 5\,\mu\text{m}$ and the coarse positioning is done by eye with an accuracy of $\sim 1\,\text{mm}$. In the fiber interferometer AFM setup there is no coarse positioning at all.

4.2.2 Laser Interference Lithography

We used laser interference lithography to fabricate our test samples since this technique enables high periodic resolution over large areas. The LIL method is also used in the μSPAM project for the patterning of magnetic films [194]. In this technique a laser beam is split and recombined to create an interference line pattern and expose a wafer with photoresist. In the laser interference setup at the MESA$^+$ Institute facilities the laser beam is expanded and directed on both a mirror and the sample to produce the interference pattern, as is shown in the schematic in figure 4.5 [193]. The exposed area can be up to a few square centimeters, depending on the diameter of the interfering beams. In our setup we use a YAG 1064 nm laser with a frequency quadrupling configuration to obtain light with a wavelength of 266 nm. The theoretical resolution

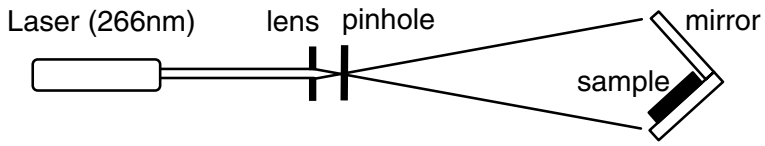

Figure 4.5: *Schematic representation of the optical interferometer setup used for laser interference lithography. A laser beam is expanded and spatially filtered by a lens and a pinhole. The broad beam is then directed onto a mirror placed perpendicular to the sample. The reflection from the mirror interferes with the part of the beam that is directly illuminating the sample, resulting in a pattern that is half the periodicity of the used wavelength. Image from [193].*

limit of this setup is a line pattern period of 133 nm. In practice, resist line patterns with a periodicity ranging from 1 μm down to 150 nm have been achieved. The dot pattern that is desired for our test samples is obtained by a double exposure of the resist, with a 90° rotation in between the exposures.

4.2.3 Pre-patterning by reactive ion etching

To transfer the resist pattern into the sample material, a new method was developed. Ion beam etching (IBE) has been used before to etch magnetic thin films and fabricate patterned magnetic media test samples [193]. A problem with this method is that due to the ion beam etching, the photoresist layer can alter due to carbonization or cross-link formation and becomes insoluble in acetone. For our experiments a very clean and well-conducting patterned surface is needed to have stable field emission at each position on the sample. Therefore in the current work a sample substrate that is not necessarily well-conducting is first pre-patterned by LIL and reactive ion etching. Once the substrate has been patterned, a metal coating is deposited by sputtering to improve the conductivity.

The first sample is made by pre-patterning a substrate that consists of 500 nm low pressure chemical vapor deposited (LPCVD) silicon nitride on a *p*-type <100> silicon wafer. The fabrication method to produce this sample is schematically represented by the left process in figure 4.6.

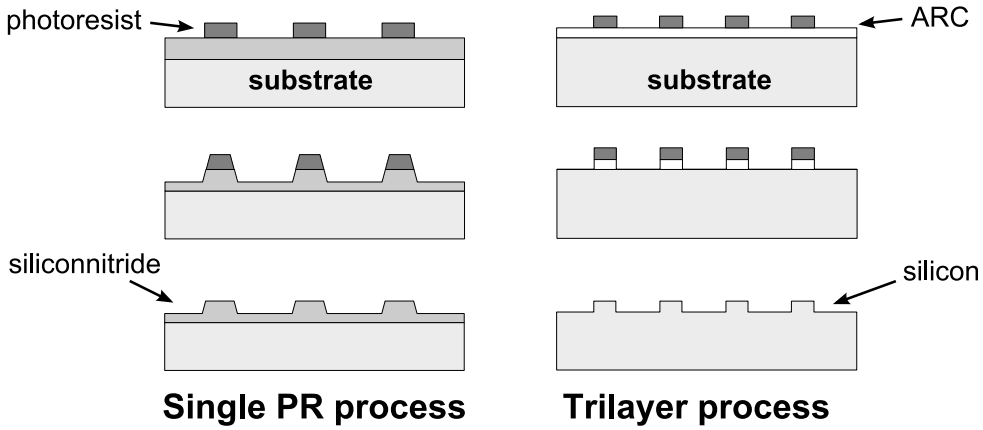

Figure 4.6: *Schematic diagram of the two different LIL processes used to fabricate the patterned samples: a single layer photoresist process and a trilayer process used to achieve a higher dot periodicity.*

As a photoresist we employed standard photolithographic i-line OiR 907/12 resist, that is thinned and spin-coated resulting in a thickness of 200 nm. The laser interference lithography (LIL) setup is used to create a sub-micrometer resist pattern. The nitride is patterned through the resist mask by a standard CHF_3/O_2 plasma in a parallel plate reactive ion etcher, resulting in dots with 280 nm periodicity, 180 nm diameter and 35 nm

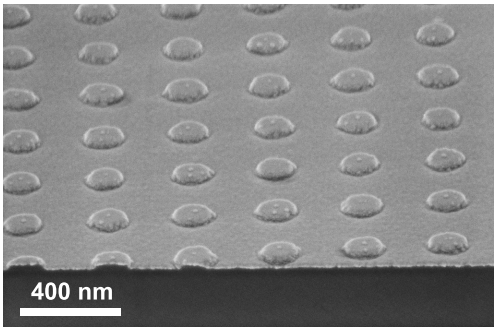

Figure 4.7: *Silicon-nitride layer on silicon, patterned by LIL and RIE using the single layer photoresist process, resulting in dots with 280 nm periodicity, 190 nm diameter and 35 nm height.*

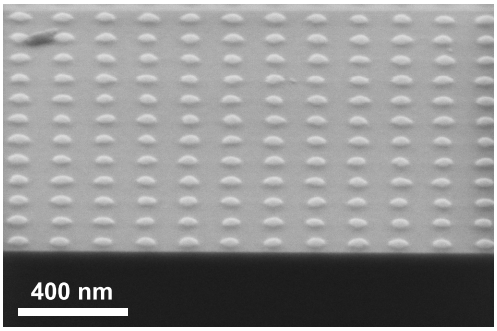

Figure 4.8: *Silicon sample, patterned by LIL and RIE using the trilayer process, resulting in dots with 160 nm periodicity, 90 nm diameter and 20 nm height.*

height. Resist removal took place in oxygen plasma. In figure 4.7 a SEM image of this sample is shown.

The standard i-line photoresist could not be used to further reduce the periodic resolution below ~ 300 nm, whereas the minimum resolution of the setup should be capable to provide features of 150 nm. Therefore a second fabrication method was developed [195] that can result in a higher dot density. A new trilayer resist system is used for which the process scheme is depicted on the right of figure 4.6. The resist layer stack consists of a positive chemically amplified resist (p-CAR PEK500) with a Deep-UV bottom antireflective (ARC-DUV46) coating. Since chemically amplified resists are severely degraded by vapor from organic bases, a protective top coating of Aquatar-6A [196] is used to seal the photosensitive layer from the ambient conditions. This coating is applied by spinning, resulting in a negligible thickness. The resist layer stack is not used on silicon-nitride but on a standard *p*-type <100> silicon wafer. The resist stack is exposed in the LIL setup and developed resulting in a resist dot pattern with a periodicity of 160 nm. To etch through the ARC, an O_2 plasma etch step is used. Subsequently, the pattern was transferred in the silicon by standard CHF_3/O_2 plasma reactive ion etching. After the pattern transfer, the residual resist was removed by oxygen plasma cleaning. The resulting dot pattern has 160 nm periodicity with 90 nm diameter and 20 nm height and is shown in figure 4.8.

4.2.4 Sample coatings

Since the top layers of the fabricated samples consist of silicon-nitride and native silicon-oxide, the samples are not sufficiently conducting to be able to perform measurements using tunneling or field emission current. Therefore the samples have been coated by a thin-film metal to provide a highly conductive layer. The sample coating has to fulfil certain requirements in order not to disturb the field emission process. Just like the emitter material, the material used should preferably have a low specific resistance, a

high melting point, high tensile stress (against wear) and a good corrosion resistance. Sputtering was used to apply the thin-films to the samples, to have a large selection of materials and a good step coverage. Coatings of molybdenum, tungsten and platinum have been applied and characterized in terms of resistivity and roughness, for which the results will be presented in chapter 6.

Chapter 5

Characteristics of field emission sensing

In this chapter the characteristics of the field emission sensing method will be examined by showing measurements on various types of probes and probe coatings. For the measurements we used the instruments and experimental procedures that have been described in chapter 3. These procedures have been applied to the two types of probes that have been shown in chapter 4. First, results for the fixed-tip probes will be given that have been measured to obtain field emission properties from micromachined emitter tips. The field emission behaviour is verified by taking *I-V* characteristics and relating them to the Fowler-Nordheim model that was presented in chapter 2. Next to the field emission characteristics, the effects of varying tip-sample distance for these tips will be given. Secondly, measurements will be discussed on the commercial AFM probes, that were used to determine if the requirement of having field emission from cantilever probes without cantilever pull-in can be met. The dependence of the field emission effect on distance is measured for these probes as well and applied for probe-sample distance control. Finally, conclusions are drawn on the applicability of field emission from cantilever probes for proximity sensing.

5.1 Field emission from fixed-tip probes

The fixed-tip probes are used to be able to very accurately control the distance between the emitter tip and the sample without the effect of electrostatic cantilever bending that is expected for the cantilever probes. The process that has been used to fabricate the tips has been given in chapter 4. For a detailed description of the measurement procedures we refer to section 3.2. Before the probes are used for tip-sample distance control, first the general field emission characteristics are determined and the Fowler-Nordheim model is applied to extract the typical field emission parameters.

5.1.1 Field emission characteristics

The specific field emission properties are generally determined by recording *I-V* characteristics. In the following sections, such measurements will be presented for the fixed-tip probe that were measured in the RHK STM. A dedicated routine is developed to fit the Fowler-Nordheim model to the measured data. Since the probes are made from *p*-type silicon wafers with a relatively high specific resistance of $5-10\ \Omega\cdot$cm, a metal coating is required to lower the resistance and have metal-like behaviour. A few coatings have been tested by measuring the emission current as function of time, in order to find a material that we can deposit in-house and that provides good current stability.

Influence of tip coating on emission current stability

As described in chapter 2 it is expected that the field emission process is susceptible to instabilities. Since we intend to use the emission current as a sensing signal to control the tip-sample distance, these current instabilities may significantly affect the tip position and cause a variation in the tip-sample distance or even lead to tip-sample contact. By coating the fabricated tips with a thin metal layer it is possible to improve the field emission properties. An overview of common materials can be found in [103, 139]. In general, the materials that are used should have a relatively low work function, a high melting point, high thermal conductivity, high tensile strength and good resistance against oxidation. To find a coating material that we can deposit in-house and provides a good emission current stability, we measured three different tips with three different metal layers which are often used in field emission applications, as given in table 5.1.

After sputtering the metal layer, the coated tips were mounted on the tip holders, as described in chapter 3. The tips and holders were annealed at 120 °C to reduce outgassing from the silver paint that is used for mounting. The tips were then loaded into the UHV system which is pumped to a pressure of $5\cdot10^{-9}$ mbar. A flat silicon sample coated with 10 nm tantalum (Ta) for adhesion and 50 nm platinum (Pt) was used as a counter-electrode for the emission current. The stability measurements were performed

	Coating	ϕ [eV]	T_m [K]	ρ [$\mu\Omega\cdot$cm]	λ [W/m·K]	σ [MPa]
(a)	Pt (20 nm)/Ta (5 nm)	5.65	2041	9.81	71.6	134
(b)	$W_{90\%}Ti_{10\%}$ (25 nm)	4.54	3693	5.49	164	550-1920
(c)	Mo (50 nm)	4.39	2893	5.2	142	485-690

Table 5.1: *Three coating materials used on the fixed-tip probes to test the influence of coating material on the field emission current stability. In order to compare the materials, several properties are listed: work function ϕ, melting temperature T_m, specific resistance ρ, thermal conductivity λ and tensile strength σ. Values taken from [99].*

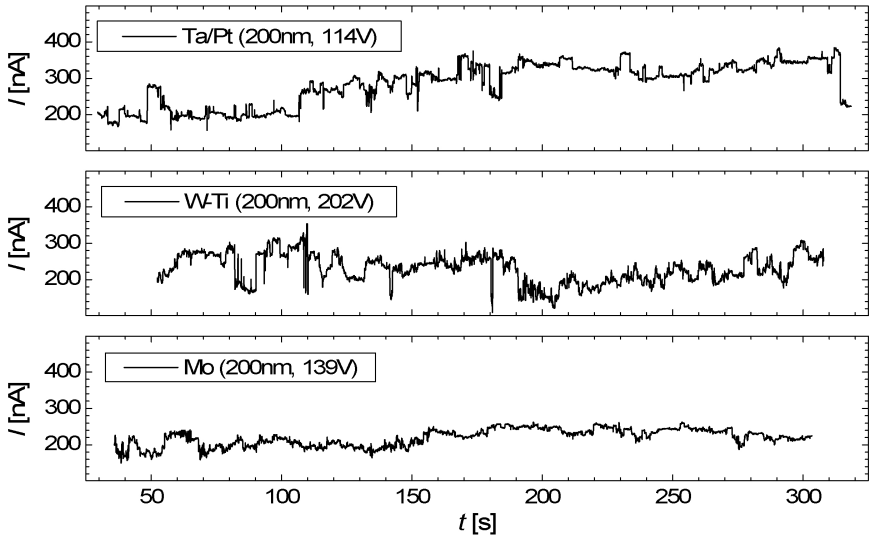

Figure 5.1: *Typical field emission current stability measured for a time interval of 300 s for fixed-tip probes coated with Pt, W and Mo.*

according to the procedure described in section 3.2. In figure 5.1 the typical results from the three probes are compared, showing the emission current recorded for 300 s.

The measurements show only a small difference in emission stability between the different coatings. For the tip coated with Pt, large instantaneous instabilities in the field emission current are observed, with changes on the order of 50%. This behaviour is typical for sharp field emitters with a small area of emission [104]. The instabilities are explained by sudden atomic variations on the tip surface and could be more pronounced for this tip coating because of the relatively low melting point and tensile strength of the material, compared to the other coatings. Although tungsten (W) is often used as a field emitter material [105] and emitters coated with W should have excellent properties [197], it was found that the emission current from this tip is not very stable as well. The reason for this behaviour is not clear and might be related to the specific deposition conditions that were used. From preliminary experiments it was found that when using a sputter target of pure W, deposited layers suffer from bad adhesion [198]. This problem was alleviated by using a sputter target with a small (10%) content of titanium (Ti), however the field emission current stability was not improved. By experimental experience, we learnt that the best stability in our setup and measurements condition is obtained for the molybdenum (Mo) coating that we deposit by sputtering. Therefore, for the subsequent measurements fixed-tip probes coated with Mo were used, with a thickness of 50 nm to ensure a good coverage of the tip apex.

Current-voltage characteristics

To determine the field emission properties for the fixed-tip probe coated with 50 nm Mo, we measured its *I-V* characteristics according to the procedure described in section 3.2.

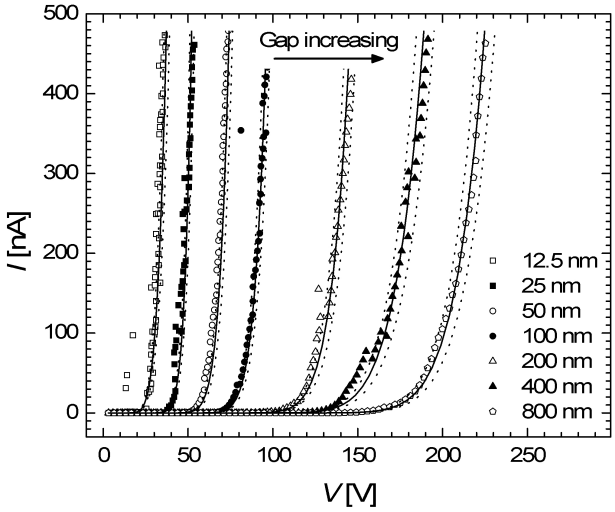

Figure 5.2: *Distance dependence of field emission in I-V characteristics measured for distances from 12.5 nm to 800 nm between a fixed-tip probe coated with 50 nm Mo and a flat silicon sample coated with Ta(10 nm)/Pt(50 nm). The measurement data is corrected for the voltage-drop caused by the 100 MΩ series resistor. The solid lines are the results from fitting whereas the dotted lines represent the effect of a variation of 30% in the emission area.*

By varying the initial distance between the tip and the sample, a sequence of curves is obtained which is shown in figure 5.2. Here the tip was first brought into the tunneling regime, so close to contact with the flat Ta(10 nm)/Pt(50 nm) coated silicon sample. Next, the tip was retracted to increase the tip-sample distance to a fixed value. A positive bias sweep was then applied to the sample to extract a current up to 500 nA from the tip. This measurement was repeated for increasing tip-sample distances from 12.5 nm to 800 nm. The data shown is corrected for the voltage-drop caused by the 100 MΩ series resistor.

The linefits in the figure are obtained from the Fowler-Nordheim model presented in chapter 2 by using a fitting procedure that will be described in the next section. The shape of these fitted lines is in good agreement with the measured data, indicating that the currents obtained are indeed the result of the field emission effect. The stability of the field emission current from the Mo coated tip is sufficient to distinguish the separate curves for each tip-sample distance setpoint. As can be observed from the measurements, for increasing distances, higher voltages are needed to extract the same field emission current, from about 30V for 12.5 nm to a maximum of 230 V for 800 nm separation. The increase in required voltage is not linearly dependent on distance, which is caused by the effect of the changing field enhancement. With increasing distance, the field enhancement increases as well, reducing the total voltage required to reach the emission field. The field enhancement factors can be derived from the measurements by fitting the data using the Fowler-Nordheim model.

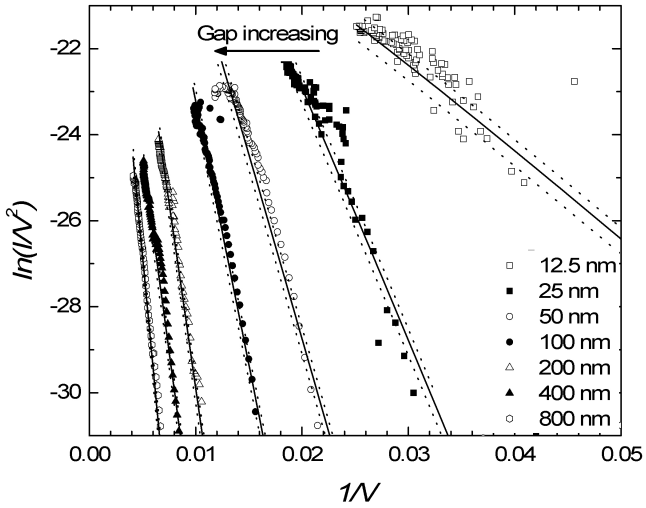

Figure 5.3: *Distance dependence of field emission in semi-logarithmic Fowler-Nordheim plots, derived from the I-V measurements of figure 5.2, for distances from 12.5 nm to 800 nm between a fixed-tip probe coated with 50 nm Mo and a flat silicon sample coated with Ta(10 nm)/Pt(50 nm).*

Fowler-Nordheim fitting procedure

By plotting the *I-V* curves on a semi-logarithmic scale as is done in figure 5.3 we can fit the Fowler-Nordheim relation of equation 2.23 to our data and determine the typical field emission parameters, i.e. the emission area A and the field enhancement factor γ. From the Fowler-Nordheim plot, the values of P_V and S_V in the equation can be derived from the intercept of the linear linefit with the vertical axis and the line slope. For this an automated fitting routine was developed in the mathematical package MAPLE, based on the model described in chapter 2. The routine is given in appendix A and below an explanation of the consecutive steps of the fitting procedure is given:

1. Read data and select measurement points above threshold current.
2. Linear fit to the selected data-points by least squares error method.
3. Calculation of the 'local-field-to-voltage-ratio' β (equation 2.16) from the slope of the linefit (S_V), the estimated work function ϕ and an initial approximation for the value of the error correction factor s. The field enhancement factor γ is related to β by $\gamma = \beta d$ and can be calculated when the tip-sample distance d is known.
4. Calculation of a better approximation for s for a given point on the fitted line using the value for β calculated in the previous step, and iteration of step 3 to derive a more exact value of β.
5. Calculation of the emission area A in the point of interest using the intercept value of $\ln(P_V)$, the calculated β and the calculated values for the error correction factors p and s in this point.

The iterative fitting routine is needed to obtain right approximations for the error correction factors p and s in the region of interest, that are calculated by using the elliptic-integral formulas t_N and v_N. It should be noted that since these error correction factors are also functions of the electric field, the theoretical FN plot is not a straight line. The small curvature results in a fitting error since we use a *linear* least squares fitting method. Verification of the fitting model using artificial data taught us that by using an iterative process, the parameters γ and A can be determined with errors of 2% for γ and 30% for A [199]. This means that our fitting model is not fully self-consistent as has also been found by others [114, 200] and should in principle be replaced by a non-linear curve fitting method or local calculation for one point on the I-V characteristic. Although this causes a significant error in the values obtained for the area of emission, fortunately for the field enhancement factor this dependence is weak and γ can be fitted with sufficient accuracy for further analysis.

Fitting results

From the MAPLE routine used to fit the Fowler-Nordheim plots presented in figure 5.3, the field enhancement factor γ and the emission area A for the fixed-tip probe have been extracted. In figure 5.4 the values for γ are given as function of the tip-sample distance. As can be seen from the graph, the field enhancement factor is ~ 1 for small separation and increases with increasing distance. This is in agreement with the theoretical relation for the field enhancement that was developed in section 2.2.2. The model of equation 2.20 is used to fit the data points, by choosing values for r and γ_∞. The best fit was obtained for $r \approx 25$ nm, which corresponds to the typical tip radius for the fixed-tip probe, although we would expect this radius to have increased due

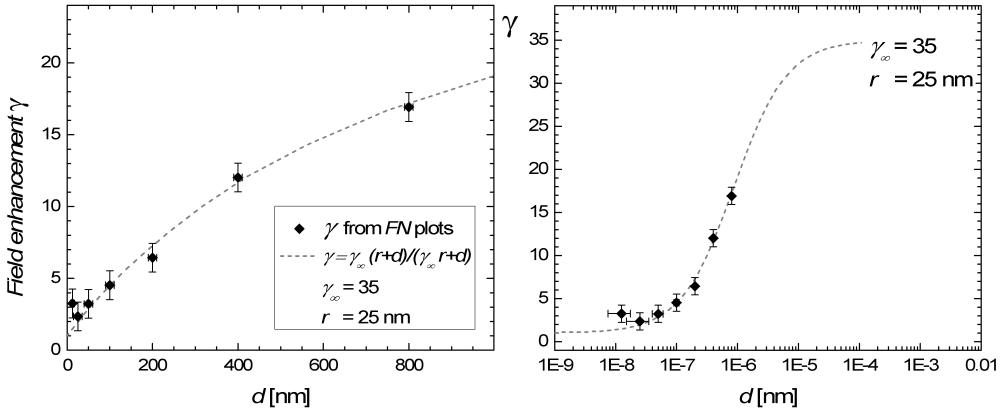

Figure 5.4: *Field enhancement factors determined for the fixed-tip probe by fitting the Fowler-Nordheim plots (Figure 5.3), plotted as function of electrode distance. The dashed line is a fit calculated using equation 2.20 with $r = 25$ nm and $\gamma_\infty = 35$. The right figure gives the same curve on a semi-logarithmic scale and shows that the linefit saturates to 35 for large distance.*

to the Mo coating. For the maximum field enhancement at large distance a value of $\gamma_\infty \approx 35$ was used. This is lower than what is expected for a tip length of $2-3\,\mu$m, since according to equation 2.17 a value in the range 80 - 120 should result. The reason for this is not completely understood but might be caused by the fact that the tip shape is not well represented by the geometric model that was used for the calculation of the field enhancement. In reality, the emitter cannot be described by an isolated sphere but the effect of the tip cone on the variation in the electric field should be included. However, according to the fit, the general dependence of the field enhancement on distance is correctly described by the calculated model.

The values for the emission area A have also been obtained from the MAPLE fitting routine that was applied to the data of figure 5.3. The values correspond to a radius varying between 2.4 and 3.3 nm, independent of the tip-sample separation. They are much smaller than what would be expected from the actual tip radius of about 25 - 50 nm and are not constant for all measurements. It is possible that the emission occurs from one or more small protrusions on the tip surface which have a smaller radius than the tip and that the emission position may vary in time. The radius of the area of emission that was found from the curve taken at the smallest gap of 12.5 nm is only 0.1 nm and thus deviates significantly from the average. This deviation is explained by the larger relative error in the Fowler-Nordheim plot that causes the linefit to be less accurate. The field enhancement factor that is also determined from this fit is less accurate as well and therefore has been ignored in the fit in figure 5.4.

To show the effect of the emission area A on the emission current, in figure 5.2 and 5.3 dotted lines have been added that indicate an upper and lower boundary for a variation of the emission area of 30%. Since most of the measurement points lie in between these boundary lines, they illustrate that by using the Fowler-Nordheim model the emission area and the field enhancement factor can be determined with rather good accuracy.

For the work function we used the value for Mo of $\phi = 4.39$ eV. The actual work function is unknown and depends on several factors like the cleanliness of the tip surface, morphology, oxidation state, etc. The tip and sample preparation procedures are of great importance, and in our setup we are limited in this respect because of the lack of a load-lock or in-situ deposition capabilities in the UHV system. The effective work function may also not be constant during the measurements, as there are many factors that can affect its value, especially when using high bias voltages. Since determination of the effective work function and its spatial variation is a research field in itself [57] and not easy to obtain, for simplicity we have assumed that indeed this constant work function can be used.

5.1.2 Tip-sample distance control

In the previous measurements we have confirmed that the field emission current from the fixed-tip probes is sensitive to the tip-sample distance and is correctly described by using our model for the variation in the field enhancement. The next step is to apply

this field emission current signal to control the tip-sample distance. This is done by feedback to the z-piezo to actuate the tip position so that a constant current is maintained. In this section the results for such tip-sample distance control are presented. First the emission current is recorded in open-loop while varying the tip-position, to investigate the emission current dependence on short distance variations. After closing the loop, the influence of current instabilities on the tip position is examined and the relation between the applied voltage and the tip position in constant current feedback is measured.

Open loop

To investigate the dependence of the field emission current on variations in the small tip-sample distances that we intend to use, the emission current is recorded while the tip is retracted from the sample surface. A sequence of curves is measured by increasing the values for the bias voltage and the tip-sample distance. It was found that for larger distances, the field emission current becomes less stable. As described in chapter 2, this increase in instability is explained by the increase in field-enhanced diffusion of contaminants on the tip and sample surfaces, as well as atom ionization causing sputtering of the tip surface and field evaporation from the tip. In order to be able to measure the typical current-spacing characteristics, a single curve is therefore recorded within 20 ms and an average of 25 curves is used to cancel out instabilities in the field emission current.

The results are presented in figure 5.5. For these measurements again a fixed-tip probe coated with a 50 nm Mo layer was used. The tip was first approached to the sample surface at 3 V bias voltage until a current of ~ 3 nA was achieved. This position was defined to be the zero-position. Then the tip was retracted several nanometers from the

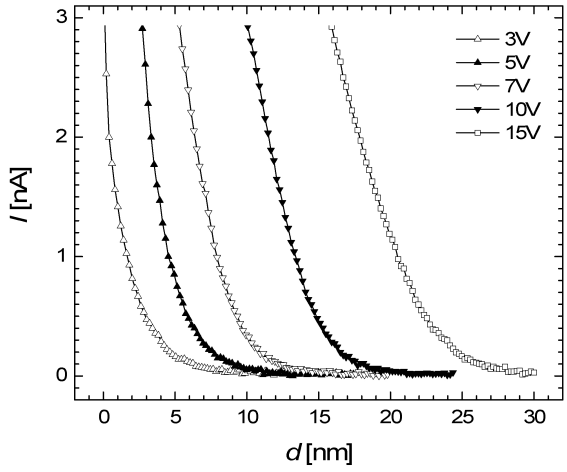

Figure 5.5: *Field emission current measured as function of distance between the fixed-tip coated with 50 nm Mo and the sample coated with Ta(10 nm)/Pt(50 nm). The measurement was repeated for increasing values of the applied voltage.*

sample surface while measuring the emission current. This measurement was repeated for increasing applied voltages, resulting in an increase of the initial distance when using the same initial current of 3 nA. Each measurement is obtained at a different lateral position on the sample surface in order to avoid effects from changes of the local sample properties due to the high voltages. The distances could be determined from the voltages that were applied to the piezo actuator and are given relative to the defined zero-position at 3V bias voltage and 3 nA current.

By increasing the bias voltage from 3 V to 15 V, the initial tip-sample distance measured at a field emission current of 3 nA is increased by ~ 16 nm. The increase is almost linear, which means that the field enhancement for this tip at these distances is ~ 1. The measured curves decay from 3 nA to zero within several nanometers, due to the strong dependence of the field emission current on distance. For higher voltages the gradients of the curves reduce, which is in agreement with Fowler-Nordheim behaviour. This effect is caused by the higher electric field and described by the increase in the pre-exponential factor of the Fowler-Nordheim equation. For small tip-sample distances the decay length is slightly larger than the expected value of ~ 1 nm, which is explained by the limited bandwidth of our setup and the averaging that we applied.

Closed-loop

Even in controlled conditions, the unstable nature of the field emission process gives rise to high current fluctuations, especially for increasing bias voltages, as was noticed in the stability measurements from figure 5.1. Since we intend to use the field emission current as a feedback signal to control the tip-sample distance, these instabilities will cause unwanted variations in the tip position. To investigate this effect, the position signal during feedback and the (constant) emission current were measured. For this measurement a fixed-tip coated with 50 nm Mo was used in conjunction with the sample coated with Ta(10 nm)/Pt(50 nm). The tip was first brought in feedback at 3 V to maintain a constant current of 3.5 nA. This position was recorded and used as an offset value. The stability and tip position were measured for the duration of 60 s for four different bias voltages of 5 V, 7 V, 10 V and 15 V. The results are shown in figure 5.6. For the applied bias of 5.0 V the tip is raised 2.3 nm with respect to the '3 V position' and during 60 s the tip position had to be varied ± 0.7 nm to maintain the current level of 3.5 nA. Raising the bias voltage to 7 V causes an increase in the tip position to 5.5 nm with a variation of ± 1.2 nm. A further increase of the bias voltage to 10 V and 15 V leads to a change of the tip position to 12.6 nm and 22.8 nm, respectively, and a deterioration of the position stability to ± 2.4 nm. Please note that the increase in the tip position is comparable to what has been observed for the starting tip positions in figure 5.5. These experimental results confirm that although the field emission process gives rise to a highly unstable behaviour, feedback can be used to keep the emission current constant by controlling the field emitter position within several nanometers from the sample. However, for higher voltages it is found that the instabilities cause larger variations in the tip position, as is shown in the following measurement.

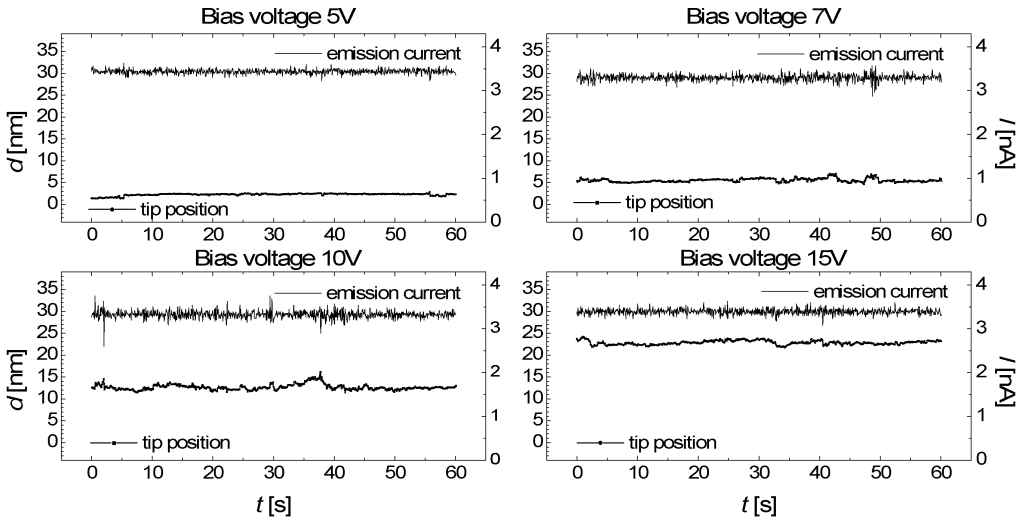

Figure 5.6: *Typical stability of the fixed-tip probe when using constant current feedback to control the tip position. The stability was measured during 60 s for bias voltages of 5 V, 7 V, 10 V and 15 V. In each graph the (constant) emission current signal and the position feedback signal is shown. For increasing bias voltage and constant emission current, the increase in initial tip position can be observed as well as the position variation due to a deteriorated emission stability.*

When using feedback to the tip position to maintain a constant current, it is possible to change the tip-sample distance by varying the applied voltage. In figure 5.7 the relationship between the applied voltage and the tip position was measured during constant current feedback for voltages up to 50 V. The current setpoint was set to 3 nA and all positions are recorded with respect to the offset value for a starting bias voltage of 3 V. The experiment is repeated four times in alternating directions: the first curve was taken by ramping up from 3 to 50 V, for the second curve the voltage was ramped down to 3 V again. This was repeated in a second measurement. While the bias voltage is ramped, the feedback loop is kept enabled, so that the tip-sample separation is adjusted in order to maintain a constant emission current. The feedback signal to the z-piezo is recorded as function of bias voltage ramp in order to obtain the required z-V curve. In the first curve, where the voltage is ramped from 3 to 50 V, the tip is retracted ~ 120 nm in order to maintain the constant current of 3.5 nA. Large stepwise changes in the tip position can be observed which limit the positioning accuracy to ± 15 nm. The position changes are caused by instabilities in the field emission current and increase at higher voltages. In the second curve, where the voltage is ramped down, the amount of instabilities seems to have reduced, but still large, instantaneous jumps can be observed. At 3 V, the tip is almost exactly returned to its starting position, indicating that no significant tip or sample damage has occurred. When this measurement was repeated a second time on the same location on the sample, the total increase in the tip position for a ramp-up of 50 V was found to be 160 nm. This value is higher than that found in the first experiment,

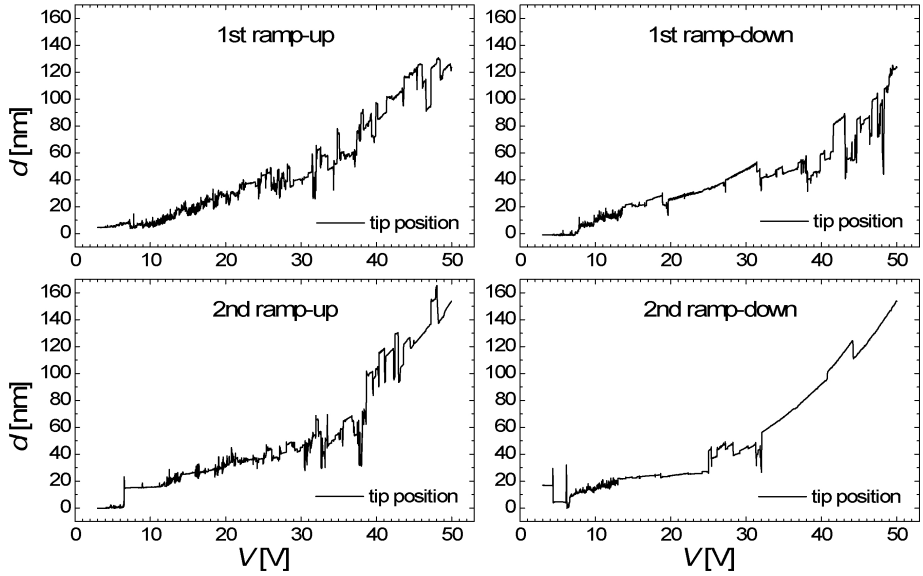

Figure 5.7: *Displacement of the fixed-tip coated with 50 nm Mo measured as function of applied voltage, in feedback to maintain a constant current of 3 nA. The experiment is repeated two times and shows an increase in the tip-sample distance of 120 and 160 nm, respectively, when ramping the bias voltage from 3 - 50 V and back.*

which is explained by a slight change in the emitter tip shape or field emission efficiency. The second ramp-down curve shows a more stable behaviour, which teaches us that the stability of the emitter can in principle be improved by repeating the experiment. This tip did not return exactly to its starting position, which indicates that the tip length has slightly changed or that there has been a minor deposit on the sample surface.

The tip position increases non-linearly with the applied bias voltage, which can be explained by the variation in the field enhancement factor. The relation between displacement and voltage is fixed by the constant electric field at which field emission takes place. With increasing voltage the tip is further retracted and the field enhancement increases, which results in a higher slope. The field enhancement effect is therefore an important factor when using field emission current to control the tip-sample distance. An elaboration on this subject will follow in the next section, where measurements obtained on AFM probes are presented.

5.2 Field emission from AFM probes

In the previous section we have shown that field emission from micromachined tips is indeed possible and can be used to control the distance between the probe tip and the medium. For the following measurements we will use AFM probes which consist of a tip on a cantilever. The typical parameters of the AFM probes that have been used are described in chapter 4. Cantilever deflection is required for read-out of magnetic forces,

but when bias voltages are applied for field emission, deflection and possibly pull-in occur due to the electrostatic interaction with the medium. This effect is investigated using the fiber interferometer setup described in chapter 3. The RHK STM is used to determine the field emission properties of these probes, by measuring the current as function of applied voltage and distance. Subsequently results are presented for the position control that can be achieved when AFM probes are used in feedback and the effect of the field enhancement on the sensitivity is discussed. For the field emission experiments that are described in this section, no coating was applied to the probe since the silicon is sufficiently doped to have good conductivity.

5.2.1 Cantilever deflection

To measure the influence of cantilever deflection during a voltage sweep we used the fiber interferometer measurement setup that has been described in section 3.1.2. The interferometer in this setup enables a sensitive and absolute measurement of the deflection. The measurements have been performed on an uncoated silicon AFM probe and a flat silicon sample coated with 50 nm of $W_{90\%}Ti_{10\%}$ was used as a counter-electrode. The probe has a spring constant of 48 N/m which should be sufficient to prevent pull-in of the cantilever according to the theoretical model given in chapter 2. Exact details on the measurement procedure can be found in section 3.2.

The measurement is started at a low bias voltage of 5 V with a constant tunneling current of 3 nA. This voltage was found to be sufficient to have stable feedback to control the tip-sample distance. During the measurement the bias voltage was increased from 5 V to 20 V while the feedback signal to the z-piezo and the interferometer signal were recorded. In figure 5.8 the measurement results are shown. In this graph, the upper curve

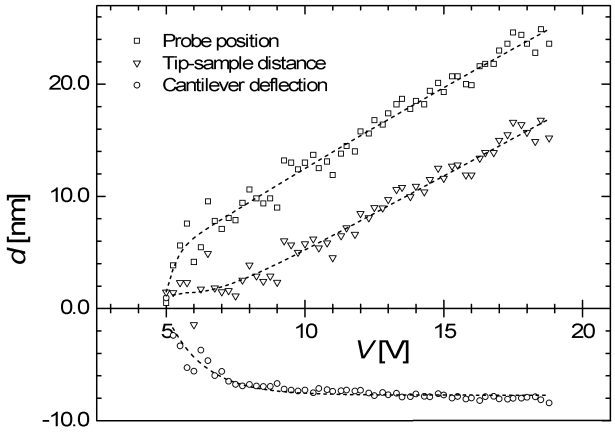

Figure 5.8: *Cantilever deflection and displacement measured for the silicon AFM probe as function of applied voltage, using feedback to maintain a constant current of 3 nA. The increase in the effective tip-sample distance is calculated by the sum of the upper and lower curve. The lines are drawn to guide the eye.*

represents the position of the probe, determined from the position feedback signal. The bottom curve gives the cantilever deflection measured by the fiber interferometer. In this measurement it was found that below ~ 10 V, the increase in electrostatic interaction starts the bending of the cantilever. With increasing voltage, the whole probe is raised due to the constant current feedback, which counteracts the electrostatic attraction between the tip apex and the sample. At higher voltage, the cantilever deflection therefore saturates to a maximum value of ~ 8 nm. This value is slightly higher than that found by the calculations in section 2.4. The difference is explained by the parameters assumed for the AFM probe: when for example the tip radius is larger then 10 nm, caused by tip damage, the electrostatic interaction increases, causing a slightly larger deflection. The importance of this measurement is that it confirms that the high spring constant (48 N/m) of the cantilever is sufficient to limit the cantilever deflection.

The resulting effective distance between the probe tip and the sample is the sum of the two curves and is also included in the figure. The measurement shows that although there is a variation in the cantilever deflection, the displacement due to the field emission effect is dominant. Please note that in the subsequent measurements, the total displacement of the probe includes the cantilever deflection. In the RHK measurement setup, we do not have the option to measure this effect. Therefore we assume that the values found with the interferometer are also valid in that system.

5.2.2 Field emission characteristics

As has been shown for the fixed-tip probes, the field emission properties for a given emitter can be determined by recording the *I-V* characteristics in the RHK STM setup. The same procedure was used to measure these characteristics for an AFM probe. First the probe was brought in tunneling, by a standard approach at 3 V bias voltage of a flat sample coated with 50 nm $W_{90\%}Ti_{10\%}$. This probe position, recorded after the feedback signal had stabilized, was used as the zero-position. The feedback loop was interrupted and by changing the initial probe-sample distance a sequence of *I-V* curves was measured. The resulting distance dependent *I-V* characteristics are shown in figure 5.9a.

The curves measured for the AFM probe are similar to those found for the fixed-tip probe. Since the silicon AFM probe is expected to have a higher resistivity compared to the metal-coated fixed-tip probe, the maximum currents in this measurement were limited to 100 nA instead of 500 nA, to assure that the sharp tip apex was not damaged by Joule heating. The probe position is raised in steps from 50 to 950 nm, increasing the voltage required to reach the emission field. The maximum voltages are higher than those needed with the fixed-tip probe. The higher work function of the silicon AFM probe is partly responsible for this, but cannot explain the differences at larger separations. Therefore we suspect that the AFM tip was slightly damaged before the start of the measurements, resulting in a lower field enhancement.

In figure 5.9b, the Fowler-Nordheim plots of the *I-V*-data are given. The lines in the figures are the results from fitting these plots using the MAPLE routine. The solid lines

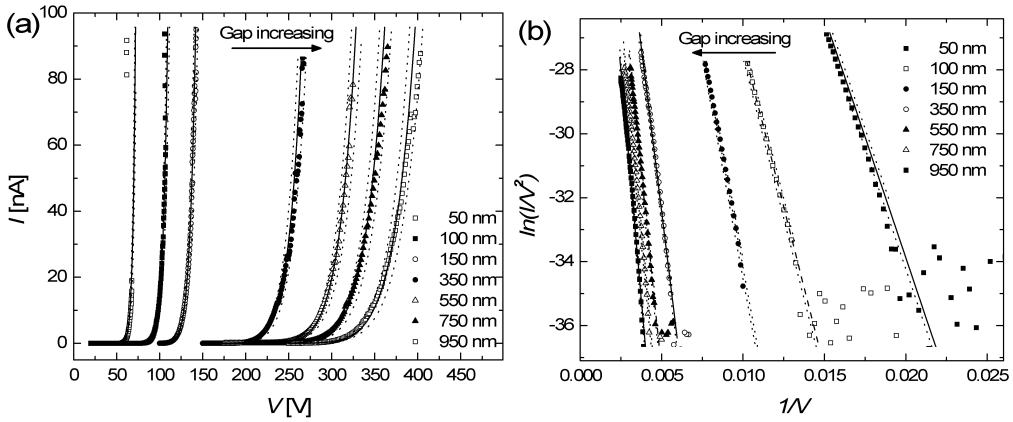

Figure 5.9: *Distance dependence of field emission in (a) I-V characteristics and (b) corresponding Fowler-Nordheim plots, measured for distances from 50 nm to 950 nm between silicon AFM probe and sample coated with 50 nm of $W_{90\%}Ti_{10\%}$. The lines in the figures are the result of fitting the Fowler-Nordheim model to the measurement data.*

represent the original fit from which the field emission parameters, the area of emission A and the field enhancement γ were obtained. The dotted lines give an indication of the influence of a variation in the emission area of $\pm 30\%$. For fitting we used the work function value of intrinsic silicon, $\phi = 4.95$ eV [99]. The used probe is n-type doped with a level of $5 \cdot 10^{18}$ atoms/cm^3 and for n-type doping a lowering of the work function is expected. A calculation for the decrease in work function is however quite complicated and has not been carried out in this work, since it is our intention to use special (metal) coatings for better current stability. In early work by Allen and Gobeli [201] it was already shown that the work function varies only from 4.7 to 4.9 eV when going from extreme n-type to extreme p-type doping, so the effect of the doping concentration on the work function may not be as large as expected. Moreover, since we cannot have an atomically clean semiconductor surface, it is expected that the work function deviates significantly from the theoretical value and is most likely higher. The used value for the work function is therefore a rather arbitrary choice, however, when choosing different values in the range from 4.0 - 5.5 eV, only small differences in the data fits are obtained, yielding similar values for the fitting parameters.

The electrostatic interaction between the AFM probe and the sample causes a deflection of the cantilever during the voltage sweep. The curves presented in figure 5.9 have not been corrected for this effect. At small distance and low voltage, the deflection will be relatively small, due to the high spring constant of 48 N/m. From the previous measurement, the total deflection at a distance of 25 nm and 20 V bias was found to be ~ 8 nm. Unfortunately, in the RHK setup we have no means of detecting the cantilever deflection. Calculations predict that for larger tip-sample distances and higher voltages, a significant deflection on the order of 10% of the initial distance can be expected. However, this is not observed in the measured I-V curves. If the deflection during

the bias sweep would play a major role, the measured curves would show a deviation from field emission behaviour. Significant bending of the cantilever during a voltage sweep will cause a decrease in tip-sample distance, causing the current to increase faster than the exponential dependence predicted by the Fowler-Nordheim model. This is not observed in the measurement results. On the contrary, the model fits the measurement data rather well. Therefore we assume that at the used distances, the deflection is relatively small and the measured curves can be presented uncorrected.

From the fits to the Fowler-Nordheim plots, the field enhancement factors have been determined. In figure 5.10 the resulting values have been plotted as function of the probe-sample distance, on a semi-logarithmic scale. The same behaviour as for the fixed-tip probe can be observed for the field enhancement factor: for small separation the value is ~ 1 and for larger distance the field enhancement increases. To analyze the obtained results, we have used the model of equation 2.20 that was obtained by finite element method simulations. The model is used to describe the field enhancement as function of distance in terms of the tip radius r and the field enhancement at large distance γ_∞. The parameter r is chosen such that the onset of the linefit from the model coincides with the first data-points. The obtained value is $r \approx 40\,\text{nm}$, which could be the tip radius of a slightly damaged AFM probe. To give a better understanding of the influence of γ_∞, three different values are used: $\gamma_\infty = 10$, 25 and 40. Note that the dashed lines corresponding to these values represent the theoretical curves that have been shown in figure 2.6. There are no measurements beyond a distance of $1\,\mu$m because of the limited z-range of the instrument. For the limited set of data, the best fit is obtained for $\gamma_\infty \approx 25$. This value for γ_∞ is lower than what is expected from equation 2.17 for an AFM tip length of $10 - 15\,\mu$m, which is explained by a deviation of the real pyramidal tip geometry from the ideal emitter sphere model that was used for the calculations.

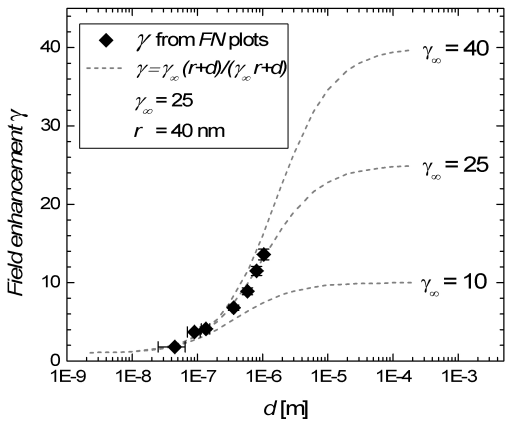

Figure 5.10: *Field enhancement factors determined for the silicon AFM probe by fitting the Fowler-Nordheim plots (Figure 5.9b), plotted as function of electrode distance. The dashed lines are the results of the model for the field enhancement of equation 2.20 using a tip radius of $r = 40\,\text{nm}$ and three values for the field enhancement at large distance $\gamma_\infty = 10$, 25 and 40.*

The probe that was used to measure the *I-V* curves of figure 5.9 could not be imaged to confirm whether the tip radius is $r \approx 40$ nm. During the handling steps of unmounting the probe from the measurement setup, the fragile probe was lost. To confirm whether damage does occur to the probes, we have imaged several other silicon and metal-coated AFM probes by SEM before and after they were used to extract field emission currents, see e.g. figures 6.14 and 6.15 in chapter 6. Various damaged probes have been observed, that showed an increase in emitter radius up to several tens of nanometers. Therefore it seems reasonable to assume that the measured probe was damaged. The results obtained with this probe give a better understanding of the field emission characteristics of AFM probes as well as the effect of probe-sample distance on the field enhancement.

5.2.3 AFM probe-sample distance control

To determine the sensitivity of control of the distance between the AFM probe and the sample using a constant field emission current, its position is measured as function of the sample bias. The feedback loop was kept enabled to adjust the probe-sample spacing and maintain a constant current of 3 nA. The feedback signal applied to the *z*-piezo was recorded while the applied voltage was ramped in alternating directions, from 3 to 40 V and back. A sequence of ten curves was measured to determine the reproducibility of this probe-sample distance control method. The resulting *z-V* curves are depicted in figure 5.11.

The measurements show that the AFM probe is retracted ~ 90 nm for the maximum applied voltage of 40 V in order to maintain a constant current of 3 nA. By comparing the curves to those obtained for the fixed-tip probe in figure 5.7, we see that the shape of the curves and the total displacements are similar. Note that for the measurements on the fixed-tip probe the bias voltage was increased to 50 V, leading to a larger total displacement of ~ 120 - 160 nm. The accuracy of positioning during a single sweep is found to be within a few nanometers. However, for low voltages the sensitivity is less and obscured by noise in the feedback signal, caused by variations in the field emission current. At higher voltages, instabilities in the field emission current cause large jumps in the probe position and limit the positioning repeatability to ± 10 nm when repeating the experiment ten times. Compared to the *z-V* curves measured for the fixed-tip probe, we see that the reproducibility is better and the instabilities are less. The reasons for this better stability are not completely understood but may be attributed to the fact that an uncoated silicon tip is used instead of a thin-film metal coating. For the fixed-tip probe, a metal coating is required because of the lower doping level of the silicon, and a comparison by current stabiliy measurents on silicon tips is difficult due to the presence of a cantilever on the AFM probes.

The influence of the cantilever deflection on the measurements can be estimated from the results obtained in section 5.2.1. These results were obtaind by using the same measurement procedure. The cantilever deflection was found to increase for low voltages and saturate to ~ 8 nm at high voltage. To correct for the effect of cantilever deflection in the *z-V* curves, we should substract this deflection curve. However, in

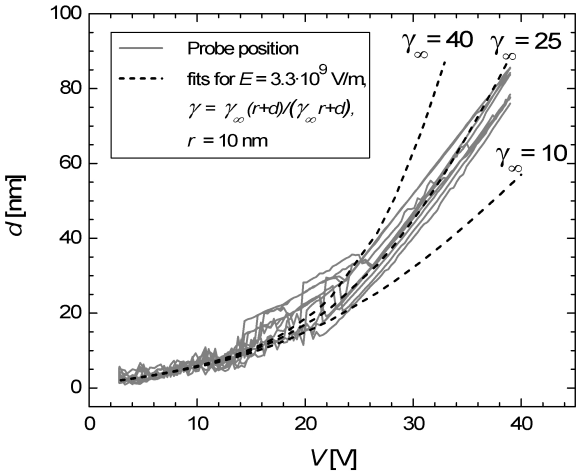

Figure 5.11: *Displacement of the silicon AFM probe measured as function of applied voltage for a constant current of 3 nA. Ten curves are presented in one plot to show that the curve shape is quite reproducible. The dashed lines are linefits that are determined by the model for the field enhancement of equation 2.20, using an emission field of* $E = 3.3 \cdot 10^9$ *V/m, a tip radius of* $r = 10$ *nm and three values for the field enhancement at large distance* $\gamma_\infty = 10, 25$ *and* 40.

the measurements we do not observe an increase of 8 nm in the probe position for low voltage. Apparently, the amount of deflection in these curves less, which may be the result of a smaller electrostatic interaction caused by a smaller (undamaged) tip radius. Therefore the measured curves are shown without correction for the deflection.

The non-linearity that is observed in the measured curves can be explained by the variation in the field enhancement factor. At low voltage, the probe is close to the sample and the field enhancement factor is ~ 1, resulting in a slow increase of the probe-sample distance with applied voltage. For higher voltages, the probe is retracted from the sample and for these larger distances the field enhancement increases. This results in a higher slope and causes a non-linear dependence in the z-V curves. The field enhancement model of equation 2.20 can be used to analyze this behaviour. The curves are measured for a constant emission current, thus the electric field at the tip apex that is required to extract this current is also constant during the measurements. The value of this field, needed for a current of 3 nA, was determined from the linefits to the I-V characteristics of figure 5.9 resulting in an average field of $3.3 \cdot 10^9$ V/m. The field enhancement model describes the relation between displacement and voltage for this constant electric field and can be used to fit the measurement data. The best fit was obtained by using a tip radius of $r = 10$ nm. Note that this measurement has been done on a different probe than the one used for the results in figure 5.10. Therefore we use a smaller tip radius, typical for an undamaged AFM probe. To determine the value for the maximum field enhancement at large distance, three values have been compared: $\gamma_\infty = 10, 25$ and 40. The dashed lines in the figure correspond to the curves that result from fitting with these values. According to this figure, the best fit is obtained for $\gamma_\infty = 25$. This value is

equal to that found from the fit to the field enhancement factors in figure 5.10. Since all experimental data can be fitted by using the same theoretical model that was developed for the field enhancement at small distances, yielding similar values for the tip radius r and field enhancement at large distance γ_∞, the experiments seem to validate that model at least qualitatively.

5.2.4 Electrical detection of the cantilever resonance

When the cantilever of the AFM probe is brought in resonance, variations in the amplitude or phase of the resonance frequency can be used to detect force with high sensitivity. In the μSPAM concept, precise determination of this frequency would permit the detection of the magnetic stray fields from the small magnetic dots. Normally an external deflection detection system is employed to measure the cantilever resonance, but in a probe recording application an integrated method should be used. If we are therefore able to measure the resonance frequency in the current signal from the probe, we would greatly extend the usefulness of the method of field emission sensing. This section describes preliminary experiments that were undertaken to achieve fully electrical detection of the cantilever resonance.

For the measurements an uncoated silicon AFM probe is loaded in the RHK STM system. The probe is vibrated by applying a sinusoidal oscillating voltage to a modulation piezo that is located under the z-piezo used for probe position control. After approach, the probe was retracted 150 nm from the sample to avoid pull-in of the cantilever and a bias voltage of 70 - 100 V was applied to extract a field emission current of several nA. During the measurement, the bias voltage had to be adjusted, to prevent instabilities in the field emission current from causing undesirably high current values. The current was measured using the RHK IVP-200 current amplifier. The signal filter of the second-stage amplifier was disabled to achieve the maximum possible bandwidth, in order to be able to detect the resonance frequency of the cantilever. The current was measured directly from the probe without 100 MΩ series resistor to avoid an electrical low-pass filtering effect. The voltage from the current amplifier was fed into an Agilent 4395A network/spectrum analyzer to measure the frequency spectrum and the phase of the current signal. A voltage of $\sim 10\,\mathrm{mV}_{pp}$ was supplied by the network analyzer to the modulation piezo and the frequency was swept with an intermediate frequency bandwidth of 30 Hz.

We successfully measured the resonance curve of the cantilever's mechanical resonance from the current signal by sweeping the frequency of the modulation piezo. Figure 5.12 shows the result that was obtained at a constant bias voltage of ~ 80 V. Note that the vertical scale of the plot cannot be interpreted as the cantilever deflection amplitude, as we do not know the parameters to convert the measured current signal to the amplitude of the cantilever deflection. We found the resonance peak to occur at $f_n = 162.25$ kHz. This value is lower than the 190 kHz that is specified by the manufacturer for resonance in air [192]. However, the resonance frequencies that we typically measure from other probes of this type are lower. A further decrease in f_n

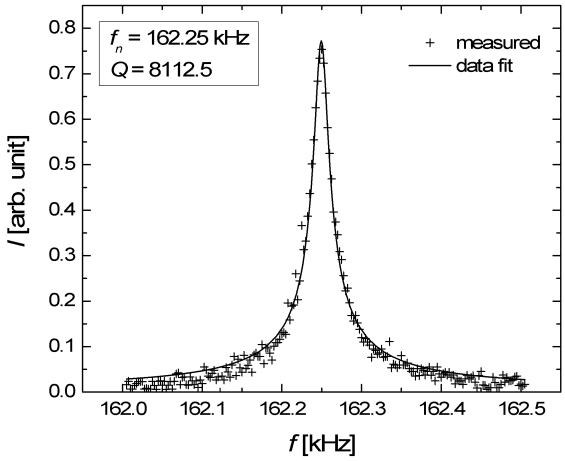

Figure 5.12: *Cantilever resonance curve obtained by electrical detection. The resonance frequency was found to be at 162.25 kHz with a quality factor of ∼ 8000, obtained by a fitting of the theoretical resonance curve.*

is observed when the voltage is increased, caused by the electrostatic forces. This decrease is due to a softening in the effective spring constant of the system and may also explain why the value of the resonance frequency is lower than that specified by the manufacturer.

For a cantilever resonating with natural angular frequency ω_n and quality factor Q, the amplitude A_0 of the cantilever vibration can be described as function of the driving angular frequency ω by the following equation [69]:

$$A_0 = \frac{F_0/m}{\sqrt{(\omega_n^2 - \omega^2)^2 + (\omega\,\omega_n/Q)^2}} \tag{5.1}$$

where F_0 is the driving force and m the cantilever mass. By fitting this relation to the measured curve, the quality factor of the resonance can be obtained. The curve fitting was done by using a Levenberg-Marquardt algorithm that was implemented in MAPLE software [202]. The quality factor that was obtained is $Q \approx 8000$, which is in rather good agreement with the expected value for the quality factor of a silicon AFM probe in vacuum at room temperature [203]. Since the measured curve corresponds well with the theoretical curve of equation 5.1, we conclude that the measurement shows the mechanical resonance of the cantilever of the AFM probe.

It is not clear how the current signal is exactly modulated by the cantilever deflection. When the probe is in resonance, the distance between the probe tip and the sample surface changes. If the tip is close and the voltage applied between tip and sample is sufficient, a field emission current will flow. However, when the tip moves away from the surface, the field emission current will decrease to zero, because of the exponential dependence predicted by the Fowler-Nordheim theory. Moreover, the current for a static deflection will not be constant, due to instabilities in the field emission current. A second possible explanation for the modulation in the current signal is the occurrence

of displacement currents. A change in the tip-sample distance generates a displacement current proportional to the capacitance between the probe and the sample [93, 204]. This current is detected by the high transimpedance amplifier that is used to measure the field emission current. Its value is difficult to calculate since we cannot define the capacitance of our system well enough. The minimum and maximum distances between the probe tip and the sample follow from the cantilever deflection amplitude, but this amplitude cannot be determined since there is no deflection detection system.

Whether the field emission current or the displacement current are responsible for the resonance curve, cannot be resolved at the present stage. Most likely the measured current is a superposition of both contributions. Clearly this result needs further study to determine the origins and possibly separate the two effects. Nevertheless, the result is promising since it provides an integrated method to determine the resonance frequency of the cantilever from the measured current, without need for a separate (optical) deflection detection system.

5.3 Discussion & Conclusions

In this chapter we showed that field emission currents from both micromachined emitter tips as well as AFM probes can be used to control tip-sample distance. By taking the fixed-tip probe and measuring *I-V* characteristics for distances varying from 12.5 - 800 nm, the distance dependence of the field emission effect could be investigated. The typical field emission parameters can be obtained by fitting the measurements to Fowler-Nordheim theory. The values for the field enhancement factor were found to vary with distance due to changes in the local geometry of the electrode configuration. For the measured fixed-tip probe, this dependence can be given by the relation found for the field enhancement factor in chapter 2 using $r = 25$ nm for the tip radius and $\gamma_\infty = 35$ for the field enhancement at large distance. The emission areas that were found correspond to an emission radius of 2.4 nm to 3.3 nm, which suggest that the emission area is smaller than the radius of the used tip.

With increasing voltage and increasing probe-sample distance, the field emission current becomes less stable. This stability can be improved by using a metal coating of Mo (fixed-tip probe) or no coating when the silicon is sufficiently doped (AFM probe). Current instabilities cause significant variation in the probe position when using feedback to the probe position. With increasing bias voltage, the variation in the probe position also increases, from ~ 1 nm for 5 V to ~ 5 nm for 10 V bias, due to a deterioration of the emission stability. To improve the tip position control, the current stability has to be improved.

By operating the AFM probe in constant current mode, it is possible to control its position with nanometer sensitivity. When increasing the applied voltage from 3 to 40 V, the probe position is raised ~ 90 nm. This includes a deflection of ~ 10 nm of the cantilever due to electrostatic interaction. Next to the material work function and area of emission that determine the field emission current, the field enhancement

factor is an important parameter for the sensitivity of this control method. The model of the distance dependence of the field enhancement also accounts for this effect and fits the measurement data for this probe when using $r = 10\,\text{nm}$ and $\gamma_\infty = 25$. It is likely that when different tips are used and there is a variation in work function, tip radius or emitter geometry, each probe will have a different sensitivity. For absolute probe-sample distance control, the probes therefore have to be calibrated separately, or the uniformity of the tip shape and conditions should be good enough to prevent this.

Although the positioning accuracy is still limited to $\pm\,10\,\text{nm}$, because of noise and instabilities in the emission current, the main outcome of the measurements is that the field emission current signal can indeed be used for position control. Moreover from the current signal the resonance frequency of the cantilever can also be obtained, which allows resonance detection without the need for an external deflection measurement system. This method therefore offers the possibility to use the mean (time-averaged) field emission current for probe-sample distance control and simultaneously measure the frequency shift of the oscillating cantilever.

Chapter 6

Scanning on patterned surfaces using field emission from cantilever probes

This chapter describes the imaging of patterned samples by STM and SFEM using cantilever (AFM) probes. As has been shown by the characterization results presented in chapter 5, field emission proximity sensing can be used to keep the probe at several nanometers above one position on the sample surface. Similar to techniques like STM and AFM, scanning field emission microscopy (SFEM) can be used to map the sample topography by *scanning* the field emitting probe relative to the sample while recording the position feedback signal. The probes that we used in our measurements are operated in the field emission mode by increasing the applied bias voltage beyond the local tunneling barrier height. By taking microscopy images of the sample surface at increased tip-sample distance we can test the suitability of this method for positioning with high lateral resolution in non-contact probe recording.

The fabrication process for the pre-patterned samples described in chapter 4 is used to produce the samples that were used for the scanning experiments presented in this chapter. The samples are characterized by AFM to obtain more information about the topography and sample roughness. As defined in section 3.2.1, the samples are first scanned in STM mode using AFM probes, at low bias voltage, as a first step towards SFEM. Subsequently, damaging effects are treated that can occur to the probe and sample when the bias voltage is increased without maximum current limitation or without proper preparation of the sample under test. At the end of this chapter results obtained by SFEM are given that are taken at increasing bias voltage and corresponding tip-sample distance. Finally a discussion on the applicability of this method is given and conclusions are drawn.

6.1 Characterization of patterned samples by AFM

In chapter 4 has been discussed that preparing samples by pre-patterning with laser interference lithography and subsequent metal sputtering provides a reliable method to obtain patterned samples with a small periodicity over a large range, a specified dot height and a low resistance. In figure 6.1 and 6.2 SEM images are shown of the samples that are used in the experiments presented in this chapter. The first image depicts the 280 nm sample which was obtained by RIE of silicon-nitride, after sputter deposition of 5 nm chromium and 15 nm platinum. The second sample with 160 nm periodicity is cut from a silicon wafer after LIL and RIE and coated with 10 nm of tantalum for adhesion and 50 nm of platinum. For more details on the fabrication process of these samples, please see section 4.2.

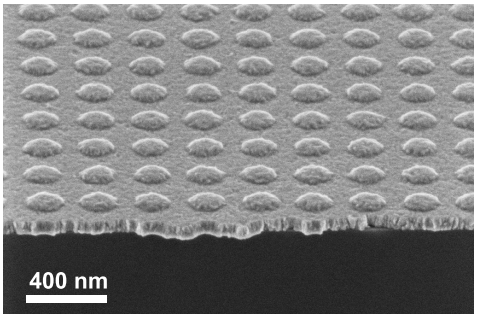

Figure 6.1: *LIL patterned sample with dots of 280 nm periodicity, 190 nm diameter and 35 nm height, coated by 50 nm Mo.*

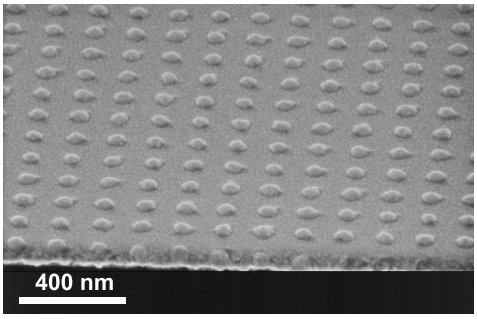

Figure 6.2: *LIL patterned sample with dots of 160 nm periodicity, 90 nm diameter and 20 nm height, coated by Ta(10 nm)/Pt(50 nm).*

Various metal coatings were applied to the patterned samples to increase the conductivity and be able to use them as an anode to extract field emission currents. Molybdenum and a tungsten-titanium alloy are considered to be most suitable, because of their low resistivity, high melting point, high tensile strength and good corrosion resistance. Next to these materials, we also used coatings of platinum on a chromium or tantalum adhesion layer.

After sputtering of the metals, the resistivity of the coated patterned samples was measured using a four point probe. The measured values averaged over the sample are compared to the bulk value for the specific resistance ρ in table 6.1. From this comparison can be concluded that the values found for the Mo (50 nm) and $W_{90\%}$-$Ti_{10\%}$ (86 nm) coating differ considerably from the bulk values whereas the Cr(10 nm)/Pt (50 nm) is in better agreement and has the lowest resistance.

AFM images were taken to get information on the sample morphology. The results are shown in figure 6.3, 6.4 and 6.5[1]. These images reveal that the molybdenum coating

[1] Image processing for the scanning images that are presented in this chapter was performed with WSXM software [205].

Coating	$R_{\square,film}$ [$\Omega/\square$]	ρ_{film} [$\mu\Omega \cdot cm$]	ρ_{bulk} [$\mu\Omega \cdot cm$]	R_z [nm]
Mo (50 nm)	15.09	75.45	5.2	~ 8
$W_{90\%}$-$Ti_{10\%}$ (86 nm)	9.97	85.75	5.49	~ 5
Cr(10 nm)/Pt (50 nm)	4.26	25.56	9.81	< 2

Table 6.1: *As deposited sheet resistances measured for the metal coatings used on the patterned samples. The films that have a higher specific resistance compared to the bulk value also have a relatively high film roughness.*

greatly increases the average roughness of the patterned sample, caused by large grains in the metal film. The sample roughness is increased with ~ 8 nm which is significant compared to the dot height of 35 nm. We expect that the higher resistivity that is found for the molybdenum film compared to the bulk value can partly be attributed to this high roughness. The granular structure is not only found when growing on silicon-nitride, but also on unpatterned silicon samples (not shown), which suggest that this behaviour is inherent to the sputter deposition of molybdenum under the system conditions that we use. The sample coated with tungsten-titanium shows a much smoother growth and smaller grain size, but the coverage of this layer over the sample is not constant. Many wide holes (dark areas) of several nanometers deep can be found at the surface of the film. This effect might be responsible for the higher resistivity that is also found for this film. The sample coated with Cr(10 nm)/Pt(50 nm) is the smoothest of the samples presented. The extra roughness induced by this coating is < 2 nm and from figure 6.5 as well as for the thinner coating in the SEM image presented in figure 4.7 can be seen that the coverage of the dots is good.

For the scanning experiments the sample roughness should be small compared to the

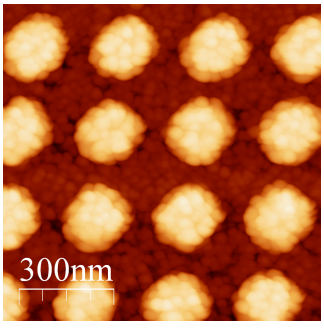

Figure 6.3: $1 \times 1\,\mu m$ *AFM image of LIL patterned sample* ($\lambda = 280\,nm$) *coated with Mo(50 nm) resulting in roughness increase.*

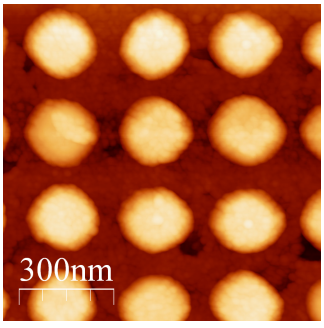

Figure 6.4: $1 \times 1\,\mu m$ *AFM image of LIL patterned sample* ($\lambda = 280\,nm$) *coated with* $W_{90\%}$-$Ti_{10\%}$*(86 nm) showing imperfect coverage.*

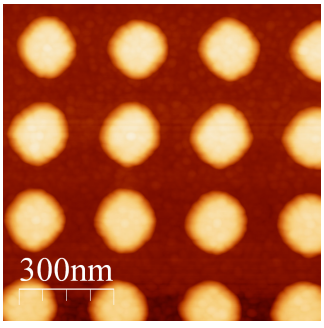

Figure 6.5: $1 \times 1\,\mu m$ *AFM image of LIL patterned sample* ($\lambda = 280\,nm$) *coated with Cr(10 nm)/Pt(50 nm) showing a smooth coverage.*

dot height. Especially when the periodicity of the patterned sample is decreased, a small grain size is required to be able to use thinner films with good properties. Moreover, to obtain a stable current during scanning it is important that the resistivity of the samples is low, also on a local scale. Incomplete coverage of the dots may cause problems and instabilities in the measured current and tip crashes when scanning in feedback. To exclude that stability issues during scanning are caused by the sample properties, we have therefore chosen to perform most measurements presented in this chapter on samples coated with a smooth Pt thin film.

6.2 STM mode imaging using AFM probes

Before using high bias voltages to extract field emission currents from the scanning probe, first imaging is done in STM mode by scanning the probe at low bias over the patterned sample. For these measururements the RHK microscope is used, that is described in section 3.1.1. Since we are using AFM probes, consisting of a tip on a flexible cantilever, this is not a trivial experiment. As has been calculated in chapter 2, the cantilever should be stiff enough to avoid pull-in before the tunneling range is reached, therefore we use AFM probes with a relatively high spring constant of 48 N/m.

To be able to accurately measure the tunneling current, the resistance of the probes was lowered by sputter deposition of a metal layer as described in chapter 4. Furthermore commercial probes with a conductive diamond coating have been used, for reasons that will be discussed in section 6.3.1. We found that also uncoated silicon probes could be used for STM imaging. When a good connection to the probe is made through the oxide layer, the doping level of the silicon is sufficient to maintain a stable tunneling current

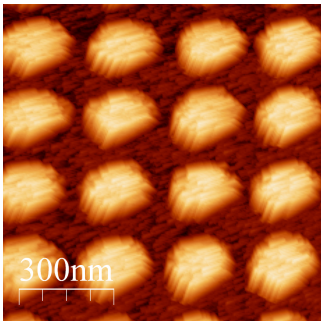

Figure 6.6: *$1 \times 1\,\mu m$ STM image (3 V bias voltage and 3 nA current setpoint) obtained by scanning an AFM probe coated with conductive diamond over the 280 nm LIL patterned sample, coated with Mo (50 nm).*

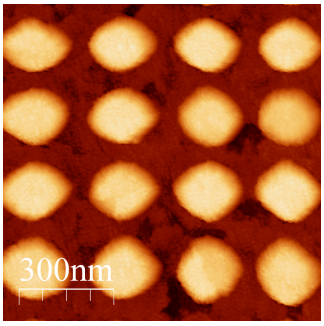

Figure 6.7: *$1 \times 1\,\mu m$ STM image (3 V bias voltage and 3 nA current setpoint) obtained by scanning an uncoated highly doped silicon AFM probe over the 280 nm LIL patterned sample, coated with $W_{90\%}Ti_{10\%}$ (86 nm).*

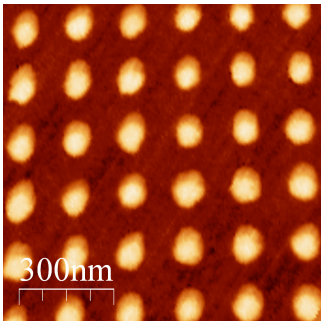

Figure 6.8: *$1 \times 1\,\mu m$ STM image (3 V bias voltage and 3 nA current setpoint) obtained by scanning an uncoated AFM probe over the 160 nm LIL patterned sample, coated with Ta(10 nm)/Pt(50 nm).*

during scanning. The best lateral resolution is obtained when using such uncoated probes, since they have a smaller tip radius compared to coated ones. Typical examples of STM images that are obtained are given in figures 6.6, 6.7 and 6.8.

The images show that tunneling from coated or uncoated AFM probes can indeed be used for STM. All images are taken at a bias voltage of 3 V and a constant current setpoint of 3 nA. These values were chosen from practical experience after conducting many scans with varying settings and give the best results when scanning on the patterned samples. Decreasing the voltage to $\sim$1 V or the current setpoint to $\sim$ 1 nA does not significantly change the imaging results obtained, but does have an effect on the control loop settings and maximum scan rate that can be used.

The first image is taken on the molybdenum-coated sample using a probe coated with conductive diamond. The smeared edges of the dots that can be observed in this image are a result of the tip shape convolution with the granular structure of the molybdenum coating. The conductive diamond coated tip has a relatively large tip radius ($r \approx 100$ nm) therefore the tip shape convolution plays an important role. In the second image an uncoated silicon AFM probe is used to scan the 280 nm periodicity patterned sample, coated with the $W_{90\%}$-$Ti_{10\%}$ alloy. Since this tip is much sharper, tip shape artifacts do not cause much distortion and the image obtained is actually in very good agreement with the AFM image of figure 6.4. The incomplete coverage of the coating can also be observed from the darker areas in the STM image. Since there are no problems with scanning near these regions, we can conclude that the local conductivity is not affected by the inconstant coverage, at least not for the used thickness. When the dot density increases, by decreasing the periodicity of the sample, the film roughness and sample coverage of the coating become more important. The third image is taken on the 160 nm periodicity patterned sample, which was coated by a layer of Ta(10 nm)/Pt(50 nm). Since this image was taken at the highest periodicity sample we have made, and does not show increased roughness or artifacts, it illustrates that Ta/Pt provides the best properties of the coating materials we tested.

Please note that the spring constant of the AFM probes used is important to be able to obtain these images. We tested this by also mounting probes with a significantly lower spring constant of 2.8 N/m. It was found that STM imaging using these probes is not possible because the probe cannot be brought in a stable feedback position. The result is that when such a probe approaches the sample surface, pull-in easily occurs. This causes an instantaneous increase in the measured current, triggering the feedback loop to retract the probe. As a result a repetitive cycle of approaching and retracting is started, causing damage to the tip. This pull-in does not occur for the high force-constant probes that were used for the measurements presented in this chapter, as long as the tunneling current is stable and the tip undamaged. These findings support the calculations presented in chapter 2; a probe with a spring constant of 2.8 N/m will pull-in before the tip starts tunneling, whereas a probe with a spring constant of 48 N/m will only deflect a few nanometers before the current set-point is reached. If however the tip radius increases due to tip damage, the capacitance of the tip apex increases and the pull-in voltage will be lowered.

6.3 Current induced damaging effects

Scanning on samples using field emission currents for positioning should not alter the tip or the surface that is scanned. However, during initial measurements was found that when the RHK system was operated in the field emission mode, significant damage can be caused to the sample and the tip. In this section an overview is given of the damaging effects that have been observed from STM results and from SEM images taken after unloading of the tip and the sample. First the effects of damage to the tip will be addressed, which occur when high currents flow due to instabilities in the small gap. Secondly the damage induced to the sample by such high current peaks will be shown. By integrating a series resistor, as has been discussed in chapter 3, the problem of tip and sample damage due to high currents can be greatly alleviated. However, even when tips with a series resistor are operated in the field emission regime, modifications of the sample surface still take place. This third effect is caused by electron-beam induced deposition (EBID) and will be discussed in more detail in the last part of this section.

6.3.1 Tip damage

When the bias voltage between the AFM probe and the sample is increased for SFEM imaging, the lifetime of the emitter tip was found to be much shortened. During scanning at increased bias, sometimes sudden peaks appeared in the emitter current that caused the feedback loop to retract the tip. When we subsequently scanned with the same tip at a lower bias in STM mode, a dramatic loss of resolution could be observed compared to the images taken before. By doing SEM analysis on these tips, the reason for this tip failure could be quickly comprehended. Figure 6.9 shows an example SEM image of a tip that was severely damaged. The tip is blunt and appears to be molten. Scanning with this tip does not allow to image the individual dots of the patterned sample. The amount of damage done to the tips is related to the applied bias voltage at the moment of failure. The tip depicted in the SEM image of figure 6.10 is also damaged, but at the moment of failure a lower bias voltage was present, so that the total damage to this tip is less. It was found that the imaging resolution of a tip quickly degrades when it is operated at bias voltages beyond 5 V. In figure 6.11 a typical STM result is presented that is obtained with the slightly damaged tip from figure 6.10. Due to the increase in tip radius and a change in tip shape, the resolution decreases and the tip-sample convolution causes the imaged dots appearing to have a larger diameter and a shape different from the real dots. When this tip is used at increased bias for a longer time, further degradation takes place, making it useless for imaging purposes.

To explain the observed effect of tip melting, several options have to be considered. The most obvious possibility is that a mechanical or current instability causes an unintended tip-sample contact during the bias-dependent SFEM measurements. Since we use AFM probes it is likely that pull-in of the cantilever can occur when the tip-sample distance is small and there is a mechanical disturbance. When the emitter tip accidentally contacts the sample surface, an unacceptably high current can flow that

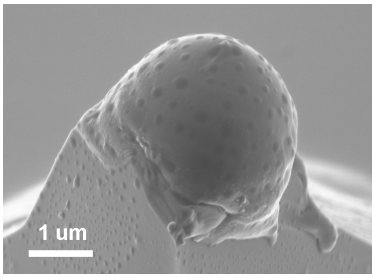

Figure 6.9: *SEM image of a silicon AFM probe that was severely damaged after a high current peak when it was operated at a bias voltage $> 50\,V$ for SFEM imaging.*

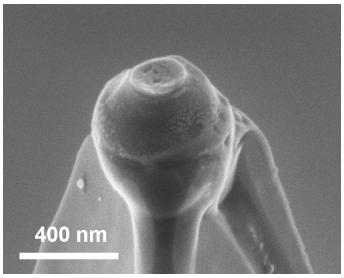

Figure 6.10: *SEM image of another silicon AFM probe that was slightly damaged by a current peak, which was used to obtain the STM image from figure 6.11.*

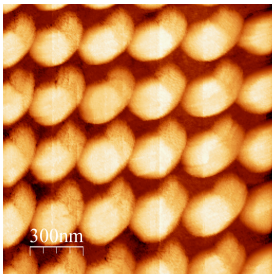

Figure 6.11: *$1.5 \times 1.5\,\mu m$ STM result obtained by scanning with a slightly damaged silicon AFM probe, showing the change in dot shape due to tip convolution.*

heats the tip and results in blunting and welding of the emitter to the sample surface. The same problem was already observed by the authors that conducted the first SFEM experiments using the topografiner and prevented them from lowering the tip-sample separation to the tunneling regime [86]. To calculate the current that is needed to start tip melting, equation 2.26 can be used. In chapter 2 it was estimated that a silicon tip with a tip radius of 10 nm will be at the melting temperature if the current density is higher than $\sim 10^{10}\,A/m^2$. For an undamaged AFM probe with this tip radius, this means that a current of $\sim 1\,\mu A$ would be sufficient. For tips with larger tip radii higher currents are needed. One can understand that when tip and sample are in contact at a relatively high bias voltage, such large currents can be easily achieved.

Another possible explanation for the melting of the tip can be a voltage breakdown as a result of a field emission initiated vacuum arc. Vacuum breakdown phenomena have been under investigation for many years [131, 197, 206, 207]. This breakdown occurs when at high current densities small asperities at the tip are heated to the melting point and create an unstable situation leading to ejection of ionizable material into the vacuum gap. Ionization of this material can eventually initiate a voltage breakdown in the form of a vacuum arc, leading to destruction of the emitter.

It may be clear that the STM images and SEM data alone, which are taken after conducting various experiments with the tips, provide insufficient information to explain exactly why the tips failed and when. The main purpose of this analysis is therefore to find a method to prevent the damage to the tip. As a first attempt to solve the issue of tip damage, we used AFM probes that are coated with conductive diamond, as described in chapter 4. The hardness of the diamond material, the low electron affinity and high thermal conductivity make the CDT probes a promising candidate to be used for bias-dependent SFEM imaging without the ill effect of tip damage. As has been shown in figure 6.6, the CDT probes are indeed capable to be used for STM imaging. The lateral resolution that can be achieved with these probes is however limited, since the

coated tips have a relatively large tip radius ($r \approx 100\,\text{nm}$). When the CDT probes are operated at increased bias they are also significantly damaged. As can be seen from the SEM image in figure 6.12, high currents can lead to rupture of the diamond coating. In the middle of the bursted tip a small cone extends, which we believe is the remainder of the molten silicon interior of the coated tip. This explains why the CDT probes fail, despite the excellent thermal properties that are provided by the diamond coating. Although the temperature at the surface coating may be well below the critical value for diamond, the silicon interior is still heated to its melting point. This generates a high thermomechanical stress inside the tip, eventually leading to rupture of the diamond coating and failure of the tip. When such a damaged CDT probe is used to scan on the patterned sample, interesting results such as in figure 6.13 can be obtained. Since the coating on the tip end has bursted into multiple parts, the remainders act as multiple tips when scanning in STM mode. These tips image multiple dots at the same time when scanning over the sample, so that we get a superposition of dot patterns measured in one STM image. Concluding we find that integration of a conductive diamond coating alone does not prevent the tip from damaging when operated at increased bias voltage.

A second approach to solve the problem of tip damage is to restrict the maximum current. The most simple implementation for this is to integrate a high value resistor in the current path to the tip. We use a resistor of 100 MΩ to limit the maximum DC current to 100 nA when a voltage of 10 V is applied. Integration of such a high resistance has a negative effect on the performance of the setup, as has been discussed in chapter 3. Since the 100 MΩ resistor together with the small capacitance of the current lead forms an electrical low-pass filter, the bandwidth of the current signal that can be detected decreases, thereby limiting the minimum response time of the feedback loop. Therefore it is important to have a capacitance as small as possible, which can be achieved by placing the resistor close to the tip.

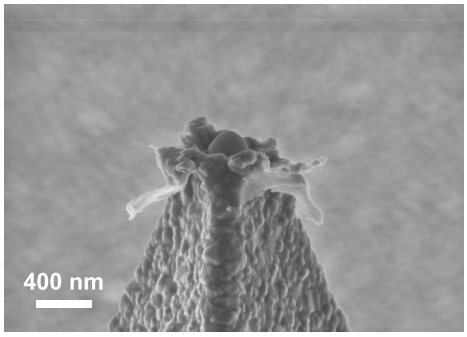

Figure 6.12: *SEM image of an AFM probe coated with conductive diamond, severely damaged after a high current peak when it was used for bias-dependent SFEM imaging.*

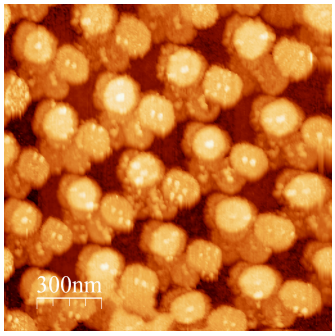

Figure 6.13: *$1.5 \times 1.5\,\mu m$ STM image obtained using the damaged CDT probe, showing the superposition of dot patterns due to the multiple tip effect.*

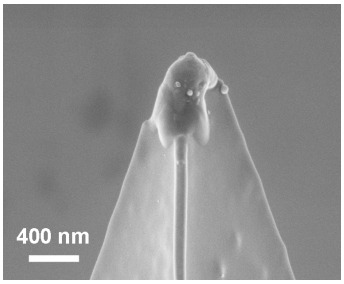

Figure 6.14: *SEM image of a silicon AFM probe after it has been used to take bias-dependent SFEM images up to 20 V, with a 100 MΩ resistor in the current lead, showing little damage to the tip end.*

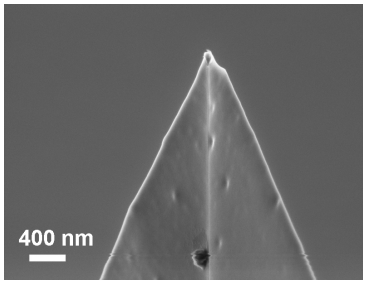

Figure 6.15: *SEM image of another silicon AFM probe after it has been used for SFEM imaging up to 15 V bias, with a 100 MΩ resistor integrated in the tip-holder, showing a tip that is almost undamaged.*

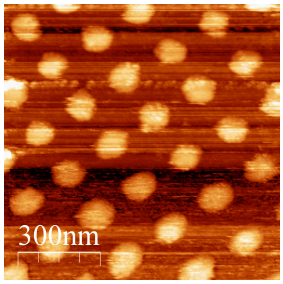

Figure 6.16: *$1 \times 1\,\mu$m SFEM image of the 160 nm patterned sample, measured at 10 V bias using the probe displayed in figure 6.15.*

We test this method by mounting a thin-film resistor in between the thin coax cable to the current amplifier and the tip connection on the STM scanner (in UHV, see figure 3.8). When this configuration is used in bias-dependent measurements, the life-time of the tips increases significantly. However, still a loss of resolution can be observed when the tips are used at bias voltages higher than ~ 10 V. Analysis with SEM taught us that the tips are still damaged, see figure 6.14. The very end of this tip is again molten, although the total damage is less than what was observed for the tips seen before. The reason for this is that although the DC current is limited by the use of a resistor, the stored energy in the capacitance of the current lead can still cause a high current peak. This electrical discharge current is not limited by the series resistor but only by the tip-sample contact resistance. For example, the contact resistance for an AFM probe with a radius of 10 nm is typically 1 kΩ. If the AFM probe is at a potential of 10 V this gives a maximum current peak of 10 mA. With a tip-sample capacitance of 1 pF, the total stored energy at 10 V is 0.5 nJ. If we assume that all this energy is dissipated in the tip apex then this would be enough to transform a sphere with a radius of ~ 100 nm silicon into 10000 K vapor. By lowering the power dissipation, the total damage to the tip can be decreased. As a consequence, a smaller capacitive load to the tip is needed to have less damage.

In an attempt to further lower the capacitance of the current lead, we used the tip-holder that was especially designed to integrate the 100 MΩ resistor, shown in figure 3.9. When using this tip-holder to scan at increased bias, the tip life-time can be further increased. Figure 6.15 shows a SEM image of a silicon tip that was used in conjunction with the 100 MΩ resistor on the tip-holder. This image was taken after performing the same type of bias-dependent measurements as have been done for the tip from figure 6.14. As is clear from the comparison of these images, the tip damage can be decreased by mounting the series resistor as close to the tip as possible. The SFEM image presented in figure 6.16 was taken at 10 V using the AFM probe mounted on the special holder. Since the scanned sample has a 160 nm periodicity, from this image

can be concluded that the tip shape is very well preserved during scanning at 10 V bias voltage and provides sufficient resolution to image the dots. The lines in the SFEM image originate from a variation in the feedback position offset of several nanometers, presumably caused by instabilities in the field emission current.

6.3.2 Sample damage

Preventing damage to the sample surface is as important as for the emitter tip, in order to be able to obtain reproducible results. In our experimental setup, we have the advantage that if the sample region under the tip is damaged, a new position can be chosen using coarse approach. Obviously in a probe recording system, this will not be an option and the recording medium has to be preserved. When high currents cause damage to the emitter tip as described in the previous section, damage to the sample surface is likely to occur. Normally the tip and the sample are damaged at the same time, so that imaging of the damaged region using the same tip is not possible. In figure 6.17 however, the sample could be imaged after a discharge event had been registered at 50 V bias, using the same tip with sufficient resolution. The sample that was affected here is the 280 nm SiN patterned sample coated with Cr(5 nm)/Pt(15 nm). At the position of discharge, a pit has formed that is surrounded by a rim of material. The SEM image of figure 6.18 shows an example detail of the same sample from which it is clear that the observed rim is the result of melting of the Cr/Pt film. The underlying patterned SiN film is exposed and damaged such that a crater has formed. These images make it clear that if the discharge current is uncontrolled, resistive heating of the sample causes melting of the metal coating and even vaporization of the underlying patterned substrate.

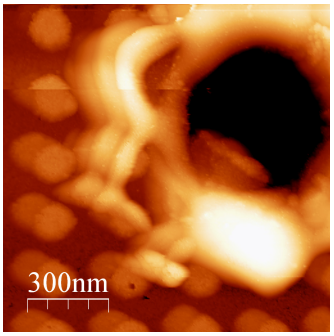

Figure 6.17: *$1.5 \times 1.5\,\mu m$ STM image obtained using a CDT probe, showing the damage to the 280 nm patterned sample after a discharge event at 50 V bias.*

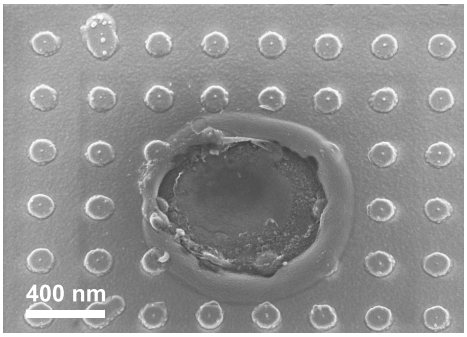

Figure 6.18: *SEM image of detailed damage caused to the patterned sample by an uncontrolled maximum discharge current. The Cr(5 nm)/Pt(15 nm) film is locally removed and a crater has formed into the silicon-nitride film.*

To restrict the damaging effects to the sample surface, the current is limited by a 100 MΩ resistor as introduced in the previous section. First a resistor was mounted

outside the UHV system in between the vacuum feedthrough connector and the current amplifier. In figure 6.19, a $1.5 \times 1.5\,\mu$m STM scan is given that was measured at 3 V bias after scanning an area of $1 \times 1\,\mu$m at 10 V bias using this configuration. It can be clearly observed that the area in the middle of the image that was scanned at increased bias is damaged. A surface profile of this measurement taught us that the middle area is ablated with indentations up to 25 nm.

We suppose that this ablation effect is the result of high current peaks caused by instabilities in the field emission current or in the probe-sample distance. Since we use AFM probes, mechanical instabilities or instabilities in the field emission current may cause frequent pull-in of the cantilever. If at increased bias the tip repetitively contacts the sample when scanning over the surface, at each intermittent tip-sample contact a capacitive discharge takes place. The discharge current causes sample and tip damage and instabilities in the field emission current, leading to the next pull-in. This means that the field emission current will not be stable enough to maintain a constant tip-sample distance and the repetitive discharges will cause damage to the whole scanned region. We observe that the current indeed fluctuates considerably when scanning at a higher bias, but since the bandwidth of the current signal is decreased by the low-pass filtering effect of the resistor and cable capacitance network, the occurrence of discharge peaks cannot be detected. Another factor which could explain the ablated region in the sample is the mechanism of vacuum discharges, as described in the previous section. The formation, heating and evaporation of small protrusions on the emitter tip can cause an instantaneous increase in the emission current leading to a plasma discharge.

Current-controlled electrical discharges have been studied also by others. Van Patten *et al* purposely created nanoscale discharges using STM tips to create a plasma plume of sample material and analyze the material composition using a this with a spectrometer. Electrode gaps of less than 10 nm and nanosecond-long pulses of 10 - 100 V resulted in ablated pits of the order of 100 nm in diameter [208, 209]. Also Farson *et al* studied the formation of electrical discharges, using voltages from 10 to 100 V and regulated currents from 35 μA to 2 mA at gaps from 20 to 750 nm [210]. From these studies can

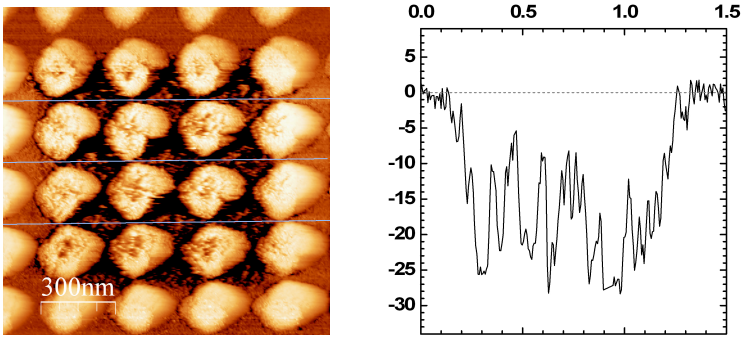

Figure 6.19: *1.5x1.5 µm STM scan of the damage region induced to the patterned sample by high field emission current peaks after scanning the center area at 10 V bias voltage. Surface topography profile is an average of the three lines indicated in the image.*

be concluded that the amount of charge stored in the effective capacitance of the tip is responsible for the amount of material that is ablated.

Our measurements are in agreement with these findings. The damage done to the sample is largely dependent on the capacitive load to the emitter tip. The results shown above were obtained with the 100 MΩ resistor mounted *outside* the UHV system, so that an extra capacitance of ~ 50 pF is added to the tip, determined by the thin coax cable. The capacitance can be decreased by mounting the 100 MΩ resistor closer to the field emitter probe or on the tip-holder. This lowers the maximum power dissipation at a given bias voltage and greatly reduces the damage to the sample.

6.3.3 Carbon deposition

By integrating a 100 MΩ resistor in the current path close to the emitter tip it is possible to limit the maximum discharge currents that damage the probe and sample. However, when sample ablation is prevented during scanning at increased bias, another effect is observed that causes modification of the sample. In figure 6.20 a $1.5 \times 1.5\,\mu$m scan is given that was measured after an area of $1 \times 1\,\mu$m was scanned at 15 V bias voltage. In this image scan the $1 \times 1\,\mu$m area in the middle of the image has a higher apparent topography compared to the surrounding area. The topography profiles that were taken indicate an average topography increase of ~ 5 nm. This is explained by deposition caused by field emitted electrons that dissociate adsorbed hydrocarbons on the sample surface [211].

To exclude that we measure a change in the local electronic properties, the fiber interferometer AFM setup (see section 3.1.2) was used to further investigate this effect. Since this system has a interferometer deflection detection system, a truly topographic image of a deposit can be obtained, see figure 6.21. This AFM image shows the result after the probe was scanned at increased bias only for a single line trace. During this trace a constant current of 3 nA from the tip was maintained, while in 30 s the bias voltage was ramped from 20 V down to 3 V and back. This resulted in material deposition up

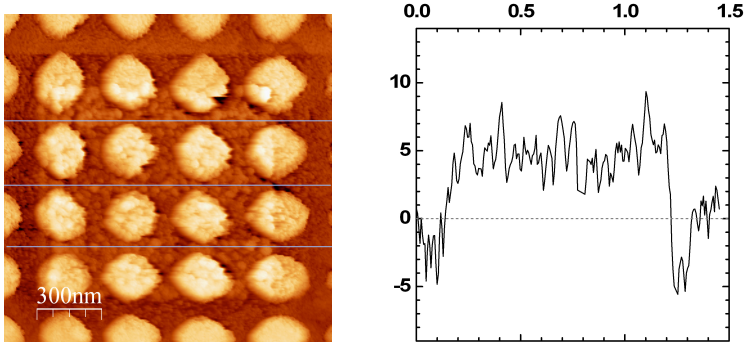

Figure 6.20: *1.5x1.5 µm scan (voltage 3 V, current 3 nA) of the patterned sample after scanning the middle area at 15 V bias voltage, showing the field emission induced deposition that has taken place.*

to $\sim 70\,\text{nm}$ high. From this measurement can be concluded that when the sample is scanned at high bias voltage, the topography increase is the result of material deposition. With the fiber interferometer it is possible to measure the surface topography with great accuracy, therefore we use the found values to derive an approximation of the deposition rate. By image analysis it was determined that the total volume of the deposited material is $\sim 2.8{\cdot}10^6\,\text{nm}^3$, so the deposition rate is approximately $1 \cdot 10^4\,\text{nm}^3/\text{s}$. This deposition rate depends on the applied voltage and is smaller for lower voltages.

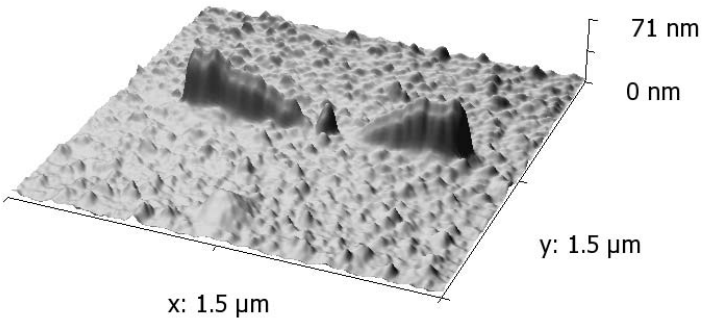

Figure 6.21: *AFM image of deposits induced by field emission currents. Lines were deposited by scanning the biased AFM probe in non-contact while ramping the voltage from 20 V down to 3 V and back.*

Electron beam induced deposition (EBID) of carbon material is a well-known effect in the field of scanning electron microscopy (SEM). When the electron beam is focussed on a substrate surface, adsorbed hydrocarbons on the sample surface can be dissociated into volatile and non-volatile parts. Non-volatile products of this process adhere to the substrate, and as a result, a deposit grows at the spot of the electron beam [212]. Ruhrig *et al* [213] have used this concept to fabricate carbon deposited needles that can be used for magnetic force microscopy when an appropriate magnetic thin film is applied. They found a deposition rate of $\sim 300\,\text{nm}^3/\text{s}$, but used a much higher beam emission current of $110\,\mu\text{A}$ and even supplied a droplet of oil close to the sample to increase the deposition rate.

It is surprising that the carbon deposition that is found in the bias-dependent SFEM experiments seems to be much more effective than what is achieved in a SEM. To explain the high deposition rate that is calculated for the SFEM experiment, we speculate that the electron beam energy that is used in our setup is better matched to what is required for dissociation of a hydrocarbon molecule. The deposition rate is related to the dissociation cross section of the electron. From calculations on the irradiation of hydrocarbon films, it is found that the dissociation cross-section shows a maximum in the 10 - 100 eV regime and is negligible for incident electron energies below 10 eV [214]. Since the dissociation cross-section peaks at low electron energies, in SEM therefore the secondary electrons are likely to be the main cause of deposition rather than the primary electrons [215]. This also explains why the lateral size of the features fabricated by EBID considerably

exceeds the diameter of the electron beam spot: lateral broadening occurs when the secondary electrons are emitted from the substrate that is irradiated by the primary electron beam. For SEM the electron beam induced deposition rate is thus dependent on the generation of secondary electrons and significantly lower than the primary electron beam current.

The beam energies that have been used in our setup for bias-dependent SFEM measurements are determined by the bias voltage only and thus range from 3 to 50 eV. These energies are close to where the hydrocarbon dissociation cross section has a peak. Therefore in the presented measurements the dissociation of hydrocarbons is done very effectively and the deposition rate is determined by the (primary) electron current density. This might explain the very high electron beam induced deposition rates that are found in the bias-dependent SFEM experiments. In figure 6.21 we observe less deposition for voltages below 10 V and this matches with the energy threshold of 10 eV that is the minimum energy needed for hydrocarbon dissociation. In order to prevent carbon deposition, we therefore have to operate the instrument at voltages below 10 V. In order to prevent carbon deposition for higher voltages as well, it was found that the amount of hydrocarbons on the sample can be reduced by heating the samples just before use in situ to about 300 °C for about 1 hour.

6.4 Bias-dependent SFEM imaging

By increasing the applied bias voltage beyond the local tunneling barrier height, the RHK microscope can be operated in the field emission regime. The results presented in chapter 5 showed that by doing so, the tip-sample separation can be increased to several tens of nanometers from a single lateral position on the sample. This does not automatically mean that this tip-sample distance can also be maintained when scanning the probe at increased bias. As instabilities in the field emission current limit the vertical positioning accuracy, it is very likely that during scanning, changes in the local conditions between tip and sample affect the field emission current and cause large variations in the tip position or even a tip crash.

SFEM is a technique known for a long time, but not many results have been published that show images taken at increased bias voltage. The first results that were obtained using the 'Topografiner' (see chapter 1) at a bias voltage of 46 V, show a vertical resolution of about 3 nm and a lateral resolution of about 400 nm [86]. Later efforts using SFEM for mapping of the local field enhancement [216] and e-beam lithography [217] show images with similar resolutions. The lateral resolution of these results is thus worse compared to STM, which is caused by the tip-sample separation being larger than for the tunneling regime and the use of relatively blunt tips ($r > 200$ nm). We intend to achieve a lateral resolution on the nanometer level by using sharper tips and scanning with better current stability. The resolution strongly depends on the tip-sample separation, since the field strength at the emitter surface is a function of the average distance to the sample surface; as the emitter is moved away from the surface, the area of the sample over

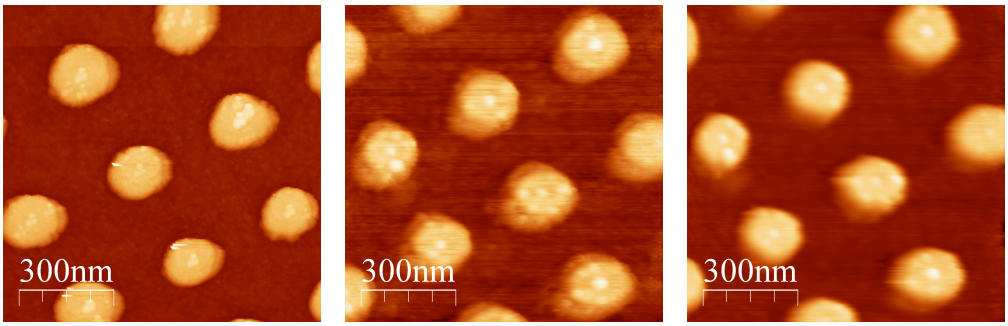

Figure 6.22: *$1 \times 1\,\mu m$ bias-dependent SFEM images obtained by using an AFM probe coated with 20 nm Cr on the 280 nm LIL patterned sample coated with Cr(5 nm)/Pt(15 nm). The bias voltage is raised from 3.0 V (left), 20.0 V (middle) to 50.0 V (right) to increase the tip-sample distance while maintaining a constant current of 0.3 nA.*

which the average is taken increases. The effect of resolution loss should thus be more pronounced for higher bias voltages, when the tip-sample separation is larger.

We tested the applicability of SFEM for high-resolution imaging by scanning on the patterned sample for varying bias voltages. The results are shown in figure 6.22. Here the patterned sample with 280 nm periodicity, coated with Cr(5 nm)/Pt(15 nm) is scanned using an AFM probe coated with 20 nm of chromium and a tip radius of ~ 20 nm. The figure shows $1 \times 1\,\mu$m scans using 3.0 V, 20.0 V and 50.0 V bias voltage, respectively, at 0.3 nA current setpoint.

For the left image, a bias voltage of 3.0 V is used to obtain an STM image at a scan rate of 333 nm/s. It was not possible to scan faster without causing unwanted tip-sample contacts, since we are measuring on a relatively rough sample with dots of 35 nm height. As can be seen from the bright spots at the top side of some of the dots, at these settings the tip occasionally touches the dots and the feedback loop had to retract the tip to compensate for a current peak.

In the middle image, the probe is operated in the field emission regime using a bias voltage of 20.0 V. According to the measurements given in section 5.2.3, such a bias voltage would result in a tip-sample distance of $15-20$ nanometers. This is in agreement with the reduction in resolution that we observe.

In the right image, the bias voltage is further increased to 50.0 V to increase the tip-sample distance. In the z-V measurements presented in chapter 5, the AFM probe was retracted ~ 90 nm when the applied voltage was increased from 3 to 40 V. Since the current SFEM measurement is done with a less sharp (coated) tip with a lower field enhancement, the total increase in tip-sample distance will be smaller, but is still expected to be several tens of nanometers. To obtain the image the scan rate could be increased and the highest rate that was tried is $4\,\mu$m/s. The high scan rate indicates that the tip-sample distance has indeed increased such that the tip cannot touch the side of the dots while scanning. This means that the distance at which the tip is scanned is at least larger than the height of the dots (~ 35 nm).

The three images have been taken using the same tip on the same sample. If we

compare the images, clearly a loss of resolution can be seen with increasing bias, which is an indication for the increasing separation. Note that for the last image, the scanning rate has been changed, making further analysis on the lateral resolutions for the three images difficult. A slight change can be observed in shape of the imaged dots between the first and the other two images. Our interpretation is that the slight elongation of the dots in the second and third image are caused by the tip shape. It is possible that the tip has been slightly damaged in between the measurement of the first and second image, causing a change in tip convolution.

The higher scan rate settings that are possible in SFEM also enable larger scan areas compared to STM at moderate imaging times. By adjusting the bias voltage it is therefore possible to scan at increased distance and quickly image a large region to get an overview of the sample topography and then zoom in to plot a detailed map. In figure 6.23 this feature has been illustrated by showing image scans of $5 \times 5\,\mu$m, $2 \times 2\,\mu$m and $1 \times 1\,\mu$m, taken at a bias voltage of 10 V and scan rate of $4\,\mu$m/s. Even for the large area scan of $5 \times 5\,\mu$m, the total time needed to obtain the image could be limited to 5 minutes.

Unfortunately, after taking these measurements, the tip was damaged and therefore it was not possible to do further analysis on the resolution loss or on the relationship between bias voltage and tip-sample distance for this specific tip.

Although the lateral resolution for these SFEM images decreases with increasing tip-sample distance, even for the image taken at 50 V bias the resolution is better than ~ 20 nm, as can be determined from the small features on top of the imaged dots. The measurements show that for this tip-sample configuration the lateral resolution at increased bias is at least sufficient to track the individual dots and give better results than earlier SFEM results presented by others. This resolution is important when we intend to apply this technique on a future recording medium with even higher dot densities. Moreover, the maximum scan rate that can be achieved when scanning over a patterned medium can be increased significantly compared to STM by increasing the tip-sample distance. The results presented in this section therefore are promising for the application

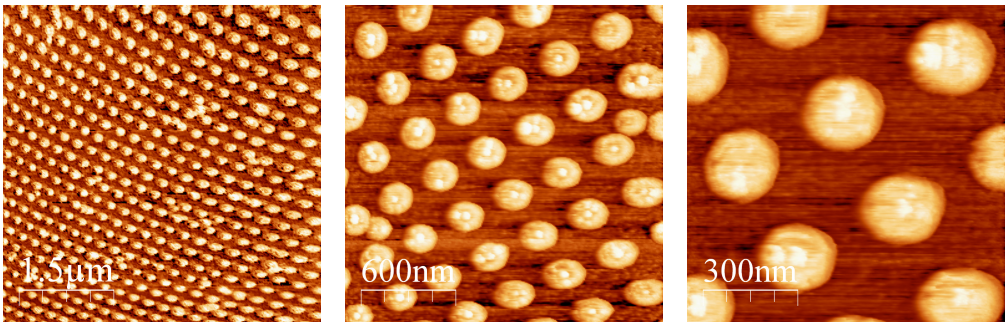

Figure 6.23: *SFEM at 10V bias (constant current 0.3 nA) using a scan rate of 4 µm/s to scan area's of $5 \times 5\,\mu$m (left), $2 \times 2\,\mu$m (middle) and $1 \times 1\,\mu$m (right) of the 280 nm LIL patterned sample coated with Cr(5 nm)/Pt(15 nm).*

of field emission proximity sensing in non-contact probe recording. However, it has proven to be difficult to repeat these measurements on a common basis and obtain similar resolutions. The causes for this are the inherent instability of the field emission current and the damaging effects to the tip and the sample that are described in the previous sections.

6.5 Discussion & Conclusions

In this chapter, we have presented the problems and results that are obtained when AFM probes are operated in the field emission regime and used to scan in non-contact on a patterned sample. To test this technique for imaging, we made several types of patterned samples by laser interference lithography. This fabrication method has proven to be very suitable to produce samples with a high periodicity dot pattern over a large surface area. To improve the conductivity of the samples, we used various metal coating materials: molybdenum, tungsten-titanium and platinum. Characterization by AFM and four-probe resistance measurements has taught us that the coatings of molybdenum and tungsten-titanium have a relatively high film roughness and a high specific resistance compared to the bulk value. Especially when the periodicity of the patterned sample is decreased, a small grain size is required to be able to use thinner films. A coating of platinum on an adhesion layer of tantalum or chromium provides these properties and gives a very smooth layer with good coverage of the dots.

AFM probes can be used for STM imaging on the coated patterned samples. In the STM mode we used a bias voltage of 3 V and a tunneling current of 3 nA. The images obtained are very similar to the AFM images used to characterize the samples and prove that a conducting patterned surface can be scanned in non-contact using cantilever probes, without external deflection detection system. In our experiments probes with a 48 N/m spring constant could be used to obtain STM images on a standard basis, whereas probes with a spring constant of 2.8 N/m were found incapable. This is in agreement with the calculations in chapter 2, that showed that a high enough spring constant is required to avoid pull-in of the cantilever before the tunneling range is reached. The resistance of the probes was lowered by using a metal or conductive diamond coating. The coatings increase the tip radius and consequently the image resolution, due to tip-sample convolution effects. It was found that probes without coating could also be used for STM, as long as a good connection to the probe tip is made by scratching through the silicon-oxide layer before applying silverpaint as an electrical connection to the probe. They provide a better lateral resolution compared to the coated probes.

A drawback of the method of using field emission currents during scanning is that several damaging effects take place: ablation of the tip and sample surface due to high current peaks and the effect of field emission induced deposition. The ablation effect is caused by high current peaks between the tip and sample. The most obvious explanation for these peaks is a mechanical contact between the tip and the sample due to mechanical or current instabilities. The current peaks are the result of an electrical discharge and

cause melting and evaporation of tip and sample materials. A field emission initiated vacuum arc can also occur when material in the vacuum gap is ionized leading to a voltage breakdown.

To eliminate the observed damaging effects it was found that integration of a high value resistor in the current path greatly reduces the tip and sample damage induced. The value of the resistor should be high enough to prevent large currents at the high voltages that are used. In our measurements we used a resistance of 100 MΩ to limit the DC current to 100 nA when a voltage of 100 V is applied. This resistor should be placed as close as possible to the emitter end to reduce the effective capacitance of the tip. Since the total power that can be dissipated at an electrical discharge is dependent on this effective capacitance, it should be minimized to reduce the damage done. When the resistor is not placed close enough to the tip end, still erosion of the sample takes place when scanning at increased bias. Therefore we used a special tip-holder with the resistor integrated and showed a drastic increase in the tip and sample life-time.

A better option to limit the maximum current between tip and sample would be to increase the contact resistance by using a sample with high resistivity. This would prevent high currents to flow when there is a capacitive discharge between the emitter and sample. The resistive effect could also be integrated into the probe tip, to further lower the capacitive load. It should be noted that although the damage through tip and sample melting may be much better controlled, tips and sample are also damaged by mechanical contacts when there is a instability. Such contacts can be prevented by using vibration isolation and very stable field emission currents, but also by increasing the tip-sample distance such that the variation in tip position due to instabilities cannot result in tip-sample contact.

The integration of a high value resistor in the current path of the field emitter also has an effect on the stability of the emission current. The resistor together with the impedance of the vacuum gap acts as a voltage divider. When the emission current largely fluctuates, the voltage over the resistor and consequently the voltage between tip and sample changes, counter-acting the current fluctuation. Thus the integrated resistor acts as a buffer and stabilizes large fluctuations in the emission current. For this reason, buffering resistors have been used for example in field emission arrays for displays [218]. For many applications however, the use of resistors is not acceptable, as they introduce an energy spread in the emitted electron beam [139]. In our setup, we expect that the buffering effect of the resistor is negligible because of the low currents used for scanning; for a current setpoint of 3 nA, the voltage drop over the resistor is only 0.3 V. The limitation to the bandwidth of the current signal is more important. With the low capacitance and relatively low scan rates, in the current setup this is not a serious issue. However when resonance detection is required or when a parallel probe array is used that should be operated at higher speeds, this should be re-considered.

Electron beam induced deposition (EBID) is another problem that occurs when the probes are used for SFEM. The dissociation of adsorbed hydrocarbons on the sample surface by the field emitted electrons is responsible for deposition of carbon-like material. This deposition effect causes not only modification of the scanned area,

but can also affect the stability of the field emission current signal, when scanning over such areas. It was observed that the deposition rate during SFEM is higher than what has been reported on the EBID effects in scanning electron microscopy. This higher rate is attributed to the fact that compared to SEM the energy of the electron beam that is used during our experiments is better matched to the energy that is required for dissociation of the hydrocarbon molecules. To prevent this, the adsorbate film that contains the hydrocarbons should be removed from the sample surface. Therefore in our experiments, the field emitter probes and counter-electrode sample have to be annealed before use and operated in an oil-free vacuum system that is frequently baked to maintain the necessary vacuum conditions.

An AFM probe can be operated in the field emission regime to do scanning field emission microscopy (SFEM). By increasing the applied voltage up to 50 V, and changing the tip-sample separation accordingly, images were obtained taken at increasing tip-sample gap distances. Although the noise levels increase due to instabilities in the field emission current, the signal is sufficient for stable operation. As a result of the tip-sample separation becoming larger, the lateral resolution reduces, but in our measurement at 50 V the resolution was still sufficient to detect features of ~ 20 nm on the sample. At low applied voltage, so at small tip-sample distance, the maximum scan rate was limited due to unwanted tip-sample contacts occurring at the edges of the dots. Scanning at higher voltage allowed much higher scan rates, which makes it plausible that the tip-sample distance has increased beyond the dot height of 35 nm. The obtained results are important for the suitability of field emission sensing in non-contact probe recording since they show that this method can indeed be used to control the tip-sample distance with high lateral resolution.

Chapter 7

Summary and conclusions

The aim of the work presented in this thesis is to investigate the applicability of field emission for probe-medium distance control in a probe recording system. The relevance and the results of this investigation are strongly related to the concept of non-contact magnetic probe recording that is proposed in the μSPAM project. Therefore in this final chapter, the main theoretical and practical results reached within this thesis will be summarised and discussed in relation to the intended application. The focus will be on what the requirements and limits are for the system conditions, field emitter probes and media in such an application. At the end of this chapter, the main conclusions and recommendations for future research will be given.

7.1 Requirements for non-contact probe recording

The main motivation to start our research on field emission sensing is its potential application in the field of probe recording. The advantage of the probe recording architecture is that an array of parallel probes and mechanical addressing scheme can be used to write and read in the storage medium. This allows to make a trade-off between data-rate, access time and power consumption for specific applications by using more or less of its probes operating in parallel. It provides good specifications in between the two main technologies for information storage: random access memories like FlashRAM and mechanically addressed devices like hard-disks. To be able to compete with current technologies, several requirements have been discussed that a probe recording system should fulfil. Ultra-high data densities ($> 1\,\mathrm{Tbit/in^2}$) are needed to achieve a large storage capacity ($> 10\,\mathrm{GB}$) when used in a small form factor device like a memory card. To ensure sufficient data rate, parallel writing and reading by an array of probes has to be used. The data-rate per probe should be several kbit/s, which means that a scan rate on the order of 1 mm/s is needed during writing and reading. It should have a low power consumption ($< 1\,\mathrm{W}$) in order to be useful in portable applications. Because of its high storage density, the system is also a possible candidate for archival and backup

applications. By increasing the size of the storage medium and using parallel operating storage clusters integrated in a single package, ultra-high capacities ($> 10\,\mathrm{TB}$) can be obtained in a relatively small product size. Low cost, long media and system lifetimes are important as well as a high data rates suitable for such applications.

The most important benefit of using probes to store information is that the knowledge gathered in the field of scanning probe microscopy can be applied for recording technology. The use of probes for storage offers a potential for scaling beyond the limits envisaged for hard-disk recording and FlashRAM, down to the nanometer or to the atomic scale. This opens up a path that might ultimately lead to molecular or even atomic storage. To reach these densities, individual control over the position of the probes is essential, to be able to operate them in non-contact. This is necessary to prevent wear of the probe tip and the recording medium and to allow surface modifications with atomic resolution, which is exclusively limited to non-contact methods like STM. For non-contact operation, individual z-feedback should be achieved by integration of an actuator, proximity sensor and feedback loop for each probe of the probe array. Whereas integration of actuators and logic circuitry in probes has already been shown, a proximity sensor with sufficient lateral resolution that can be integrated in each probe is not yet available.

Several transducer principles have been discussed that can be applied for proximity sensing using probes. The principles discussed are based on the different interactions between probe and a medium: optical near fields, capacitance changes, thermal conductance, force dissipation and tunneling and field emission currents. The relative merits and limitations of these interactions were judged on several criteria relevant for integration in a probe recording system. Using field emission as a sensing principle to detect the probe-medium distance was found to provide the most elegant method since it has several advantages over other methods. The lateral resolution is determined by the probe tip radius, providing a resolution on the same order as the targeted bit sizes for the first generation probe recording systems ($< 25\,\mathrm{nm}$). The vertical range of interaction is in the same regime, which makes it very suitable to operate a probe at several nanometers from the medium, where van-der-Waals forces are low and mechanical interactions can be prevented. The difficult problem of sensor integration is smoothly solved since only one wire per probe is needed to connect to the tip, that is used as a field emitter itself. Moreover the measured current signal is largely temperature independent and the critical interaction area can be very small without sacrificing sensitivity or signal-to-noise. Since the principle of field emission sensing seems to comply with most of the stringent requirements needed for non-contact probe recording, we have concentrated our research on this method.

7.2 System conditions needed for field emission sensing

From the development of field emitters for practical applications such as field emission displays or electron beam sources for electron microscopy, it is well-known that achie-

ving good current stability is the major challenge. In this work the unstable behaviour of the field emission process is the main limiting factor and greatly reduces the sensitivity and reproducibility of the measurements. To alleviate the problems caused by the current instabilities, in our experiments the field emitters have been operated under special environmental conditions. A UHV scanning probe microscope was assembled and used to measure field emission characteristics and provide more insight in the vacuum conditions, field emitter materials and electronics needed for stable operation of field emission distance control. Although it will be difficult to achieve the same conditions in a practical probe recording system, there are possibilities to use e.g. vacuum packaging for MEMS devices. Below the main requirements on the system conditions needed for field emission sensing that follow from our work will be discussed.

7.2.1 Vacuum conditions

The field emission experiments have been carried out in ultra-high vacuum to minimize the possible effects of current instabilities on the sensing performance. Vacuum conditions are at least necessary to have a sufficiently large mean free path for the electrons. However, for field emitter applications a better vacuum is required to prevent bombardment of the tip surface by ions that are accelerated towards the tip. This ion bombardment causes sputtering of the tip and is believed to be the main cause for field emission current instability. Calculations showed that for the small tip-sample distances that are used in this work, direct ionization of residual gas atoms in the tip-sample gap is not the main source of ions. Instead, ions are likely to be created from molecules that are adsorbed at the sample surface and desorbed due to electron stimulation. It was calculated that for vacuum conditions better than 10^{-6} mbar, the rate of desorption is high enough compared to the rate of incoming gas atoms so that the layer of adsorbates under the tip during operation is depleted.

Another well-known phenomenon leading to instabilities are changes of the emitter due to surface migration of adsorbed gas molecules under influence of the high electric fields. Such adsorbates affect the field emission process since they change the electron tunneling probability through modification of the local work function. Changes in the effective work function thus are reflected in the field emission current and its stability in time. It is important to prevent these changes which is possible by using even better vacuum conditions. In most reports in literature and also in this work, the characteristics of field emitters are therefore determined for pressures below 10^{-8} mbar. Achieving such vacuum conditions in a practical device however will be extremely difficult. This stringent requirement may be alleviated by using chemically inert gasses and inert materials to be able to operate the field emitters at elevated pressures.

During the field emission experiments in chapter 6 it was found that electron-beam induced deposition of carbon material takes place on the sample surface. The rate of deposition was determined to be higher compared to what is normally observed in scanning electron microscopy (SEM). This is explained by the fact that the process of carbon deposition is more effective in field emission experiments than in SEM. The

electron beam energies that are used in field emission sensing are determined by the bias voltage and range from a few to $\sim 50\,\mathrm{eV}$. These energies are close to where the hydrocarbon dissociation cross section has a peak. Since the carbon deposition on the sample surface affects the local work function, this is expected to be one of the sources for the current instabilities that we observe during our experiments. Prevention of carbon deposition on the emitter and sample surfaces might therefore be a more important issue than solely achieving the lowest possible vacuum conditions. In order to achieve this, the amount of hydrocarbons on the sample should be reduced and the diffusion over the sample surface limited. In the experiments this is done by annealing the samples *in situ* before use. In a practical application, it is important to use very clean, possibly annealed surfaces and appropriate packaging to prevent the build-up of contamination during operation of the device. The diffusion of hydrocarbons over the sample surface might be reduced by preventing surfactant layers on the used surfaces, e.g. by using hydrophobic materials or inert coatings.

7.2.2 Mechanical stability

An advantage of using field emission for proximity sensing rather than for supplying a constant intensity electron beam is that current instabilities have only a limited effect on the control signal. Since the field emission current strongly depends on the distance, only small variations are needed to return to the same current set-point. However, to prevent damage to the tips and sample, the mechanical stability should be such that the probe can be operated in true non-contact, within minimum and maximum limits. If a tunneling current would be used for distance control, like in STM, the amplitude of vibrations should be sub-nanometer to prevent tip-sample contact. In the field emission mode, the requirements for mechanical stability can be relieved. By increasing the bias voltage, the initial tip-sample distance is increased and a higher value of vibrational noise can be tolerated.

As has been shown in chapter 5, when using the constant current method, the tip can be positioned at tens of nanometers from the sample surface and kept at this distance within a range of several nanometers. With increasing bias voltage, also the variation in the probe position increases, from $\pm 0.7\,\mathrm{nm}$ for $3\,\mathrm{V}$ to $\pm 2.4\,\mathrm{nm}$ for $10\,\mathrm{V}$ bias, due to a deterioration of the emission stability. For higher voltages, larger variations in probe position are required, up to $\pm 10\,\mathrm{nm}$ for voltages up to $40\,\mathrm{V}$. It may be clear that the stability requirements are a trade-off between the amount of instability that can be allowed in the field emission current and the amplitude of the vibrational noise. By increasing the stability of the field emission current, the requirements for vibration isolation can be lowered.

In the setup used for the experiments, the main source of vibrations are resonances from the building and from instruments and acoustic noise. Vibration isolation was achieved by using external air legs combined with viton rings in the sample stage that act as springs and dampers. The STM scan head has a high resonance frequency of $2.1\,\mathrm{kHz}$ to obtain a good resistance against external disturbances. The system noise

level was measured from the power spectrum of the tunneling current and showed no specific resonance peaks, so the vibrations are effectively damped. In the experimental setup, proper vibration isolation is imperative for obtaining usable results. In a practical device, such damping systems of course cannot be used. The advantage of using MEMS for actuation and positioning is that the requirements on mechanical stability can be more easily met. The small dimensions of the structures result in high resonance frequencies and due to their small mass, they are highly resistant against vibration and shock.

7.2.3 Series resistor

During the field emission measurements it was found that operation of the probes in the field emission regime can cause significant damage to the emitter tip and sample. In chapter 6 the resulting effects were shown that have been observed in STM and SEM images taken after the measurements. Parts of the tip and the sample are ablated by high current peaks that result from electrical discharges. The most obvious explanation for these peaks is a mechanical contact between the tip and sample due to mechanical or current instabilities. The peak can also be caused or enhanced by a field emission initiated vacuum arc, when material in the vacuum gap is ionized leading to a voltage breakdown.

By integrating a high value series resistor, the problem of tip and sample damage due to high currents can be greatly alleviated. We used a resistance of 100 MΩ to prevent high current flows even at high applied voltage. The resistor should be placed as close to the emitter as possible to reduce the capacitive load to the tip. Since the total power that can be dissipated at an electrical discharge depends on the effective capacitance, this capacitance should be minimized to reduce the damage done. First the resistor was placed inside the vacuum chamber just before the connection to the scan head. This greatly increases the tip and sample lifetime during field emission measurements. To further lower the capacitance an isolating tip holder with integrated resistor was custom made. The total capacitance between the sample and the probe using this holder is estimated to be less than 1 pF, mainly determined by the dimensions of the probe's handling chip. This allows an increase of the bias voltage up to 10 V without significant damage to the tip or sample. When MEMS techniques are used to produce field emitter arrays, resistors can be integrated into the mechanical structure. The emitters can be fabricated on top of high resistance substrates or doped so that parts of the probe have a higher resistance. Another option to limit the maximum current between tip and sample would be to increase the contact resistance by using a recording layer with high resistivity.

7.3 Probes suited for field emission sensing

In this work we investigated two types of probes to characterize the field emission properties and its applicability for proximity sensing: fixed-tip probes made by silicon

micromachining and commercially available AFM probes. Both were used to obtain the field emitter properties and determine the sensitivity of the field emission effect for distance variation. The AFM probes were used to scan on patterned media using field emission for distance control. The main findings with respect to the used materials, spring constant and resulting sensitivity are summarized below.

7.3.1 Materials

From the considerations on field emission current stability discussed in chapter 2 it was concluded that the materials that are used for field emission should have a relatively low work function, a high melting point, high tensile strength and good resistance against oxidation. In the selection of an emitter material we benefited from the extensive knowledge accumulated in the area of field emitter research. The primary materials from which field emitters are typically fabricated are doped silicon and molybdenum. Other materials that are used for coating of the emitters are tungsten, platinum and tantalum. Metal nitrides and carbides can also be used as well as overcoatings of carbon, conductive diamond and carbon nanotubes.

To investigate the current stability of our field emitters, we used different tips with sputtered metal coatings of Mo, W and Pt. The coatings increase the tip radius and consequently the image resolution, due to tip-sample convolution effects. The best current stability was achieved for tips coated with 50 nm Mo. AFM probes without coating could also be used for STM, as long as a good connection to the probe tip is made by scratching through the silicon-oxide layer before applying silverpaint as an electrical connection to the probe. They provide a better lateral resolution compared to the coated probes.

For better durability we used AFM probes coated with conductive diamond. The conductive diamond tip (CDT) probes were expected to be very suitable for field emission applications, since they have good wear resistance, good thermal conductivity and a low electron affinity. We found that the CDT probes are indeed capable to be used for STM and imaging in the field emission mode. However, high currents can still cause damage of the probes, when the silicon interior is heated to its melting point and the diamond coating ruptures. By using a series resistor this effect can be prevented. The lateral resolution that can be achieved with the CDT probes is limited, since the coated tips have a relatively large tip radius. Therefore, uncoated or metal-coated probes provide better properties in terms of resolution for imaging in the field emission mode.

7.3.2 Spring constant

When magnetic media are used to store data, cantilever probe are required to be able to sense magnetic information from shifts in the resonance frequency. This complicates the probe-medium system, since the incorporation of a cantilever introduces a highly unstable component in the mechanical loop. Due to electrostatic interaction between the cantilever probe and the sample, the cantilever deflects when applying a bias

voltage. When the deflection is increased beyond a critical value, electrical pull-in of the cantilever beam occurs. In order to predict the pull-in, in chapter 2 we used a model to calculate the bending behaviour of the cantilever with increasing bias voltage. The model considers the total energy of the system, by calculating the elastic energy of the bending cantilever and the Van der Waals energy. The electrostatic energy is modelled by three parallel capacitances representing the capacitance between the sample and the cantilever, tip cone and tip apex. The calculations showed that by choosing a high enough spring constant for the probe's cantilever, the field emission current is at the current set-point before pull-in of the cantilever occurs.

In the measurements shown in chapter 5 and 6, AFM probes with a spring constant of 2.8 N/m and 48 N/m were used. It was found that when a probe is mounted with the low spring constant of 2.8 N/m, imaging is not possible because the probe cannot be brought in a stable feedback position. By measuring the deflection as function of applied voltage using a fiber interferometer setup, we determined that a spring constant of 48 N/m is sufficient to prevent pull-in of the cantilever. With increasing voltage and tip-sample spacing, the cantilever deflection saturates to a maximum value of ~ 8 nm. By using probes with a high spring constant, pull-in can therefore be prevented and the AFM probes can be used for STM and imaging in the field emission mode. In the STM mode we used a bias voltage of 3 V and a tunneling current of 3 nA. The images obtained are similar to the AFM images taken on the same samples and prove that a conducting surface can be scanned in non-contact by using cantilever probes, without the need for an external deflection detection system.

7.3.3 Sensitivity

To determine the sensitivity of the tip-sample distance control, a model was developed to calculate the dependence of the field emission current on the distance between a field emitter tip and a counter-electrode. The field emission current for a constant electric field is calculated using Fowler-Nordheim theory. The distance dependence is determined by the variation in the electric field with distance, described by the field enhancement factor γ. We used finite element analysis to determine the enhancement factor for a simplified geometrical model as function of distance. The result can be approximated by the relation $\gamma = \gamma_\infty (r+d)/(\gamma_\infty r + d)$, with d as the electrode gap, r the tip radius and γ_∞ for the saturation field enhancement at large distance.

The field enhancement properties of the field emitters have been measured by taking *I-V* characteristics for varying distance. The *I-V* curves were recorded at distances varying from 12.5 - 800 nm for a fixed-tip probe coated with Mo and distances varying from 50 - 950 nm for an uncoated silicon AFM probe. A dedicated fitting routine was developed to fit the Fowler-Nordheim model to the measured data, to derive the values for the field enhancement. For the measured probes, the variation of the field enhancement can indeed be described by the theoretical model and the results can be fitted by choosing proper values for the tip radius and field enhancement at large distance.

The sensitivity at which the tip-sample distance can be controlled is a function of the tip radius and the variation in field enhancement. This sensitivity could be determined by operating the probes in constant current mode and measuring the variation in tip-sample distance with varying applied voltages. For the fixed-tip coated with Mo, the tip is retracted ~ 120 - 160 nm when the applied voltage is increased from 3 to 50 V, in order to maintain a constant current of 3 nA. At high voltages, instabilities in the field emission current cause large stepwise changes in the tip position which severely limit the positioning repeatability. For the AFM probe, the probe position is raised ~ 90 nm when increasing the applied voltage from 3 to 40 V. This includes the deflection of the cantilever due to the electrostatic attraction. Also in this measurement, instabilities in the field emission current cause changes in the probe position and limit the positioning repeatability to $\pm$ 10 nm, a value that was obtained by repeating the experiment ten times. The differences in sensitivity between the two probes are explained by the different emitter geometries and consequently different field enhancement factors.

The measured voltage-displacement curve can be fitted using the same model of the distance dependence of the field enhancement. The model clarifies the non-linearity that is observed in the relation between displacement and voltage. Due to the increase in the field enhancement factor with distance, the tips are retracted from the sample non-linearly with the applied voltage. At low voltage, the tip is close to the sample and the field enhancement factor is ~ 1, resulting in a slow increase in tip-sample distance with applied voltage. When the tip is further retracted and the field enhancement is increased up to values as high as ~ 25, the tip-sample distance rises faster with voltage. Next to the material work function and area of emission that determine the field emission current, the field enhancement factor is therefore an important parameter for the sensitivity of this control method. It is likely that when an array of tips is used and there is a variation in work function, tip radius or emitter geometry, each probe will have a different sensitivity. For absolute tip-sample distance control, each probe therefore has to be calibrated separately, depending on the specific requirements.

7.4 Scanning on patterned media using field emission

The recording architecture using an array of probes eventually allows molecular or atomic storage. As an intermediate step towards storage in molecular and atomic patterned media, in the μSPAM concept recording on magnetic patterned media is pursued, so that issues like write-synchronization and coding can comfortably be addressed. In this magnetic probe recording application, the patterned medium will have magnetic dots with a very high periodicity. In the current work we tested the method of using field emission currents to scan in non-contact on patterned media. Special patterned samples were developed consisting of uniform dot patterns over a large area. Below a summary can be found of the requirements that such a sample should fulfil in order to be useful for scanning in non-contact using field emission and the main results for the bias-dependent scanning measurements on these samples are given.

7.4.1 Medium requirements

The periodicity of the patterned media determines the bit densities that can be attained in probe recording. The pattern should extend over a large area in order to be useful for application in recording and in our setup to be able to trace the patterned area. Therefore in this work we used laser interference lithography (LIL) to define the periodic structures. The LIL setup is the same as used in the μSPAM project for fabrication of the magnetic patterned samples. It enables to produce uniform exposures over a range of 5 x 5 cm which can be extended to full wafer size. During this work the fabrication process was improved. With the standard i-line resist only structures with a periodicity of ~ 300 nm could be made with good reproducibility. By using a new trilayer resist layer stack, the periodicity could be reduced to 160 nm which is near the resolution limit of the setup. The lowest periodicity that can be obtained is determined by half the wavelength of the laser ($\frac{1}{2}\lambda = 133$ nm), limiting the maximum achievable areal density using this setup to 36 Gbit/in^2. Although this is not sufficient for a practical storage application, it allows us to study the principles of non-contact probe recording.

Since the topography signal fluctuates due to instabilities in the field emission current, the height of the produced dots has to be sufficiently large so that they can be distinguished and used for position servo control. It was found that for high bias voltages, the accuracy to which a probe can be positioned at a certain distance from a single location on the sample surface is limited to < 20 nm. Therefore in this work dot heights of 20 nm and 35 nm were used. For low bias voltage and increased current stability, the required dot height is less.

A relaxation for the samples used for scanning in the field emission mode, is that they do not yet need to be magnetic. Only the conductivity should be sufficiently high to enable field emission currents to flow. Insulating materials should be avoided, to prevent electrical charging of the sample. We used silicon and silicon-nitride substrates, pre-patterned by LIL and reactive ion etching. To improve the conductivity, a metal coating was deposited by sputtering after the substrate has been patterned. The coating material should have a high melting point, good substrate coverage and good wear resistance to prevent sample damage by high current peaks. We tested metal coatings of molybdenum, tungsten-titanium and platinum to find a suitable material. Characterization by AFM, STM and four-probe resistance measurements taught us that a coating of platinum with tantalum or chromium underlayer provides the best properties, since the smooth layer (< 2 nm roughness) results in a low resistance and good coverage of the dots. Samples with this coating can be used at increased bias voltages without significant damage, as long as the occurrence of high peaks in the field emission current can be prevented.

In our setup the maximum field emission current is limited by using a high value resistor in the current path. When this resistor is not placed close enough to the tip end, erosion of the tip and sample still take place when scanning at increased bias. A better option to limit the maximum current between tip and sample would be to use a sample with high specific resistance. This prevents high currents to flow even when there is a capacitive discharge between the emitter and sample.The required specific resistance

is a delicate balance between sufficient conductivity to prevent charging of the sample surface due to the field emission currents and enough resistance to limit the maximum current peaks caused by instabilities.

7.4.2 Bias-dependent scanning

When using field emission to scan over the patterned samples in non-contact, the lateral positioning accuracy should be such that the individual features can be distinguished. The resolution in scanning field emission microscopy is determined by the tip radius and the tip-sample distance. Previous results reported in literature show a lateral resolution of about 400 nm, which is rather large since tips were used that were relatively blunt or damaged during operation. To achieve better resolution we used AFM probes that have a sharp tip of ~ 7 nm to scan on the patterned samples.

The best result was obtained using a probe coated with 20 nm of chromium with a resulting tip radius of ~ 20 nm. By operating the probe in constant current mode and varying the applied voltage, the average tip-sample separation can be controlled. Instabilities in the field emission current increase for higher applied voltages and cause variations in the topographic signal, but the probe can still be operated in non-contact. We used voltages up to 50 V to obtain images at increasing tip-sample separation. A larger tip-sample distance leads to a decrease in lateral resolution, but at 50 V features of ~ 20 nm could be resolved. The precise increase in tip-sample distance depends on the sensitivity of the particular probe and therefore on its specific field enhancement. At low applied voltage, so at small tip-sample distance, the maximum scan rate was limited due to unwanted tip-sample contacts occurring at the edges of the dots. Scanning at higher voltage allowed much higher scan rates, which makes it plausible that the tip-sample distance has at least increased beyond the dot height of the scanned sample (35 nm).

The measurements confirm that field emission can be applied to control the spacing between probe and medium, with sufficient resolution and current stability. Moreover, the maximum scan rate that can be achieved when scanning over a patterned medium can be increased significantly compared to STM by increasing the tip-sample distance. The increase in tip-sample distance therefore alleviates the requirements on the mechanical and current stability and enables higher data rates in a storage application. These results are in agreement with our expectations and show the proof-of-principle for application of field emission proximity sensing in non-contact probe recording. However, it was found to be difficult to repeat these measurements on a common basis and obtain similar resolutions. The causes for this are the inherent instability of the field emission current and damaging effects to the tip and the sample.

7.5 Conclusions

On the path towards ultra-high data densities in information storage we expect to see a change in recording technology to the probe recording architecture. Probe recording will ultimately lead to molecular and atomic storage densities, but this will require non-contact operation of individual probes. The most critical issue in non-contact probe recording is the method to detect and control the probe-medium distance. For distances on the order of 10 nm, required for magnetic probe recording, we conclude that using field emission current is the only method that can be relatively easy integrated (Section 1.3).

By assembling a dedicated measurement setup we were able to measure the field emission characteristics as function of distance and we showed that field emission current can indeed be used to scan in non-contact on a patterned sample with high lateral resolution. However, there are several factors that seriously impair the applicability of the method of field emission sensing in a practical probe recording system:

- Atomic changes at the emitter surface cause instabilities in the field emission current (section 2.3), resulting in large variations in the tip-sample distance and accidental tip-sample contact. When experimenting under UHV conditions, some improvement can be obtained.
- Electrostatic interactions between probe and sample cause the cantilever of the probe to bend when a bias voltage is applied. Tip-sample contact (pull-in) can be prevented by using AFM probes with a sufficiently high spring constant (section 5.2.1).
- Capacitive discharges lead to ablation of tip and sample surfaces due to large current peaks (section 6.3.1 and 6.3.2). By integration of a high value resistor in the current path as close to the probe tip as possible, the capacitive load to the tip is minimized and the maximum currents are limited.
- Electron-beam induced deposition of carbon material takes place on the sample surface (section 6.3.3), which can be minimized by proper annealing of probes and samples in UHV.

Even with these stringent conditions, instabilities in the field emission current and damaging effects to tip and sample persist and strongly reduce the accuracy and reproducibility. Only by exchanging probes and coarse positioning to new positions on the sample surface, we were able to measure reproducibly. Field emission characteristics were measured as function of distance, providing a better understanding of the process of field emission at distances in the nanometer regime:

- A new model based on finite element calculations was developed to calculate the sensitivity of the field emission current for small tip-sample distances (section 2.2.2).

- The model was verified by measuring *I*-*V* characteristics for distances varying from 12.5 - 800 nm for fixed-tip probes (section 5.1.1) and 50 - 950 nm for AFM probes (section 5.2.2). An iterative fitting procedure was developed to calculate the right error correction factors in the Fowler-Nordheim relation and determine the emission area A and the field enhancement factor γ.

- The tip-sample distance can be controlled by operating the probes in constant current mode and varying the applied voltage (section 5.1.2 and 5.2.3). The non-linearity in the measured voltage-displacement curve agrees with our model. The sensitivity of this positioning method depends on the emitter tip radius and on the variation in field enhancement.

- Bias-dependent imaging can be used to scan on conducting patterned samples for increasing tip-sample distance. At larger distances the lateral resolution reduces, but higher scan rates can be used (section 6.4). At 50 V the resolution is still sufficient to detect features of ~ 20 nm, which exceeds the value of 400 nm reported so far in literature.

The short emitter lifetime and the requirement for UHV conditions and ultra-clean surfaces pose a serious obstacle for practical application of field emission currents in a probe recording device. The experimental reality has taught us that using field emission currents might therefore not be a very practical solution for application in a probe recording device. Still it is the only method that has a relatively large range of operation, up to the regime where magnetic forces can be sensed and for which integration in a probe array seems to be attainable.

7.6 Recommendations for future work and applications

When at the beginning of this research project the method of field emission sensing was selected for application in probe recording, it was expected that it would be possible to engineer its typical characteristics such that this method could also be applied in a practical probe recording device. This should be achieved by improving tip and sample materials and avoid the need for UHV conditions, by using inert gasses and hydrophobic layers to avoid contamination. However, even under UHV conditions and using clean surfaces, it was found to be difficult to maintain constant field emission properties for a long period of time. It is likely that when an array of tips is used and there is a variation in work function, tip radius or emitter geometry, each probe will have a different sensitivity. For absolute tip-sample distance control, the probes would have to be calibrated separately, depending on the specific requirements. The application of field emission sensing with many probes in (magnetic) probe recording seems therefore difficult to achieve.

The question arises whether recording on magnetic media using parallel probes will ever be a viable step on the road towards non-contact probe recording. Other methods

that could be used for proximity sensing are typically operated at very short distance, where magnetic forces cannot be distinguished from the other acting forces. For research, magnetic probe recording can still be a useful tool to address issues like write-synchronization and coding. For future storage applications however, it seems more logical to investigate molecular or atomic storage, especially when the fast advances in hard-disk recording and FlashRAM are taken into account.

The outcomes of this work can be used to further investigate the use of field emission currents in probe recording and in other applications. The sensitivity of the field emission effect for the electrode spacing and the small critical sensing area make this an interesting method for sensing, especially in very small-scale systems, where other sensors are difficult to integrate. For stable operation in such applications, the current stability of the emitters should be further improved. Fixed-tip probes can be used to test the field emission properties of more coating materials and develop an emitter that provides high current stability and long emitter lifetime. Such an emitter can be integrated in a functional device and used for sensitive displacement or resonance detection.

Carbon nanotube (CNT) field emitters can be used to improve the field emission current stability and to increase the sensitivity for proximity sensing. We have done preliminary tests in an attempt to show their applicability, unfortunately without success until now. However, because of their unique properties of high aspect-ratio, high mechanical strength and chemical stability, they have a large potential. The high aspect-ratio lowers the voltage needed for extraction of a field emission current, due to a high field enhancement. When used for tip-sample distance control, this high field enhancement also gives rise to a better sensitivity compared to other tips.

When the field emitters are used in probe recording for tip-sample distance control, it is important to limit the maximum current. This may be achieved by applying a coating of diamond-like carbon to the medium, which is also used to protect hard-disk platters and read-heads. The resistance of this coating layer can be tuned by changing the doping concentration and used to prevent voltage discharges. Next to controlling the tip-sample distance, integration of field emitters in recording probes may also open possibilities for heat-assisted writing in magnetic or phase-change media.

In practical applications, the pressure at which the field emitters operate is likely to be considerably higher than used in this work. Chemically inert gasses and inert materials may be used to reduce the effects caused by the higher pressure on the stability of the field emission current. Further study is therefore required to investigate the performance of the field emitters at elevated pressures and in the presence of inert gasses.

In general, the measurement setup that has been built, can be used for further research on the influence of separation distance on field emission current. Field emission studies are often conducted with several millimeters distance between the field emitter and counter-electrode. In STM, the separations are typically a few nanometer and field emission is applied for tip conditioning or to characterize the tip sharpness. The measurement methods that have been developed in this work, can be used to study the intermediate range and gain a better understanding of the field emission effect at small distances.

Appendix A

Fowler-Nordheim fitting routine in MAPLE software

In this appendix the MAPLE routine is given which was used to automate the fitting of the *I-V* measurement data. The fitting procedure is based on the Fowler-Nordheim theory as discussed in chapter 2. The routine is used in chapter 5 to determine the typical field emission parameters, the field emission area A and the field enhancement factor γ, for various measurements. Below, the main procedure used in the fitting routine will be shortly explained, after which the source code of the MAPLE worksheet will be given.

A.1 Fitting procedure

The main procedure in the MAPLE source code is called `fitSR`. It has three arguments: `filename`, which is the filename of the file with measurement data; `thresholdcurrent`, which gives the value of an treshold current for selecting data points for fitting the model; and `measurement_nr`, which selects the measurement curve in the data file. In `fitSR` two subprocedures are used, `getdata` and `getSR`. The procedure `getdata` is used for retrieving the measurement results from a `.txt`-file into MAPLE and extracting the number of measurement points. The procedure `getSR` takes care of the linear least squares fitting of the measurement points, represented by two lists called `p1` and `p2`.

The steps that are required in the fitting procedure to obtain the right approximation for the correction factors have been given in section 5.1.1. Below, the numbers between braces indicate to which of these steps the MAPLE code refers to. After reading the data (1) from the `.txt`-file into MAPLE using `getdata`, a selection of data points is made and the data is transformed into a FN-representation given by $\log_{10}(I/V^2)$ *versus* $(1/V)$. Then a linear linefit is made (2) using `getSR`. From the slope of the line fit S_V is determined, whereas R_V is the value for the intersection with the vertical axis. A first calculation for the value of β is made (3) by using

`beta := .95 * (-b * phi^(3/2)) / Sv`, where 0.95 is the starting estimate for the error correction factor s. Using this first approximation for β, the other parameters for the voltage V, the electric field F, the current I and the Nordheim parameter y_N are calculated for a specific point on the fitted line, given by $\ln\left\{\frac{I}{V^2}\right\} = pp$. Using these values, a better approximation for s, that depends on y_N and F, can be calculated in this point (4) and used to derive a new value for β which is more exact than the previous value. By re-calculating the other parameters, the right values for the error correction factors r[1] and s, 'local-field-to-voltage-ratio' β and the emission area A can be derived (5). The field enhancement factor follows from β, when the tip-sample distance d is known, by $\gamma = \beta d$. Since the value of A depends on the parameter β, this value has to be determined before A can be derived. The error correction factors can only be calculated for a point where the requirement $y_N < 1$ is still valid. In the point of intersection with the vertical axis $\frac{I}{V^2} = 0$ this is not the case, since there $V \to \infty$ and y_N as well. Therefore, in step 5 the intercept value of $\ln(S_V)$ is derived for the point `pp` and not for $\frac{I}{V^2} = 0$.

The last procedure is `fitplot`, which generates plots of the data points and fitted functions, both in I-V and FN representation. From the fitting procedure, all necessary parameters have been determined and the fitted curves are generated by using the expression for the field emission current I from equation 2.5. The arguments of this procedure are used to define the voltage range for the plots and the colours of the fitted lines. As a final step, the data is written to files for further processing.

A.2 MAPLE source code for fitting of I-V measurement data

```
1   # ------------------------------------------------------------------------------------ #
2   #     'Fitting of field emission I-V curves'
3   #
4   #      Maple version 9.50
5   #
6   #      Calculate the field emission parameters gamma and A
7   #      using the Fowler-Nordheim emission model and fitting
8   #      procedure as described by R. Forbes
9   #      J. Vac. Sci. Technol. B 17, 526 (1999)
10  #
11  #      by A.J. le Febre & L.A.A. Bouwman, 2006-2008
12  #
13  # ------------------------------------------------------------------------------------ #
14
15  # ------------------------------------------------------------------------------------ #
16  #                     Initialization: restart and selecting packages
17  # ------------------------------------------------------------------------------------ #
18  > restart:
19  > Digits:=5:
20  > with(plots):
21  > with(stats):
22  > with(fit):
23
24  # ------------------------------------------------------------------------------------ #
```

[1] In this appendix, the original parameters R_V and r as proposed by Forbes [113] are used, whereas in the rest of this thesis they have been replaced by P_V and p.

```
25  #                       Select filename and data set
26  # ------------------------------------------------------------------------------------------ #
27  > startDIR := currentdir();
28  > filename := cat(startDIR, "filename.txt");
29  > measurement_nr := 12:
30  > nr_set := [2,4,6,8,10,12];
31
32  # ------------------------------------------------------------------------------------------ #
33  #                         Define constants
34  # ------------------------------------------------------------------------------------------ #
35  > phi := 4.95:
36  > threshold := 0.50e-9:
37  > resistance := 124.4e6:
38  > e := 1.60217653e-19:
39  > m_e := 9.1093826e-31:
40  > h := 6.6260693e-34:
41  > h_bar := evalf(h/2/Pi):
42  > epsilon_0 := 8.854187817e-12:
43  > a := evalf(e^3/8/Pi/h)/e:                                          #a := 1.541434e-6
44  > b := evalf(4/3*sqrt(2*m_e)/(e*h_bar))*e^(3/2):                     #b := 6.830888e9
45  > c := evalf(sqrt(e^3/4/Pi/epsilon_0))/e:                            #c := 3.794687e-5
46  > g := b * c^2:
47
48  # ------------------------------------------------------------------------------------------ #
49  #                         Define data arrays
50  # ------------------------------------------------------------------------------------------ #
51  > Td := array(1..measurement_nr):
52  > Td[1] := 100e-9 : Td[2] := Td[1]:
53  > Td[3] := 150e-9: Td[4] := Td[3]:
54  > Td[5] := 200e-9: Td[6] := Td[5]:
55  > Td[7] := 400e-9: Td[8] := Td[7]:
56  > Td[9] := 600e-9: Td[10] := Td[9]:
57  > Td[11] := 800e-9: Td[12] := Td[11]:
58
59  > TplotIV := array(1..measurement_nr):
60  > TplotFN := array(1..measurement_nr):
61  > TplotIV_n := array(1..measurement_nr):
62  > TplotFN_n := array(1..measurement_nr):
63  > T_Ifitplot := array(1..measurement_nr):
64  > T_FNfitplot := array(1..measurement_nr):
65  > Tnumberofmeasurements := array(1..measurement_nr):
66  > Tdata := array(1..measurement_nr):
67  > TA := array(1..measurement_nr):
68  > Tbeta := array(1..measurement_nr):
69  > Tgamma := array(1..measurement_nr):
70  > Tr := array(1..measurement_nr):
71  > TV_fe := array(1..measurement_nr):
72  > TE_fe := array(1..measurement_nr):
73
74  > Tcolour := array(1..measurement_nr):
75  > Tcolour[1] := blue: Tcolour[2] := Tcolour[1]:
76  > Tcolour[3] := green: Tcolour[4] := Tcolour[3]:
77  > Tcolour[5] := sienna: Tcolour[6] := Tcolour[5]:
78  > Tcolour[7] := plum: Tcolour[8] := Tcolour[7]:
79  > Tcolour[9] := cyan: Tcolour[10] := Tcolour[9]:
80  > Tcolour[11] := magenta: Tcolour[12] := Tcolour[11]:
81  > Tcolour[13] := orange: Tcolour[14] := Tcolour[13]:
82  > Tcolour[15] := black: Tcolour[16] := Tcolour[15]:
83  > Tcolour[17] := red: Tcolour[18] := Tcolour[17]:
84
85  # ------------------------------------------------------------------------------------------ #
```

```
#                          Good and Mueller functions
# ------------------------------------------------------------------------------------------ #
> K := k -> Int( 1 / ( sqrt(1 - k^2 * (sin(theta))^2 ) ),theta=0..(Pi/2)):
> E := k -> Int(sqrt(1 - k^2 * (sin(theta))^2),theta=0..(Pi/2)):
> v := y -> evalf( sqrt( 1 + y ) * ( E( ( sqrt( 1 - y ) ) / ( sqrt( 1 + y ) ) ) -
>                                    y * K( ( sqrt( 1 - y ) ) / ( sqrt( 1 + y ) ) ) ) ):
> s := y -> evalf( v(y) - .5 * y * D(v)(y) ):
> t := y -> evalf( v(y) - (2/3) * y * D(v)(y) ):
> u := y -> evalf( ( -1 / ( 2 * y ) ) * D(v)(y) ):
> r := y -> evalf( t(y) )^( -2 ) * exp( g * u(y) / sqrt(phi)):
> yN := F -> (c * sqrt(F)) / phi:

# ------------------------------------------------------------------------------------------ #
#                          Fitting procedures
# ------------------------------------------------------------------------------------------ #

# ------------------------------------------------------------------------------------------ #
#                      'Read data from file' procedure
#                      column1=V1, column2=I2, column3=v2, column4=I2, ...
#                      encoding in .txt file shoud be UTF-8
# ------------------------------------------------------------------------------------------ #
> getdata := proc(filename,thresholdcurrent,measurement_nr)
>                                    # each measurement_nr is one IV-curve (up or down)
>                                    # even nr is curve up
>                                    # odd nr is curve down
>
>  local datafromfile, IVdatafromfile, IVdatafromfilereverse, i:
>  global data, data_uncorrected, numberofmeasurements, thresholdindex:
>
>  datafromfile := readdata(fopen(filename,READ),100):
>  fclose(filename):
>
>  numberofmeasurements := round(datafromfile[2,measurement_nr]):
>
>  IVdatafromfile := datafromfile[3..numberofmeasurements+2,
>                                    2*(measurement_nr-1)+1..2*(measurement_nr-1)+2]:
>  IVdatafromfilereverse := ListTools[Reverse](convert(IVdatafromfile,list)):
>
>  if type(measurement_nr-1,odd)
>   then data_uncorrected := IVdatafromfilereverse
>   else data_uncorrected := IVdatafromfile
>  end if;
>
>  thresholdindex := 0:
>
>  for i from 1 to numberofmeasurements do
>   if (data_uncorrected[i,2]<thresholdcurrent) then thresholdindex:=i+1 end if;
>  end do:
>
>  data := Matrix(1..numberofmeasurements,1..2):
>
>  for i from 1 to numberofmeasurements do
>     data[i,2] := data_uncorrected[i,2]:
>   if (resistance>0)
>     then data[i,1] := data_uncorrected[i,1] - data_uncorrected[i,2]*resistance:
>     else data[i,1] := data_uncorrected[i,1]:
>   end if:
>  end do:
>
> end:
```

```
147  # ------------------------------------------------------------------------------------------ #
148  #                 'Define values of Rv and Sv' procedure
149  # ------------------------------------------------------------------------------------------ #
150  > getSR := proc(p1,p2)
151  >  local f, x, eq:
152  >  global Sv, Rv:
153  >
154  >  f := (solve(leastsquare[[x,y]]([p1,p2]),y));     # also possible with leastmediansquare
155  >  Sv:= diff(f,x):
156  >  eq:= ln(Rg) = f:
157  >  x := 0:
158  >  Rv := solve(eq,Rg);
159  >
160  > end:
161
162  # ------------------------------------------------------------------------------------------ #
163  #                               'Iterative fitting' procedure
164  # ------------------------------------------------------------------------------------------ #
165
166  > fitSR := proc(filename,thresholdcurrent,measurement_nr)
167  >  local i, p1, p2, fitt, xg, Vg, Fg, Ig, arraysize, pp:
168  >  global dataFN, data_n, dataFN_n, beta, beta_uncorr, A, A_uncorr,Ifit,ygplot, yg, sg:
169  >
170  > getdata(filename,thresholdcurrent,measurement_nr);
171  >
172  >  dataFN := array(1..numberofmeasurements,1..2):
173  >   for i from 1 to numberofmeasurements do
174  >    dataFN[i,1] := 1 / data[i,1]:
175  >    dataFN[i,2] := ln(abs(data[i,2])/(data[i,1])^2)
176  >   end do:
177  >
178  > # ---------------------------------------------- #
179  > #            Select data points
180  > # ---------------------------------------------- #
181  >
182  > arraysize := numberofmeasurements-thresholdindex:
183  >
184  > data_n := data[thresholdindex..numberofmeasurements,1..2]:
185  >
186  >  dataFN_n := array(1..arraysize, 1..2):
187  >   for i from 1 to arraysize do
188  >    dataFN_n[i,1] := 1 / data_n[i,1]:
189  >    dataFN_n[i,2] := ln(data_n[i,2]/(data_n[i,1])^2)
190  >   end do:
191  >
192  > # ---------------------------------------------- #
193  > #  Get Sv and Sv from the selected data points
194  > # ---------------------------------------------- #
195  >
196  >  p1 := seq(dataFN_n[i,1], i=1..arraysize):
197  >  p2 := seq(dataFN_n[i,2], i=1..arraysize):
198  >
199  >  getSR([p1],[p2]);
200  >
201  > # ---------------------------------------------- #
202  > #               Get beta and A
203  > # ---------------------------------------------- #
204  >
205  >  beta := .95 * (-b * phi^(3/2))/Sv:
206  >
207  >  pp := -27:                                # pp is the value for ln(I/V^2) for fitting A
```

```
>
>  xg := -( ln(Rv) - pp )/Sv:
>  Vg := 1 / xg:
>  Fg := beta * Vg:
>  Ig := Vg^2 * exp(pp):
>
>  beta := s( yN(Fg) ) * ( -b * phi^(3/2) ) / Sv :
>                                          # get a new value with an iterative value of s
>  Fg := beta * Vg:
>  Ig := Vg^2 * exp(pp):
>
>  yg := yN(Fg):
>
>  A := solve(ln(Ig/(Fg^2)) = ln (r(yg)*Ag*a / phi ) - s(yg) * b * phi^(3/2) / Fg ,Ag ):
>
> # ---------------------------------------------- #
> #   Make IV equation with fitted parameters
> # ---------------------------------------------- #
>
> Ifit := V ->  r( ( c * sqrt( beta * V)) / phi ) * ( A * a/phi ) * (beta * V)^2 *
>            exp( - ( s( ( c * sqrt( beta * V)) / phi ) * b * phi^(3/2) ) / ( beta * V ) );
>
> ygplot := pointplot([xg,pp], color=black, symbol=cross):
>
> end:

# ------------------------------------------------------------------------------------ #
#                  'Plot' procedure
# ------------------------------------------------------------------------------------ #
> fitplot := proc(colour)
>
> global plotIV, plotFN, plotIV_n, plotFN_n, Ifitplot, FNfitplot, Vthreshold, V1, V2:
> local xplot, yplot:
>
> V1 := min(seq(data[i,1],i=1..numberofmeasurements));
> V2 := max(seq(data[i,1],i=1..numberofmeasurements));
> Vthreshold := data[thresholdindex,1];
>
> plotIV := pointplot(data, color=black, symbol=point);
> plotFN := pointplot(dataFN, color=black, symbol=point, labels=["1/V","ln(I/V^2)"]);
> plotIV_n := pointplot(data_n, color=red, symbol=point, labels=["V","I"]);
> plotFN_n := pointplot(dataFN_n, color=red, symbol=point, labels=["1/V","ln(I/V^2)"]);
>
> Ifitplot := plot(Ifit(v), v=V1..V2+1, color=colour, thickness=1):
>
> xplot := V -> 1 / V:
> yplot := V -> ln( Ifit(V) / (V^2) ):
>
> FNfitplot := plot([xplot(V), yplot(V), V=Vthreshold-10..V2], color=colour, thickness=1):
>
> end:

# ------------------------------------------------------------------------------------ #
#                                    Data fitting execution
# ------------------------------------------------------------------------------------ #

> for i in nr_set do
> print(i):
> print(Td[i]);
>  fitSR(filename,threshold,i):
>  fitplot(Tcolour[i]):
```

```
>  TplotIV[i] := plotIV:
>  TplotFN[i] := plotFN:
>  TplotIV_n[i] := plotIV_n:
>  TplotFN_n[i] := plotFN_n:
>  T_Ifitplot[i] := Ifitplot:
>  T_FNfitplot[i] := FNfitplot:
>  Tdata[i] := data:
>  Tnumberofmeasurements[i] := numberofmeasurements:
>
>  TA[i] := A:
>  Tbeta[i] := evalf(beta):
>  Tgamma[i] := evalf(beta*Td[i]):
>  Tr[i] := evalf(sqrt(A/(2*Pi))):
>  print("r = ", Tr[i]);
>  print("gamma = ", Tgamma[i]);
>
>  print(display(TplotIV[i],TplotIV_n[i]));
>  print(display(TplotFN[i],TplotFN_n[i]));
>
>  TV_fe[i] := evalf( fsolve(Ifit(V)=3e-9,V,Vthreshold..V2) ):
>  TE_fe[i] := evalf( beta*TV_fe[i] ):
>  print("V_fe = ", TV_fe[i]);
>  print("E_fe = ", TE_fe[i]);
>
> end do:

# ------------------------------------------------------------------------------------------ #
#                              Plotting I-V and FN curves
# ------------------------------------------------------------------------------------------ #
> display( seq( [ TplotIV[i],TplotIV_n[i],T_Ifitplot[i] ], i in nr_set ),
>                                                              view=[40..150,0..500e-9]);
> display( seq( [TplotFN[i], TplotFN_n[i], T_FNfitplot[i] ], i in nr_set ),
>                                                           view=[0.001..0.022,-36..-23]);

# ------------------------------------------------------------------------------------------ #
#                                      Write fitting results
# ------------------------------------------------------------------------------------------ #

> currentdir( cat(startDIR, "\\results") );
> for i in nr_set do
>  fileIV:= cat( "plotIV_", i, ".txt" ):
>  fprintf( fileIV, "%e", Array([op([1,1..-1], TplotIV[i] ) ] ) ):
>  close(fileIV):
>
>  fileIV_fit:= cat( "plotIV_fit_", i, ".txt" ):
>  fprintf( fileIV_fit, "%e", Array([op([1,1..-1], T_Ifitplot[i] ) ] ) ):
>  close(fileIV_fit):
>
>  fileFN:= cat( "plotFN_", i, ".txt" ):
>  fprintf( fileFN, "%e", Array([op([1,1..-1], TplotFN[i] ) ] ) ):
>  close(fileFN):
>
>  fileFN_fit:= cat( "plotFN_fit_", i, ".txt" ):
>  fprintf( fileFN_fit, "%e", Array([op([1,1..-1], T_FNfitplot[i] ) ] ) ):
>  close(fileFN_fit):
> end do:

# ------------------------------------------------------------------------------------------ #
#                                             End
# ------------------------------------------------------------------------------------------ #
> currentdir(startDIR);
```

Bibliography

[1] J. Gantz et al. "The Expanding Digital Universe - A Forecast of Worldwide Information Growth Through 2010". *An IDC White Paper - sponsored by EMC*. Retrieved from http://www.emc.com/about/destination/digital_universe (March 2007). 1.1

[2] R. Waser (editor). "Nanoelectronics and information technology". In: *Nanoelectronics and information technology*. Pages 607–703. Wiley - VCH. Weinheim (2003). 1.1

[3] I. T. R. for Semiconductors. "Executive summary 2007 edition". *ITRS*. Retrieved from http://www.itrs.net (2007). 1.1

[4] S. Charap, P. Lu and Y. He. "Thermal stability of recorded information at high densities". *IEEE Transactions on Magnetics* **33**, 978–983 (1997). 1.1

[5] D. Weller and A. Moser. "Thermal effect limits in ultrahigh-density magnetic recording". *IEEE Transactions on Magnetics* **35**, 4423–4439 (1999). 1.1

[6] R. Rottmayer et al. "Heat-Assisted Magnetic Recording". *IEEE Transactions on Magnetics* **42**, 2417–2421 (2006). 1.1

[7] B. Terris and T. Thomson. "Nanofabricated and self-assembled magnetic structures as data storage media". *Journal of Physics D: Applied Physics* **38**, R199–R222 (2005). 1.1

[8] T. Thomson, L. Abelmann and H. Groenland. "Magnetic Nanostructures in Modern Technology". In: *Magnetic Nanostructures in Modern Technology*. B. Azzerboni, G. Asti, L. Pareti and M. Ghidini (editors). Pages 237–306. Springer. New York (2008). 1.1, 1.1.1

[9] M. Brown. "The growing disparity between magnetic density improvement and individual disk drive performance". In: *Abstracts 44th Annual Conference on Magnetism and Magnetic Materials*. Page 330 (1999). 1.1

[10] G. Binnig, H. Rohrer, C. Gerber and E. Weibel. "Tunneling through a controllable vacuum gap". *Applied Physics Letters* **40**, 178 (1982). 1.1.1, 3.2.2

[11] G. Binnig, C. Quate and C. Gerber. "Atomic Force Microscope". *Physical Review Letters* **56**, 930–933 (1986). 1.1.1

[12] C. Quate. "Method and means for data storage using tunnel current data readout". US Patent 4,575,822 (1986). 1.1.1

[13] H. Mamin and D. Rugar. "Thermomechanical writing with an atomic force microscope tip". *Applied Physics Letters* **61**, 1003 (1992). 1.1.1, 1.1.1

[14] R. Ried, H. Mamin, B. Terris, L. Fan and D. Rugar. "6-MHz 2-N/m piezoresistive atomic-force microscope cantilevers with INCISIVE tips". *Journal of Microelectromechanical Systems* **6**, 294–302 (1997). 1.1.1

[15] E. Grochowski and R. Halem. "Technological impact of magnetic hard disk drives on storage systems". *IBM Systems Journal* **42**, 338–346 (2003). 1.1.1, 1.5

[16] P. Vettiger et al. "Ultrahigh density, high-data-rate NEMS-based AFM data storage system". *Microelectronic Engineering* **46**, 1–4 (1999). 1.1.1

[17] P. Vettiger et al. "'Millipede' - more than one thousand tips for future AFM data storage". *IBM Journal of Research and Development* **44**, 323–340 (2000). 1.1

[18] E. Eleftheriou et al. "Millipede - A MEMS-based scanning-probe data-storage system". *IEEE Transactions on Magnetics* **39**, 938–945 (2003). 1.1.1

[19] A. Knoll et al. "Integrating nanotechnology into a working storage device". *Microelectronic Engineering* **83**, 1692–1697 (2006). 1.2, 1.3, 1.1.1, 1.1.2

[20] M. Lantz, H. Rothuizen, U. Drechsler, W. Haberle and M. Despont. "A Vibration Resistant Nanopositioner for Mobile Parallel-Probe Storage Applications". *Microelectromechanical Systems, Journal of* **16**, 130–139 (2007). 1.1.1

[21] H. Pozidis et al. "Demonstration of thermomechanical recording at 641 Gbit/in2". *IEEE Transactions on Magnetics* **40**, 2531–2536 (2004). 1.1.1, 1.1.2

[22] M. Bolks et al. "Micro Scanning Probe Array memory μSPAM". *2nd PROGRESS Workshop on Embedded Systems, Veldhoven, The Netherlands,* pages 17–26 (2001). 1.1.1

[23] L. Abelmann, T. Bolhuis, A. Hoexum, G. Krijnen and J. Lodder. "Large Capacity Probe Recording using Storage Robots". *IEE Proceedings Science, Measurement & Technology* **150**, 218–221 (2003). 1.1.1

[24] E. Sarajlic. *Electrostatic microactuators fabricated by vertical trench isolation technology*. Ph.D. thesis. University of Twente. Enschede (2005). 1.1.1

[25] M. Patrascu. *Characterization, modeling and control of the μWalker - a micro actuator for data storage*. Ph.D. thesis. University of Twente. Enschede (2006). 1.1.1

[26] A. Hoexum. *Unleashed Microactuators electrostatic wireless actuation for probe-based data storage*. Ph.D. thesis. University of Twente. Enschede (2007). 1.1.1

[27] M. Khatib, B. van der Zwaag, F. van Viegen and G. Smit. "Striping Policy as a Design Parameter for MEMS-based Storage Systems". In: *The 2nd International Workshop on Software Support for Portable Storage*. (2006). 1.1.1

[28] A. Sato and Y. Tsukamoto. "Nanometre-scale recording and erasing with the scanning tunnelling microscope". *Nature* **431**, 432 (1993). 1.1.1

[29] Y. Cho, S. Hashimoto, N. Odagawa, K. Tanaka and Y. Hiranaga. "Realization of 10 Tbit/ in. memory density and subnanosecond domain switching time in ferroelectric data storage". *Applied Physics Letters* **87**, 232907 (2005). 1.1.1

[30] R. Barrett and C. Quate. "Charge storage in a nitride-oxide-silicon medium by scanning capacitance microscopy". *Journal of Applied Physics* **70**, 2725 (1991). 1.1.1, 1.2.2

[31] H. Hamann, M. O'Boyle, Y. Martin, M. Rooks and H. Wickramasinghe. "Ultra-high-density phase-change storage and memory". *Nature Materials* **5**, 383–387 (2006). 1.1.1

[32] Y. Martin, S. Rishton and H. Wickramasinghe. "Optical data storage read out at 256 Gbits/in^2.". *Applied Physics Letters* **71**, 1 (1997). 1.1.1

[33] L. Carley et al. "Single-chip computers with microelectromechanical systems-based magnetic memory (Invited)". *Journal of Applied Physics* **87**, 6680–6685 (2000). 1.1.1

[34] L. Carley, G. Ganger, D. Guillou and D. Nagle. "System design considerations for MEMS-actuated magnetic-probe-based mass storage". *IEEE Transactions on Magnetics* **37**, 657–662 (2001). 1.1.1

[35] S. Lam. "Overview of field-emission information storage devices". *Journal of Vacuum Science and Technology B* **21**, 479 (2003). 1.1.1

[36] G. Gibson et al. "Phase-change recording medium that enables ultrahigh-density electron-beam data storage". *Applied Physics Letters* **86**, 051902 (2005). 1.1.1

[37] H. Kuo, S. Lam, X. Sheng, H. Birecki and S. Naberhuis. "Ultracompact electron-beam column". *Journal of Vacuum Science and Technology B* **24**, 1030 (2006). 1.1.1

[38] Y. Kim et al. "Thermo-piezoelectric Si3N4 cantilever array on CMOS circuit for high density probe-based data storage". *Sensors and Actuators A: Physical* **135**, 67–72 (2007). 1.1.1

[39] C. Lee et al. "Thermal analysis of micro cantilevers integrated with heaters for low power nano-data-storage application". *Sensors and Actuators A: Physical* **139**, 12–16 (2007). 1.1.1

[40] H. Shin et al. "Construction of probe-based data storage with ultra-high areal density". *Proceedings of the 1st IEEE Conference on Nanotechnology* pages 207–212 (2001). 1.1.1

[41] D. Min and H. Seungbum. "New positional error detection algorithm for a probe-based data storage". *Proceedings of IEEE Sensors* pages 601–604 (2004). 1.1.1

[42] Nanochip Inc. (Santa Clara USA). "Array nanoprobe mass storage IC". Retrieved from http://www.nanochipinc.com (2008). 1.1.1

[43] B. Gotsmann and U. Durig. "Thermally activated nanowear modes of a polymer surface induced by a heated tip". *Langmuir* **20**, 1495–1500 (2004). 1.1.2

[44] R. Bennewitz et al. "Atomic scale memory at a silicon surface". *Nanotechnology* **13**, 499–502 (2002). 1.1.2, 1.6

[45] K. Horn. "Charging atoms, one by one". *Science* **305**, 483–484 (2004). 1.1.2

[46] C. Bauschlicher Jr. and C. So. "Using hydrogen and chlorine on Si(1 1 1) to store data". *Chemical Physics Letters* **333**, 1–5 (2001). 1.1.2

[47] U. Quaade, K. Stokbro, R. Lin and F. Grey. "Single-atom reversible recording at room temperature". *Nanotechnology* **12**, 265–272 (2001). 1.1.2

[48] M. Cuberes, R. Schlittler and J. Gimzewski. "Room-temperature repositioning of individual C60 molecules at Cu steps: Operation of a molecular counting device". *Applied Physics Letters* **69**, 3016–3018 (1996). 1.1.2

[49] R. Stadler, M. Forshaw and C. Joachim. "Modulation of electron transmission for molecular data storage". *Nanotechnology* **14**, 138–142 (2003). 1.1.2

[50] S. Porthun, L. Abelmann, S. Vellekoop, J. Lodder and H. Hug. "Optimization of lateral resolution in magnetic force microscopy". *Applied Physics A: Materials Science & Processing* **66**, S1185–S1189 (1998). 1.1.2

[51] T. Albrecht, S. Akamine, M. Zdeblick and C. Quate. "Microfabrication of integrated scanning tunneling microscope". *Journal of Vacuum Science and Technology A* **8**, 317 (1990). 1.1.2

[52] S. Minne, S. Manalis and C. Quate. "Parallel atomic force microscopy using cantilevers with integrated piezoresistive sensors and integrated piezoelectric actuators". *Applied Physics Letters* **67**, 3918 (1995). 1.1.2, 1.3

[53] S. Miller. "Microelectromechanical scanning probe instruments for array architectures". *Review of Scientific Instruments* **68**, 4155 (1997). 1.1.2

[54] M. Tortonese, R. Barrett and C. Quate. "Atomic resolution with an atomic force microscope using piezoresistive detection". *Applied Physics Letters* **62**, 834 (1993). 1.1.2

[55] J. Wagner and J. Spicer. "Theoretical noise-limited sensitivity of classical interferometry". *Journal of the Optical Society of America B: Optical Physics* **4**, 1316–1326 (1987). 1.2.1

[56] E. Synge. "A suggested method for extending microscopic resolution into the ultra-microscopic region". *Philosophical Magazine* **6**, 1 (1928). 1.2.1

[57] R. Wiesendanger. *Scanning Probe Microscopy and Spectroscopy: Methods and Applications*. Cambridge University Press. (1994). 1.2.1, 1.2.5, 3.2.1, 3.2.2, 3.2.2, 5.1.1

[58] D. Pohl, W. Denk and M. Lanz. "Optical stethoscopy: Image recording with resolution λ/20". *Applied Physics Letters* **44**, 651 (1984). 1.2.1

[59] U. Dürig, D. Pohl and F. Rohner. "Near-field optical-scanning microscopy". *Journal of Applied Physics* **59**, 3318 (1986). 1.2.1

[60] K. Karrai et al. "Piezoelectric tip-sample distance control for near field optical microscopes". *Applied Physics Letters* **66**, 1842 (1995). 1.2.1

[61] F. Zijp et al. "High-density near-field optical recording with a solid immersion lens, conventional actuator, and a robust air gap servo". *IEEE Transactions on Magnetics* **41**, 1042–1046 (2005). 1.2.1

[62] A. Ruf et al. "Integrated Fabry–Pérot distance control for atomic force microscopy". *Journal of Vacuum Science and Technology B* **15**, 579 (1997). 1.2.1

[63] A. Kuijpers. *Micromachined capacitive long-range displacement sensor for nanopositioning of microatuator systems*. Ph.D. thesis. University of Twente. Enschede (2004). 1.2.2

[64] S. Lanyi and M. Hruskovic. "The resolution limit of scanning capacitance microscopes". *Journal of Physics D: Applied Physics* **36**, 598–602 (2003). 1.2.2

[65] L. Chu and Y. Gianchandani. "A micromachined 2 D positioner with electrothermal actuation and sub-nanometer capacitive sensing". *Journal of Micromechanics and Microengineering* **13**, 279–285 (2003). 1.2.2

[66] W. van Spengen and T. Oosterkamp. "A sensitive electronic capacitance measurement system to measure the comb drive motion of surface micromachined MEMS devices". *Journal of Micromechanics and Microengineering* **17**, 828 (2007). 1.2.2

[67] D. Wiesmann. "Reduction of read power". Unpublished. Presentation at International Probe Storage Workshop, Zurich (2005). 1.2.3

[68] M. Lantz, G. Binnig, M. Despont and U. Drechsler. "A micromechanical thermal displacement sensor with nanometer resolution". *Nanotechnology* **16**, 1089–1094 (2005). 1.2.3

[69] T. Albrecht, P. Grutter, D. Horne and D. Rugar. "Frequency modulation detection using high-Q cantilevers for enhanced force microscope sensitivity". *Journal of Applied Physics* **69**, 668–673 (1991). 1.2.4, 5.2.4

[70] F. Giessibl. "Atomic Resolution of the Silicon (111)-(7x7) Surface by Atomic Force Microscopy". *Science* **267**, 68–71 (1995). 1.2.4

[71] T. Arai. "Simultaneous imaging of tunneling current and damping energy by noncontact-AFM in ultra-high vacuum". *Applied Physics A: Materials Science & Processing* **72**, 51–54 (2001). 1.2.4

[72] G. Couturier, R. Boisgard, D. Dietzel and J. Aimé. "Damping and instability in non-contact atomic force microscopy: the contribution of the instrument". *Nanotechnology* **16**, 1346–1353 (2005). 1.2.4

[73] S. Porthun. *High Resolution Magnetic Force Microscopy: Instrumentation and Application for Recording Media*. Ph.D. thesis. University of Twente. Enschede (1996). 1.7, 3.1.2

[74] D. Sarid. *Scanning Force Microscopy: With Applications to Electric, Magnetic, and Atomic Forces*. Oxford University Press USA. (1994). 1.2.4, 1.2.4, 1.2.4, 2.4

[75] J. Israelachvili. *Intermolecular and Surface Forces*. Academic Press. New York (1992). 1.2.4, 1.2.4, 1.2.4

[76] S. Porthun, L. Abelmann and J. Lodder. "Magnetic force microscopy of thin film media for high density magnetic recording". *Journal of Magnetism and Magnetic Materials* **182**, 238–273 (1998). 1.2.4

[77] L. Abelmann, A. van den Bos and J. Lodder. "Magnetic Microscopy of Nanostructures". In: *Magnetic Microscopy of Nanostructures*. H. Hopster and H. Oepen (editors). Pages 253–282. Springer (2004). 1.2.4

[78] S. O'Shea et al. "Force based displacement measurement in micromechanical devices". *Applied Physics Letters* **78**, 4031 (2001). 1.2.4

[79] S. Minne et al. "Centimeter scale atomic force microscope imaging and lithography". *Applied Physics Letters* **73**, 1742–1744 (1998). 1.2.4

[80] G. Binnig and H. Rohrer. "In touch with atoms". *Reviews of Modern Physics* **71**, 324–330 (1999). 1.2.5

[81] C. Liu and T. Kenny. "A high-precision, wide-bandwidth micromachined tunneling accelerometer". *Journal of Microelectromechanical Systems* **10**, 425–433 (2001). 1.2.5

[82] R. Kubena, D. Vickers-Kirby, R. Joyce, F. Stratton and D. Chang. "A new tunneling-based sensor for inertial rotation rate measurements". *Sensors and Actuators A: Physical* **83**, 109–117 (2000). 1.2.5

[83] D. DiLella et al. "A micromachined magnetic-field sensor based on an electron tunneling displacement transducer". *Sensors and Actuators A: Physical* **86**, 8–20 (2000). 1.2.5

[84] R. Young, J. Ward and F. Scire. "The Topografiner: An Instrument for Measuring Surface Microtopography". *Review of Scientific Instruments* **43**, 999 (2003). 1.8

[85] R. Young. "Field Emission Ultramicrometer". *Review of Scientific Instruments* **37**, 275–278 (1966). 1.2.6

[86] R. Young, J. Ward and F. Scire. "The Topografiner: An Instrument for Measuring Surface Microtopography". *Review of Scientific Instruments* **43**, 999–1011 (1972). 1.2.6, 3.2.2, 6.3.1, 6.4

[87] R. Young, J. Ward and F. Scire. "Observation of Metal-Vacuum-Metal Tunneling, Field Emission, and the Transition Region". *Physical Review Letters* **27**, 922–924 (1971). 1.2.6

[88] H. Busta, J. Pogemiller and B. Zimmerman. "Field emitter triode as a displacement/pressure sensor". *Journal of Micromechanics and Microengineering* **3**, 49–56 (1993). 1.2.6

[89] A. Hariz, H. Kim, M. Haskard and I. Chung. "Field-emitter cathode for acceleration sensors". *Journal of Micromechanics and Microengineering* **5**, 282–288 (1995). 1.2.6

[90] K. Yamashita, W. Sun, K. Kakushima, H. Fujita and H. Toshiyoshi. "rf microelectromechanical system device with a lateral field-emission detector". *Journal of Vacuum Science and Technology B* **24**, 927–931 (2006). 1.2.6

[91] K. Ekinci and M. Roukes. "Nanoelectromechanical systems". *Review of Scientific Instruments* **76**, 061101 (2005). 1.2.6

[92] D. Pohl. "Some thoughts about scanning probe microscopy, micromechanics, and storage". *IBM journal of Research and Development* **39**, 701–711 (1995). 1.3

[93] K. Wilder. "Nanometer-scale patterning and individual current-controlled lithography using multiple scanning probes". *Review of Scientific Instruments* **70**, 2822 (1999). 1.3, 5.2.4

[94] L. Zhang, J. Bain, J. Zhu, L. Abelmann and T. Onoue. "Heat-assisted magnetic probe recording on a granular CoNi/Pt multilayered film". *Journal of Physics D: Applied Physics* **39**, 2485–2487 (2006). 1.3

[95] S. Gidon et al. "Electrical probe storage using Joule heating in phase change media". *Applied Physics Letters* **85**, 6392 (2004). 1.3

[96] S. Berveling. *The 'MFET': Electrical properties and fabrication of polysilicon nanogaps*. MSc. thesis. University of Twente. Enschede (2006). 2.1

[97] R. Wood. "A New Form of Cathode Discharge and the Production of *X*-Rays, together with Some Notes on Diffraction. Preliminary Communication". *Physical Review (Series I)* **5**, 1–10 (1897). 2.1

[98] R. Fowler and L. Nordheim. "Electron Emission in Intense Electric Fields". *Proceedings of the Royal Society of London. Series A, Containing Papers of a Mathematical and Physical Character* **119**, 173–181 (1928). 2.1, 2.2.1

[99] W. Martienssen and H. Warlimont (editors). *Springer Handbook of Condensed Matter and Materials Data*. Springer. Berlin (2005). 2.1.1, 5.1, 5.2.2

[100] J. Simmons. "Generalized Formula for the Electric Tunnel Effect between Similar Electrodes Separated by a Thin Insulating Film". *Journal of Applied Physics* **34**, 1793–1803 (1963). 2.1.1

[101] A. Modinos. *Field, thermionic, and secondary electron emission spectroscopy*. Plenum Press. New York (1984). 2.1.2, 2.2.1, 2.3.2

[102] W. Schottky. “Uber kalte und warme Elektronenentladungen”. *Zeitschrift fur Physik A: Hadrons and Nuclei* **14**, 63–106 (1923). 2.1.3

[103] D. Temple. “Recent progress in field emitter array development for high performance applications”. *Materials Science & Engineering R: Reports* **24**, 185–239 (1999). 2.2, 2.3.2, 3.1.1, 3.2.2, 4.1.3, 5.1.1

[104] M. Fransen. *Towards high-brightness, monochromatic electron sources*. Ph.D. thesis. TU Delft (1999). 2.1.4, 5.1.1

[105] G. Fursey. *Field Emission in Vacuum Microelectronics*. Springer. Berlin (2005). 7, 2.2.1, 2.3.3, 2.3.3, 5.1.1

[106] K. Jensen. “Electron emission theory and its application: Fowler–Nordheim equation and beyond”. *Journal of Vacuum Science and Technology B* **21**, 1528 (2003). 2.2.1

[107] E. Murphy and R. Good. “Thermionic Emission, Field Emission, and the Transition Region”. *Physical Review* **102**, 1464–1473 (1956). 2.2.1, 2.2.1

[108] K. Jensen and E. Zaidman. “Analytic expressions for emission characteristics as a function of experimental parameters in sharp field emitter devices”. *Journal of Vacuum Science and Technology B* **13**, 511 (1995). 2.2.1

[109] P. Cutler, J. He, N. Miskovsky, T. Sullivan and B. Weiss. “Theory of electron emission in high fields from atomically sharp emitters: Validity of the Fowler–Nordheim equation”. *Journal of Vacuum Science and Technology B* **11**, 387 (1993). 2.2.1

[110] C. Edgcombe and N. de Jonge. “Properties of a field emitter deduced from curvature of its Fowler-Nordheim plot”. *Journal of Vacuum Science and Technology B* **24**, 869 (2006). 2.2.1

[111] J. Barbour, W. Dolan, J. Trolan, E. Martin and W. Dyke. “Space-Charge Effects in Field Emission”. *Physical Review* **92**, 45–51 (1953). 2.2.1

[112] R. Stratton. “Field Emission from Semiconductors”. *Proceedings of the Physical Society, Section B* **68**, 746–757 (1955). 2.2.1

[113] R. Forbes. “Refining the application of Fowler-Nordheim theory”. *Ultramicroscopy* **79**, 11–23 (1999). 2.2.1, 2.2.1, 1

[114] R. Forbes. “Field emission: New theory for the derivation of emission area from a Fowler-Nordheim plot”. *Journal of Vacuum Science and Technology B* **17**, 526–533 (1999). 2.2.1, 2.2.1, 5.1.1

[115] R. Burgess, H. Kroemer and J. Houston. “Corrected Values of Fowler-Nordheim Field Emission Functions v (y) and s (y)”. *Physical Review* **90**, 515–515 (1953). 2.2.1

[116] C. Spindt, I. Brodie, L. Humphrey and E. Westerberg. “Physical properties of thin-film field emission cathodes with molybdenum cones”. *Journal of Applied Physics* **47**, 5248 (1976). 2.2.1

[117] N. de Jonge et al. “Characterization of the field emission properties of individual thin carbon nanotubes”. *Applied Physics Letters* **85**, 1607 (2004). 2.2.1, 3.2.2

[118] R. Forbes. “Simple good approximations for the special elliptic functions in standard Fowler-Nordheim tunneling theory for a Schottky-Nordheim barrier”. *Applied Physics Letters* **89**, 113122 (2006). 2.2.1

[119] R. Forbes and K. Jensen. "New results in the theory of Fowler-Nordheim plots and the modelling of hemi-ellipsoidal emitters". *Ultramicroscopy* **89**, 17–22 (2001). 2.2.1

[120] R. Forbes, C. Edgcombe and U. Valdre. "Some comments on models for field enhancement". *Ultramicroscopy* **95**, 57–65 (2003). 2.2.2, 2.2.2, 2.2.2, 2.2.2

[121] W. Dyke, J. Trolan, W. Dolan and G. Barnes. "The Field Emitter: Fabrication, Electron Microscopy, and Electric Field Calculations". *Journal of Applied Physics* **24**, 570–576 (1953). 2.2.2

[122] H. Miller. "Change in Field Intensification Factor beta of an Electrode Projection (Whisker) at Short Gap Lengths". *Journal of Applied Physics* **38**, 4501–4504 (1967). 2.2.2, 2.2.2

[123] H. Kosmahl. "Analytic evaluation of field emission enhancement factors for ellipsoidal cones and elliptic cross-section wedges". *Electron Devices, IEEE Transactions on* **38**, 1534–1537 (1991). 2.2.2

[124] J. Bonard et al. "Can we reliably estimate the emission field and field enhancement factor of carbon nanotube film field emitters?". *Diamond and Related Materials* **11**, 763–768 (2002). 2.2.2

[125] R. Smith, J. Carey, R. Forrest and S. Silva. "Effect of aspect ratio and anode location on the field emission properties of a single tip based emitter". *Journal of Vacuum Science and Technology B* **23**, 632 (2005). 2.2.2

[126] F. Hecht, O. Pironneau and A. le Hyaric. "FreeFem++, a finite element PDE solver". Software retrieved from http://www.freefem.org (Version 2.14, March 2007). 2.2.2

[127] M. Denhoff. "An accurate calculation of spreading resistance". *Journal of Physics D: Applied Physics* **39**, 1761–1765 (2006). 2.2.2

[128] T. Tsong. "Dynamic behavior and instability of field emitter surfaces". *IEEE Transactions on Electron Devices* **38**, 2317–2319 (1991). 2.3

[129] R. Gomer. *Field emission and field ionization*. Harvard University Press. Cambridge (1961). 2.3.1, 2.3.2

[130] R. Smith. "Sputtering of field electron emitters by self-generated positive ions". *Journal of Physics D: Applied Physics* **17**, 1045–1053 (1984). 2.3.1, 2.3.1

[131] P. Schwoebel and I. Brodie. "Surface-science aspects of vacuum microelectronics". *Journal of Vacuum Science and Technology B* **13**, 1391 (1995). 2.3.1, 2.3.2, 6.3.1

[132] N. Miyamoto, H. Adachi, H. Nakane and K. Yamane. "Emission stability of a field emitter array observed by an emission microscope". *Papers from the 14th International Vacuum Microelectronics Conference* **21**, 436–439 (2003). 2.3.1

[133] K. Ashihara, Y. Saito, S. Tsuchida, H. Nakane and H. Adachi. "Field Emission Characteristics at Short Emitter-to-Anode Distances: A Rough Estimate of the Number of Admolecules". *Electronics and Communications in Japan, Part 2* **6**, 52–57 (1998). 2.3.1

[134] K. Ashihara, H. Nakane and H. Adachi. "Experimental study of field emission characteristics as a function of the emitter to anode distance". *Journal of Vacuum Science and Technology B* **16**, 1180 (1998). 2.3.1

[135] K. Yeong, J. Law and J. Thong. "Field-emission-induced growth of nanowire between electrodes". *Applied Physics Letters* **88**, 193116 (2006). 2.3.2

[136] J. Macaulay, I. Brodie, C. Spindt and C. Holland. "Cesiated thin-film field-emission microcathode arrays". *Applied Physics Letters* **61**, 997 (1992). 2.3.2

[137] F. Charbonnier, W. Mackie, R. Hartman and T. Xie. "Robust high current field emitter tips and arrays for vacuum microelectronics devices". *Journal of Vacuum Science and Technology B* **19**, 1064 (2001). 2.3.2

[138] B. Chalamala et al. "Field emission characteristics of iridium oxide tips". *Journal of Applied Physics* **91**, 6141 (2002). 2.3.2

[139] W. Zhu (editor). *Vacuum Microelectronics*. Wiley-Interscience. (2001). 2.3.2, 3.1.1, 4.1.2, 4.1.2, 5.1.1, 6.5

[140] W. Zhu, G. Kochanski and S. Jin. "Low-Field Electron Emission from Undoped Nanostructured Diamond". *Science* **282**, 1471–1473 (1998). 2.3.2, 4.1.2

[141] F. Baker, A. Osborn and J. Williams. "The carbon-fibre field emitter". *Journal of Physics D: Applied Physics* **7**, 2105–2115 (1974). 2.3.2

[142] N. de Jonge, Y. Lamy, K. Schoots and T. Oosterkamp. "High brightness electron beam from a multi-walled carbon nanotube". *Nature* **420**, 393–395 (2002). 2.3.2

[143] T. Tsong. *Atom-probe field ion microscopy*. Cambridge University Press. New York (1990). 2.3.2, 2.3.3, 2.3.3, 2.3.3

[144] P. Chatterton. "A theoretical study of field emission initiated vacuum breakdown". *Proceedings of the Physical Society* **88**, 231–245 (1966). 2.3.3

[145] W. Karain, L. Knight, D. Allred and A. Reyes-Mena. "Emitted current instability from silicon field emission emitters due to sputtering by residual gas ions". *The 40th National Symposium of the American Vacuum Society* **12**, 2581–2585 (1994). 2.3.3

[146] F. Charbonnier, R. Strayer, L. Swanson and E. Martin. "Nottingham Effect in Field and TF Emission: Heating and Cooling Domains, and Inversion Temperature". *Physical Review Letters* **13**, 397–401 (1964). 2.3.3

[147] J. Barbour et al. "Determination of the Surface Tension and Surface Migration Constants for Tungsten". *Physical Review* **117**, 1452–1459 (1960). 2.3.3

[148] P. Keck and W. Van Horn. "The Surface Tension of Liquid Silicon and Germanium". *Physical Review* **91**, 512–513 (1953). 2.3.3

[149] L. Whitman, J. Stroscio, R. Dragoset and R. Celotta. "Manipulation of Adsorbed Atoms and Creation of New Structures on Room-Temperature Surfaces with a Scanning Tunneling Microscope". *Science* **251**, 1206–1210 (1991). 2.3.3

[150] T. Tsong and G. Kellogg. "Direct observation of the directional walk of single adatoms and the adatom polarizability". *Physical Review B* **12**, 1343–1353 (1975). 2.3.3

[151] L. Abelmann and J. Lodder. "Oblique evaporation and surface diffusion". *Thin Solid Films* **305**, 1–21 (1997). 2.3.3

[152] D. Brandon. "Structure of field-evaporated surfaces". *Surface Science* **3**, 1–18 (1965). 2.3.3, 2.3.3

[153] H. Mamin, P. Guethner and D. Rugar. "Atomic emission from a gold scanning-tunneling-microscope tip". *Physical Review Letters* **65**, 2418–2421 (1990). 2.3.3

[154] I. Lyo and P. Avouris. "Field-Induced Nanometer-to Atomic-Scale Manipulation of Silicon Surfaces with the STM". *Science* **253**, 173–176 (1991). 2.3.3

[155] T. Tsong. "Effects of an electric field in atomic manipulations". *Physical Review B* **44**, 13703–13710 (1991). 2.3.3

[156] J. Pascual et al. "Quantum contact in gold nanostructures by scanning tunneling microscopy". *Physical Review Letters* **71**, 1852–1855 (1993). 2.3.3

[157] U. Gratzke and G. Simon. "Mechanism of nanostructure formation with the scanning tunneling microscope". *Physical Review B* **52**, 8535–8540 (1995). 2.3.3

[158] M. Lu and G. Fedder. "Position control of parallel-plate microactuators for probe-based data storage". *Microelectromechanical Systems, Journal of* **13**, 759–769 (2004). 2.4

[159] J. Colchero, A. Gil and A. Baró. "Resolution enhancement and improved data interpretation in electrostatic force microscopy". *Physical Review B* **64**, 245403 (2001). 2.4, 2.4, 2.4

[160] A. Gil, J. Colchero, J. Gomez-Herrero and A. Baro. "Electrostatic force gradient signal: resolution enhancement in electrostatic force microscopy and improved Kelvin probe microscopy". *Nanotechnology* **14**, 332–340 (2003). 2.4, 2.4, 2, 2.4

[161] N. Tas, T. Sonnenberg, H. Jansen, R. Legtenberg and M. Elwenspoek. "Stiction in surface micromachining". *Journal of Micromechanics and Microengineering* **6**, 385–397 (1996). 2.4, 2.4

[162] S. Sadewasser et al. "Integrated tunneling sensor for nanoelectromechanical systems". *Applied Physics Letters* **89**, 173101 (2006). 2.4

[163] J. Toset, I. Casuso, J. Samitier and G. Gomila. "Deflection–voltage curve modelling in atomic force microscopy and its use in DC electrostatic manipulation of gold nanoparticles". *Nanotechnology* **18**, 015503 (2007). 2.4, 2

[164] S. Hudlet, M. Saint Jean, C. Guthmann and J. Berger. "Evaluation of the capacitive force between an atomic force microscopy tip and a metallic surface". *The European Physical Journal B-Condensed Matter* **2**, 5–10 (1998). 2.4, 2.4

[165] C. Argento and R. French. "Parametric tip model and force-distance relation for Hamaker constant determination from atomic force microscopy". *Journal of Applied Physics* **80**, 6081–6090 (1996). 2.4, 2.4

[166] M. Guggisberg et al. "Separation of interactions by noncontact force microscopy". *Physical Review B* **61**, 11151–11155 (2000). 2.4

[167] N. Tas, J. Wissink, A. Sander, T. Lammerink and M. Elwenspoek. "Modeling, design and testing of the electrostatic shuffle motor". *Sensors and Actuators A: Physical* **70**, 171–178 (1998). 2.4

[168] RHK Technologies (Troy USA). "UHV 300 - External Vibration Isolation subsystem". Retrieved from http://www.rhktech.com (2008). 3.1.1, 3.1

[169] RHK Technologies (Troy USA). "UHV 300 Scanning Tunneling Microscope user's guide". Manual (2008). 3.1.1

[170] Electrolube Ltd. (Reading UK). "Silver conductive paint SCP03B". Properties available through http://www.electrolube.com/docs/tds/044/044SCP.pdf (2007). 3.1.1

[171] RHK Technologies (Troy USA). "XPMPro User's Manual". Manual (2008). 3.1.1

[172] Newport Corp. (Irvine USA). "I-2000 LabLegs Stabilizer Pneumatic Isolators with Automatic Leveling". Retrieved from http://www.newport.com/ (2008). 3.1.1

[173] National Instruments Inc. (Austin USA). "NI LabVIEW Intuitive Graphical Programming Language". Product information on http://www.ni.com/labview/ (2007). 3.1.1

[174] Quatech Inc. (Hudson USA). "ESU-100 8-port USB to RS-232 Serial Adapter". Technical data sheet on http://www.quatech.com/pdf/usb.pdf (2006). 3.1.1

[175] Ontrak Control Systems Inc. (Ontario CA). "ADR2205 RS-232 Relay I/O interface". Technical data sheet on http://www.ontrak.net/adr2205.htm (2007). 3.1.1

[176] Keithley Instruments Inc. (Cleveland USA). "Model 6487 Picoammeter/Voltage Source". Retrieved from http://www.keithley.com/products/locurrhiresist/?mn=6487 (2006). 3.1.1

[177] Corning Inc. (Corning USA). "Macor Machinable Glass Ceramics". Material properties on http://www.corning.com/docs/specialtymaterials/pisheets/Macor.pdf (2007). 3.1.1

[178] D. Rugar, H. Mamin, R. Erlandsson, J. Stern and B. Terris. "Force microscope using a fiber-optic displacement sensor". *Review of Scientific Instruments* **59**, 2337 (1988). 3.1.2

[179] D. Rugar, H. Mamin and P. Guethner. "Improved fiber-optic interferometer for atomic force microscopy". *Applied Physics Letters* **55**, 2588 (1989). 3.1.2

[180] S. Morita, R. Wiesendanger and E. Meyer. *Noncontact Atomic Force Microscopy*. Springer. Berlin (2002). 3.1.2

[181] J. Bono and R. Good, Jr. "Conductance oscillations in scanning tunneling microscopy as a probe of the surface potential". *Surface Science* **188**, 153–163 (1987). 3.2.1

[182] J. Bonard, C. Klinke, K. Dean and B. Coll. "Degradation and failure of carbon nanotube field emitters". *Physical Review B* **67**, 115406 (2003). 3.2.2

[183] M. McCord and R. Pease. "High resolution, low-voltage probes from a field emission source close to the target plane". *Journal of Vacuum Science and Technology B* **3**, 198 (1985). 3.2.2

[184] T. Mayer, D. Adams and B. Marder. "Field emission characteristics of the scanning tunneling microscope for nanolithography". *Journal of Vacuum Science and Technology B* **14**, 2438 (1996). 3.2.2

[185] C. Marrian, E. Dobisz and R. Colton. "Lithographic studies of an e-beam resist in a vacuum scanning tunneling microscope". *Journal of Vacuum Science and Technology A* **8**, 3563 (1990). 3.2.2

[186] K. Wilder, C. Quate, D. Adderton, R. Bernstein and V. Elings. "Noncontact nanolithography using the atomic force microscope". *Applied Physics Letters* **73**, 2527 (1998). 3.2.2

[187] D. Adams, T. Mayer and B. Swartzentruber. "Nanometer-scale lithography on Si (001) using adsorbed H as an atomic layer resist". *Journal of Vacuum Science and Technology B* **14**, 1642 (1996). 3.2.2

[188] K. Gundlach. "Zur berechnung des tunnelstroms durch eine trapezformige potentialstufe". *Solid-State Electron* **9**, 949–957 (1966). 3.2.2

[189] R. Becker, J. Golovchenko and B. Swartzentruber. "Electron Interferometry at Crystal Surfaces". *Physical Review Letters* **55**, 987–990 (1985). 3.2.2

[190] R. Garcia, J. Saenz, J. Soler and N. Garcia. "Distance-voltage characteristics in scanning tunneling microscopy". *Journal of Physics C: Solid State Physics* **19**, L131–L134 (1986). 3.2.2

[191] C. Yang, A. le Fèbre, G. Pandraud, E. van der Drift and P. French. "Field emission for cantilever sensors". *Journal of Vacuum Science and Technology B* (Accepted for publication). 4.1.1, 4.1, 4.2

[192] NanoWorld AG. (Neuchatel CH). "Nanosensors PPP-NCLR". Properties on http://www.nanosensors.com/PointProbePlus.pdf (2006). 4.1.2, 4.1.2, 5.2.4

[193] R. Murillo, H. van Wolferen, L. Abelmann and J. Lodder. "Fabrication of patterned magnetic nanodots by laser interference lithography". *Microelectronic Engineering* **78**, 260–265 (2005). 4.2.2, 4.5, 4.2.3

[194] R. Murillo-Vallejo. *Magnetic Media Patterned by Laser Interference Lithography*. Ph.D. thesis. University of Twente. Enschede (2006). 4.2.2

[195] R. Luttge, H. A. G. M. van Wolferen and L. Abelmann. "Laser interferometric nanolithography using a new positive chemical amplified resist". *Journal of Vacuum Science and Technology B* **25**, 2476–2480 (2007). 4.2.3

[196] AZ Electronic Materials Corp. Branchburg (USA). "AZ Aquatar (Top Antireflective Coating)". Properties on http://www.az-em.com (2008). 4.2.3

[197] F. Charbonnier. "Developing and using the field emitter as a high intensity electron source". *Applied Surface Science* **94**, 26–43 (1996). 5.1.1, 6.3.1

[198] A. Groenland. *Hot tips for chemistry: Development of a carbon nanotube based field emitter array for plasma chemistry on chip*. MSc. thesis. University of Twente. Enschede (2006). 5.1.1

[199] L. Bouwman. *Modeling and fitting field emission currents from tips for probe recording applications*. IOO assignment. University of Twente. Enschede (2007). 5.1.1

[200] R. Forbes, J. Deane, N. Hamid and H. Sim. "Extraction of emission area from Fowler-Nordheim plots". *Journal of Vacuum Science and Technology B* **22**, 1222–1226 (2004). 5.1.1

[201] F. Allen and G. Gobeli. "Work Function, Photoelectric Threshold, and Surface States of Atomically Clean Silicon". *Physical Review* **127**, 150–158 (1962). 5.2.2

[202] J. Redwood. "Fitting a Strength Function by the Levenberg-Marquardt Method". Maple worksheet retrieved from http://www.maplesoft.com/applications/app_center_view.aspx?AID=926 (2001). 5.2.4

[203] K. Yasumura et al. "Quality factors in micron-and submicron-thick cantilevers". *Journal of Microelectromechanical Systems* **9**, 117–125 (2000). 5.2.4

[204] Y. Majima, S. Uehara, T. Masuda, A. Okuda and M. Iwamoto. "The waveform separation of displacement current and tunneling current using a scanning vibrating probe". *Thin Solid Films* **393**, 204–209 (2001). 5.2.4

[205] I. Horcas et al. "WSXM: A software for scanning probe microscopy and a tool for nanotechnology". *Review of Scientific Instruments* **78**, 013705 (2007). 1

[206] W. Dyke, J. Trolan, E. Martin and J. Barbour. "The Field Emission Initiated Vacuum Arc. I. Experiments on Arc Initiation". *Physical Review* **91**, 1043–1054 (1953). 6.3.1

[207] W. Dolan, W. Dyke and J. Trolan. "The Field Emission Initiated Vacuum Arc. II. The Resistively Heated Emitter". *Physical Review* **91**, 1054–1057 (1953). 6.3.1

[208] P. Van Patten, J. Noll, M. Myrick, C. Li and T. Sudarshan. "Spark-Gap Atomic Emission Microscopy". *Journal of Physical Chemistry* **100**, 3646 (1996). 6.3.2

[209] P. Van Patten, J. Noll and M. Myrick. "Spark-gap atomic emission microscopy. II. Improvements in resolution". *Journal of Vacuum Science and Technology B* **15**, 282–286 (1997). 6.3.2

[210] D. Farson, H. Choi and S. Rokhlin. "Electrical discharges between platinum nanoprobe tips and gold films at nanometre gap lengths". *Nanotechnology* **17**, 132–139 (2006). 6.3.2

[211] M. A. McCord, D. P. Kern and T. H. P. Chang. "Direct deposition of 10-nm metallic features with the scanning tunneling microscope". *Journal of Vacuum Science and Technology B* **6**, 1877–1880 (1988). 6.3.3

[212] A. Broers, W. Molzen, J. Cuomo and N. Wittels. "Electron-beam fabrication of 80-Å metal structures". *Applied Physics Letters* **29**, 596 (1976). 6.3.3

[213] M. Ruhrig, S. Porthun and J. Lodder. "Magnetic Force Microscopy Using Electron-Beam Fabricated Tips". *Review of Scientific Instruments* **65**, 3224–3228 (1994). 6.3.3

[214] D. Alman, D. Ruzic and J. Brooks. "A hydrocarbon reaction model for low temperature hydrogen plasmas and an application to the Joint European Torus". *Physics of Plasmas* **7**, 1421 (2000). 6.3.3

[215] N. Silvis-Cividjian, C. Hagen, L. Leunissen and P. Kruit. "The role of secondary electrons in electron-beam-induced-deposition spatial resolution". *Microelectronic Engineering* **61**, 693–699 (2002). 6.3.3

[216] P. Niedermann, C. Renner, A. Kent and O. Fischer. "Study of field-emitting microstructures using a scanning tunneling microscope". *Journal of Vacuum Science and Technology A* **8**, 594 (1990). 6.4

[217] C. Marrian, E. Dobisz and J. Dagata. "Electron-beam lithography with the scanning tunneling microscope". *Journal of Vacuum Science and Technology B* **10**, 2877 (1992). 6.4

[218] J. Levine. "Benefits of the lateral resistor in a field effect display". *Journal of Vacuum Science and Technology B* **14**, 2008 (1996). 6.5

About the author

Alexander le Fèbre was born in Apeldoorn on October 6th, 1977. From 1990 he was educated at the 'Christelijk Lyceum Apeldoorn' where he received his VWO diploma in 1996. In the same year he started studying Electrical Engineering at the University of Twente in Enschede, the Netherlands. In 2001 he did a practical training at the Seagate Research department in Pittsburgh, USA, where he carried out dynamic coercivity measurements on longitudinal and perpendicular recording media using a contact write/read tester. His graduation work, entitled 'Fabrication and characterization of magnetic nanowires', was carried out in the Systems and Materials for Information-storage (SMI) group, led by prof. Cock Lodder. After finalizing this work in 2003, he received his MSc (ir.) degree and continued to work in the SMI group as a PhD. His work was part of the project 'A high capacity, low volume Scanning Probe Array Memory for application in embedded systems', funded by the Dutch Technology foundation (STW). The outcomes of his PhD research project are the subject of this thesis.

Journal publications

- Fèbre, A.J. le, Abelmann, L. and Lodder, J.C. (2008). "Field emission at nanometer distances for high-resolution positioning". Accepted for publication in: *Journal of Vacuum Science and Technology B*. ISSN: 1071-1023.
- Yang, C.K., Fèbre, A.J. le, Pandraud, G., Drift van der, E. and French, P.J. (2008). "Field emission for cantilever sensors". Accepted for publication in: *Journal of Vacuum Science and Technology B*. ISSN: 1071-1023.
- Fèbre, A.J. le, Luttge, R, Abelmann, L. and Lodder, J.C. (2007). "Field emission tip-sample distance control for multiprobe applications". *Journal of Physics: Conference Series* **61**, pp. 673-677. ISSN: 1742-6596.

Conference proceedings

- Fèbre, A.J. le, Abelmann, L. and Lodder, J.C. (2007). "Field emission to control nanometer tip-medium distances in probe storage". *Technical Digest of the 20th International Vacuum Nanoelectronics Conference*, pp. 223-224. ISBN: 1-4244-1134-3.

- Fèbre, A.J. le, Bouwman, L.A.A., Abelmann, L. and Lodder, J.C. (2007). "Field emission to control tip-sample distance in probe recording". *Proceedings of the Innovative Mass Storage Technologies Workshop 2007*, pp. 81-82.
- Fèbre, A.J. le, Siekman, M., Abelmann, L. and Lodder, J.C. (2007). "Displacement sensing by field emission with nanometer resolution". *Digest of technical papers of the 14th International Conference on Solid-State Sensors, Actuators and Microsystems - Transducers'07 & Eurosensors XXI*, pp. 2361-2364. ISBN 1-4244-0841-5.
- Yang, C.K., Fèbre, A.J. le, Pandraud, G., Drift, E. van der, and French, P.J. (2007). "Field emission for resonance sensing in MEMS/NEMS". *Technical Digest of the 20th International Vacuum Nanoelectronics Conference*, pp. 72-73. ISBN: 1-4244-1134-3.
- Fèbre, A.J. le, Luttge, R., Abelmann, L. and Lodder, J.C. (2006). "Field emission tip-sample distance control for multiprobe applications". *Proceedings of the International Conference of Nanoscience and Technology (ICN+T) 2006*, pp. 24-25.
ISBN 3-905084-71-6.
- Fèbre, A.J. le, Lodder, J.C. and Abelmann, L. (2006). "Tip-sample distance control for magnetic probe recording". *Proceedings of the Joint European Workshop IMST and E*PCOS 2006*, pp. 253-254.
- Bos, A.G. van den, le Fèbre, A.J., Saito, H., Ramstöck, K., Siekman, M.H., Abelmann, L. and Lodder, J.C. (2003). "High resolution magnetic tips and integrated multi-wire probes for scanning probe microscopy". *AIP Conference Proceedings: Scanning Tunneling Microscopy / Spectroscopy and Related Techniques, 12th International Conference STM'03* **696**, pp. 320-327.
- Veerdonk, R.J. van de, Crawford, T.M., Wu, X.W., Langzettel, A.K., Fèbre, A.J. le, Wang, S., Batra, S. and Weller, D. (2002). "Remanent dynamic coercivity measurements below 1 ns timescales for perpendicular and longitudinal recording media". *Digest of the 47th Annual Conference on Magnetism and Magnetic Materials 2002*, pp. 64.

Conference contributions

- Fèbre, A.J. le *et al* (2007). *Field emission to control nanometer tip-medium distances in probe storage*, 20th International Vacuum Nanoelectronics Conference, 8 - 12 July 2007, Chicago, USA.
- Fèbre, A.J. le *et al* (2007). *Field emission to control tip-sample distance in probe recording*, Innovative Mass Storage Technologies Workshop, 18 - 20 June 2007, Enschede, The Netherlands.
- Fèbre, A.J. le *et al* (2007) *Displacement sensing by field emission with nanometer resolution*, Transducers'07 & Eurosensors XXI, 10 - 14 June 2007, Lyon, France.
- Fèbre, A.J. le *et al* (2006) *Field emission tip-sample distance control for multiprobe applications*, Joint conference STM'06 en NANO9 (ICN+T 2006), 30 July - 4 August 2006, Basel, Switzerland.
- Fèbre, A.J. le *et al* (2006) *Tip-sample distance control for magnetic probe recording*, Innovative Mass Storage Technologies Workshop, 29 - 31 May 2006, Grenoble, France.
- Fèbre, A.J. le *et al* (2005) *Tip-sample distance control for μSPAM* , International Probe Storage Workshop, 28 February - 1 March 2005, Zurich, Switzerland.

- Fèbre, A.J. le *et al* (2004) *Tip-sample distance control for μSPAM* , Innovative Mass Storage Technologies Workshop, 28 - 29 September 2004, Aachen, Germany.

Other contributions

- Abelmann, L. and Fèbre, A.J. le (2008) *Doorslaan in veld emissie* (in Dutch). 'Doorgeslagen', Jaarboek E.T.S.V. Scintilla 2006-2007. University Twente.
- Miltenburg, O. van, Fèbre, A.J. le and Abelmann, L. (2004) *De harde schijf voorbij* (in Dutch). HCC Magazine (available through http://www.hccmagazine.nl/index.cfm?fuseaction=home.showArtikelen&id=46410)

Dankwoord

Aan het einde gekomen van dit proefschrift komt er dan ook een einde aan de lange weg van mijn promotie. Er moesten een aantal behoorlijke hobbels worden genomen, zowel in het onderzoek als in mijn persoonlijke leven, maar het is gelukt en nu kan ik terugkijken op een leerzame periode. Graag wil ik dit dankwoord gebruiken om een aantal mensen speciaal te noemen die mij hebben geholpen in de afronding van dit project.

Allereerst wil ik natuurlijk mijn begeleider Leon Abelmann en promotor Cock Lodder bedanken voor hun inzet en onvoorwaardelijke steun. Dankzij de positieve instelling en het geduld van Leon is 'doorslaan' voorkomen en is dit boekje er gekomen. Door de inspirerende persoonlijkheid van Cock ben ik ooit aan deze promotie begonnen en hij heeft me er met zijn pep-talks ook doorheen geholpen. Fijn dat we nog een paar maanden kunnen samenwerken. De Technologiestichting STW wil ik graag bedanken voor het financieren van het project.

In het onderzoek hebben heel wat mensen een bijdrage geleverd. Aan het begin van mijn promotie heb ik gebruik gemaakt van een 'golden oldie' STM van Harold Zandvliet, die ik hier hartelijk voor wil bedanken. Hoewel er geen resultaten van in dit proefschrift staan, is deze wel van grote waarde voor mij geweest in het leren omgaan met STM en het bedenken van eisen voor het aan te schaffen exemplaar. Graag wil ik Lodewijk Bouwman bedanken voor zijn hulp en slimme ideeën. Hij was de enige van mijn studenten die het aandurfde om zich bezig te houden met veld-emissie, en dan de theorie nog wel! Tijdens de metingen stuitte ik al snel op de weerbarstige praktijk van de experimenten. Gelukkig heb ik veel hulp gehad van onze technici: Martin Siekman, Johnny Sanderink, Jos Pasop en Thijs Bolhuis. Hen wil ik daarom ook hartelijk bedanken, niet in de laatste plaats vanwege hun persoonlijke aandacht naast het werk. Ook Jan Talman wil ik graag bedanken voor zijn hulp bij het bouwen van het vacuüm-systeem. Door de samenwerking met Chung-Kai Yang uit Delft kon ik eindelijk een belangrijke stap voorwaarts zetten in het onderzoek. Dankzij zijn hulp kreeg ik probes om aan te meten zonder me druk te hoeven maken over cantilevers of vreemde tip vormen. Hopelijk kunnen we, nadat hij mij heeft bijgestaan als paranimf, nog een tijdje samenwerken en een paar mooie metingen laten zien. Dat geldt ook voor

Tjerk Oosterkamp en Anne France Beker, die in Leiden carbon nanotube tips maken. Hen wil ik graag hartelijk bedanken voor hun inspanningen tot nu toe. Regina Luttge, Henry Kelderman en Henk van Wolveren hebben mij enorm geholpen door de patterned samples te fabriceren. Een hele zoektocht, maar uiteindelijk heeft dit geleid tot de zeer kleine patronen van dots die nodig waren voor mijn metingen en die van anderen. Mark Smithers is verantwoordelijk voor de SEM plaatjes in dit proefschrift. Hij weet in no-time scherpe opnames tevoorschijn te toveren en daarnaast is er bij hem altijd een leuk gesprek mogelijk. Ook de staf van de MESA$^+$ cleanroom wil ik natuurlijk heel hartelijk bedanken. Dankzij hen functioneert de cleanroom zo goed, en dan zijn ze nog reuze gezellig ook: de Batavieren-race was tof en de jaarlijkse Glühwein-party zal ik zeker gaan missen.

Tijdens mijn tijd bij de vakgroep SMI heb ik veel veranderingen meegemaakt en uiteindelijk is de groep zelfs opgesplitst. Graag wil ik mijn vriendelijke collega's van zowel TST-SMI als NE hartelijk bedanken. Met plezier zal ik terugdenken aan het vele taart-eten met de groep aan de koffietafel en de vrijdagmiddag-borrels met een al dan niet serieus gesprek. Ik ben blij dat sommigen van mijn (internationale) collega's nu mijn vrienden zijn geworden. Bij het overlijden van mijn moeder heb ik gemerkt hoe belangrijk het is dat je collega's meeleven en dat heeft veel voor mij betekend. Mijn kamergenoten, Ehtsham, Mink, Regina, bedankt voor de goede sfeer en de leuke gesprekken. Wabe en Johan wil ik speciaal bedanken omdat zij in mijn plaats naar een conferentie gingen vanwege de geboorte van mijn zoon, en Wabe natuurlijk omdat hij mijn paranimf wil zijn. Secretaresses Karen en Thelma wil ik graag bedanken voor hun inzet voor de groep en hulp aan mij. Na de groepssplitsing kwamen wij gelukkig terecht in de leukste vakgroep van de UT: MicMec. Het was leuk om mee te doen aan de Smikkel-parties, Feuerzang-bowle en natuurlijk Sinterklaas. Bedankt voor jullie gastvrije ontvangst! Mijn mede-bestuursleden van promovendi-vereniging P-NUT wil ik graag bedanken voor de fijne samenwerking.

Een belangrijke ontdekking die ik deed tijdens mijn promotie is de ontspanning van het hardlopen. Al begon ik alleen maar om af te komen van het 'studenten-buikje', dit is nu een belangrijk ingrediënt in mijn leven. Samen met collega's lopen tijdens de lunch-pauze of na werktijd is de moeite waard. Grote Aanjager Martin wil ik hier graag speciaal voor bedanken, en natuurlijk voor al zijn hulp bij de metingen en support voor mij persoonlijk. Hopelijk kunnen we nu weer verder lopen, nu het proefschrift af is en de zon weer begint te schijnen.

Mijn familie en vrienden, ik zal niet alle namen noemen, maar ik ben enorm blij dat zij er zijn, voor de persoonlijke aandacht en natuurlijk de gezelligheid. Mijn ouders wil ik op deze plek graag bedanken omdat zij zo goed voor mij gezorgd hebben, en in het speciaal mijn moeder, die we nu helaas moeten missen. Marianne, jij was gelukkig al die tijd aan mijn zijde: ik heb je lief, wat moet ik zonder jou? Michiel, zo klein als je nog bent, bedankt voor het bieden van afleiding tijdens mijn lange nachten achter de laptop en voor je stralende lach... nou ja, ná de fles dan. Hopelijk kunnen we vanaf nu nog meer van onze tijd samen gaan genieten!

Field Emission Sensing for Non-Contact Probe Recording

Alexander le Fèbre

In probe recording an array of thousands of nanometer-sharp probes is used to write and read on a storage medium. Such a system is expected to offer a promising route towards extremely high density recording, with bits of several nanometer or even atomic size. To reach these densities, individual control over the position of the probes is essential, to be able to operate them at several nanometers above the medium.

For non-contact operation, individual z-feedback should be achieved by integration of an actuator, proximity sensor and feedback loop in each probe of the array. Current research still lacks a sensor with sufficient lateral resolution that can be integrated in each probe.

Field emission can be used for proximity sensing, since the emission current varies exponentially with the electric field, which in turn is proportional to the electrode gap. The objective of this thesis is to investigate whether field-emission can be applied as an integrated method to control nanometer probe-medium distances in non-contact probe recording.

ISBN 978-90-8570-300-6